# STRUCTURAL, OPTICAL AND ELECTRICAL CHARACTERIZATION OF NANO-SIZED C-$TiO_2$ QUAMTUM DOTS SYNTHESIZED BY SPRAY PYROLYSIS

**RAYMOND TICHAONA TAZIWA**

Department of Chemistry

University of Fort Hare, Alice Eastern Cape

Republic of South Africa

[1]**Promoter**: Prof. E.L. Meyer Director: Institute of Technology, University of Fort Hare, Private Bag X1314, Alice 5700, Republic of South Africa

[2]**Co Promoter**: Prof. P.A. Ajibade Department of Chemistry University of Fort Hare Private Bag X1314, Alice 5700, Republic of South Africa

**MAY 2014**

## DECLARATION

I, the undersigned, hereby declare that the work contained in this doctoral thesis is my own original work and that I have not previously submitted it, in it's entirely or in part, at any university or any other academic institution for degree purposes.

_____

*(Signature of candidate)*

_____

*(Date)*

This work is dedicated to

to God Almighty who has been my eternal rock and source of refuge

to my brother, Tendai Clever Taziwa for bringing me up and giving me financial support up to the University undergraduate level

to Thabisa Taziwa, my wife
for her support and inspiration throughout my studies

to my mother and father for their endurance during my long absence from home

## PREFACE

In the 21st century, scientific communities face challenges and opportunities concerning future development, where innovations must be a key driver over the past, evolution of African societies were based on incomplete models, only taking into account economical growth and not paying attention to environmental deterioration as a consequence of anthropogenic activity and environmental pollution. We have to learn from our past mistakes in order not to repeat them. Education and research of today as the embryonic stages of the development models of tomorrow should be directed toward a sustainable mentality. In this sense, solar energy technologies have emerged as key instruments for minimizing environmental impact as well as reducing economic cost in the field of renewable energies.

Titanium dioxide is a fascinating low cost material exhibiting unique properties of stability and photo catalytic activities, leading to clean technologies in water purification and energy conversion of sunlight. However, conventional techniques (high temperature, high vacuum, high pressures) of processing titanium dioxide are a technological limitation due to excessive energy consumption. This poses a handicap for practical applications in areas such as preparation of hybrid organic/Titanium dioxide materials or devices on thermo flexible substrates such as plastic material. It is for this reason that the investigation presented in this Ph.D thesis deals with the development of spray pyrolysis techniques for preparation of carbon doped titanium dioxide nano powders for solar cell applications.

This thesis is therefore structured as follows: *Chapter 1* gives a general overview of the work done in this thesis. This work relies greatly on the excellent structural optical and electrical properties of $TiO_2$ thin films, as well as its chemical resistance and insulating properties. A summary of the physical, optical, electrical and chemical properties reported in the literature, with an emphasis on those relevant to solar cell fabrication, is presented in *Chapter 2*. *Chapter 3* gives a concise literature review on models governing droplet formation in ultrasonic spray pyrolysis (USP) techniques, the limitations of these models have been exposed and a new relation model for estimating the final particle size given a set of initial reaction conditions has

been proposed. The presently derived model is quite advantageous in that it does not require the investigator to look up values of surface tension and density for every precursor solution. *Chapter 4* presents in detail the designed and constructed spray pyrolysis system capable of realizing desired nano structures for photovoltaic applications. The first system employed an ultrasonic atomization spray nozzle in order to create an aerosol of the $TiO_2$ precursor. The reasons for choosing ultrasonic spray deposition (USP) and the $TiO_2$ precursors, titanium iso propoxide and titanium tetra butoxide are discussed. *Chapter 5* outlines experimental methodologies used in synthesis and characterization of the materials used in this study. *Chapter 5* further provides experimental methodologies used in fabrication of a new type of photo electrochemical solar cells (PECs). *Chapter 6* reveals the opto-electrical results of PECs solar cells fabricated. There are numerous properties that are affected by the size but emphasis will be placed on nano-size and confinement effects. *Chapter 7* presents a confirmation of the phonon confinement effects in C-$TiO_2$ QDs for the first time. In addition *Chapter 7* also presents a new phonon confinement model. *Chapter 8* reveals the optical, structural and electronic properties of C-$TiO_2$ QDs synthesized by USP and PSP techniques. In addition the electrical properties of C-$TiO_2$ QDs PEC solar cells devices are reported in *Chapter 8*. Concluding remarks, with potential future research projects are presented in *Chapter 9*. Through these 9 chapters, all research questions have been answered satisfactorily and all objectives met. Most of the work contained in this thesis has been subjected to external reviews through publication of these peer reviewed articles:

## ACKNOWLEDGEMENTS


- It has been possible to produce this thesis due to significant contributions many people have made. Although, it is not possible to list here the names of all those I am indebted to in this regard, I want them to know that I deeply appreciate their contributions.

- I would like to thank my promoter Prof. Edson Meyer and all members of the Renewable energy group at Fort Hare Institute of Technology for the good working atmosphere. I would like to express my gratefulness to Prof E.L Meyer for giving me the opportunity to present scientific results and represent our group in international and regional scientific meetings. This showed his faith and confidence in my work which was important to gain self-confidence and grow as an independent scientist. Furthermore I learned from him that it is important to keep always the big picture in mind, put scientific aspects together and see the work in broader context.

- My co-promoter Prof P. Ajibade for his excellent motivation and guidance throughout the study.

- Temperature dependence analyses and laser power dependence analyses of C-$TiO_2$ quantum dots where done at the School of Physics, University of Witwatersrand and I would like to thank Rudolph Erasmus for his assistance.

- I would like also to kindly acknowledge the assistance the CSIR Nanotechnology centre has rendered to me with regard to equipment for analyses of semiconductor quantum dots. Special thanks are due to Professor Thembela Hillie, for the warm welcome. I am also highly indebted to Dr. B. Mwakikunga for his unwavering support, advice on choice of equipment and the quantum confinement analyses, without them most of my work would been have fruitless.

- The Chemistry department, University of Fort Hare for their constant support throughout the duration of the project.

- Funding Eskom TESP, DTi through THRIP and DST through the n SANERI PV Spoke hosted jointly by UFH and NMMU.

- To all these people, any merit this volume may possess is without doubt due to their individual and collective participation; the defects are probably all my fault.

## EXECUTIVE SUMMARY

This thesis provides a concise review on ultrasonic spray pyrolysis (USP) techniques. The USP technique at the Fort Hare Institute of Technology (FHIT), University of Fort Hare, Republic of South Africa was designed and assembled by the candidate for the sole purpose of producing $TiO_2$ quantum dots (QDs), nano-particles (NPs) and thin films (TFs). Due to its inherent properties, $TiO_2$ and derivates of $TiO_2$ are the most suitable candidates for photovoltaic applications more particularly in photochemical solar cell (PEC) devices. The thesis pursues small particles of these materials in order to observe, evaluate and analyze the change in their properties at nano-scale. Novel nano-structures that were not expected to be found were discovered in carbon doped Titanium dioxide (C-$TiO_2$) QDs synthesized by the USP system. Furthermore the droplet relation models for estimating droplet size produced in USP has been reviewed, revisited and a new droplet correlation model that estimates final nano-particle size has been developed. This new final nano-particle size correlation model uses only initial reaction conditions, which has been done here for the first time. High resolution transmission electron microscopy (HRTEM) on the QDs shows differences in lattice spacing in the QDs structures prepared by the two methods – 2.02 Å for the USP QDs and an average of 3.74 Å for the (PSP) QDs. The most probable particle size is for USP and PSP respectively are 3.11± 0.02 nm and 5.5 ± 0.02 nm. The carbon doping changes the lattice spacing's of the $TiO_2$. The most predominant plane is the (101) in $TiO_2$ reciprocal lattice as determined from the Fast Fourier Transform of most of the particle images. Raman spectroscopy supported by FTIR confirms the $TiO_2$ polymorph to be Anatase with the intense phonon frequency at 153 $cm^{-1}$ blue-shifted from 141 $cm^{-1}$ due to both carbon doping and particle size. Electronic measurements show "negative conductance" at some critical voltage bias which is characteristic of *n*-type conductivity in the carbon doped $TiO_2$ QDs as confirmed by the calculated areas under the *I-V* curves. In Raman spectra of the as-obtained C-$TiO_2$ QDs asymmetric broadening of the Raman peaks was observed. These findings prompted the development a novel phonon confinement model. We also used a modified form of the Faucet-Campbell equation which incorporates a particle size distribution factor equation, also the size distribution integral in the new modified Faucet–Campbell has been replaced by an expression $A_1 + m\omega = 0.25 + 0.008\ \omega$ to take into account the background noise inherent in the fluorescent nano-structures. From this fit the following

parameters have been extracted, $A_0' = 10^{-17}$, $\alpha = 3\,\pi^2$ (~ 30), $\omega_0 = 150.4$ cm$^{-1}$, $B = 0.005$ cm$^{-2}$ and $\Gamma_0 = 20$ cm$^{-1}$. These results show that the blue-shift of the central Brillouin zone phonon frequency from 143.4 cm$^{-1}$ for particles of mean diameter of 50 nm of pure $TiO_2$ to 150.4 cm$^{-1}$ for particles of mean diameter of 6 nm is not only due to reduction of particle size but also due to the presence of carbon in the $TiO_2$ structure. Temperature dependence of Raman spectroscopy was done for the first time on C-$TiO_2$ nano-particles and it revealed that the as-synthesized nano-particles are predominantly Anatase with the $E_{g(1)}$ peak at 152.9 cm$^{-1}$ blue shifted due to carbon doping and decrease in particle size. We have also demonstrated solid state photochemical solar cell (PEC) devices using C-$TiO_2$ photo electrodes, synthesized by USP. Carbon doping of nano crystalline titanium dioxide was found to be beneficial for PEC solar cell device performance, with significant improved open circuit voltage ($V_{OC}$) of 0.817 V as compared to pure dye sensitized solar cells devices which employ pure un-doped $TiO_2$ with a open circuit voltage ($V_{OC}$) of 0.75 V. This improvement in photo voltage output is found to be correlated with the electronic and optical properties of the nano-powders used in fabrication of PEC devices. Furthermore the C-$TiO_2$ QDs produced by USP have shown properties that would not only make the materials suitable for photo-catalytic activity, but also for electrodes in Grätzel-type solar cells. Efficiency values for solar cells of varying carbon concentrations in their $TiO_2$ electrodes show up to 15% improvement over the pure $TiO_2$ electrode based in PEC device.

# TABLE OF CONTENTS

## LIST OF SYMBOLS, ABBREVATIONS AND ACRONYMS

| | |
|---|---|
| USP | Ultrasonic spray pyrolysis |
| FHIT | Fort Hare Institute of Technology |
| QDs | Quantum dots |
| NPs | Nano-particles |
| TFs | Thin Films |
| PEC | Photo electrochemical device |
| HRTEM | High resolution transmission electron microscopy |
| Prof | Professor |
| CSIR | Council for Scientific Research |
| Ph.D | Doctor of Philosophy |
| MSc | Masters in Science |
| TW | Terawatts |
| CNT | Carbon Nano tubes |
| RTITT | Rio Tinto Iron & Titanium |
| RBM | Richards Bay Minerals |
| TPT | tetra-isopropyl titanate |
| TiCl4 | Titanium tetrachloride |
| F: $SnO_2$ | Fluorine doped Tin oxide |
| $TiO_2$ | Titanium Dioxide |
| VB | Valence Band |
| CB | Conduction Band |
| MOSFET | Metal oxide semiconductor field effect transistor |
| ZnO | Zinc Oxide |
| TCO | Transparent conductive oxide |
| AM | Air Mass |
| CVD | Chemical Vapor Deposition |
| SP | Spray Pyrolysis |
| kHz | Kilo hertz |
| MHz | Mega hertz |

| | |
|---|---|
| PECV | plasma enhance chemical vapor deposition |
| LPCVD | Low pressure chemical vapor deposition |
| APCVD | atmospheric pressure chemical vapor deposition |
| MOCVD | Metal organic chemical vapor deposition |
| GLAD | Glancing angle deposition |
| FTO | Fluorine doped tin oxide |
| SEM | Scanning electron microscopy |
| EDX | Energy dispersive x-ray spectroscopy |
| TEM | Transmission Electron Microscopy |
| XRD | X-ray Diffraction technique |
| RS | Raman spectroscopy |
| mW | milliwatt |
| KBr | Potassium bromide |
| FTIR | Fourier transform infrared spectroscopy |
| Uv-Vis | Ultraviolet–visible spectroscopy |
| USA | United State of America |
| SCS | Semiconductor characterization system |
| TIP | Titanium iso-propoxide |
| mM | mill molar |
| OA | Oxalic acid |
| TBA | Tetra-butyl ammonium bromide |
| DSSC | Dye sensitized solar cell |
| HOMO | Highest occupied molecular orbital |
| LUMO | Lowest un-occupied molecular orbital |
| FWHM | Full width at half maximum |
| EDS | Energy dispersive spectrum |
| *I-V* | Current Voltage |
| $\beta$ | A constant in the sensor sensitivity function |
| $C_{pr}$ | Concentration of the precursor solution |
| $\omega(q)$ | Dispersion relation for the phonon |
| $\rho$ | Density of the precursor solution |

| | |
|---|---|
| $M$ | mass in kilograms |
| $L$ | length in meters |
| $T$ | time in seconds |
| $e^-_{CB}/h^+_{VB}$ | Electron-hole photon generated in a semiconductor |
| $eV$ | Electron Volts |
| $f$ | Frequency of the ultrasonic transducer |
| $f_{PSP}$ | Frequency of pneumatic spray pyrolysis |
| $\Gamma_0$ | Full width at half maximum in Raman spectra for bulk material Raman peak |
| $P$ | Gauge pressure in the SP system |
| $D$ | Grain size |
| $\varphi$ | rate potential |
| $M_{pr}$ | Molar mass of precursor solution |
| $M_p$ | Molar mass of the particles after decomposition of the precursor |
| $\xi$ | Normal coordinates used in describing the polarizing function |
| $\omega$ | Peak Raman shift or Raman frequency |
| $E_g$ | Phonon modes allowed in Raman spectroscopy |
| $A1g$ | Phonon modes allowed in Raman spectroscopy |
| $B1g$ | Phonon modes allowed in Raman spectroscopy |
| $\Gamma$ | Phonon distribution function |
| $\alpha$ | Polarizability function of molecules used in Raman spectral theory |
| $q$ | Phonon wave number |
| $\sigma$ | Surface tension of precursor solutions |
| $T_{pre}$ | Temperature of precursor solution |
| $\eta$ | Viscosity of precursor solutions |
| $V$ | Volume of the SP system |
| $We$ | Weber number |

## CERTIFICATION

This is to certify that this work was carried out by Mr. Raymond Tichaona Taziwa at University of Fort Hare institute of Technology (FHIT)

_____

Promoter

**Prof. E.L. Meyer (PhD, CEM, CMVP, MS.c.)**

**Director: Fort Hare Institute of Technology (FHIT)**

**University of Fort Hare**

_____

Co Promoter

**Prof. P.A. Ajibade (PhD, MRSC, MSc)**

**Senior Lecturer**

**Department of Chemistry**

**University of Fort Hare**

# CHAPTER 1

# TITANIUM DIOXIDE

*''The principles of science, as far as I can see, do not speak against the possibility of maneuvering things atom by atom. It is not an attempt to violate any laws: It is something in principle that can be done; but in practice it has not been done because we are too big.'' (Feynman, 1959)*

## 1.1 BACKGROUND OF STUDY

The need for inexpensive, clean energy is increasing every day as more and more nations develop and the world's population increases. One of the most promising sources of energy for powering the planet is solar energy. Approximately 120 000 terawatts (TW) of solar power strike the earth every day. Currently, only 0.005% of the world's energy production is from solar energy [1]. This brings us to the question, "Why are we not harnessing the sun to power the planet?" The fundamental answer to the question as to why the worlds isn't using solar is cost. Solar energy is more expensive than conventional means of energy, such as coal and fossil fuels. In South Africa 2012 the cost of electricity produced from coal was about R0.52-R0.65 per kilowatt hour and the cost of solar electricity was about R2.69-R2.72 per kilowatt hour. The high cost of solar energy explains why 77% of the South African energy comes from coal and 80-90% of the world's energy comes from fossil fuels [2].

In order to overcome such high cost, solar cells must be made from either cheaper materials, cheaper technologies and/or become more efficient. In order to be as efficient as possible solar cells must make efficient use of the solar spectrum shown in Figure 1.1. The region between 400-1100 nm has the highest photon density in the AM 1.5 solar spectrum. A material that can absorb sunlight within this region would be the ideal solar absorber. Silicon solar cells accomplish this task, because silicon's band gap is 1.1 eV. Despite their reputation as a sustainable alternative, solar cells still lack the efficiency necessary to replace other cheaper modes of electricity generation on a larger scale. Solar energy is a good and much needed alternative to the present reliance on fossil fuels for energy. It is a source of energy that has been

thoroughly researched and is continously developing. Through the use of nanotechnology, solar cells are being revolutionized. This third generation of solar cells is the future of low cost and high efficiency solar energy and will hopefully mark the end of non-renewable sources of energy. New technologies, such as quantum dot solar cells, are being researched and developed and are more efficient and cost-effective than the traditional silicon solar cells.

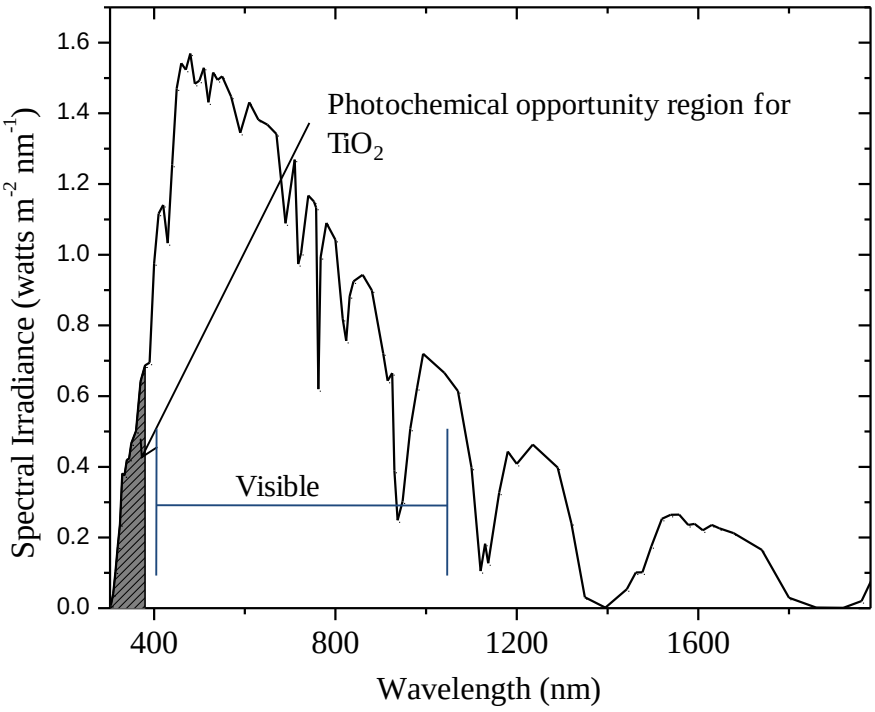


*Figure 1.1: Solar spectral distribution at AM=1.5 [3]. The area signaled with an arrow indicates the useful wavelength range for $TiO_2$ photo excitation*

The nanotechnology of quantum dots is being incorporated into solar cells to make them ultra-efficient energy convertors. Nanotechnology is the concept of building systems on the molecular scale, which are only a few nanometers in size [4, 5]. These nano-particles, ranging in size from one nanometer to twenty nanometers, are typically made out of compounds such as titanium oxide and zinc oxide [5]. One type of quantum dot solar cell is called dye-sensitized solar cells. Dye-sensitized solar cells are a low cost type of solar cell with a different structure that incorporates quantum dots in order to improve the efficiency. The semiconductor quantum dots

are typically made out of titanium oxide or zinc oxide [6, 7]. A diagram of a quantum dot dye-sensitized solar cell is depicted in Figure 1.2.

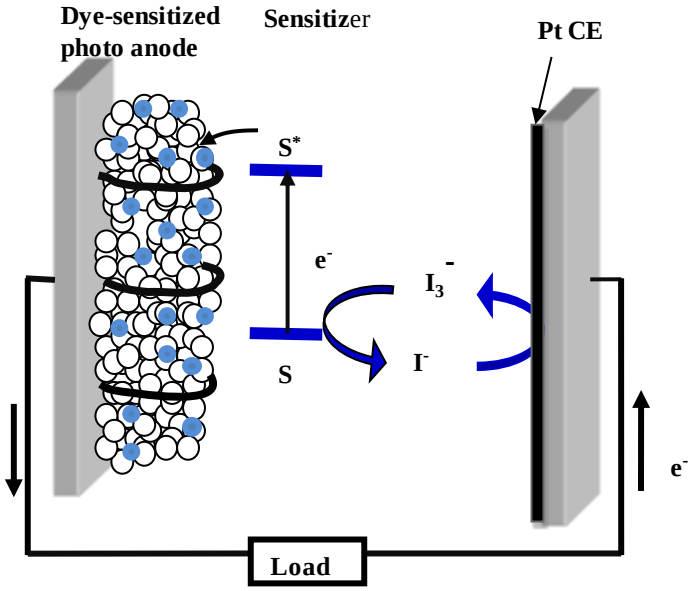


*Figure 1.2: Dye-sensitized $TiO_2$ solar cell (DSSC) and the electron transfer processes involved in Energy conversion (S represents the dye sensitizer and $I^-/I_3^-$ is the charge mediator)*

This dye-sensitized solar cell has an efficiency of roughly eleven percent, implying that there is still plenty of room for improvement [7]. The efficiency of this cell is due to the specific combination of the semiconducting dye and the quantum dot. A suitable matching of substances that have similar qualities allows for the upsurge of electrons and holes in two separate particles, which in turn allows enough time to capture the charge carriers at the surface [6, 7]. This process allows for a steady flow of large quantities of charge, which leads to an increase in the efficiency.

## 1.2 **PROBLEM STATEMENT:** WHY NANO-TECHNOLOGY?

The sun is our primary source of energy in the solar system, yet the devices we have created to harness that energy are among the weaker energy sources compared to hydroelectric power, coal, natural gases, and nuclear power. In convectional p-n junction solar cells, the current generation mechanism is far less efficient than that in quantum dot solar cell. Therefore, it seems reasonable to place more emphasis and effort into the development of quantum dot solar cells. The quest to significantly improve the efficiency of practical quantum dot solar cells necessitates the need for research, development and innovation in nano-scale science. Nano-science, the study of the materials less than 20 nm, is becoming one of the most pursued multi-disciplinary fields. Nano-technology is the application of it.

The cost-effectiveness and the wide range of methods available for practicing nano-scale science make this route ideal for making the anticipated rainbow solar cell, if accomplished, available to the general public.

### 1.2.1 WHY TITANIUM DIOXIDE?'

One of the elements of the periodic table that had been earmarked to override silicon in photovoltaic industry has been its upstairs neighbor "***CARBON***". Carbon is in the same period as silicon both with four valence electrons. It has been noted that carbon is capable of forming different allotropes: diamond, graphene, nano-tubes and fullerenes. Carbon nano tubes were known to the public in 1981 [8] and the first carbon solar cell made from fullerenes, and graphene "has been recently reported [9]". Despite carbon being less expensive and the most abundant element as compared to silicon. It presents its own challenges such as the reproducibility and repeatability of producing carbon nano-tubes (CNT) with the same electronic properties has been almost impossible to do. Some CNTs can be metallic or semiconducting depending on whether the atomic arrangement or chirality of the chain is armchair or zig-zag or novel atomic arrangement such as bamboo shapes. The success of a method for producing good CNT will be on going dilemma. Figure 1.3 shows the relative abundances of elements in the universe.

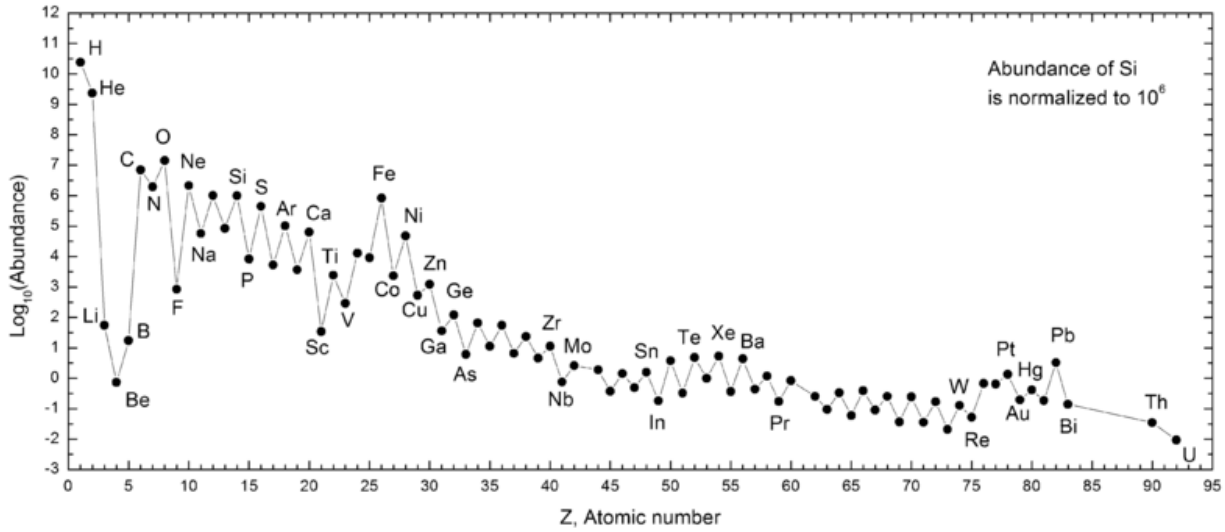


*Figure 1.3: Relative abundances of elements in the Earth's Crust [4]*

On the other hand, there have been other nano-structures based on metals and metallic compounds. Most metal oxides especially those derived from the first row of transition metal elements such as Zinc (Zn) and Titanium (Ti) possesses semiconducting properties. Transitional metal oxides are more easily synthesized especially with wet chemical methods. Wet chemical methods are quite advantageous in the preparation of nano-structures with homogeneous composition as well as adjustable particle size, crystallinity, shape, and microstructure, to be utilized as bulk powder, single particles or deposited film. The main interest of this study is therefore on inorganic nano-structures of titanium dioxide ($TiO_2$).

$TiO_2$ is a cheap, non toxic and one of the most efficient semiconductor photo catalysts for extensive environmental applications because of its strong oxidizing power, high photochemical corrosive resistance and cost effectiveness. Due to these inherent properties, $TiO_2$ is the most suitable candidate for photovoltaic applications. There are several motivations for investigating titanium dioxide ($TiO_2$) nano-structures in this work. $TiO_2$ thin films are used currently as the PV industry standard anti-reflection coating on the vast majority of screen-printed solar cells. The important implications of this are *firstly*, that the industry is familiar with the technology and will not be reluctant to adapt to fabrication processes based around $TiO_2$ and, *secondly*, that the necessary deposition equipment is operating today in the factories. Thus, the development of a

new solar cell technology that included $TiO_2$ processing steps could be readily adopted by the PV industry without the typical long lead-in time for a new technology.

## 1.3 RATIONALE OF THE STUDY

Recent years have seen the importance of energy being brought into sharp. As world's economic demands keep on growing amidst, ever increasing prices for fossil fuels. Despite the 2008-2009 world economic melt-down, the demand for energy still ranks high, thus creating a general sense of energy crisis. The way to alleviate the crisis is to incorporate clean and less costly renewable sources of energy. Solar energy has the most modest potential among the other renewable forms of energy. Renewable energy sources are increasingly being used but their contribution to total energy supply still remains significantly low. The available sources include wind energy, solar, geothermal, bio-fuel and hydro power. Wind energy regime finds its applications in water pumping for household use and irrigation with a possibility of electricity generation in areas where the wind speed exceeds 5 $ms^{-1}$. Geothermal energy is constrained by the limited presence of hot springs in most countries and its exploitation also remains limited except in very few cases. While hydroelectricity ranks high in energy supply, it faces the challenge of limited installed capacity and high running cost which makes it unaffordable for poor families and inaccessible to people in remote settlements. We have seen wide spread shortages of hydro power leading to repeated power cuts and load shading in Zimbabwe, Zambia in particular and the Sothern Africa Development Community (SADC) in general. The same trend has been recorded in many other parts of the world. All this has been as a result of energy demand overriding supply. There remains hope, however, due to the fact that solar energy technologies are rapidly developing and giving high hopes to the world that the shortages presently being experienced and those projected in the near future could be averted with fully developed clean solar technologies. This is the reason why the world today has to think of solar as a reliable alternative and give it the attention that it deserves.

There have been remarkable developments in the utilization of solar by way of solar cells, solar collectors and architectural designs in the recent past. However, the biggest challenge in making solar energy cheaper and reliable lies in the development of cost effective and efficient solar

energy materials for both thermal and photovoltaic applications. Therefore the major objective of this study is to develop a cost effective spray pyrolysis methods for producing titanium dioxide nano-powders and further our knowledge of particle and crystal formation. In order to improve the properties of various products the production methods and properties still need to be studied. Knowledge of particle production and crystallization, on the other hand, is fundamental in controlling microstructure and, thus, the material properties. The production of titanium dioxide powders is technologically interesting and, in this thesis, USP and PSP techniques for producing titanium dioxide powders have been studied.

### 1.3.1 TITANIUM RESOURCES IN SOUTH AFRICA

South Africa is the second largest producer of mineral sands in the world, after Australia, contributing about 23-30% of global production of heavy mineral sands. Of this, 90% accounted for ilmenite ($FeTiO_3$) production, with Rutile ($TiO_2$) the remaining 10%. Figure 1.4 illustrates the location of one of the major producers of $TiO_2$ ore in Richards Bay.

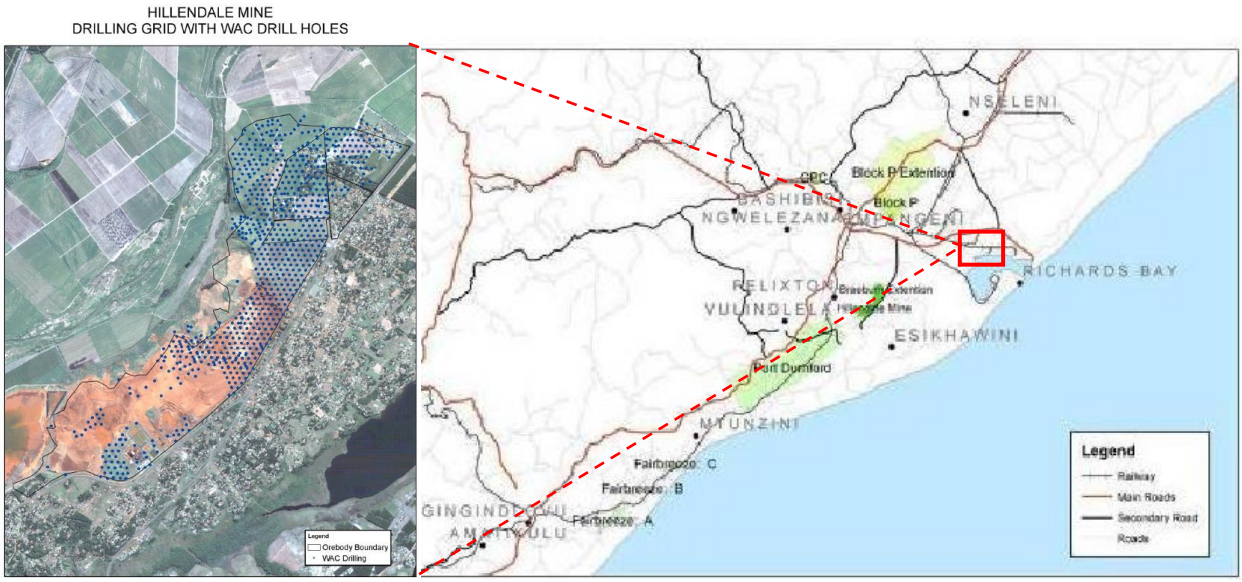


*Figure 1.4: Map of part of Kwa Zulu Natal province in South Africa showing Hillendale mine, one of the major producers of ilmenite titanium dioxide ore in Richards Bay [8]*

South Africa produced 1100 thousand metric tons of ilmenite and Rutile in 2009. Ilmenite, zircon and Rutile are the main minerals produced from the extensive beach placer deposits located along the eastern, southern and northeastern coasts of South Africa. Smaller deposits are located on the west coast of South Africa, north of Cape Town. Richards Bay Minerals (RBM) in KwaZulu-Natal, in which Rio Tinto Iron & Titanium (RTIT) has a 50% interest, is the largest titanium slag producer in the world. RBM has enormous reserves along the Kwa Zulu Natal coastlines situated along the eastern coast of South Africa with mining reserves estimated at lasting around 20 years at current production rates. Exxaro's Namakwa Sands operation is located on the west coast of South Africa and operates facilities at three separate sites. The mine and the concentration plants are located at the Brand-se-Baai, 385km north of Cape Town. The

company has a mineral separation plant at Koeknaap, 60 km from the mine. Here ilmenite, zircon and Rutile are recovered before the products are transported to the smelter by rail. Namakwa Sands operates two furnaces where ilmenite is smelted to produce titanium slag and pig iron. The Namakwa Sands operation started in 1994 and is one of the largest mineral sand operations in the world.

### 1.3.2 WHY, PNEUMATIC AND ULTRASONIC PYROLYSIS?'

Advances in materials synthesis have often been led by the development of new synthetic methods that provide control over size, morphology and structure. The preparation of materials in a scalable and continuous manner is critical when development moves beyond lab-scale quantities. The ease and scalability for preparing materials has been a driving force for the development of new methodologies for several decades. In this respect, there is a need for development of aerosol syntheses has been particularly successful. Spray pyrolysis has been widely used in industry for preparing fine powders, in addition to thin film deposition. This technique has been generally accepted because the apparatus is simple, continuous, and easily scaled up to mass production. In general, spray pyrolysis involves the thermal reactions of aerosols (i.e., solid or liquid droplets suspended in a gas) generated by a nebulizer (e.g. pneumatic, ultrasonic, or electrostatic) carried in a gas flow through a furnace. Among the various nebulization techniques available use of ultrasonic nebulizers has been favored because of their outstanding energy efficiency in aerosol generation, affordability, and the inherent low velocity of the initially formed aerosol. Ultrasonic spray pyrolysis (USP) has been shown to be particularly effective for the preparation of a wide array of materials, and it has the advantage of being highly scalable and continuous. Like sol gel process, USP technique is also a solution based method wherein high frequency ultrasound is passed through a liquid precursor solution, impinging on a liquid-gas interface, which forms an aerosol of micron-sized liquid droplets. The ultrasonically generated droplets of reaction precursors thus become individual chemical micro reactors as they are carried by gas flow into a heated furnace where reactions occur. Evaporation of volatile solvent can be followed by chemical reactions either of the remaining solid or, in the presence of high boiling co-solvents or molten salts, in submicron-sized liquid droplets. Such reactions can occur in the interior of the droplet or on the droplet surface. A very wide range of nano-materials have been prepared by USP, including nano-porous metal oxides and sulfides, nano-composites, very high surface area carbons, semiconductor quantum dots, and conductive metal inks [5, 9]. It's imperative to develop an USP technique capable of realizing $TiO_2$ nano-particles for photo voltaic applications.

## 1.4 SPECIFIC OBJECTIVES OF THIS STUDY

Functional semiconducting materials have been found to reveal interesting structural, electronic, semiconducting and optical properties especially as their geometrical dimensions reduce down to nano scale. There are numerous properties that are affected by the particle size and presence of impurity dopants in semiconductors. The change in properties is chiefly due to the increase in surface to volume (bulk) ratio as the particle shrinks in size. Amongst these, pure un-doped $TiO_2$ and doped $TiO_2$ has become a material of interest in the photovoltaic community. The important technological applications of nanoscale $TiO_2$ are in photo-catalysis, photochemical solar cells, optoelectronic devices, chemical sensors, and dielectric material of ultra-thin thin-film capacitors and more recently in quantum dot C-$TiO_2$ photo-electrochemical solar cells.

The main objectives of this study are

1. To expose the limitations of existing models for predicting droplet size produced from spray pyrolysis. So as to use the knowledge gathered to provide a new droplet relation model that includes thermodynamic properties of the precursor such as pressure of the spray pyrolysis and volume of the spray pyrolysis in the model would improve agreement between theoretical estimations and experimental findings;

2. To design and assemble a simple and cost effective ultrasonic and pneumatic spray pyrolysis technique capable of realizing Anatase titanium dioxide ($TiO_2$), carbon doped titanium (C-$TiO_2$) nano-structures and photo-electrodes for solar cell application;

3. To obtain a new phonon dispersion model to explain the quantum confinement effects observed in Raman spectroscopy data of C-$TiO_2$ synthesized from spray pyrolysis. Use the present quantum dot relation model to explain the red shift observed in Raman spectroscopy and obtain phonon dispersion relation parameters of C-$TiO_2$. Furthermore the objective of this work was to carry out an intensive analysis of Raman spectroscopy temperature dependence analysis of C-$TiO_2$ quantum dots [15, 16];

4. To evaluate the Structural, Optical and Electronic properties of pure un-doped $TiO_2$ and C-$TiO_2$ nano-sized structures produced by ultrasonic and pneumatic spray techniques;

5. To develop C-$TiO_2$ QDs sensitizers with the motivation to further enhance the spectral absorption properties of PECs and increase overall PEC solar cell efficiency [15];

6. To design, fabricate and characterize self assembled C-$TiO_2$ quantum dot photo-electrochemical solar cell (PEC). This work will attempt to understand the relationship between semiconductor properties and device performance. This could provide guide lines for future PEC solar cell devices [15].

## 1.5 RESEARCH QUESTIONS

1. What are the desired electronic, optical and structural properties for Anatase $TiO_2$ for photovoltaic applications? Is it possible to add dopants into $TiO_2$, without converting photo active Anatase phase of $TiO_2$ into Rutile phase? Is it possible to extend the absorption properties of $TiO_2$ into the visible section of the solar spectrum without converting into the inactive Rutile polymorph? Does the doping of $TiO_2$ with carbon change the structural, optical and electronic properties of $TiO_2$? Is it possible to use the knowledge gathered to provide a guide line for synthesis of photo active Anatase $TiO_2$? Is it also possible to use the knowledge gathered as a guideline in designing a spray pyrolysis system for production of $TiO_2$?

2. What are the current models in literature for predicting droplet size by USP? Do these models sufficiently predict the droplet size produced by ultrasonic spray pyrolysis? What are the main limitations of these models when predicting the droplet size in USP? Is it possible to produce a new droplet relation model for predicting the final nano-particle size produce from USP systems specifically for $TiO_2$ nano-particles only known the initial reaction parameters?

3. Is it possible to design a simple cost effective USP system capable of realizing C-$TiO_2$ nano-particles for solar cell application? Is it possible to design USP system for production of C-$TiO_2$ quantum dots, nano-particles and or thin films for solar cell applications? Is it also possible to develop a photochemical solar cell using the USP system employing a tube furnace reactor?

4. Is it possible to use existing models to fit to Raman spectral line for C-$TiO_2$ QDs without any modifications? Do these models fail to fit to Raman spectral line data for C-$TiO_2$ QDs? Is it also possible to develop a new model specific for Raman spectral line for C-$TiO_2$ QDs? Can the available phonon dispersion relations in literature be used for C-$TiO_2$ Raman spectral lines? Is it also possible to extract new phonon dispersion relations for C-$TiO_2$ QDs? Does the Raman temperature dependence of C-$TiO_2$ nano-particles

show the same behavior as for pure un-doped Anatase $TiO_2$? Is there any significant difference between Raman temperature dependence behavior of C-$TiO_2$ nano-particle as compared to those of un-doped $TiO_2$?

5 Do the structural, optical and electrical properties of pure un-doped $TiO_2$ QDs and nano-particle show any similarity or any significant difference? Do the structural, optical and electrical properties of C-$TiO_2$ quantum dots synthesized by USP and PSP show any similarity or any significant difference? Is possible to report these similarities or differences to any peer reviewed journal?

6 Is it possible to construct a solar cell using the synthesized C-$TiO_2$ QDs? Does the efficiency of the solar cell change with the change in the dopant level? Is there any relationship between semiconductor properties and device performance?

7 Is it possible to fabricate a photochemical solar cell with a C-$TiO_2$ photo electrode? Is there any relationship between semiconductor properties and device performance?

## 1.6 REFERENCES


1. http://en.wikipedia.org/wiki/Renewable_energy_in_developing_countries
2. http://www.dailymaverick.co.za/article/2012-06-15-eskoms-results-the-facts#.Uku79X8S81M
3. ASTM Standard G173, Standard Tables for References Solar Spectral Irradiances: Direct Normal and Hemispherical on 37º Tilted Surface, ASTM International, West Conshohocken, PA: http://ww.astm.org, accessed on 12/14/2007
4. What is Nanotechnology? Centre for Responsible Nanotechnology: http://www.crnano.org/whatis.htm
5. Kamat P.V. J. *Phs. Chem. C*. **2008**, 112(48), 18737-18753
6. Grätzel, M.; *Inorg Chem.* **2005,** 44, 20-25
7. Grätzel, M.; *J Photochem. Photobiol*. A**. 2004,** 164, 3-7.
8. Iijima S. *Nature*. 1991, 354, 56-58
9. Ramuz M.P.; Vosgurtchian M.; Peng Wei.; Chenggong Wang.; Yongli Gao.; Yingpeng Wu.; Yongsheng Chen.; Zhenan Bao.A *ACS Nano*. **2012,** 6(11), 10384–10395
10. Dea-Woen Kim.; Naoya Enomoto, Zenbe-e Nakagawa.; Kastuyuki Kawamura.*Journal of American Ceramic Society*. **2005**,79(4), 1095-1099
11. Nam H.Vu.; Hieu V.Le.; Thi M. Cao.; Viet V.Pham.; Hung M.Le.; Nguyen-Manh Duc. *J Phys.Condens. Matter*. **2012**, (24), 5501-5509
12. Bardzinski P.J. *Material Science-Poland*.**2011**, 3, 223-232
13. Buschow K.H.J. E. *Encyclopedia of Materials: Science and Technology (second Edition).* **2001**,85-89
14. Latroche M.; Brohan L.; Marchand R.; Tournoux. *J Solid State Chem*. **1989**,79, 78-87
15. Taziwa R.; Meyer E.L.; Sideras-Haddad.; Erasmus R.M.; Manikandan E.; Mwakikunga B.W. *Internal Journal of Photoenergy*. **2012,** 2012, 1-15
16. Taziwa R.; Meyer E.L.; Chinyama K.G.; *Journal of Material Science*, **2011**, 47(3) ,1531-5140

# CHAPTER 2

# STRUCTURAL, OPTICAL AND ELECTRICAL PROPERTIES OF $TiO_2$

## 2.1 INTRODUCTION

The structural, optical, electrical and chemical properties of titanium dioxide ($TiO_2$) depend greatly on the amorphous or crystalline phase of the material. $TiO_2$ is a complex material with three crystalline phases, two of which are commonly observed in thin films Anatase and Rutile [1]. Anatase is commonly observed at film deposition temperatures of 350 − 700ºC, while higher temperatures promote the growth of Rutile. Deposition temperatures lower than 300ºC generally result in the formation of amorphous $TiO_2$ of these phase Amorphous $TiO_2$ has the highest band gap of about 3.5 eV, and exhibits a low refractive index of about 1.9 − 2.0 at 600 nm wavelength light and extinction coefficient [2]. The chemical resistance of amorphous $TiO_2$ films is poor in many acidic and basic solutions which makes it unsuitable for development electrodes for solar cells. Anatase thin films, with an optical band gap of about 3.2 eV, exhibit a much higher refractive index (as high as 2.532 at 600 nm for single crystal material) and a slightly increased absorption coefficient [2]. With the crystalline structure comes increased chemical resistance, and dense Anatase films are insoluble in many acids and bases. Rutile thin films (3.05 eV band gap) have extremely high refractive indices (up to 2.70 at 600 nm for single crystal Rutile) absorption coefficient is still low. The chemical resistance of Rutile is excellent, and after annealing at temperatures above 1000ºC it is insoluble in nearly all acids and bases.

The sole purpose of this work is to (i) develop a simple and cost effective method for synthesis of $TiO_2$, C-$TiO_2$ nano particles and Quantum Dots (QDs), and (ii) to evaluate the performance of the synthesized nano structures (QDs, C-$TiO_2$ nano structures). $TiO_2$ was chosen due to the ability of depositing films at low temperatures and at atmospheric pressure; the non-toxicity of the available liquid precursor; the familiarity of solar cell manufacturers with this film and, their existing ownership of the necessary deposition equipment. It was anticipated that these factors would facilitate an easy transfer of a successful laboratory device into a commercial product.

However, $TiO_2$ is a relatively complex material, and three crystalline phases as well as the amorphous form of $TiO_2$ exist. Since $TiO_2$ exist in almost three different polymorphs that have different optical, electrical, and chemical properties. It was necessary to perform an extensive literature review in order to predict how the $TiO_2$ films would behave in different processing conditions.

This chapter describes the properties of the crystallite phases most commonly observed in thin films, that of Rutile and Anatase as well as amorphous $TiO_2$. The third natural crystalline phase, Brookite, is a less stable and less common form of $TiO_2$ and was rarely observed in deposited thin films and hence will not be discussed here. There are many different parameters that affect the phase of a deposited $TiO_2$ thin film. Some of these parameters are deposition method, deposition temperature, annealing temperature, deposition rate, deposition pressure, precursor type, reaction atmosphere, impurities present, and substrate type. The resulting phase or mixture of phases plays a large role in determining the physical, optical, chemical, and electrical properties of the film.

This work relies greatly on the excellent structural, optical and electrical properties of $TiO_2$ thin films, as well as its chemical resistance and insulating properties. A summary of the physical, optical, electrical and chemical properties reported in the literature, with an emphasis on those relevant to solar cell fabrication, is presented in the following sections of this chapter.

## 2.2 STRUCTURAL PROPERTIES OF $TiO_2$

Titanium dioxide ($TiO_2$) is a crystalline material with seven reported polymorphs, from which four are natural (*i.e.* Rutile (tetragonal), Brookite (orthorhombic), Anatase, (tetragonal), $TiO_2$-B (monoclinic) and others are synthetic. Of the four natural polymorphs, Rutile, Anatase and Brookite are commonly encountered in inorganic synthesis [1, 2].

Rutile and Anatase were the only polymorphs of $TiO_2$ synthesized in this work. Henceforth the description of the properties of $TiO_2$ will concentrate on these two phases. Rutile is the most stable phase [3, 4 and 5]. Anatase is meta-stable at room temperature. It transforms irreversibly

into Rutile upon heating above a threshold temperature. At atmospheric pressure, the transition occurs usually at about 1000°C. The critical temperature can vary from 400°C to 1200°C, depending on the grain size, atmosphere, as well as the nature and amount of impurities [6, 7]. Figure 2.1 presents the Units cells of $TiO_2$ crystal structures in the Rutile and Anatase phases.

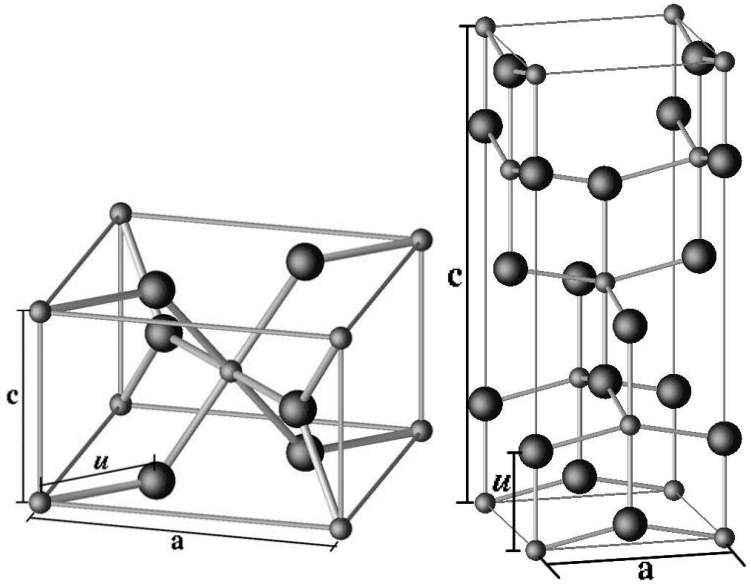


*Figure 2.1: Rutile (left) and Anatase (right) crystallographic unit cells. Small spheres represent Ti atoms; large spheres represent oxygen atoms after [11]*

Natural Rutile crystals exhibit predominantly (110) surfaces [8], and there is agreement on the fact that the (110) stoichiometric surface is the most stable surface for Rutile [8-10]. For Anatase, the (101) surface is the most stable [4]. The unit cell of Rutile contains two Ti atoms situated at (0, 0, 0) and (1/2, 1/2, 1/2), and four oxygen atoms. The oxygen atoms form a distorted octahedron around every Ti cation. The unit cells of Anatase contains four Ti atoms located at (0, 0, 0), (1/2, 1/2, 1/2), (0, 1/2, 1/4), and (-1/2, 0, -1/4), and eight oxygen atoms. In Anatase, too, the Ti cation is surrounded by a distorted oxygen octahedron [8].

Figure 2.2 depicts the main differences in the two polymorphs of $TiO_2$ (Rutile and Anatase). Rutile and Anatase $TiO_2$ differ from each other by the arrangement and the distortion of the octahedral as in illustrated below in Figure 2.2.

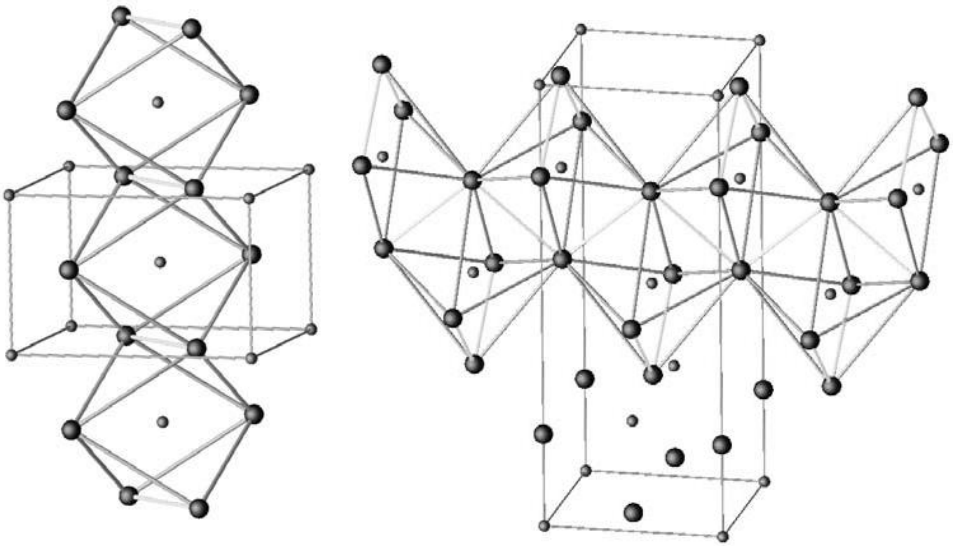

*Figure 2.2: Arrangement of $TiO_6$ octahedra in relation to the unit cells in Rutile (left) and Anatase (right). Only one chain is shown for each structure. Highlighted bonds are the O-O bonds after [11]).*

$TiO_6$ octahedra constitute the basic building units for the various polymorphic structures of $TiO_2$. In the Rutile crystal, each octahedron is connected to 10 neighboring octahedra, among which 2 share an edge and 8 share a corner with it. The edge-shared octahedra are aligned along the [001] direction [12]. In the case of Anatase, each octahedron shares 4 edges. The edge-shared octahedra are aligned along the [100] and [010] direction forming zigzag double chains perpendicular to the c-axis. These arrangements of $TiO_6$ octahedra in Rutile and Anatase give rise to open channels parallel to the c-axis in Rutile and perpendicular to the c-axis in Anatase.

### 2.2.1 $TiO_2$ LATTICE PARAMETERS

The lattice parameters of a semiconductor usually depend on the following factors (i) free electron concentration acting via deformation potential of a conduction band minimum occupied by these electrons, (ii) concentration of foreign atoms, defects and their difference of ionic radii with respect to the substituted matrix ion, (iii) external strains (for example, those induced by substrate), and (iv) temperature. On the other hand, the strict periodicity of the lattice is disturbed by many imperfections or defects. These imperfections have a considerable and, sometimes, even the controlling influence on the mechanical, thermal, electrical and optical properties of

semiconductors. They determine the plasticity, hardness and thermal and optical and electrical conductivities.

Anatase structure is tetragonal, with two $TiO_2$ formula units (six atoms) per primitive cell. Lattice parameters are: $a = b = 3.7710$ Å and $c = 9.430$ Å with $c/a$ ratio of 2.5134 [13]. Whilst the Rutile polymorph has as its unit cell contains Ti atoms occupy the center of a surrounding core composed of six oxygen atoms placed approximately at the corners of a quasi-regular octahedron. The lattice parameters correspond now to $a = b = 4.5933$ Å and c = 2.9592 Å with $c/a$ ratio of 0.6442. The change in lattice parameter with change in $TiO_2$ polymorph is illustrated in Table 2.1.

*Table 2.1: $TiO_2$ Rutile and Anatase structures and physical properties [13, 14]*

| **Property** | **Rutile** | **Anatase** |
|---|---|---|
| Crystal structure | Tetragonal | Tetragonal// |
| Space group | $P4_2/mm$ | I41/amd |
| Lattice spacing (nm) | 0.459//0.296 | 0.378//0.951 |
| Density ($g/cm^3$) | 4.25 | 3.895 |
| Refractive Index, 550 nm | 2.75 | 2.54 |
| Band gap (eV) | 3.05 | 3.25 |
| Melting point (ºC) | 1830 | Conv. To Rutile @ 600 ˚C |

### 2.2.2 ANATASE TO RUTILE PHASE TRANSFORMATION

It has been observed in literature that the inclusion of a certain quantity of impurities into the $TiO_2$ crystalline structure has serious effects on the structure of $TiO_2$. It has been revealed that the inclusion of *carbon*, *nitrogen*, silicon and phosphorous inhibits the conversion of Anatase to Rutile with 100% Anatase phase being retained even at high deposition temperatures as high as 800°C for up to 3 hr for thin films. Conversely, it is well known that other impurities enhance the formation of Rutile at even lower temperatures. These impurities include $CuO_2$;$V_2O_5$; and NiO, CoO, $MnO_2$, $Fe_2O_3$ [15-19].

Most researchers agree that oxygen vacancies are responsible for the overall transformation mechanism. Thus, the oxides and fluorides (such as $Li^{+1}$, $Co^{+2}$ and $Mn^{+4}$) that assist the

transformation can substitute for $Ti^{+4}$ in the Anatase lattice, resulting in the creation of oxygen vacancies. On the other hand, the inhibiting effect of other impurities ($PO^{-}_{3}SO^{-}_{2}$ $Nb_2O_5$) has been explained by the reduction of oxygen vacancies due to the substitution of P and S into the Anatase lattice. Oxygen vacancies are also known to be created in hydrogen ambients, thereby favoring the transformation to Rutile [20-23].

It should be noted that during the growth of $TiO_2$ thin films, contamination from the various chemical precursors can result. Titanium alkoxides are common $TiO_2$ precursors, with the most frequently used being titanium isopropoxide (also called tetraisopropyl titanate, TPT). The residue of the organic binders results in carbon contamination of typically a few at 2%, but as high as 13%, has been observed. It is likely that carbon incorporation could be higher at low growth temperatures. Titanium tetrachloride ($TiCl_4$) is another common $TiO_2$ precursor, and this result in chlorine contamination of the deposited film [24]. In this project titanium iso-propoxide and titanium tetra butoxide were the only precursors employed in the synthesis of various $TiO_2$ nano structures.

### 2.2.3 SUBSTRATE

The effect of substrate type on the deposited $TiO_2$ nano-structures will be discussed only briefly, as nearly all experiments performed in this work used fluorine doped tin oxide quartz (F: $SnO_2$) glass substrate. Several researchers have studied the properties of $TiO_2$ films deposited onto various substrate types, including silicon, silica, quartz, alumina, titanium, copper, gallium arsenide, stainless steel, as well as several types of glass. The different substrate types influence the physical properties of the deposited film, including the phase, texture or surface roughness. Optical and chemical properties also change, however these are primarily dependent on the phase and density of the polycrystalline $TiO_2$ film [22-24]. Possible reasons for the dependence of the $TiO_2$ phase and properties on the substrate include the substrate's surface conditions affecting the orientation and packing density of the molecules, and, with glass, the diffusion of metal ions into the film. Deposition of titanium dioxide on stainless steel substrates results in formation of Anatase phase of titanium dioxide [25]. Use of barium fluosilicate glass substrates and or aluminum substrates result in formation of a mixed Anatase-Rutile phase at 1100 ºC [25-28.]

Film depositions on glass substrates are typically limited to Anatase, or Anatase-Rutile mixed phases due to the low melting point (typically @ 650 ºC) of most glasses. However, results of depositions on quartz indicate a preference for the formation of anatase, even at temperatures greater than 1000 ºC [27, 28]. This is also true for glasses containing sodium since it is possible for the $Na^+$ ion to out-diffuse from the substrate and retard the formation of Rutile [31, 32]. In contrast, alumino-silicate glasses such as Corning 7059 are known to favor the formation of the Rutile phase due to the $Al_2O_3$ impurity [33-35]. Diffusion of substrate elements has also been observed, where up to 30% copper concentration was found in a $TiO_2$ film deposited onto copper sheet and annealed at 800 ºC [36]. Hence in this project fluorine doped tin oxide (FTO) glass substrates will be used.

## 2.3 OPTICAL PROPERTIES OF $TiO_2$

The optical properties of a semiconductor are associated with both intrinsic and extrinsic effects. Intrinsic optical transitions take place between the electrons in the conduction band and holes in the valence band, including excitonic effects due to the Coulomb interaction. The main condition for exciton formation is that the group velocity of the electron and hole is equal. Excitons are classified into free and bound excitons. In high quality samples with low impurity concentrations, the free exciton can also exhibit excited states, in addition to their ground-state transitions. Extrinsic properties are related to dopants or defects, which usually create discrete electronic states in the band gap, and therefore influence both optical absorption and emission processes. It is well known that a shift in the band gap edge appears with an increase in the carrier concentration. This shift is known as Burstein-Moss shift. Optical transitions in $TiO_2$ have been studied by a variety of experimental techniques such as optical absorption, transmission, reflection, spectroscopic, ellipsometry, photoluminescence, cathodoluminescence, calorimetric spectroscopy, etc. In this thesis we are going to adhere to discussions that involve UV-Vis absorption and transmittance spectra to obtain the optical parameters of the thin films and as for the nano structures.

Now a days most authors prefer to present optical absorption or transmission of the resulting nano structures and or thin films. The sole aim of these spectra is usually to show that the synthesized materials are of high quality. Figure 2.3, shows theoretical transmission spectra for an optical $TiO_2$ thin film.

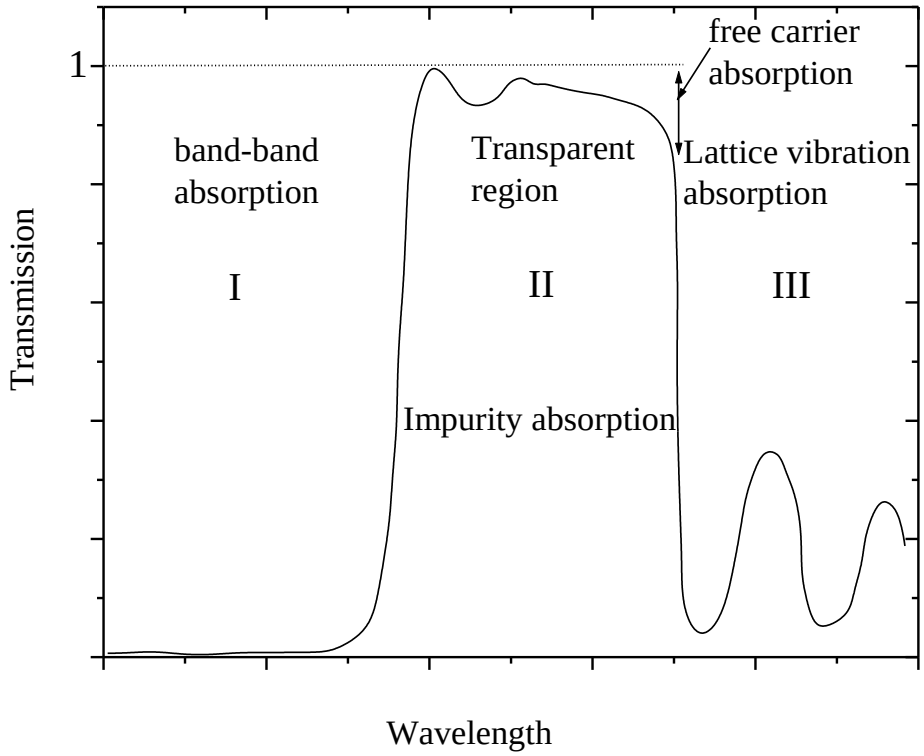


*Figure 2.3: Theoretical transmission curve for an optical $TiO_2$ thin film.*

It can be clearly observed that a region of high transmittance (region II) is sandwiched between the region of short wavelength band-band absorption (region I) and the long wavelength lattice vibration absorption (region III). The region of fundamental absorption is dependent on the electronic structure of the material, while absorption in region III is due to lattice vibrations and/or free carrier absorption. The transmission of region II is strongly linked to the stoichiometric and purity of the nano materials.

### 2.3.1 OPTICAL ABSORPTION AND ABSORPTION EDGE FOR $TiO_2$

The fundamental absorption is the most important absorption process which involves the transition of electrons from the valence band (VB) to the conduction band (CB), which manifest itself by a rapid rise in absorption and this can be used to determine the energy band gap of the semiconductor. The semiconductor absorbs photon from the incident beam. Absorption depends on the photon energy ($h\upsilon$), where $h$ is Plank's constant, $\upsilon$ is the incident photon frequency. Absorption is associated with the electronic transition between the VB and the CB in the material starting at the adsorption edge. The absorption edge corresponds to minimum energy difference ($Eg$) between the minimum of the CB and the maximum of the VB. If the photon energy ($h\upsilon$) is equal to or more than energy gap ($Eg$) then the photon can interact with a valence electron, excites the electron into the CB and creates an electron-hole pair. The maximum wavelength ($\lambda c$) of the incident photon which creates the electron-hole pair is defined as

$$\lambda(\mu m) = \frac{hc}{E_g} = \frac{1.24}{E_g(eV)} \tag{2.1}$$

The intensity of the photon flux decreases exponentially with the distance through the semiconductor according to the following equation:

$$I = I_o e^{(-\alpha t)} \tag{2.2}$$

where $I_o$, $I$ are the incident and the transmitted photon intensity respectively and $\alpha$ is the absorption coefficient, which is defined as the relative number of photons per unit distance of semiconductor and $t$ is the thickness of the material.

## 2.4. ELECTRICAL PROPERTIES OF $TiO_2$

$TiO_2$ can be synthesized as single crystals quantum dots (QDs), nano powders, nano wires and thin films. Transition metal oxides are often non-stoichiometric and at near-atmospheric oxygen pressure the oxygen vacancies is the predominant defect in $TiO_2$. The oxygen deficiency introduces an excess of electrons in the material resulting in an increase of the electrical conductivity [37-39]. The oxygen vacancies act as electron donors, thus $TiO_{2-x}$ is an *n*-type semiconductor, in contrast with *p*-type semiconductors which contain electron acceptors and where the charge carriers are holes rather than electrons. Sub-stoichiometric $TiO_{2-x}$ is both a poor insulator and a modest semiconductor. Therefore several attempts have been made either to control the oxygen vacancy concentration or to introduce charge carriers (doping) inside $TiO_2$ in order to increase or decrease the electrical conductivity, depending on the desired application. During the last four decades, almost half the atoms of the periodic table have been incorporated into $TiO_2$. Figure 2.4 presents an overview of their effects on conductivity.

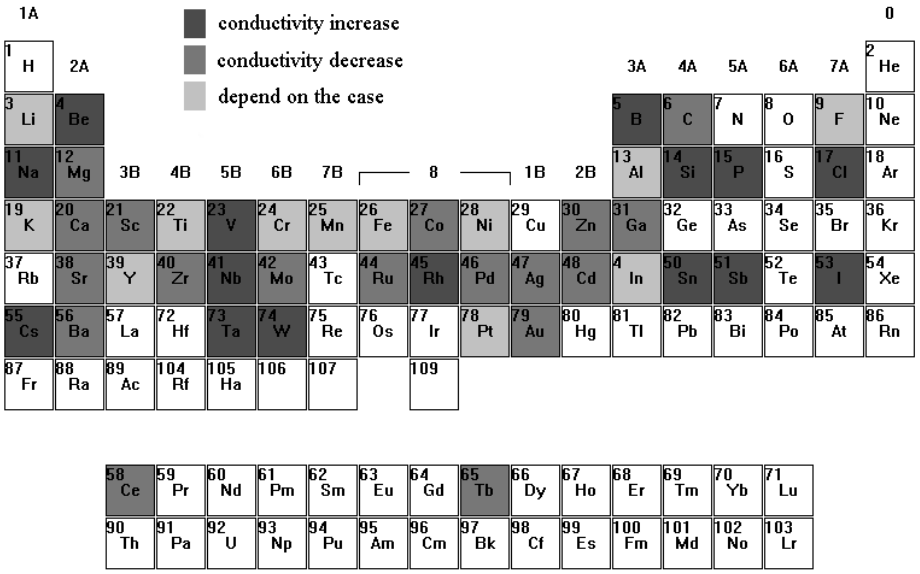


*Figure 2.4 Periodic table illustrating impurities included inside $TiO_2$ in the past decades [38]*

For example, when niobium or tantalum atoms are incorporated into $TiO_2$, they act as electron donors resulting in an increased electrical conductivity [37-39]. Chromium, manganese, and iron are reported as electron acceptors increasing or decreasing the $TiO_2$ electrical conductivity

depending on the ratio between their concentration and the oxygen vacancy concentration. These incorporations do not only modify the electrical conductivity of $TiO_2$, but also influence the structure and morphology of $TiO_2$. For instance, silicon incorporation favors the Anatase structure, while tin incorporation favors the Rutile structure. Large atoms like cerium can break the crystal lattice resulting in amorphous $TiO_2$. In spite of the work done on this subject, it is difficult to draw general conclusions on the behavior of the impurities incorporated into $TiO_2$, in particular when the morphology of the $TiO_2$ samples changes. For instance the electrical properties of a single crystal depend essentially on bulk properties, while grain boundary contributions could be important in thin films [40]. In this case, it is necessary to know where the impurities are located, either inside the grains or at their surface, to relate the properties of the thin films to the properties of the single crystals. Because of the large potential of $TiO_2$ in applications and the lack of a basic understanding of this material, the research on this material is mostly relevant. The applications are essentially focused on $TiO_2$ thin films. If the electrical conductivity of $TiO_2$ is high enough, it could be used as a cheaper alternative as transparent conducting oxide (TCO) like indium-tin oxide, fluorine doped tin oxide or zinc oxide. In any case, more conducting *n*-type and *p*-type $TiO_2$ are useful for catalytic applications, and solar cell applications.

### 2.4.1 $TiO_2$ INSULATOR OR CONDUCTOR?

$TiO_2$ is an *n*-type semiconductor with a relatively wide band gap of $3.05 - 3.5$ eV. Single crystal titanium dioxide $TiO_2$ has a resistivity of about $10^{-13}\ \Omega^{-1}cm^{-1}$ at room temperature, and about $10^{9}\ \Omega^{-1}cm^{-1}$ at 250ºC. These values are similar to conductivities reported for single crystal Rutile at 30ºC the conductivity was $5 \times 10^{-14}\ \Omega^{-1}cm^{-1}$ while at 260ºC it had decreased to $3.3 \times 10^{-9}\ \Omega^{-1}\ cm^{-1}$. Therefore, $TiO_2$ is generally considered to be an insulator at temperatures less than 200ºC. [40, 41].

There are a wide number of applications for highly insulating $TiO_2$ films, including its use as a super-thin gate dielectric in MOSFET devices. However, the electrical properties of the $TiO_2$ film can be altered to become highly conductive for various applications, such as photo electrodes for solar cells, humidity and gas sensors, or as an corrosion-resistant electrode. The

properties of $TiO_2$ thin films have been compared to those of zinc oxide (ZnO), with typically a large band gap, small grain size, low carrier density, n-type conductivity, long photoconductivity relaxation, and low mobility.

### 2.4.2 NON STOICHIOMETRIC EFFECTS IN $TiO_{2-x}$

The semiconducting properties of non-stoichiometric titanium dioxide are very dependent on the extent of the oxygen deficiency in the film. The conductivity mechanism in un-doped $TiO_2$ relies on a deficiency of oxygen atoms in the material. These oxygen deficiencies behave like *n*-type defects, with a typical density of $10^{18}$–$10^{19}$ $cm^{-3}$. As the stoichiometry departs from the ideal Ti:O ratio of 1:2, several changes in the film result. Firstly, $TiO_{2-x}$ films exhibit a blue, purple or black colour depending on the film stoichiometry. Secondly, due to the increased number of oxygen vacancies, the optical absorption in the visible region is dramatically increased for these films as well as for nano structures [40].

### 2.4.3 DOPED $TiO_2$

Doped $TiO_2$ films have been used as transparent conducting oxides (TCO) for creating heterojunction solar cells, for suppressing leakage currents in capacitors, increasing the sensitivity of gas detectors, and as photo electrodes for electrolysis devices and as photo anodes in dye solar cells. The majority of dopants enhance the *n*-type semiconducting properties of $TiO_2$.

The majority of dopants enhance the *n*-type semiconducting properties of $TiO_2$. These dopants that include carbon (C), nitrogen (N), niobium (Nb), tantalum (Ta), vanadium (V), fluorine (F), and hydrogen (H) [41-46]. Dopants that change the film to being *p*-type include aluminium (Al), iron (Fe), and indium (In) [47]. There are instability issues with both hydrogen-doped (*n*-type) and all *p*-type TiO2 thin films. In the former case, the hydrogen is very mobile and is likely to result in electrically unstable devices. In the latter case, the electrical behaviour of the Al- or Fe-doped film depends on the oxygen concentration, and it is possible for the film to revert to *n*-type

material. Furthermore, dopants such as aluminium, iron, chromium and cadmium, are known to extend the photoactive response from the $TiO_2$ film under visible light.

Titania is a wide band gap semiconductor material (3.0-3.2 eV) depending on the crystalline phase as previously indicated in Table 2.1, capable of converting energy from the light into chemical redox energy. When a photon with energy equal or higher than the energy of the energy band gap impinges on the semiconductor, an electron from the VB is promoted into the CB ($e^-_{CB}$) leaving a hole behind ($h^+_{VB}$). The number of photogenerated electron-hole pairs depends on the semiconductor band structure as well as the energy and the effective intensity of the incident light. Unfortunately light activation of titania occurs in the near UV region from $(\lambda \leq 385-400\ \text{nm})$, meaning that only a 5-8% fraction of the sunlight can be absorbed by the bare material [40] as illustrated in Figure 1.1.

Due to the inherent relatively large energy band gap characteristic of $TiO_2$ materials, a great deal of research has been focused on lowering the threshold energy for excitation in order to utilize a wider fraction of the solar spectrum. Considerable efforts have been made to extend the photon response of *n*-$TiO_2$ based systems further into the visible-light region using dopants. Carbon doping has demonstrated improved photocatalytic activity in water splitting with a total conversion efficiency of up to 11%. [43, 44]

Carbon doping is responsible for the lowering of the band gap of *n*-$TiO_2$ and consequent high photocatalytic activity under visible light illumination. Nie and Sohlberg [48], reported the lowering of the band gap of *n*-$TiO_2$ to 2.32 eV (535 nm) by carbon incorporation and predicted that the band gap value of 1.58 eV (784 nm) may be possible to achieve by some complex carbon doping. It was found experimentally that carbon doping lowered the band gap of $n-TiO_2$ up to 1.45 eV (855 nm). Hence in this project visible light sensitization of titanium dioxide photo anode will be done by doping with carbon as a non metal using USP and PSP techniques.

## 2.5 SUMMARY

The physical, chemical, electrical, optical and structural properties of the final $TiO_2$ product rely on nature of the starting reaction conditions. It was therefore imperative to conduct a detailed literature review on the pros and cons of engineering the $TiO_2$ band gap with various methods and processes. For example, the temperature at which deposition is carried out, nature and amount of impurities introduced in the starting reaction mixture. The phase is usually directly related to the substrate temperature, with amorphous $TiO_2$ forming at temperatures less than 300ºC, the crystalline phase of Anatase in the temperature range 300-700ºC. Various impurities and substrate types are known to partially or totally impair or enhance the transformation of a $TiO_2$ thin film to Rutile. This chapter provided the necessary backbone required in synthesis of Anatase titanium dioxide and Anatase doped titanium dioxide.

The electrical properties are briefly discussed. Although $TiO_2$ is a wide band gap *n*-type semiconductor, at room temperature it behaves like an insulator. The film resistivity is extremely sensitive to the deposition method and on the availability of oxygen to the system from literature, films deposited in oxygen poor ambients exhibit greatly increased electrical conductivity and optical absorption; however subsequent furnace oxidation processes can reduce these oxygen vacancies. Doping of $TiO_2$ thin films in order to increase the electrical conductivity or photoconductivity of the film has been experimented with in many different applications. It has been found to be an effective method for improving the efficiency of quantum dots solar cells as shall be presented in Chapters 6, 7 and 8

## 2.6 REFERENCES


1. Khataee A.; Mansoori G.A. *Nanostructured Titanium dioxide Materials. Properties, Preparation and Applications*. **2011**. ISBN 978-981-4374-72-9.p204
2. Cao Guozhong.; Ying Wang. N*anostructured Titanium dioxide Materials. Synthesis, Properties and Applications.* **2011**, 2. ISBN 978-9814322-50-8.p 596
3. Dea-Woen Kim.; Naoya Enomoto, Zenbe-e Nakagawa.; Kastuyuki Kawamura.*Journal of American Ceramic Society*. **2005**,79(4), 1095-1099

4. Nam H.Vu.; Hieu V.Le.; Thi M. Cao.; Viet V.Pham.; Hung M.Le.; Nguyen-Manh Duc. *J Phys.Condens. Matter*. **2012**, (24), 5501-5509
5. Bardzinski P.J. *Material Science-Poland*.**2011**, 3, 223-232
6. Debnath R.; Chaudhuri J. *Journal of Materials Research*. **1992**, 7, 3348-3351
7. Fitzgibbons E.T: Sladek.; Hartwig W.H. *Journal of the Electrochemical Society*. **1972**, 119, 735-739
8. Muscat J.; Swamy V.; Harrison N.M. *Phys.Rev*. **2002**, B65,224112
9. Burdett J.K.; Hughbanks T.; Miller G.J.; Richardson J.W.; Smith J.V. *J Am. Chem Soc*.**1987,** 109, 3639
10. Rao V.K.; Naidu S.V.; Iyengar L. *J. Am. Ceram. Soc*. **1970**, 53, 124
11. Cangiani G. Ab.-intitio *Study of the Properties of $TiO_2$ Rutile and Anatase Polytypes. Faculte des sciences de base, Ecole polytechnique Federale de lausane EPLFL, Lussane*. **2003**
12. Cronemeyer D.C. *Phys. Rev*. **1972**, 87, 876
13. Kroschwitz, J.I.;Howe-Grant, M. Kirk *encyclopedia of chemical technology*. **1997**, 24, 4th edition. John wiley & Sons, New York
14. Zhang, H., Banfield, J.F. *J. Phys. Chem*. B. **2000**, 104, 3481-3487
15. Rao. C.N.R.; Turner A.; Honig J.M. T*he Physics and Chemistry of Solids, an International Journal*. **1959**, 11, 173-175
16. Akhtar M.K.; Prastinis S.E.; Mastrangelo. *Materials Research Symposium Proceedings*. **1992**, 271, 951-956
17. Mardare D.; Hones P. *Materials Science and Engineering*. **1999**, 68, 42-47
18. Kenevey M.A.; Morris J.; Cunningham J. Ferrad G. *Key Engineering Materials*. **1996**, 118-110, 303-310
19. Iida Y.; Ozaki S. *Journal of American Ceramic Society*. **1961**, 44, 120-127
20. Dorian A.H.; Charles C.S. *Journal of Materials Science*. **2011**, 46, 855-874
21. Zhu Y.U.; Lan Y.; Gao X.P.; Ringer S.P.; Zheng Z.F.; Song D.Y.; Zhao J.C. *J. Am. Chem. Soc***. 2005**, 127(18),6730-6736
22. Xiaoting Hong.; Zhengpeng Wang.; Weimin Cai.; Feng Lu.; Jun Zhang.; Yanzhu Yang.; Na Ma.; Yingjun Liu. *Chem. Mater*. **2005**, 17(6), 1548-1552
23. Cheng Wang.; Zhao-Xiang Deng.; Yadong Li. *Inorg. Chem*. **2001**, 40(20), 5210-5214

24. Fan Dong.; Haiqiang Wang and Zhongbiao Wu. *J Phys. Chem*. **2009**. 113(38), 16717-16723
25. Ljubica M.N.; Radonjic L. Vladimir V.S. *Ceramics International*. **2005**. 31, 261-266
26. Guglielmi M.; *Encyclopedia of Materials: Science and Technology*. **2001**, 45, 3575-3579
27. Kukubo T.; *Yamaguchi S. Comprehensive Biomaterials*. **2011**, 1, 231-244
28. Buschow K.H.J. E. *Encyclopedia of Materials: Science and Technology (second Edition).* **2001**,85-89
29. Latroche M.; Brohan L.; Marchand R.; Tournoux. *J Solid State Chem*. **1989**,79, 78-87
30. Notrotsky A.; Jamieson J.C. Kleppa O.J.; *Science*.**1967**, 158, 338-357
31. El-Bahy Z.M.; Ismail A.A.; Mohamed R.M. *J Hazard. Mater*. **2009**, 166, 138-143
32. Stengly V.; Bakardjieva S.; Murafa N. Mater. *Chem. Phys*. **2009**, 114, 217-226
33. Shivalingappa L.; Sheng J.; Fukami T. *Vaccum*.**1997**, 48, 413-416
34. Zhang X.W.; Han G.R. *Thin Solid Films*.**2008**, 516, 6140-6144
35. Moses Ezhil Raj A.; Agnes V.; Bena Jothy V.; Ravidhas C.; Joachim Wollschlager, Suendorf M.; Neumann M. Jayachandran M.; Sanjeeviraja C. **2010**. *Thin Solids Films*, 519, 129-135
36. Behrens R.; Umland F. *Journal of less Common Metals*. **1988**, 137, 353-365
37. Pulker, H.K, *Applied Optics*.**1979**, 18, 1969-1977
38. Ardakani H.K. *Thin Solid Films*. **1994**, 248, 234-239
39. Takashi Y.; Ogiso A.; Tomoda R.; Sugiyama K.; Minoura H.; Tsuiki M. *Journal of Chemical Society, Faraday Transaction.* **1982**, 1, 2563-2571
40. Kim Y.S. *Applied Optics*. **1996**, 35(34), 6703–6707
41. R.J. Meyer R.J.; Pietsch E.H.E. *Gmelins Handbuch Der Anorganischen Chemie: Titan*. **1951**, 41, 668-695
42. Gole, J.L. ;Stout, J.D.; Burda, C.; Lou, Y.; Chen, X. *J. Phys. Chem*. B **2004**,108, 1230-1240
43. Nagaveni, K.; Hegde, M.S.; Ravishankar. N.; Subbana, G.N.; Madras, *G Langmuir*, **2004**, 20, 2900-2907
44. Thompson, T.L.; Yates, J.T. *Chem. Rev*. **2006**, 106, 4428-4453
45. Wong M.S.; Hsu S.W.; Rao K.K.; Kumar C.P. *J. Mol, Cata. A: Chem*. **2008**, 279,20-26
46. Li Xi.; Xiong R.; Wei G. *J Hazard*. **2009**, 164, 587-591

47. Tian B.; Li C.; Gu F.; Jiang H.; Hu Y. Zhang J. *Chem, Eng. J*. **2009**, 151, 220-227

48. Nie, X.; Solberg, K., Matter. *Res. Soc. Symp. Proc.Matter.Technol. Hydrogen Econ*. **2004**

49. Nagaveni, K.; Hegde, M.S.; Ravishankar. N.; Subbana, G.N.; Madras, *G Langmuir*, **2004**, 20, 2900-2907

50. Mills, A.;Le Hunte, S. .*J Photochem. Photobiol*. A: Chem. **1997**, 108, 1-35

# CHAPTER 3

# MODELLING DROPLET SIZE AND PARTICLE SIZE IN SPRAY PYROLYSIS

"*If any macro-phenomenon is found to be reproducible, then it follows that all microscopic details that were not reproduced must be irrelevant for understanding and predicting it. E.T. Jaynes, 1985"*

## 3.1 INTRODUCTION

This chapter shows the adaptability of an ancient technique in material synthesis that is based on the phenomenon of sound and how sound interacts with matter in liquid state. It also shows how this phenomenon is employed in the synthesis of nano-sized materials in chemical vapor synthesis. The chapter further entails the overwhelming progress that ultrasonic spray pyrolysis has achieved and the future challenges.

The deposition of semiconductor thin films in modern technology is extensive. The methods employed for thin film deposition can be divided into two groups based on the nature of the deposition process that are physical or chemical. The physical methods include pulsed laser ablation [1-3], molecular beam epixaty, sputtering [4-7] etc. On the other hand, chemical methods employ gas phase deposition methods and solution techniques as illustrated in Figure 3.1. The gas phase chemical methods are chemical vapor deposition (CVD), while spray pyrolysis (SP), sol gel, spin coating employ liquid precursor solutions [8, 9]. When dealing with vapors or gases as starting materials, the methods are referred to as chemical vapor deposition (CVD) and there are many forms of CVD, whereas the term "spray pyrolysis" SP is used when dealing with liquid droplets as precursor material.

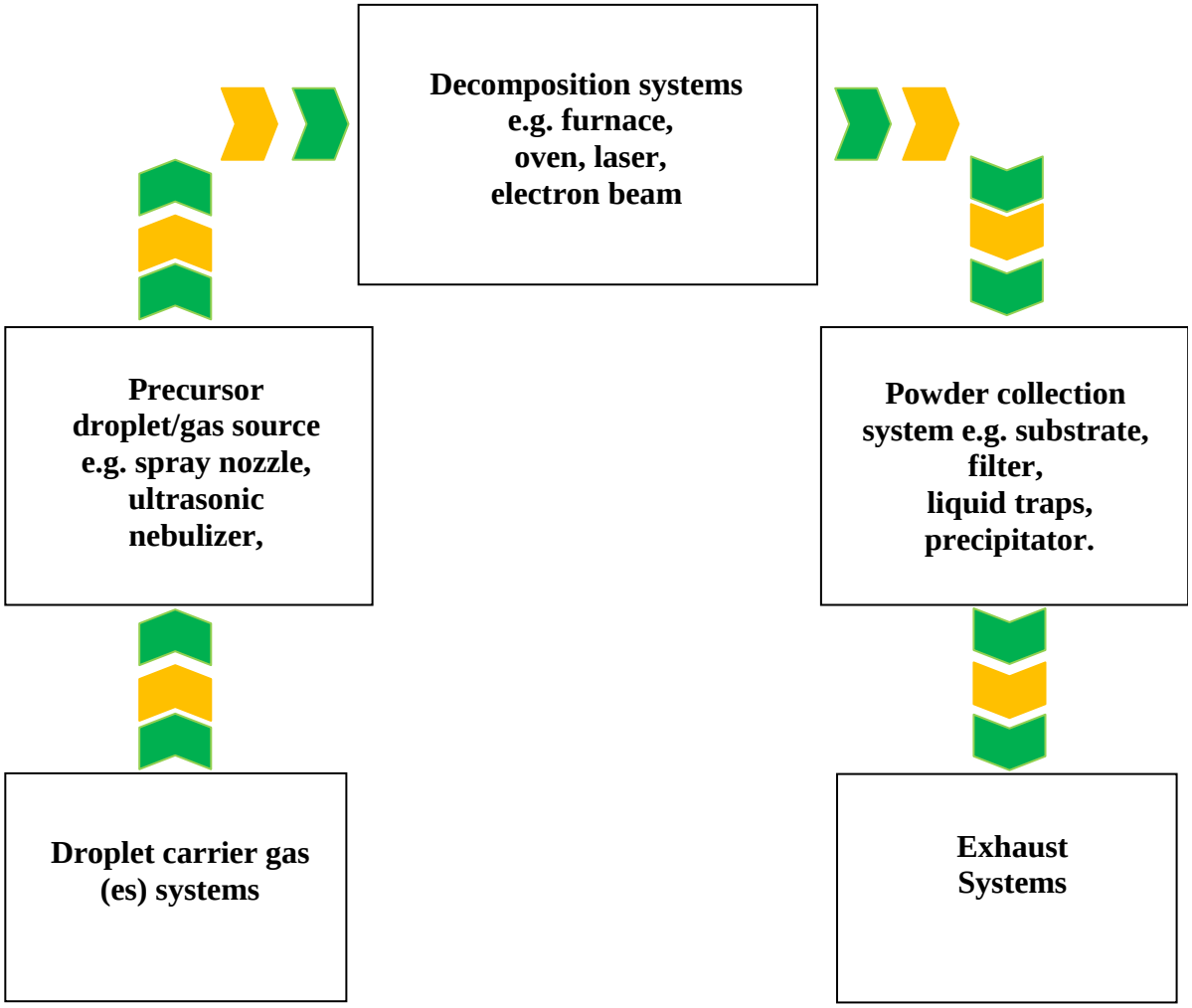


*Figure 3.1: Illustration of general chemical deposition methods*

The phrase pyrolysis has its roots in Greek, **πυρ** "pyre" which means "fire" and ***λυσϊσ*** lysis "breakdown" [10, 11]. Pyrolysis is usually understood as the decomposition of organic/inorganic material at elevated temperatures in the absence of oxygen. In this thesis, pyrolysis will refer to the decomposition of liquid precursor solution at elevated temperatures to produce semiconductor nano structures. The general process entails a source of chemical vapors/droplets generated by an atomizer, which is carried by means of a carrier gas into a heated zone. The generated chemical vapors/droplets undergo evaporation, decomposition and finally formation of nano structures at a heated substrate or a filter/trap for nano powders. This process is illustrated in Figure 3.2.

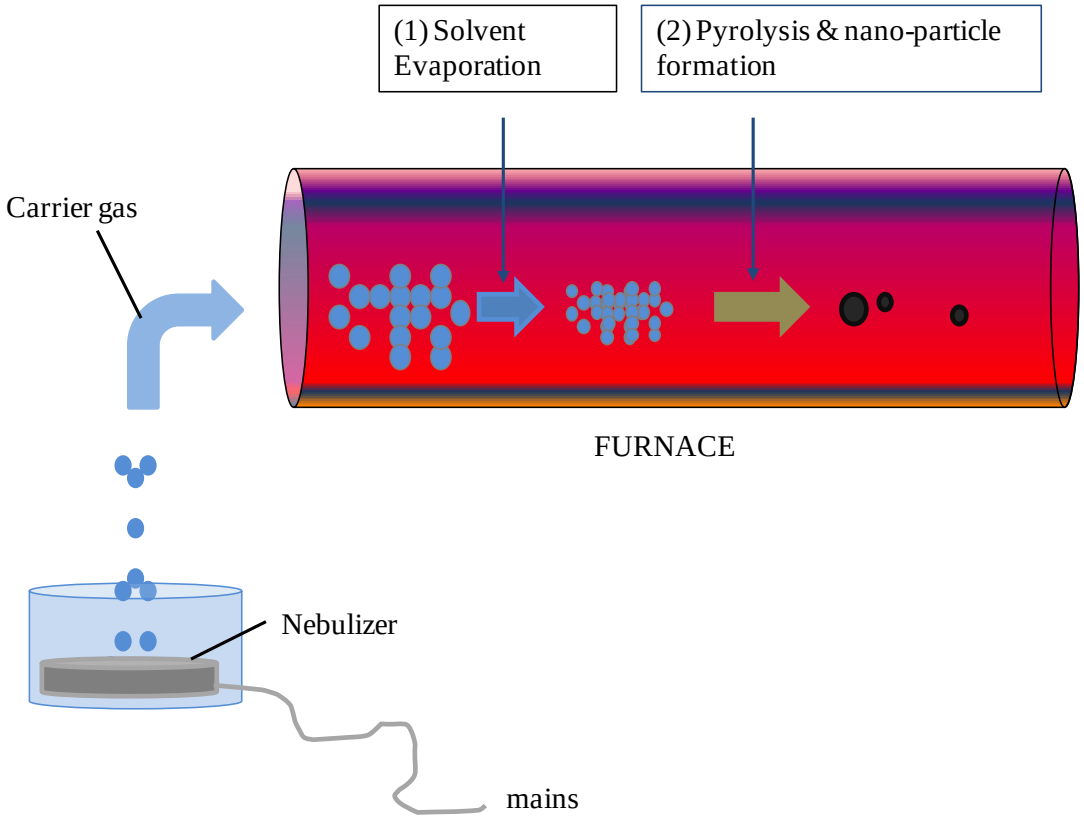


*Figure 3.2: Schematic presentations illustrating the pyrolysis of materials*

In spray pyrolysis the droplets or vapors are generated either by whistle type nebulizers or by ultrasonic nebulization. The former process is simply called spray pyrolysis (SP) and in the latter the case, the process assumes the name "ultrasonic spray pyrolysis" (USP).

The purpose of this chapter is to offer novel contributions to wet chemistry preparation methods for obtaining nano-sized powders. The present chapter is focused on production of titanium dioxide ($TiO_2$) nano-powders via low cost approaches. Special emphasis will be based on production of $TiO_2$ nano-powders using USP and PSP techniques. Furthermore the shortage of specific scientific review papers on production of nano-sized $TiO_2$ employing USP techniques was also the main motivation of the compilation of this chapter. Firstly, the present compilation begins by providing a theoretical framework of the mechanism of droplet generation employed

in USP. The triumphs and challenges of USP technique are presented. Lastly a new droplet relation model that includes thermodynamic properties of the precursor is presented. The new model includes thermodynamic properties such as pressure of the spray pyrolysis and volume of the spray pyrolysis in the droplet relation model. This greatly improves agreement between theoretical estimations and experimental findings.

## 3.2 ULTRASONIC SPRAY PYROLYSIS

When a liquid is subjected to a high intensity of ultrasonic fields, the splitting of liquid occurs to form droplets. The droplets are ejected from the liquid ultrasonic source interface into the surrounding air. A very fine dense mist of tiny droplets is formed as shown in Figure 3.3.

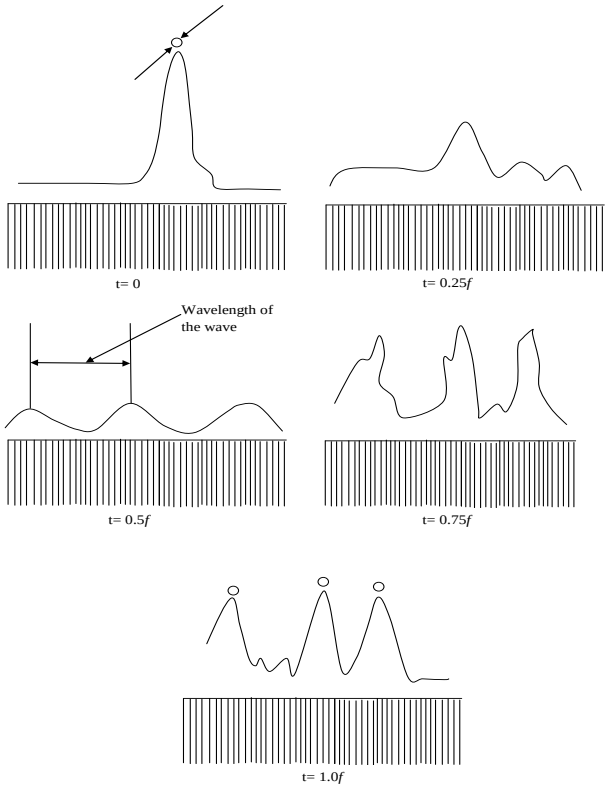


*Figure 3.3: Illustration of idealized droplet formation from standing wave crests showing one period of wall vibration, Adapted from [12]*

If sufficient ultrasonic energy is applied, the capillary waves are ruptures at the liquid surface to produce droplets. The received opinion in the literature is that droplets are formed periodically from the apexes of an orderly pattern of standing waves. Thus the droplets are produced at the crest that is proportional to the wavelength. The perceived mechanism of droplet formation is illustrated in Figure 3.3, where time $t$=0 is the start of vibration. It was further reviewed in literature how this mechanism of droplet formation may be incorrect in that, after droplet formation commences, the orderliness of standing wave pattern is lost due either constructive or destructive interference. [13-17]. The major advantage of ultrasonic atomization is that the size of the resulting particle and its density can be independently controlled unlike in the case of most spray pyrolysis techniques. The droplet size is controlled by the ultrasonic frequency for a liquid at specific flow rate having specified physic-chemical properties such as density, viscosity, and surface tension. The droplet size density is adjusted by varying the air flow past the liquid surface.

Ultrasonic atomization is a very effective way of generating small droplets. After the droplets are pyrolysed. Nano powders are formed can be achieved. Three approaches are common in this technique

1. Passing the flow of liquid across standing ultrasonic waves [13];
2. Depositing the liquid over an ultrasonic transducer [14]; and
3. Immersing a focusing ultrasonic transducer in the liquid in such a way that the depth of liquid is equal to the focal length of the ultrasound lenses in the transducer [15].

The second case generates a fine mist of droplets that are ejected from the transducer at very low velocity.

The possibility of generating a cloud of droplets by means of ultrasound waves was first reported by Wood and Looms [14]. Two mechanisms have since been invoked to explain the ultrasonic atomization, *capillary* wave mechanism and *cavitation* wave mechanism. Generation of droplets by capillary wave mechanism occurs at low excitation frequencies (20-100 kHz), where only surface atoms respond to form droplets. At higher frequencies (0.1-5 MHz), bulk atoms of the

liquid respond to form droplets and the droplet generation mechanism is called *cavitation* wave mechanism [13, 14].

### 3.2.1 CAPILLARY WAVE MECHANISM

The first studies on stationary waves on the free surface of a liquid mass subjected to periodic vertical forcing were reported by Faraday [15]. In 1871, Kelvin [16] derived the well known equation for capillary waves. The wavelength of these waves is given as

$$\lambda = \left( \frac{2\pi\sigma}{\rho f^2} \right)^{\frac{1}{3}} \tag{3.1}$$

where $\lambda$ is wavelength, $\sigma$ is surface tension, $\rho$ is density of the liquid and $f$ is the frequency of the surface waves.

Equation 3.1 was later modified by Rayleigh [17] to give

$$\lambda = \left( \frac{8\pi\sigma}{\rho F^2} \right)^{\frac{1}{3}} \tag{3.2}$$

where $F = 2f$ the frequency of the forcing sound.

The fact that the frequency of the surface waves is half the exciting frequency was empirically obtained [18]. Numerous experimental workers in the 1950s pointed out to unstable surface capillary waves as the origin of droplet formation relying on simplified linear analyses. The experimental determination by Lang [18] of the relationship between the wavelength of the capillary waves and the size of the corresponding droplets spurred the capillary wave mechanism to greater heights. Lang [18] reported that roughly 90% of the droplets were found to be smaller than twice the number-median diameter. A comparison of number mean median diameter with capillary wavelength indicated that the drop size is a constant fraction of the capillary wavelength and this turned out to be 0.34. Hence Lang proposed the following correlation:

$$D_{L\,ANG} = 0.34\left(\frac{8\pi\sigma}{\rho f^2}\right)^{\frac{1}{3}} \tag{3.3}$$

Lang showed that the droplet size ($D_L$) and the capillary wavelength ($\lambda$) were related by the empirical equation

$$D_L = 0.34\lambda \tag{3.4}$$

The droplets produced would have a certain distribution as there is a variation as to how much portion of surface wave peak is ejected as droplets. The non uniformity is also due to collision and agglomeration of droplets after being ejected from the liquid surface. Lang's correlation indicates no dependence of liquid phase viscosity and volumetric flow rate which is contrary to experimental observations. Also, it has been pointed out that Lang's correlation is applicable only when the liquid phase viscosity and volumetric liquid flow rate have no effect on droplet size. This is not always true as there are experimental observations indicating a dependence on liquid phase viscosity and volumetric flow rate [18].

A major revision to the Lang's equation was done in 1963 by Peskin & Raco [19] and later, in 1996 by Jokanovic *et al.,* [20], who rather than adopting an existing empirical equation, chose to derive a general equation from first principles by applying the Bernoulli's equation to an incompressible fluid of density ($\rho$), surface tension ($\sigma$) under pressure (*p),* due to an ultrasonic excitation *(f),* from a depth ***(y)*** and thereby generating a disturbance of amplitude $\xi$ (x, t)given by

$$\rho g h + \rho\frac{\partial\varphi}{\partial t^2} + \sigma\frac{\partial^2\xi}{\partial t^2} = 0 \tag{3.5}$$

where $\varphi$ is the Rate potential, *y* is equal to-*h* (height), *v* is equal to *0* (velocity), with $\partial^2\varphi/\partial x^2 = 0$ as boundary conditions

$$\varphi = \frac{1}{h}\frac{dy}{dt}c.h.[k(y+x)]e^{ikh} \tag{3.6}$$

Where $c$ is a constant, $k$ was taken to be the wave number ($2\pi/D_J$) and in turn $D_J$ is the Jokanovic aerosol droplet diameter. The Mathieu's function was then adopted to explain the typical shape of the relationship between the amplitude of oscillation of the meniscus surface and the wave number. The Mathieu's function is given as

$$\frac{dy}{dt} + \left[\frac{\sigma k^3}{\rho} t.h(k.h) - k.g.t.h(k.h)\right].y = 0 \tag{3.7}$$

The solution for equation (3.7) for $h >>> \xi(x,t)$ that is for small disturbances found by Jokanovic can be given as

$$D_{JOKANOVIC} = \left(\frac{\pi\sigma}{\rho f^2}\right)^{\frac{1}{3}} = \frac{1}{0.68} D_L \tag{3.8}$$

The relationship between droplet diameter and the Kelvin relation [16] for capillary wave length was also derived from dimensional analysis

$$D = k_1\left(\frac{\sigma}{\rho f^2}\right)^{\frac{1}{3}} \tag{3.9}$$

Where $k_1$ is a dimensionless constant which according to Lang [18] is $0.68\pi^{1/3}$ while according to

theoretical derivation by Peskin and Raco, and Jokanovic [19 ,20], the constant $k_1$ is equal to $\pi^{1/3}$. This means that the droplet diameter as calculated by Lang's equation is smaller by a factor of 0.68 in comparison with that determined by Jakanovic's equation. Jakanovic *et al*. [20] were able to show experimentally that their freshly derived equation yielded better agreement between calculated and experimentally determined droplet sizes. It must also be noted that Jokanovic *et*

*al*., [20] have used various forms of the equation of motion of the liquid at the surface including one given by

$$\frac{\partial \varphi}{\partial t} + g\xi - \frac{\sigma}{\rho}\left[\frac{\partial^2 \xi}{\partial x^2} + \frac{\partial \xi}{\partial z^2}\right] = 0 \qquad (3.10)$$

However, a number of more studies employing ultrasonic spray pyrolysis and using either the Lang's empirical formula have shown that both equations have limitations. A serious conflict between theory and experiment was reported by Nedelijovic *et al.,* [21] and Saponjic *et al*., [22]. Nedelijovic *et al.* reported that comparisons of the theoretically ($D_L$ = 132 nm, $D_J$= 195 nm*)* obtained results with the experimental determined ($D_{exp}$ = 286 nm) regardless of the equation employed for the determination of droplet diameters. Saponjic *et al.,* [22] also conducted the same experiments and they discovered that there was a significant difference between theoretical estimated ($D_L$ = 132 nm, $D_J$= 195 nm*)* as compared to the experimentally determined droplet size ($D_{exp}$ = 286 nm).

The reasons for this under-estimation by the theory of the experimentally determined droplet size could be due to assumptions in the original equation (3.1) which was derived by Kelvin in 1871 [16]. This gross underestimation could have also originated from Rayleigh in 1833 [17] who modified the Kelvin equation (3.1) and derived expression in equation (3.2). A major catastrophe of estimating droplet size relation was then continued by Lang in 1962 [18]. Lang published a famous expression relating wavelength to the droplet size through an empirical constant *k*, whose value was obtained from fitting his experimental measurements. The value of the experimental constant *k* was reported to be 0.34, which was placed in front of equation (3.1). This gross underestimation in determining final droplet size was continued when equation (3.3) was derived for estimating the droplet size on the basis of equation (3.1). Centuries later Jakanovic *et al*. [20] used Lang's equation to derive a droplet relation. The absence of the dependence of droplet size on liquid viscosity and volumetric flow rate which is contrary to experimental observations.

This calls for the consideration of the liquids bulk properties in the models. These short falls are discussed in the unsolved problems in the next section.

### 3.2.2 CAVITATION MECHANISM

Cavitation theory is necessary in explaining the capillary wave hypothesis and is generally applied to high frequency and high energy intensity systems. When a liquid is exposed to an intense ultrasound field, cavitation bubbles are formed during the implosive collapse of the generated liquid bubbles near the surface of the liquid. High intensity hydraulic shocks are generated which in turn initiate disintegration into droplets. At such large intensities the excitation is beyond the liquid surface but extends into the liquid bulk, contrary to the capillary hypothesis. Properties of the liquid such as viscosity come into play as parameters affecting the nature of the final droplet. The effect of viscosity and surface tension on the Taylors instability [12] has been studied. The rate of growth of amplitude disturbance is affected by viscosity has been observed. The increasing importance of viscosity as surface tension decreases has been suggested and the effects of density, viscosity. Interfacial tension and relative fluid velocity on formation has been elaborated by Clark [23]. Another empirical equation for the prediction of the droplet size at high liquid flow rates was proposed in 1978 by Mochida [24] as

$$D_{MOCHIDA} = 31.7\left(\frac{\sigma}{\rho}\right)^{0.354} \mu^{0.303} Q^{0.139} \tag{3.11}$$

where Q is equal to the volumetric flow rate, $\sigma$ is the surface tension, $\rho$ is equal to the density of the liquid and $\mu$ represents liquid Viscosity

Mochida's correlation takes into account the effect of physical properties and volumetric flow rate. It also correlates the radial distances of the spray to liquid flow rate, amplitude and the density. The complete spray was observed to fall in a parabolic orbit using high speed photography. Their observations gave evidence to capillary wave mechanism of droplet formation. However Mochida's *et al*., [24] droplet relation (equation (3.11)) does not account for the excitation frequency and the amplitude of oscillation.

The studies on droplet formation and breakage have shown that the numbers which dictate droplet size are Weber number and the Ohnseorge number. It was also reported that depending

on the flow pattern, above a certain critical Weber number the maximum stable drop breaks into many daughter droplets. This concept is extended to ultrasonic atomization to suggest that there is a maximum possible flow rate below which, the droplet size formed is dependent on flow rate. Tsai *et al*., [25] studied the resonate effect of air flow and ultrasound to amplify the growth of the instability. The experimental observations of Tsai *et al*., [25] also indicated that such a possibility and droplet size dependence was observed to follow equation (3.12) is given as

$$D_{ISAI} \approx Q^{0.25\text{-}0.30} \tag{3.12}$$

Experimental observations by, Clark *et al*., [23] have indicated the dependence of droplet size on liquid viscosity as

$$D_{CLARK} \approx \mu^{0.166\text{-}0.303} \tag{3.13}$$

This observed prediction of droplet size is believed to be based on the intuition or at the most heuristic arguments to include the effect of viscosity.

Peskin and Raco [19] studied the dependence of the average droplet diameter on the amplitude of forced vibration and liquid layer thickness present on the vibrating surface and developed the following correlation for prediction of droplet diameter:

$$D_{P\&R} = \pi A_m \left[ \left( \frac{2\sigma}{\rho \omega_0^2 A_m^3} \right) 2 \tanh \left( \frac{\pi A_m}{D} \right) \left( \frac{t}{A_m} \right) \right]^{\frac{1}{3}} \tag{3.14}$$

Peskin and Raco correlation (equation 3.14) was found to be rather complicated and like other correlations above it does not cater for physiochemical properties of the solution.

The above discussions indicate the lack of either theoretical or empirical correlation available to predict the droplet size formed by ultrasonic atomization, accounting for the observed dependence of liquid phase viscosity and the volumetric liquid flow rate. There is a need for an

universal correlation to predict droplet sizes during ultrasonic atomization considering the dependence on all physic-chemical properties of liquid atomized and ultrasonic parameters. Due to the non availability of such a correlation, there are no guidelines for the design of the ultrasonic atomizers for any specific application. In the subsequent sections, such an attempt will be made and it will be shown that Lang's equation (3.3) is a special case of the proposed generalized equation and is valid over a limited range'.

## 3.3 THEORETICAL PREDICTIONS OF DROPLET SIZE

Considering the limitations in the droplet correlations outlined in the previous section. Such a correlation is proposed here based on certain established logics in conventional nozzle atomization and the experimental observations using ultrasound. Hence from this stage onwards the candidate literature will be reviewed to try and solve the problem, estimating final droplet diameter taking into consideration all physicochemical parameters that affect the final droplets size.

### 3.3.1 ALTERNATE DROPLET SIZE CORRELATIONS

***Using the Rayleigh's instability criteria*** [26]

(1) According to the Rayleigh's instability criteria. The droplet size prediction can be made based on the number of drops formed on the vibrating surface area. Let us consider a unit surface area on a flat vibrating surface with frequency '$f$'. One drop is ejected from one node/wave and drop ejection takes place at every one wavelength. Therefore, number of points per unit surface area for drop ejection is $N=(1/\lambda)^2$; here, $\lambda$ is the wavelength that is the same as the threshold amplitude "$A_{mcrit}$ "and a simplified correlation was obtained for prediction of final droplet size formulae

$$d_{Rayleigh} = \frac{nQk}{3.74\sigma Am} \tag{3.15}$$

where Q is the volumetric flow rate, $\sigma$ is the surface tension, $A_m$ is the amplitude of sound wave *and* $\mu$ represents liquid Viscosity

The value of the constant *k* can be taken as 0.3. This expression is independent of liquid density and the frequency of oscillation and is applicable only at steady state conditions.

***Using Walzel's relation***

(2) Walzel [27] proposed relation between drop size and diameter of jet incorporating the viscous effect which is given as

$$D_W = \frac{1.06kQ\dfrac{n}{\rho}\left(\dfrac{\rho}{\pi\sigma f}\right)^{0.33}\left(\dfrac{\rho f^2}{\pi\sigma}\right)^{0.66}}{\left(fA_m\right)\left[2+0.6\dfrac{\mu}{fA_m{}^2\rho}\right]^{\frac{1}{3}}} \tag{3.16}$$

The value ***k***, is taken as 0.1. This correlation takes into account the influence of frequency, viscosity, and flow rate apart from liquid properties and ultrasound parameters.

***Using Davies approach***

(3) Davies [28] proposed a droplet correlation equation based on turbulent energy dissipation rates. Davies *et al.* considered the effect of dispersed phase viscosity by adding an extra resistance term of dispersed phase viscosity divided by the relevant energy dissipation for drop breakage. This was given as ($\eta\nu/d_{max}$). Thus along with the interfacial tension pressure ($4\sigma/d_{max}$) resisting drop breakage, the viscous resistance term was also added. His equation for drop break up in a turbulent emulsion system is given as

$$d_{max} = k_1(\sigma + \mu v/4)^{0.6}\rho^{-0.6}\ P_m^{\ 0.4} \tag{3.17}$$

where $P_m$ is power dissipated per unit mass, $\rho$ is liquid density, $\mu$ is liquid viscosity and $v$ is the mean velocity.

Davies [28] then extended the power dissipation concept to the ultrasonic atomizer to obtain the equation for prediction of droplet size. However, equation (3.17) was meant to predict the equilibrium droplet size after breakage and coalescence due to turbulence. This may not be the case in ultrasonic atomization as the breakage process may not be completed due to short residence times on the atomizing surface. Equation (3.17) when suitably modified for power dissipated per unit mass in terms of ultrasonic parameters would give a correlation which would predict the minimum equilibrium size that can be obtained. Taking into consideration that the short residence times would not allow the liquid jets/sheets to break up to the equilibrium size, the constant $k_1$ is introduced.

Davies [28] also considered the power dissipated per unit mass in a sonication system. The power intensity is given by $\frac{1}{2}\rho C A_m^{\ 2}(2\pi f)^2$. This was then multiplied by area to get the power and then divided by volume (Area×$A_m$) to get the power per unit volume of liquid which was given by

$$power/volume = \frac{1}{2}CAm(2\pi f)^2 W.Kg \tag{3.18}$$

Equation (3.18) was then divided by the liquid density to get the power per unit mass, $P_m$. which is given here as equation (3.19)

$$P_m = \frac{1}{2} CAm(2\pi f)^2 W.Kg \tag{3.19}$$

Equation (3.19) was the substituted into equation (3.17) to get a correlation for droplet size by introducing a constant and *v* (mean velocity) is substituted by the product of Am and *f* resulting in,

$$D_{DAVIES} = k_1 \left[ \sigma + \frac{\mu(Amf)}{4} \right]^{0.8} P^{-0.6} \left[ \frac{1}{2} (A_m)(2\pi f)^2 \right]^{-0.4} \tag{3.20}$$

The derived correlation is dimensional in nature. Hence it predicts the droplet size by considering the power dissipated per unit mass. It considers the influence of ultrasonic parameters and physico-chemical properties of the liquid. This correlation predicts different dependence of droplet size on these properties compared to previous correlations. Although the term included to account for viscous resistance indicates a dependence on amplitude and frequency, it is very insignificant unless the interfacial tension is too small. Hence, excluding this term, the exponent value of frequency is −0.8 (slightly high compared to the Lang's exponent value of −0.67) and for the amplitude the exponent value is −0.4.

The major drawback of this correlation is that it does not explicitly take into account the influence of liquid flow rate on the droplet size. This was proved Rajan and Pandit [29] in their experiments when they took account of the effect of liquid flow rate. This is illustrated Table 3.1

*Table 3.1: Comparison between droplet sizes predicted by different correlations and the experimental observation of Tsai et al., [25]*

| P (W) | *f* (kHz) | $A_m$ (µm) | Q $10^{-18}$ $m^3/s$ | D (µm) | Rajan & Pandit | Rayleigh | Walzel | Davies |
|---|---|---|---|---|---|---|---|---|
| | | | | | A=0.1 | K=0.3 | K=0.3 | $K_1$=30 |
| **1.0** | 54 | 2.02 | 2.16 | 50 | 60 | 12 | 9 | 50 |
| **1.5** | 54 | 2.48 | 2.16 | 45 | 58 | 10 | 8 | 46 |
| **1.8** | 54 | 2.72 | 8.47 | 80 | 65 | 35 | 29 | 44 |
| **2.0** | 54 | 2.86 | 27.46 | 90 | 83 | 108 | 91 | 43 |
| **2.5** | 54 | 3.20 | 8.47 | 60 | 60 | 30 | 26 | - |
| | | | 27.6 | 75-80 | 78.5 | 96 | 83 | 41 |
| **3.5** | 54 | 3.78 | 27.6 | 70 | 72 | 81 | 73 | 38 |

In Table 3.1 one can clearly note that the predictions made by Davies [28], is qualitatively in line as far as the amplitude effect is considered. However, as Davies correlation predicts independent of liquid flow rate, the predicted values deviate from experimental values as was observed by Tsai *et al.*, [25].

(4) Rajan and Pandit proposed a correlation by introducing the dimensionless numbers incorporating the physico-chemical properties of the atomizing liquid and the operating parameters of the ultrasound, which is given below [29]:

$$D_{R\&P} = \left(\frac{\pi\delta}{\rho f^2}\right)^{0.33}\left[1 + A(N_{We})^{0.22}(N_{Oh})^{0.166}(I_{In})^{-0.0277}\right] \quad (3.21)$$

Rajan and Pandit correlation equation (3.21) was based on Weber number ($N_{We}$), (which is the ratio between the aerodynamic forces and the surface tension forces), Ohnesorge number $N_{oh}$, (which is the ratio between the internal liquid viscosity to surface force and vibrational amplitude). Rajan and Pandit used these dimensionless numbers with an objective of explaning the effect of different physioco-chemical properties such as the surface tension, viscosity and

denstity of the liquid on the final droplet size. The dimensionless numbers were also modified by inserting the variable ultrasonic vibrational conditions to account for the ultrasound induced cavitation. A new dimensional number called intenstity number ($N_{In}$) was also propsed based on the ultrasonic intenstity.

The right-hand side of equation (3.21) indicates the change in the diameter of the drops due to the influence of parameters other than only '$\sigma$' and '$f$' as considered by Lang [18]. Rationale for choosing the exponents in this correlation are based on the experimental observations reported in literature [20-28] where few of the parameters have been studied whilst trying to include all the parameters to offer a universal correlation. Figure 3.4 shows the parity plot of predicted droplet sizes plotted against experimental determined droplet sizes.

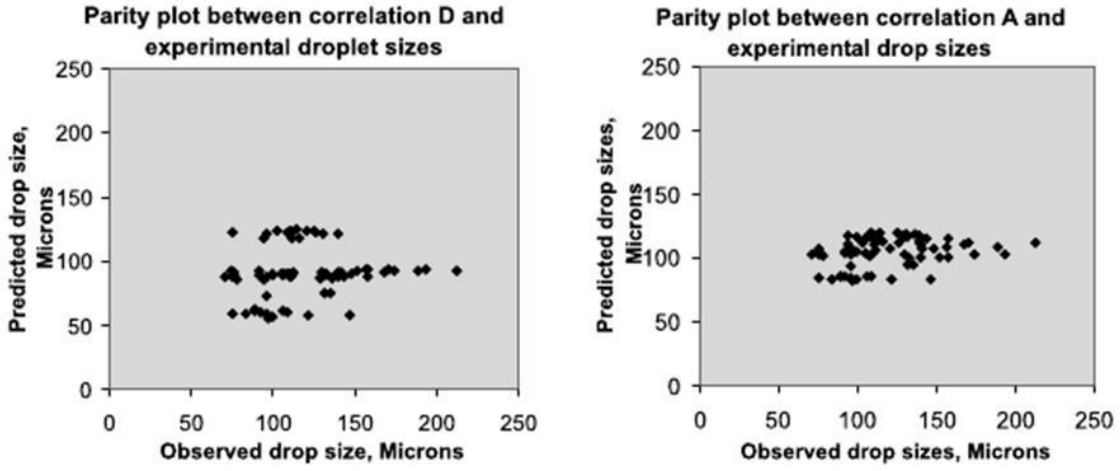


*Figure 3.4: Parity Plot between predicted droplet sizes and observed droplet sizes* [28]

However experimental observations have illustrated inconsistent results between the theoretical determined and experimentally determined droplet sizes. Rajan and Pandit correlation equation (3.22) was reported to be overestimating the droplets sizes [29]. The parity plots indicated significant shift from linearity from theoretical estimated droplet sizes from the experimentally determined droplet sizes above 100 μm as shown in Figure 3.4.

Rajan and Pandit highlighted the significance of incorporating all the parameters such as the liquid flow rate, vibrational amplitude, liquid viscosity and the parameters considered by Lang [18] such as liquid phase tension, density, and the vibrational frequency effects, amongst others. Avvaru *et al*., [30] proposed a correlation based on dimensionless numbers accounting for the effects of all these parameters mentioned above on droplet size. Avvaru *et al*. [30] correlation for prediction of droplet size for the pseudo-plastic liquid and the Newtonian glycerine solution was given as

$$D_{AVVARU}=\left(\frac{\pi\sigma}{\rho f^{2}}\right)^{\frac{1}{3}}+0.0013\left(N_{We}\right)^{0.008}\left(N_{Oh}\right)^{=0.14/n}\left(N_{In}\right)^{0.28} \tag{3.22}$$

The parity plot for the correlation showed the trend prescribed by the equation but with a significant scatter. The possible reasons for the scatter were attributed to Cavitation effects. Also the Parity plots shown in Figure 3.5 showed deviation for higher mean droplet size above 400 microns. The presence of the Cavitation phenomena generated longer spread in the distribution, which was equivalent in obtained higher standard deviation for higher droplet sizes.

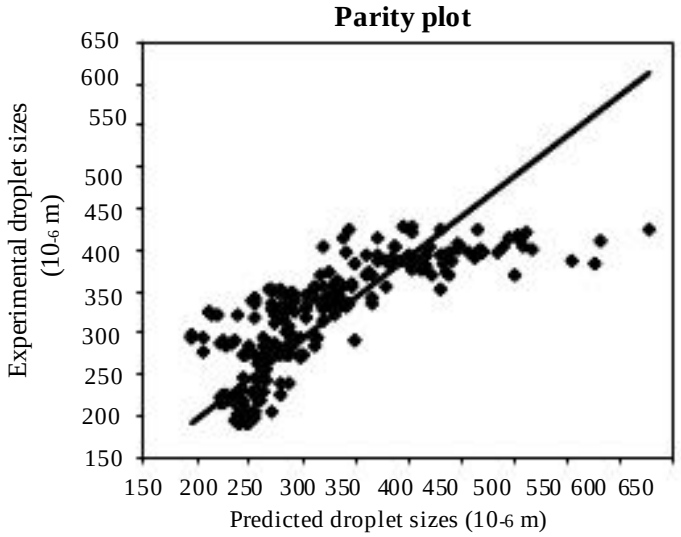


*Figure 3.5: Parity plot between predicted droplet size and observed droplet size* [30]

Based on the variations in the droplet size with operating parameters (both equipment as well as physic-chemical properties and flow rates of the liquid precursor) an empirical correlation was recently developed by Kiran *et al*., [31]. The correlation development was done by incorporating all the experimental values in polymath software. Number of model equations was used to get a good fit from the experimental data. An initial approximation, a simplest approach was based on fitting a correlation assuming power law for the independent variables (*Q, μ, σ, ρ, f, I*) and obtained correlation with the best fit which was given as follows:

$$D_K = 2Q^{0.156} f^{-0.180} \rho^{0.840} \mu^{-0.050} I^{0.017} \tag{3.23}$$

Equation (3.23) even though it gave a good fit ($R^2$=0.84) had its own limitation in terms of the dependency of the actual value of the variables and does not use none-dimensional numbers. Kiran *et al.,* [31] went further on in deriving another correlation that incorporated dimensionless numbers. The dimensionless numbers based correlation was adopted from the work of Rajan and Pandit [29], which they modified to include the effect of frequency of irradiation. The developed correlations that included dimensionless numbers gave a good fit ($R^2$=0.94) which is given here as predicted

$$D_K = 0.00154\left(\frac{\pi\sigma}{\rho f^2}\right)^{0.33}\left(1+\left(\frac{\pi\sigma}{\rho f^2}\right)^{-0.2} N_{Oh}^{-0.111} N_{We}^{-0.154} N_{In}^{-0.333}\right) \tag{3.24}$$

And the experimentally determined

$$D_K = 0.00154\left(\frac{\pi\sigma}{\rho f^2}\right)^{0.33} + \left(\frac{\pi\sigma}{\rho f^2}\right)^{-0.2} N_{Oh}^{-0.111} N_{We}^{0.154} N_{In}^{-0.333} \tag{3.25}$$

The parity plot for the obtained data as predicted by equation (3.24) and available from experimental measurements is shown here in Figure 3.6. It can be seen that the parity plot gave good agreement between the observed equation (3.24) and experimentally determined data sets equation (3.25).

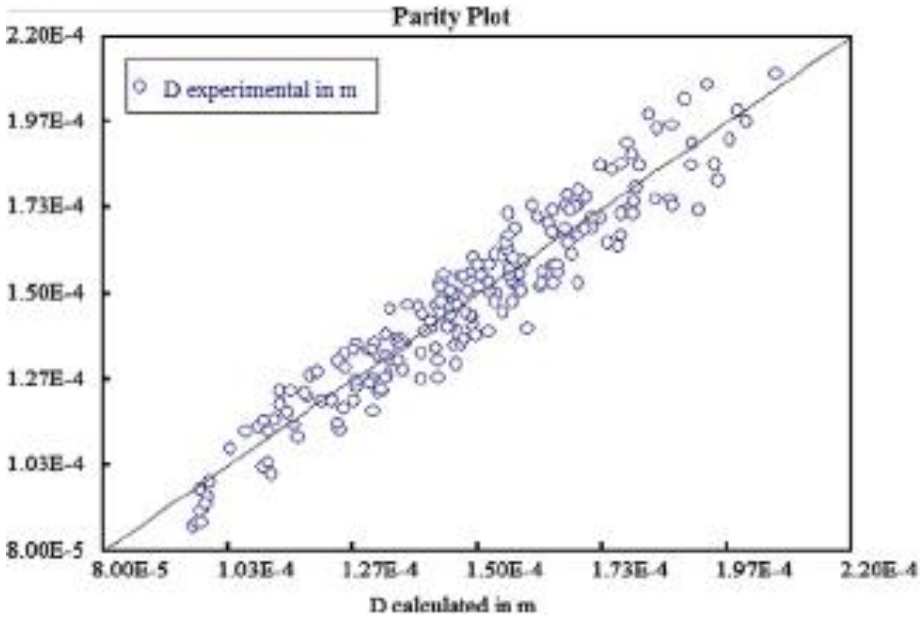


*Figure 3.6: Parity plot between experimental and calculated values of droplet size [adopted from [31].*

From equation (3.25) it has been observed that there was positive power on the Weber number. This showed that the droplet size dependence on flow rate [18] and negative sign of the power of Ohnesorge number (viscous number) gives an idea of decrease in the droplet size with an increase in the viscosity of the solution. Similarly, the intensity number showed a negative exponent on droplet size, which can be attributed to the simultaneous dependency on the power dissipation, frequency and liquid flow rate. The first term in equation (3.25) gave the representation of the ultrasonic atomization based on the capillary wave phenomena [3]; the second term in the equation (3.25) is the representation of dependence of the liquid physicochemical properties on the ultrasonic atomization with capillary and cavitational phenomena. Comparison of Kiran *et al*., [31] correlation with other correlations reported by several authors have shown an improved agreement between predicted droplet size and experimentally determined droplet sizes. [19-29].

Kiran *et al.*, [31] droplet correlation model is a perfect model for prediction of droplet sizes generated from ultrasonic nebulizers, but we have to stop and ask ourselves as material scientists. How then does one apply the droplet correlation model in prediction of the final nano-particle size in material synthesis? Kiran *et al.*, [31] droplet correlation model is very suitable for prediction of droplet sizes of ultrasonic vapors prior to pyrolysis in a reactor i.e. furnace reactors.

Up to date there is no model to predict the final nano-particle size after pyrolysis either be it in a furnace reactor or laser reactor. In the next section of this thesis, we attempt to produce a final nano-particle correlation model for prediction of nano-particles after the pyrolysis and hydrolysis of droplets in a reactor. We will use the knowledge gathered in this section to predict a nano-particle correlation rather than a droplet correlation model.

## 3.4 MODELLING FINAL DROPLET SIZE

As already introduced in the previous sections, the first explanation for the phenomenon of droplet generation from liquids by ultrasound waves was given by Lang [18] and his semi-empirical equation is given

$$D_{LANG} = 0.68(\pi)^{\frac{1}{3}}\left(\frac{\sigma}{\rho f}\right)^{\frac{1}{3}} \tag{3.3}$$

In 1999, Jakanovic *et al*., [20] formulated another parallel equation based on a partial differential equation of motion of the droplet in an ultrasonic mechanical wave field and managed to show that droplet diameters from ultrasonic spray could be calculated from the following equation:

$$D_{JOKANOVIC} = (\pi)^{\frac{1}{3}}\left(\frac{\sigma}{\rho f^2}\right)^{\frac{1}{3}} \tag{3.8}$$

Both of the above models assumed that the thermodynamic properties of the precursor liquid in the USP systems (such as pressure and volume) are negligible. However, in a real experimental situation, it is observed that every ultrasonic nebulizer increases the temperature of the precursor solution. Inclusion of a temperature dependent surface tension and density in the above models would improve the agreement between theory and experiment. Also, the pressure ($p$) in the USP system, shape and size ($v$) of the USP system are considered as a pertinent factor in the ensuing model. The droplet diameter can then be expressed as

$$D\left(p,V,T_{pr}\right)=k\left(\frac{\sigma T}{\rho\left(p,V,T_{pr}\right)f^{2}}\right)^{\frac{1}{3}} \tag{3.26}$$

And the deviation of the droplet diameter from the expected value due to change in surface tension and density which in turn are due to changes in precursor solution temperature and USP system pressure can be found by taking a first derivative of equation (3.26) above and this can be shown to take the form of

$$\frac{\Delta D}{D}=\frac{1}{3}\left(\frac{\Delta\sigma}{\sigma}-\frac{\Delta\rho}{\rho}\right) \tag{3.27}$$

Also, in a case where the ultrasound-focused surface level is not constant with time, the out of focus effects of bulk precursor properties such as viscosity may also need to be included in the models. (In this case, running through the dimensional analysis for the case of $D$ being dependent on viscosity, $\eta$ rather than density, $\rho$, the following expression for $D$ is obtained as,

$$\frac{\Delta D}{D}=\frac{1}{3}\left(\frac{\Delta\sigma}{\sigma}-\frac{\Delta\eta}{\eta}\right) \tag{3.28}$$

Equations (3.27) and (3.28) show similar characteristics. This means that the density of the starting liquid and its viscosity has similar error effects on droplet diameter. Since many researchers have used density rather than viscosity, the present discussion opts to use density throughout this thesis. In addition, the effects of substrate temperature and annealing temperature and duration of annealing all need to be inserted in the models when estimating the size of the so-obtained grains on a substrate [32].

From thermodynamics it is possible to deduce that surface tension reduces as temperature of the liquid increases. The relation between $\sigma$ and $T_{pr}$ (temperature of the precursor) from a rigorous analysis is given as:

$$\sigma = H + T_{pr}\frac{d\sigma}{dT_{pr}} \tag{3.29}$$

where $H$ is the energy required to increase the area of the surface of the liquid in contact with air by unit area and $T_{pr}$ is the temperature of the precursor solution in Kelvin units. It should be noted that the energy $H$ is always positive and it follows from the fact that σ decreases as $T_{pr}$ increases that the derivative is always negative. For many liquids $H$ is about +50 mJ/m$^2$ and the derivative about -0.1 mJ/m$^2$/K. Density $\rho$ can be written as a function of temperature from van der Waals real gas equation (in present study, the real gases are droplets or vapors) [48].

$$\left[p + \frac{a\rho^2}{M_{pr}^2}\right]\left[V - \frac{\rho V b}{M_{pr}}\right] = \frac{\rho V R T}{M_{pr}} \tag{3.30}$$

where $a$ and $b$ are the usual constants that depend on the real gas which for this case are very close to those of water vapour ($a$ = 0.5507 Jm$^3$/mol$^2$ $b$ = 3.04 x 10$^{-5}$ m$^3$/mol), $M_{pr}$ is the molar weight of the precursor solution material, p is the pressure in the chamber and V is the volume of the chamber, $R$ is the universal gas constant (0.082025 atm/mol/K). This has been accomplished by substituting in the original van der Waal's equation the following facts:

$$n = \frac{m}{M_{pr}} = \frac{\rho V}{M_{pr}} \tag{3.31}$$

where $n$ is the number of moles from equation (3.31) one gets three solutions of density ρ two of which have imaginary parts in them. The one solution that is completely real is given as:

$$\rho\left(p, T_{pr}\right) = \frac{M_{pr}}{3b} + \frac{0.42\Omega_1\left(p, T_{pr}\right)}{ab\Omega_2\left(p, T_{pr}\right)} + \frac{0.264\Omega_2\left(p, T_{pr}\right)}{ab} \tag{3.32}$$

$$\Omega_1\left(p, T_{pr}\right) = 3abM_{pr}^{\ 2}\left(bp + RT\right) - a^2bM_{pr}^{\ 2}RT \tag{3.33}$$

$$B = \sqrt{\left(\chi + 4\Omega_1\left(p, T_{pr}\right)\right)} \tag{3.34}$$

By substituting equations (3.29) and (3.31) into equation (3.3), one obtains a droplet size relation that predicts the final droplet size that is dependent of density of the precursor solution and surface tension of the precursor solution:

$$D\left(p,T_{pr}\right) = k\left[\frac{H - CT}{f^2\left(\frac{M}{3b} + \frac{0.42\Omega_1\left(p,T_{pr}\right)}{ab\Omega_2\left(p,T_{pr}\right)}\right) + \frac{0.264\Omega_2\left(p,T_{pr}\right)}{ab}}\right]^{\frac{1}{3}} \tag{3.35}$$

After substituting the constants *a*, *b*, $M_{pr}$, *R*, *H* as presented in Table 3.2 the final nano-particle relation reduces to

$$D(p,T_{pr}) = k\left[\frac{0.05 - 0.0001T_{pr}}{1.1\times10^5 M_{pr} + 1.6\times10^5\left(\sqrt{M_{pr}F^2 + 4G^3 + M_{pr}^3}\ F\right)^{\frac{1}{3}} + \frac{M^2{}_{pr}\left(7.6\times10^{-3} - 3.83\times10^{-5} - 10.33T_{pr}\right)}{\left(\sqrt{M_{pr}^6F^2 + 4G^3 + M_{pr}^3}F\right)^{\frac{1}{3}}}}\right]^{\frac{1}{3}} \tag{3.36}$$

When calculations are done for temperatures between room temperature and boiling point of water (100ºC) and for pressures around atmospheric pressure the terms then *F* and *G* tend to be negligibly small and the final nano-particle diameter expression finally reduces to

$$D(p,T_{pr}) = k\left[\frac{0.05 - 0.0001T_{pr}}{1.1\times10^5 M_{pr} + \frac{M^2{}_{pr}\left(7.6\times10^{-3} - 3.83\times10^{-5} - 10.33T_{pr}\right)}{\left(\sqrt{M_{pr}^6F^2 + 4G^3 + M_{pr}^3}F\right)^{\frac{1}{3}}}}\right]^{\frac{1}{3}} \tag{3.37}$$

*Table 3.2:* *Table of constants for the present proposed model for prediction of $TiO_2$ nano-particles final nano-particle size*

| SYMBOL | VALUE | UNIT |
|---|---|---|
| $M_{pr}$ | 235.867 | g/mole |
| $R$ | 8.2 | J/mol/K |
| $a$ | 0.5507 | $m^3$/mol |
| $b$ | $3.04 \times 10^{-5}$ | $kg/m^3$ |
| $C_pr$ | 0.01 | mole/L |
| $M_p$ | 79.867 | g/mol |
| $\rho_p$ | 1726 | $kg/m^3$ |

This present relation has been previously applied to predict the droplet size of pure solutions of $VO_2$ and $WO_3$ before by Mwakikunga *et al*., [32] and in this project the present relation will not be used to predict the droplet size of C-$TiO_2$ nano-particles. This is due to the presence of impurities in the precursor solution. This means that in addition to the precursor molecules there were other impurities present such as the dopant solution. The presence of impurity molecules has tremendous effects on the surface tension, viscosity of the solution and these cannot be accounted for by the present model. However, the presently derived nano-particle correlation model is quite advantageous in that it does not require listed values of surface tension and density for every precursor solution. Indeed these values are usually not available in literature. These difficult to measure constants have been replaced by constants that are widely available in literature. The present model however adds sophistication to the USP set up in that the system pressure, volume and the precursor temperature have to be monitored during experiment by additional instrumentation. This section adds to new knowledge of prediction of final nano-particle size when using existing models. Once again the model is specific to $TiO_2$ and that there is also a need for development of another model that is able to predict final nano-particle size regardless of the nature of the solution.

## 3.5 PNEUMATIC SPRAY PYROLYSIS

In pneumatic atomizers, pressurized gas is introduced via an orifice in such a way that the expanding gas stream moves perpendicularly to the end of a tube connected to the liquid reservoir. Due to the Bernoulli Effect [33], the low pressure created at end draws the liquid from the reservoir into the gas stream. The high forces occurring at the gas-liquid interface cause the solution to break up into small liquid droplets which become airborne and are carried away by the gas stream. The spray stream is then directed back to the liquid reservoir or breaks up into smaller droplets and exit the atomizer in the outlet stream

The mechanism for pneumatic spray generation can be divided into two main processes: *primary* atomization in which the liquid stream is broken into small sheets or ligaments. This takes place in the region close to the nozzle orifice. *Secondary* atomization, were the large drops from the primary atomization are further disintegrated into smaller droplets [34, 35]. The former one is influenced by internal nozzle flow and interaction of the liquid with the ambient air further downstream from the nozzle. These processes together determine the spray characteristics such as drop size, droplet velocity and spray angle. Liquid properties such as density, viscosity and surface tension also play significant part on atomization.

### 3.5.1 CLASSICAL MODEL: BREAKUP OF LIQUID JETS

In pneumatic spray pyrolysis the classical model of sheet and jet breakup is the *primary* process governing droplet formation unlike in ultrasonic spray pyrolysis where the capillary wave mechanism is the primary mechanism governing droplets formation. The classical model of sheet and jet breakup is based on the method of small disturbances, which are formed on the liquid surface or within the liquid [36]. These disturbances may be in the form of surface displacement, pressure or velocity fluctuations as well as fluctuations in liquid properties. They support the formation and propagation of waves that lead to disintegration into drops. The phenomena of breakup is time-dependent, i.e. a finite amount of time for the development of the instabilities is required. An increase in liquid viscosity extends the breakup time and causes that the breakup processes will occur further downstream resulting in larger drops. The first studies of the liquid

jet breakup were carried out by Rayleigh [17, 26]. According to his findings, the growth of small disturbances leads to breakup of the jet, when a certain wavelength, $\lambda_{opt,}$ of the most significant disturbance is reached. Weber [24] later extended Rayleigh's work and included the effect of viscosity on the jet disintegration. According to their studies, the mechanism of jet breakup is strongly dependent on the velocity of the issuing jet. At low velocities, the droplets from the disintegrated jet are fairly uniform, with diameters around the double of the initial jet diameter (Rayleigh breakup mechanism) [26]. With increasing jet velocity, the optimal wavelength for jet breakup decreases and so does the droplet diameter. For very high jet velocities, atomization occurs rapidly and very close downstream from the nozzle orifice [30].

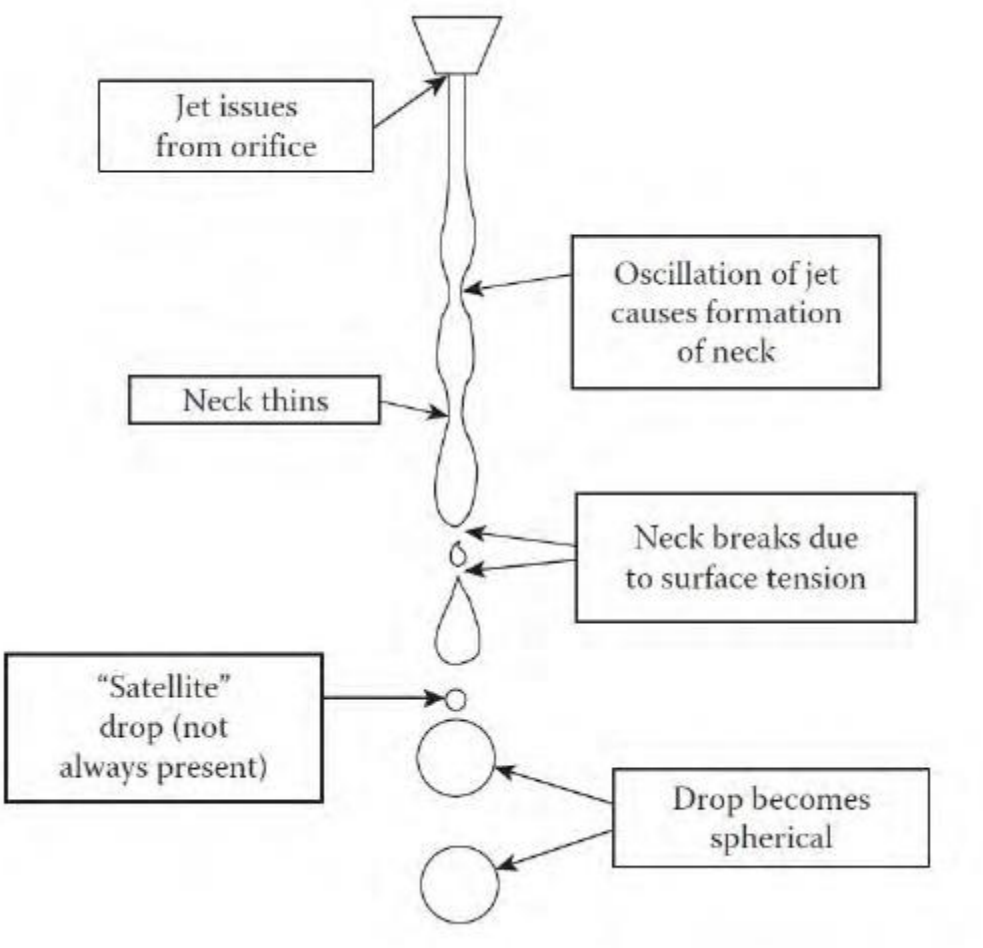


*Figure 3.5: Schematic presentation of breakup of a circular liquid jet with velocity Adapted from [37]*

### 3.5.2 BREAK UP OF LIQUID JETS

Most atomizers generate a conical liquid sheet which is broken up into droplets. The spray droplet sizes are generally about the same order as the liquid sheet thickness. The disintegration of a sheet, like that of a jet, depends mainly on the discharge velocity. Bayvel & Orzechowski [36] described the characteristic modes of sheet disintegration as a function of carrier gas discharge velocity. For the lower discharge velocity the thickness of the sheet decreases and the sheet is torn by perforations developed in thin areas. For higher carrier gas velocities, waves occur on the liquid sheet and ring of liquid break away from its edge and further disintegrate into drops (Figure. 3.6). For very high carrier gas discharge velocities, atomization starts at the nozzle exit (prompt atomization). There have been numerous studies on liquid sheet instabilities and factors influencing breakup [37].

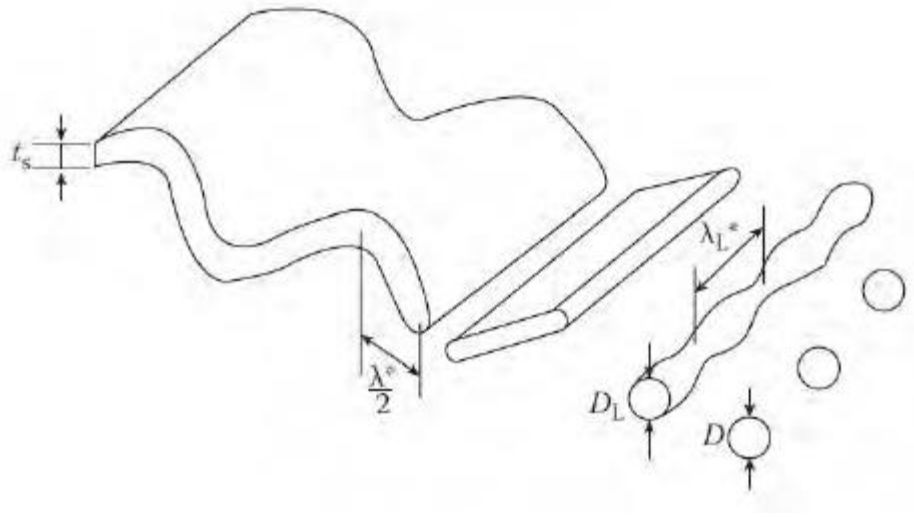


*Figure 3.6* *Planar liquid sheet disintegration and drop formation, Adapted from [37]*

## 3.6 CONCLUSIONS

In summary this chapter has given in detail, the theoretical background of the operation principles of ultrasonic and pneumatic spray pyrolysis. In addition the author has gone further in discussing the mechanism responsible for droplet generation. In this chapter we have also

discussed the physical factors that affect the final droplet size and eventually the final particle size. We went further into deriving a relation for estimation of the final nano-particle size given a set of initial reaction condition which has been done for the first time. Other droplet relations given in literature, when estimating final particle size, do not consider the physical conditions such as temperature of the precursor solution, viscosity of the precursor solution or the volume of the ultrasonic chamber. The derived nano-particle correlation model in this work considers all of these factors. However we have to admit that the presently derived nano-particle correlation model is specifically for $TiO_2$ precursor solution and there is need to develop a model that is independent of the precursor solution type.

## 3.7 REFERENCES


1. Amuroso S.; Tuzi S.; Palloti D.K.; Aruta C.; Bruzzese R.; Chiarella F.; Fittipaldi R.; Lettieri S.; Maddalena P.; Sambri A.; Vechhione A.; Wang X. *Applied Surface Science*. **2013**, 270, 307-311
2. Giacomo A.; Shakhatov V.A.; Pascale O.De. *Spectrochimica Acta Part B*. **2001**, 56, 733-776
3. Boutinguiza M.; Rodriguez-Gonzalez B.; Del Val J.; Comesana R.; Lusquinos F.; Pou J. *Applied Surface Science*. **2012**, 258, 9484-9486
4. Rawat R.S.; Aggarwal V.; Hassan M.; Lee P.; Springham S.V.; Tan T.L.; Lee S.; *Applied Surface Science*. **2008**, 255, 2932-2941
5. Abdollahi Nejand B.; Sanjabi S.; Ahmadi V. *Vaccum*. **2010**, 85, 400-405
6. Serio S.; Melo Jorge M.E.; Maneria M.J.P.; Nunes Y. *Material Chemistry and Physics*. **2011**, 126, 73-81
7. Chappe J.M.; Martin N.; Pierson J.F.; Terwagne G.; Lintymer J.; Gavoille J.; Takadoum J. *Applied Surface Science*. **2004**, 225, 29-38
8. Jih-Hsing Chang.; Ellis V.A.; Yung-Hsu Hsieh.; Cheng- Hung Tung, Shan-Yi Shen. *Science of the Total Enviroment*.**2009**,407,5914-5920
9. Na Jin, Yanqing Yang, Xian Luo, Zhenhai Xia. *Progress in Material Science*.**2013**. Article in press
10. Mooney J.B.; Radding S.B. *Annual Reviews of Material Science*. **1982**, 12, 81-101
11. Todorovsky D.; Todorovska R.; Petrova N.; Uzunova-Bujnova M.; Milanova M. *Chemical Technology and Metallugry*.**2006**. 41(1), 93-96
12. Yale, A.J.; Al-Suleimani, X.*; The Royal Society* **1999**
13. Bendig, L., **1988**. In: *Proceedings of the 4th International Conference on Liquid Atomization and Spray Systems.* ***The Fuel Society of Japan, Tokyo***, 133-138
14. Wood, R.W.; Looms, A.L.; *Phil Mag 7* **1927**, 417-433
15. Faraday M. *Phil. Trans. R. Soc. AM*. **1831**, 52, 319-340
16. Kelvin lord , W.T. *Phil Mag* **1871**, 42 362-377
17. Rayleigh L. *Phil. Mag*. 1883, 15, 50-58
18. Lang R.J.; *J Acoustic Soc Am*, **1962**, 34, 6-8

19. Peskin, R.L.; Raco, R.J.; *J. Acoust Soc Am* **1963**, 35, 1378-1381
20. Jakanovic, V.; Janackovic, Dj.; Uskokovic, D.; *Ultrasonic Sonochemistry* **1999**, 6 157-167.
21. Nedeljkovic, J.M.; Saponjic, Z.V.; Rakocevic, Z.; Jokanovic, V.; Uskokovic, D.P, *Nanostructured Materials*, **1997**, 9, 125-128
22. Saponjic Z.V; Rakocevic Z.; Dumitrijevic N.M.; Nedelikovic J.M; Jokanovic V.; Uskokovic D.P. *Nanostructured Mater*. **1998**, 10(3), 333
23. Clark, M.M.; *Conceptual and modeling considerations*, **1988**, CES 43(3) 671-679
24. Mochida, T.; *Proc. Class-78***, 1978**, 6, 178
25. Tsai S.C.; Childs P.; Luu P. *AIChE. J*. 1996, 42(12), 3340-3350
26. Rayleigh L. *Proc. London Math Soc*. **1878**, 10, 4
27. Walzel P. Int. *Chem. Engng*. **1993**, 33(1), 46-60
28. Davies J.T., *Academic Publishers London* **1972**
29. Rajan, R.; Pandit, A.B.; *Ultrasonic*, **2001**, 39, 235-255
30. Avvaru B.; Mohan N.; Patil N.; Parag R.; Gogate, Pandit A.B. *Ultrasonics*. **2006**, 44, 146-158
31. Kiran A.R.; Pandit A.B.; Parag R.G. *Ultrasonics Sonochemistry*. **2013**, 20, 254-264
32. Mwakikunga, B. W.;. Sideras-Haddad, E.; Witcomb, M.; Arendse, C.; Forbes, A.; *Nanoscale Res. Lett*.; 2008, 3, 372
33. Milosevic O.; Mancic L.; Rabanal M.E.; Gomez L.S.; Marinkovic K. *Kona Powder and Particle Journal*.**2009**, 27,84-106
34. Linsebigler, A.L., Lu, G., Yates, J.T. *Chem. Rev*. **1995**, 95, 735-738
35. Okuyama K.; Lenggoro W.I. *Chemical Engineering Science*. **2003**, 85,537-547
36. Bayvel L.; Orzechowski Z. *Types of atomizers, in Liquid Atomization*. Washington D.C.Taylor and Francis; **1993**. Chapter 4.
37. Squire H.B.*British Journal of Applied Physics*. **1953**,4. 1229-1232

# CHAPTER 4

# SPRAY PYROLYSIS DEPOSITION SYSTEM

## 4.1 INTRODUCTION

Spray pyrolysis (SP) provides a fast and reliable way or means of depositing various materials as thin films, nano-particles and nano-structures. This method is rather intricate and in Chapter 2, an extensive background on ultrasonic spray pyrolysis (USP) and pneumatic spray pyrolysis (PSP) was presented with particular attention given to droplet size determination in USP. In the context of USP, chapter 3 focused on $TiO_2$ nano-particle syntheses as the desired properties were evaluated. Based on experiences gained, while working on a spray pyrolysis system at the University of Witwatersrand and iThemba laboratories in Gauteng, a similar system was designed and constructed by the candidate at the University of Fort Hare. This system was optimized for the synthesis of thin films and nano-structures for photovoltaic (PV) applications with enhanced light absorption properties

This chapter starts off with an overview of $TiO_2$ deposition methods. Then it presents the various considerations that were used during the design and construction phase. The Fort Hare SP system is also presented together with its operation mode.

## 4.2 OVERVIEW OF $TiO_2$ THIN FILM DEPOSITION METHODS

Titanium dioxide has been deposited by many different techniques such as hydrolysis [1, 2], pyrolysis [3, 4], dip coating, plasma enhanced chemical vapor deposition (PECVD) [5-7], low pressure chemical vapor deposition (LPCVD) [6, 8], atmospheric pressure chemical vapor deposition (APCVD) [9-11], metal organic chemical vapor deposition (MOCVD) [12-15], evaporation, spin on methods [16-18], sputtering [19], ion assisted deposition [20], plasma anodization [21], reactive ion plating [22], laser ablation [23], filtered arc deposition [24], atomic layer epixaty[25] and more recently screen printing [26-28].

A principal consideration is that the growth morphology, crystalline structure and stoichiometry of $TiO_2$ thin films are very sensitive to the deposition conditions. This is a disadvantage for many physical vapor deposition methods. [25-28]. Such as laser ablation [28] were there are large variations in the optical and structural properties of the synthesized nano structures. These variations arise from small changes in the deposition conditions [22]. Therefore, the need for stoichiometric $TiO_2$ films suggests that a deposition method were the film stoichiometry is controlled by a chemical reaction would enable more consistent results.

The chemical reaction of a $TiO_2$ precursor to form $TiO_2$ can either succeed by hydrolysis or pyrolysis. With hydrolysis systems, separate gas lines of nitrogen or argon are bubbled through heated baths of a liquid $TiO_2$ precursor and water [1, 2]. The two delivery lines are then brought together close to the substrate where the reaction takes place. Pyrolysis systems are similar, except that a water bath is not required as the $TiO_2$ precursor decomposes upon reaching the heated substrate. Both of these systems have the advantage of simplicity, although they may be relatively inflexible, as tubing diameters have to be designed around predicted flow rates.

To keep the deposition system as simple as possible, maximize throughput, and keep costs at a minimum, systems with a vacuum chamber were not considered to be a viable option. This excluded evaporation, sputtering, and the majority of CVD systems.

Spin-on methods were not seriously considered, as the throughput of any such system would be limited in a production environment. Screen-printing is commonly used in the PV industry for depositing metallic contacts, about 30−50 μm. Szlufcik *et al.*, demonstrated that screen-printing could also be used for depositing $TiO_2$ thin films [30]. As the thickness of the metallic contacts are about 500 times thicker than the $TiO_2$ thin films it is not known how the thinner films behaved with regard to reproducibility, squeegee wear, and thickness uniformity. Following the screen-printing of the organometallic ink, the samples were fired in a three-step process of 30 min duration. The firing is a relatively slow process as first the thick film needs to settle for 15 min to obtain a uniform film, with subsequent drying performed at 125ºC for 5min. The final crystallization was performed in a belt furnace at temperatures between 500ºC and 900ºC. Lengthy drying procedures are required to remove the substantial amount of organic solvents added to the $TiO_2$ precursor. Therefore, to lower thermal the budget and processing costs it would be attractive to deposit a nano-crystalline $TiO_2$ thin film in one step without subsequent heat treatment steps [28].

## 4.3 DESIGN CONSIDERATIONS OF ULTRASONIC SPRAY SYSTEM

This section deals with some experiences obtained at iThemba laboratory, which helped to shape the various considerations for the present University of Fort Hare SP system. Furthermore, consideration is given to various material properties and deposition conditions that were used to optimize the design and construction of the University of Fort Hare SP system. This was done specifically for $TiO_2$ nano-structures used in solar cell applications.

### 4.3.1 EXPERIENCES AT iTHEMBA LABORATORIES

The previously constructed system at iThemba laboratories consisted of a tube furnace, pneumatic nebulizer and quartz tube as the reaction zone. Spray deposition was done on glass substrates lying horizontally on the floor of the quartz. In the study we employed titanium tetra-chloride as the precursor. The system also employed argon gas as the carrier gas in case where the ultrasonic nebulizers were used.

There were a number of problems with the $TiO_2$ films and the deposition system. ***Firstly,*** the use of titanium tetra chloride as a precursor for synthesis of $TiO_2$ created huge problems with chloride impurities. As cubic structures of sodium chloride crystals where formed during the cooling process on top of the $TiO_2$ thin films. It was speculated that at temperatures above 400°C sodium ions percolate from the quartz tube which could cause sample contamination as shown in Figure 4.1. Furthermore titanium tetra chloride fumes are toxic and with poor ventilation system the fumes have serious health risks.

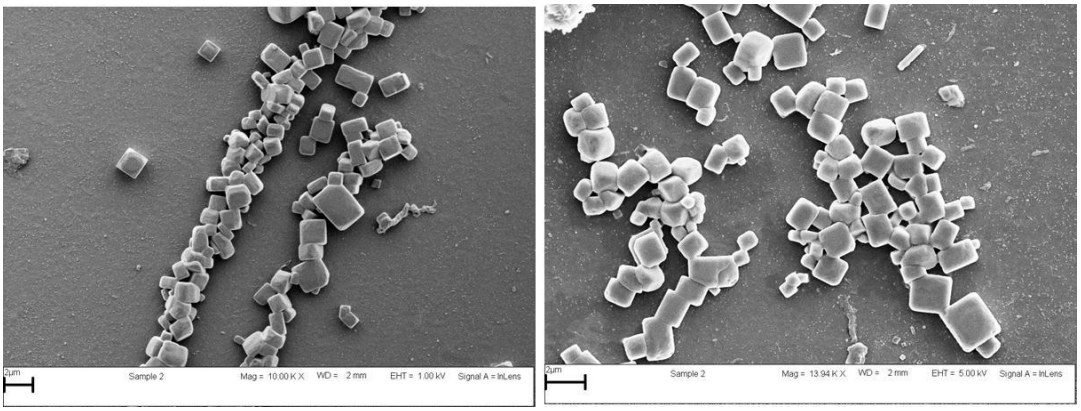


*Figure 4.1: SEM image showing formation of NaCl crystals on top of $TiO_2$ thin films*

*Secondly,* it took over an hour to deposit thin films of about 10 μm in thickness. In addition the deposited thin films were not uniformly coated. This was due to low aerosol volumes as most of the titanium tetra chloride easily hydrolyses to form white precipitates of hydroxides in a anhydrous ethanol solution at temperatures above 25 °C. This makes it almost impossible for the carrier gas to lift solid particles onto a heated substrate. Furthermore there was non uniform deposition of $TiO_2$ thin film as some areas on the substrate were found to be thicker than others and other areas contained no $TiO_2$ nano-particles at all as shown below in Figure 4.2.

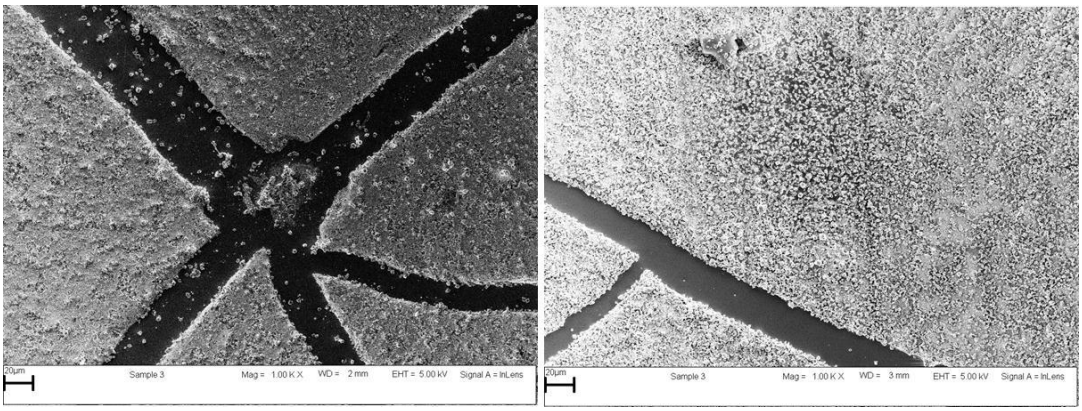


*Figure 4.2: SEM image of non-uniformly coated $TiO_2$ thin film.*

It was also discovered that only some areas of the substrate facing the aerosol flow were fully coated. Areas on the substrate downward the aerosol flow where partially coated. *Thirdly*, the deposited thin films had cracks in them due to sudden temperature drop when the system was turned off. There was no proper temperature regulation (furnace temperature ramping). Also the substrates cracked under sudden temperature loss. *Fourthly,* it took several hours for the system to cool down to room temperature. As a result thin film depositions were limited to 3 samples a day. *Fifthly*, the round tube furnace employed had poor heat insulation. Hence after some hours of operation the temperature of the laboratory could rise to as far 38°C, which made monitoring of the spray pyrolysis deposition very difficult. *Furthermore,* it was impossible to mount such a spray pyrolysis system directly to a normal laboratory workbench as this presented a higher fire risk. In addition all rubber tubing, and O rings could not withstand the high temperatures as they needed to be constantly replaced. This posed a further health risk due to leakage of argon and titanium precursor vapors into the working environment. *Lastly*, there was no way of regulating the relative humidity, and the relative humidity on rainy or overcast days (humidity up to 65%) made spraying impossible due to the formation of white $TiO_2$ hydroxides in the precursor solution. This made it very difficult to atomize the precursor solution. Also atomization of large particulates of $TiO_2$ hydroxides led to the development of large nano agglomerates inside the thin film structure of amorphous $TiO_2$ phase inside the Anatase $TiO_2$ thin film which is not desirable in developing thin films for photo voltaic applications.

### 4.3.2 MATERIAL PROPERTIES

***STRUCTURAL PROPERTIES***: The synthesized nano structures must be defect free (defects creates electron sinks), with thickness for thin films of less than 10 μm. The synthesized nano structures must contain un-doped $TiO_2$ and/or C-$TiO_2$ in the Anatase polymorph which is more photo-active as compared to Rutile polymorph phase of $TiO_2$. Furthermore the synthesized nano structure(s) must not at all contain amorphous $TiO_2$ phase as this form of $TiO_2$ is prone to chemical attack such as in application of thin films as photo electrodes in solar cells. The $TiO_2$ films should be polycrystalline Anatase in order to withstand the necessary wet chemical processing during solar cell fabrication.

***OPTICAL PROPERTIES***: The synthesized nano structures must be capable of absorbing solar radiation in the visible section of the solar spectra, but must be of Anatase polymorph for solar cell applications. Introduction of impurity atoms (carbon) must be done carefully so as not to initiate transformation of Anatase to Rutile during synthesis.

***ELECTRICAL PROPERTIES***: The synthesized nano structures must be at least semiconducting at room temperature and preferably highly conductive; but should never be insulating. This requires that the synthesized nano structures be of good stoichiometric ratio and should not exhibit oxygen vacancies. The synthesized nano structures must contain certain levels of impurities to enhance electron transport and hinder electron recombination. It's has been shown that carbon doped titanium dioxide has better electron transport mechanism as compared to pure un doped titanium dioxide. [31-34]

### 4.3.3 OPERATIONAL CONDITIONS

***SAFETY***: The system should be enclosed so that it can safely operate on a standard laboratory bench. It also needs to have exhaust facilities into a sufficiently ventilated area. There was also a need to replace the tube furnace with a split tube furnace that had heat guides on. This made it easy and safe to operate with aluminum tubing and/or quartz tubes as reaction vessels. The furnace was built in such a way that no heat was dissipated into the work environment. It was

also desirable to discontinue use of titanium tetrachloride as a precursor because of the reasons mentioned before. Titanium iso-propoxide and titanium butoxide were also more attractive to use as precursors since these are safe, non-toxic liquid, and obviate the need for expensive gas handling systems.

***GEOMETRY CONTROL***: The other problem that needed urgent attention was issue of substrate orientation. It was discovered that disposition of thin films at an oblique angle of 30°or with substrate lying on the floor of the quartz tube caused inhomogeneous thin film coating. We designed an aluminum substrate holder that secured the substrate at 90° of the reaction vessel axis, facing the incoming aerosol flow.

Aluminum was chosen as the metal of choice because its stable at deposition temperatures of 400-500°C and it is a good conductor of heat. It also allowed preheating of FTO substrate prior to thin film deposition. In addition significant fluctuations in the temperature at about 400°C could result in the $TiO_2$ film having a mixed amorphous-Anatase phase. Naturally, this outcome is undesirable.

***DEPOSITION AREA***: As this project had commercial relevance, it was desirable that the substrate be masked; this allowed production of a thin film area of 0.5 $cm^2$ which are desirable for dye solar cell and photo electrochemical solar cell application.

***RELATIVE HUMIDITY***: Excess humidity will result in $TiO_2$ particulates sticking to deposited film. Our initial aim was to have adjustable and repeatable humidity control. It was anticipated that mixtures of dry nitrogen ($N_2$) and wet nitrogen ($N_2$+$H_2O$) could be fed into the system in order to control the relative humidity as was previously used by other authors [35]. However this proved to be costly we opted to use the carrier gas argon to provide dry environment with success.

***DEPOSITION TIME***: To achieve accurate control of the film thickness, the system was calibrated to produce sufficient thin films in deposition times of 20-30 min..

## 4.4 FORT HARE SPRAY PYROLYSIS SYSTEM

Following the $TiO_2$ nano-structured material properties and the operational conditions considerations as has been discussed in section 4.3 of chapter 4 and section 2 of Chapter 2. An ultrasonic spray pyrolysis (USP) system was designed and constructed at the University of Fort Hare. Figure 4.3 shows a schematic diagram of the USP system that was optimized for $TiO_2$ nano-structures deposition.

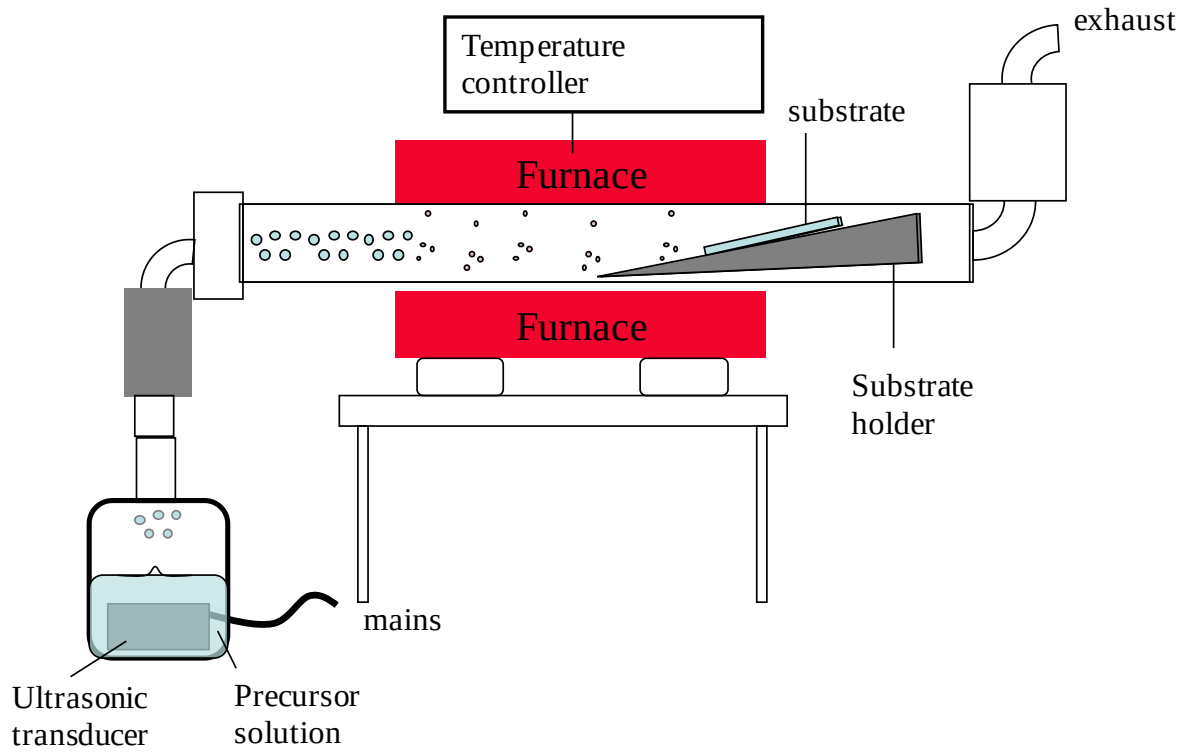


*Figure 4.3: A schematic diagram of the full USP system*

The design USP system comprises of a ultrasonic chamber, a carrier gas system, a heated zone or furnace with temperature control, substrate holder and exhaust system. The ultrasonic chamber houses a transducer producing ultrasound waves at a frequency of 1.67 MHz that were focused to the precursor solution surface to produce a vapor of ultrasound droplets. The argon carrier gas system was used to deliver the precursor droplets into quartz or aluminum tube at a constant flow rate of 6 ml/min. The quartz or aluminum tube was in a temperature controllable furnace with the substrate holder placed perpendicular to the direction of gas flow inside the tube. Both deposition

temperatures and flow rate influenced the shape, size and structure of the deposited layers. These $TiO_2$ layers were deposited on fluorine doped tin oxide (FTO) glass substrates.

### 4.4.1 SELECTION OF $TiO_2$ PRECURSOR

Studies of the effects of preparation method and titanium precursor on the resulting titania crystal structure has been comprehensive. The effects of titanium (IV) sulfate and titanium (IV) chloride solutions were studied [36]. It has been reported that although the initially dried products were always amorphous, the first crystalline forms present varied with preparation method and precursor solution. Samples originating from titanium (IV) sulfate solutions always gave the Anatase structure, while samples produced from the boiling of titanium (IV) chloride solutions always gave the Rutile structure. Other methods of synthesis such as hydrolysis of titanium (IV) phosphate solutions or hydrolysis at room temperature gave either the Anatase structure or a mixture of both the Anatase and the Rutile structure. Wilska [36] found that an amorphous phase always existed prior to the crystalline phase, even in the cases of direct Rutile formation. No mechanism was proposed to explain the different effect of sulfate and chloride precursors on the phase transformation.

Proper choice of a precursor is a primary issue in material synthesis. Titanium isopropoxide also known as tetraisopropyl titanate (TPT) was chosen as the $TiO_2$ precursor. Apart from being the most commonly used precursor in the literature, this titanium alkoxide is also used in many solar cell production lines.

Titanium tetrachloride/ titanium (IV) chloride ($TiCl_4$) is another common $TiO_2$ precursor, which results in chlorine contamination [36]. In addition, its corrosive by-products (HCl) are produced in the reaction. It has been reported in literature that levels can be so high as to prevent nano material crystallization on FTO glass substrates and can also cause thin film poor film adhesion onto the substrate [36] In any case, the level of contamination observed with Titanium iso-propoxide is much smaller than with titanium (IV) chloride. Also it has been reported that the use of titanium (IV) chloride results in formation in Rutile and Anatase phase mixture [37] and we also discovered that the use of titanium butoxide resulted in the formation of 95% Anatase

phase. Hence in this project titanium iso-propoxide and titanium butoxide where used as the precursors for the synthesis of $TiO_2$ nano structures.

In addition these precursors have the following added advantages;

(1) non-corrosive and non-toxic, listed as being a mild skin and eye irritant
(2) can be highly purified and has an almost indefinite shelf-life
(3) as a liquid, it is relatively easy to handle, although it should not be exposed to a naked flame. The fact that it is not dangerous makes the addition of titanium iso-propoxide system a relatively easy and safe task, as no special gas handling equipment is required
(4) very volatile at low temperatures (50 °C), which means that it will be readily decomposed.
(5) can be ultrasonically sprayed directly without dilution.
(6) has been observed that there is enough oxygen in the titanium iso-propoxide molecule that the reaction to form $TiO_2$ can proceed without additional oxygen in the ambient

### 4.4.2 PYROLYIS OF TITANIUM ISO-PROPOXIDE

Many processes occur simultaneously before a droplet hits the surface of the substrate. When a precursor droplet hits the surface of the substrate: evaporation of residual solvent, spreading of the droplet, and salt decomposition occurs. Many models exist for precursor decomposition depending upon the chemical environment.

The mechanism of the reaction of titanium iso-propoxide aerosol to form $TiO_2$ depends on the droplet size. If the majority of the aerosol is a gas when it contacts the substrate then the deposition conditions are similar to a CVD process. Aerosols with larger droplet sizes will not have had time to vaporize completely, while smaller droplets will be decomposed by pyrolysis before striking the substrate. Since the droplet size distribution is small in ultrasonic spraying, the same decomposition conditions will apply to nearly the entire aerosol.

Viguie and Splitz [39] proposed the following processes that occur with increasing temperature as illustrated diagrammatically in Figure 4.4.

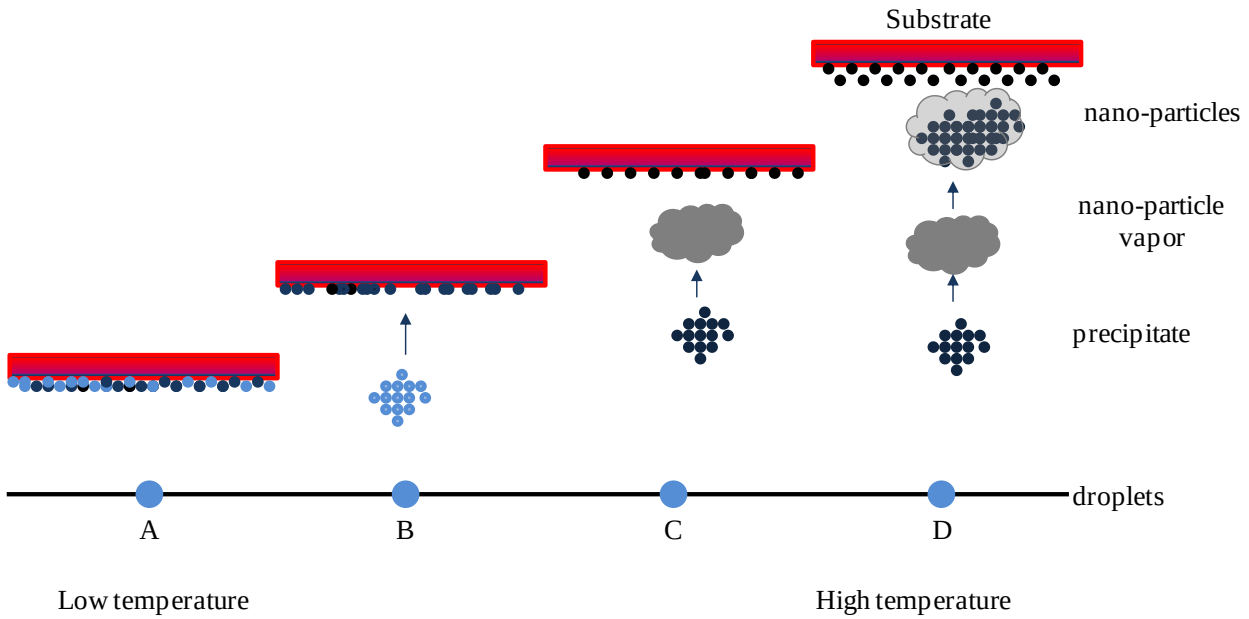


*Figure 4.4: Illustrations of aerosol droplet transport, decomposition and deposition on substrate at various temperatures.*

In process A, the decomposition rate at very low temperatures (<100ºC) will be slower than the deposition rate and a liquid film will form on the surface. This layer will slowly dry, however it will still contain many organics and probably cracks. At this stage titanium dioxide will be present as hydrated white hydroxide and in its amorphous phase. As the temperature of the substrate increases in process B, the solvent from the droplets evaporate during its flight before reaching the surface and a precipitate strikes the substrate where decomposition occurs. In process C, the solid precipitate melts and vaporizes (or sublimes) and the vapor diffuses to the substrate and undergoes a reaction there. This corresponds to true CVD. At higher temperatures (process D), the vapor undergoes a chemical reaction before impinging upon the substrate. The droplets in the aerosol have formed solid particles that stick to the surface of the substrate. Titanium iso-propoxide pyrolyses at temperatures greater than 350ºC, and films deposited in this

method at 450−600ºC are considerably harder than films produced by colloidal synthesis methods [39].

In an inert and dry argon environment and assuming the absence of water vapor the decomposition of titanium iso-propoxide occurs should occur via pyrolysis process to form $TiO_2$ proceeds as follows:

$$Ti(OC_3H_7)_4 \xrightarrow{\text{Pyrolysis}} TiO_2(s) + \text{Olefins} \quad (4.1)$$

However such an assumption is very dangerous as there are various sources of water vapor, for instance the solvent ethanol, the carrier gas and the spray pyrolysis vessel itself. There is to some extent formation of titanium dioxide via a hydrolysis process which is governed by equation (4.2).

$$Ti(OC_3H_7)_4 + 4H_2O \xrightarrow{\text{Hydrolysis}} 2Ti(OH)_4 + 4C_3H_8O \quad (4.2)$$

$$TiOH)_4 \xrightarrow{\text{Condensation}} TiO_2.xH_2O + (2-x)H_2O \quad (4.3)$$

$$TiO_2xH_2O \longrightarrow TiO_2 + \uparrow H_2O \quad (4.4)$$

One should note that the formation of titanium dioxide occurs to a larger extent by equation (4.1) and to a negligible extent by equations (4.2), (4.3) & (4.4). The size stability and morphology of the produced titanium dioxide is determined by the molar ratio of adsorbed water in equation (4.3). i.e $(x=[H_2O])/[Ti]$. At *x<10,* spherical, relatively mono disperse particles are formed. On the other hand at higher *x* values, particles formed are unstable and precipitate in the form of large aggregates which can be chemically peptized to final nano-particle sizes that are usually greater than 100 nm.

## 4.5 ULTRASONIC SPRAY SYSTEM

### 4.5.1 SELECTION OF ULTRASONIC VESSEL

The Bernoulli's theorem of conservation of energy of fluid flow in channels of varying cross-sectional area was considered useful in deriving the relationship between droplet size and volume it occupied. This theorem was also applied here in determining the proper volume to house the ultrasonic nebulizer. This is mainly because the volume of the reaction vessel plays an important role in determining the final nano–particle size The Bernoulli's theorem states that:

$$\mathrm{P} + \frac{1}{2}\rho v^2 + \rho \mathrm{gy} = \text{constant} \tag{4.5}$$

For a droplet distribution of mass (*m)* moving at mean speed (*v),* and occupying a volume (V) under pressure (P) the chain rule, for $\mathrm{P} = mV$ substitution results in:

$$dp + \left[\frac{1}{2}mv^2 + \mathrm{mgy}\right]\mathrm{dV} + \mathrm{pvdv} + \mathrm{g}\rho\mathrm{dy} = 0 \tag{4.6}$$

and assuming small variations in the droplet size change with change in velocity, which is typical in materials deposition processes, then $dv$ is approximately equal to zero. Equation (4.6) then reduces to:

$$dp = -\mathrm{EdV} - \mathrm{g}\rho\mathrm{dy} \tag{4.7}$$

where ***E*** is the total energy of the droplet. If the droplet diameter is introduced into this equation, it is possible to rewrite equation 4.7;

$$\frac{\mathrm{d}D}{dp} = -\frac{dD}{EdV + g\rho dy} \tag{4.8}$$

Therefore, at a constant position y

$$\frac{dD}{d\rho} = -\frac{dD}{EdV} \tag{4.9}$$

Similarly, at a constant volume of the system but varying position,

$$\frac{dD}{dp} = -\frac{dD}{g\rho dy} \tag{4.10}$$

Figure4.5 shows the importance of droplet diameter as a function of USP volume.

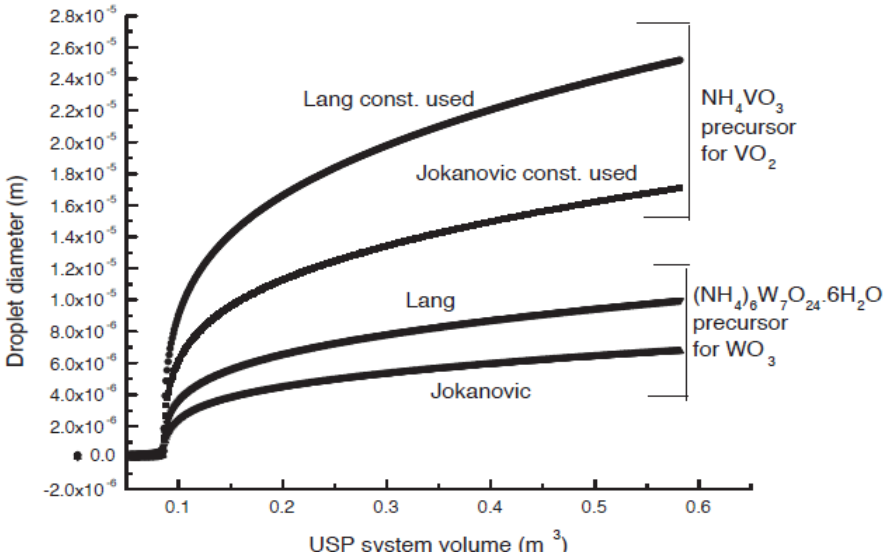


*Figure 4.5: Experimental evidence of droplet diameter dependence on USP system volume [42].*

The theoretical data models have shown a sharp increase of droplet sizes with change in USP system volume. This effect of volume change has also been observed by droplets generated by Mwakikunga *et al*., [41] and Priol *et al*., [42].

The main goal for this work was to develop an ultrasonic spray pyrolysis system capable of realizing nano-sized powders, considering previous findings by Mwakikunga *et al.,* [41] and Priol *et al*., [42] an ultrasonic reaction system with maximum volume of 0.1 $m^3$ was developed.

Figure 4.6 shows the USP reaction vessel used in this study. The quartz glass used for the vessel provided a non-corrosive environment for housing the acidic precursors of $TiO_2$.

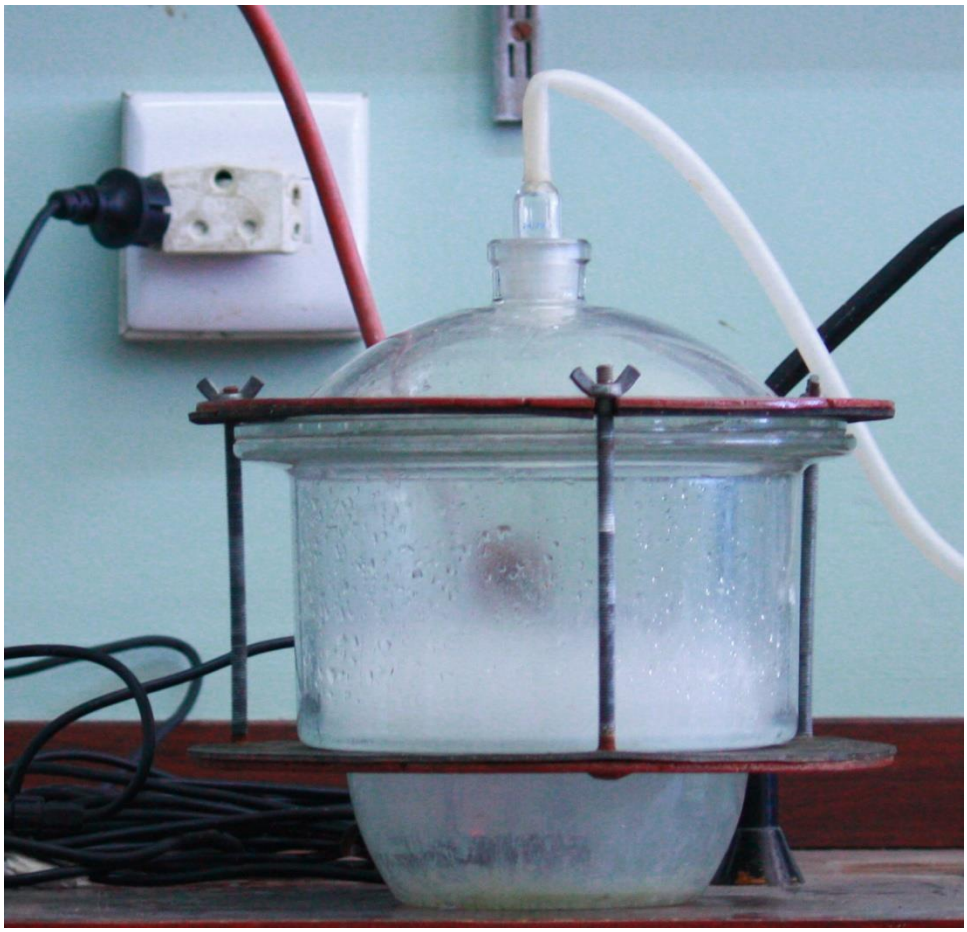

*Figure 4.6: Actual photograph of the USP reaction vessel used in this study*

### 4.5.2 SELECTION OF ULTRASONIC NEBULIZERS

Ultrasonic nebulizers used in this project were purchased from TDC power products Co. Ltd, Germany. The ultrasonic nebulizer employed composed of 3 and 5 piezoelectric transducers driven at frequency of 1.7 and 4.8 MHz each driven by a dedicated ultrasonic generator. There were several reasons for selecting an ultrasonic nebulizer, rather than pneumatic nebulizers. ***Firstly,*** pneumatic nebulizers require high pressurized gas systems that are either form a compressor or gas tank. This inherent property would increase the initial production cost of titanium dioxide. This meant that the designed system would require sophisticated equipment to control the flow gas flow rates, pressure regulator, high pressure valves and tubing. We therefore

preferred a nebulizer that could operate at standard atmospheric pressures. *Secondly*, it was believed, that with proper control of nebulizer operation frequency, the reaction mechanism for droplet generation would be tuned to behave similarly to a belt furnace APCVD system used in the PV industry. *Thirdly*, there is a huge potential in scaling the project to industrial scale for fabrication of dye solar cell considering the ease of assembly, and the need of low operation skill. In addition the ultrasonic nebulizer housing is manufactured from titanium alloy and a stainless steel housing. The titanium alloy is chosen for its high mechanical durability, excellent ability to resist conversion of vibrational energy into heat (hence does not heat up the precursor during material deposition) and also have high chemical resistance towards most titanium alkoxide precursors which are highly acidic Figure 4.7 shows the nebulizers used in this study.


*Figure 4.7: Ultrasonic nebulizers employed in the study. (a) Shows the 1.7 MHz ultrasonic nebulizer with power supply unit and (b) shows the 4.8 MHz ultrasonic nebulizer with power supply unit.*

After some trial runs we discovered that the 4.8 MHz nebulizer would be unsuitable for our application shown here in insert (b) of Figure 4.7. This was due to the extremely high volume of aerosol produced [$(300 \times 7) \pm 50$ *cc/hr*] which also caused high flow rates. The resulting titanium dioxide deposited thin films on the FTO glass substrates were too thick. Titanium dioxide yields were just too high and uncontrollable. It was also suspected that due to the high flow aerosol rates and short residence times of the aerosol inside the heating zone of the furnace, amorphous phase of titanium dioxide was formed. We therefore opted to use the 1.7 MHz nebulizer to synthesize titanium dioxide thin films. We discovered that with controlled flow rates of 6 ml/min we could deposit a thin film which was approximately 10 micrometers.

However, to achieve longer deposition times, the lowest flow rates had to be used. Although a fine mist often emerged from the nozzle the low volumes being pumped were not sufficient to create a cloud of droplets of several inches in diameter. Occasionally, the nebulizer would also "stall" and produce high volumes of aerosol which would cause deposition of liquid vapor onto the substrate. This resulted in high agglomerates $TiO_2$ nano particles being incorporated into the film. These defects reduced the chemical resistance and produced high electrical resistance on carbon doped titanium films, which was undesirable for dye solar cell applications. We therefore resorted to carry out thin deposition with 30minute spray breaks. Spray deposition using the 1.7 MHz nebulizer over the 4.8 MHz ultrasonic nebulizer poised several advantages:

(1) The 1.7 MHz nozzle enabled use of very low flow rates of almost $2 \times 10^{-2}$ ml/min, which increased the residence time of the aerosol vapor inside the heating zone. This gave enough time for complete pyrolysis/hydrolysis of titanium dioxide precursors to Anatase phase of titanium dioxide.

(2) The use of low flow rate gives allowance for achieving with high success well controlled consistent repeatable thins films. This set up resulted in thin film deposition times at 450ºC of 25-30 min.

(3) In addition the power required by 1.7 MHz ultrasonic nebulizer required from the ultrasonic generator to atomize titanium dioxide precursors was in the order of 2.5 W. Table 4.1 shows the specifications of the nebulizers chosen.

*Table 4.1: Specifications of the 1.7 MHz ultrasonic nebulizer and 4.8 MHz ultrasonic nebulizer*

| | **1.7MHz ultrasonic nebulizer** | **4.8MHz ultrasonic nebulizer** | **Test condition 1.7 MHz nebulizer** | **Test condition 4.8 MHz nebulizer** |
|---|---|---|---|---|
| **Resonant frequency** | *1.7 MHz ± 0.1 MHz* | *4.8 MHz ± 0.1 MHz* | | |
| **Resonant impedance** | *5 Ω max.* | *3 Ω Max.* | | |
| **Static capacitance** | *1400pF± 15%* | *2400pF ±15%* | | |
| **Mist output** | *(300×3) ± 50 ml/hr* | *(300 ×7) ± 50 ml/hr* | *Precursor temperature of 25ºC and precursor level of 38 mm* | *Precursor temperature of 25ºC and precursor level of 38 mm* |
| **Life time** | *5000 hr min* | *5000 hr min* | | |
| **Power in put** | *2.5 W* | *6.5 W* | *Standard circuit pin* | *Standard circuit pin* |

### 4.5.3 SELECTION OF SPRAY REACTOR

Nano-sized powders can be synthesized by wet-chemical routes and gas phase processes. However, gas-phase processes are often advantageous compared to liquid-phase processes since washing, drying and annealing process stages are redundant. Furthermore, the use of high liquid volumes and surfactants, which are necessary to produce high purity materials at high yields, can be avoided.

Spray pyrolysis reactors that have been developed for the manufacture of ultrafine powders include flame reactors [45], furnace reactors [43, 44], gas-condensation methods [16], plasma reactors [26], laser ablation [28] (the precursor of the previous three examples is preferentially a highly pure metal rod) and spray pyrolysis [44]. Through the use of these methods, it is possible to make virtually all kinds of inorganic materials at the nano size level, giving potential for new or more cost-efficient applications. In addition to existing industrial processes such as pigment

generation, optical fiber fabrication, and carbon black production [46], The specific aerosol methods differ primarily in the technology of how thermal energy is transferred to the precursor species. They also differ on how the precursor is delivered to the reaction site, economic aspects, and the final product characteristics do affect the choice of spray reactor.

The workhorses of the aerosol processes are flame reactors for the synthesis of nano-particles from gaseous precursors, were first investigated in detail using diffusion and premixed flames [45]. Today, flame reactors are widely used for the manufacture of commercial quantities of nano-particles such as carbon black (made by Cabot, Columbia, Degussa., etc.), fumed silica (Cabot, Degussa., Wacker, etc.), pigmentary titania (DuPont, Ishihara, Millennium, Kerr-McGee, etc.) and optical fibers (Corning, Hereaus, Sumitomo, etc.).

Using vapor flame reactors, the variety of products is limited by the choice of metal precursors with sufficient vapor pressure to deliver the desired amount of the metal species into the reactor. Problematic examples include the low production rates for bismuth oxide [46] or Pt/TiO2 catalysts [42] from vapor flame reactors. Furthermore, it is difficult to produce multi component materials with homogeneous chemical composition. This is mainly because of the differences in the chemical reaction rate and vapor pressure of the reactants.

However, in spray pyrolysis systems (where tubular furnace reactors are employed), each droplet contains the precursor in the exact stoichiometry as desired in the product [43, 44]. The droplet essentially serves as a discrete *microreactor.* This is a huge advantage over vapor-phase routes since in vapor flame reactors, several reactants have to be vaporized simultaneously with special care to obtain the desired stoichiometry. Furthermore, flame reactors have high operational costs and the quality of the final product in either stoichiometry or crystalline morphology leaves a lot to be desired. Spray pyrolysis system that use furnace reactors offer superior quality at low operational cost and minimum operator skill.

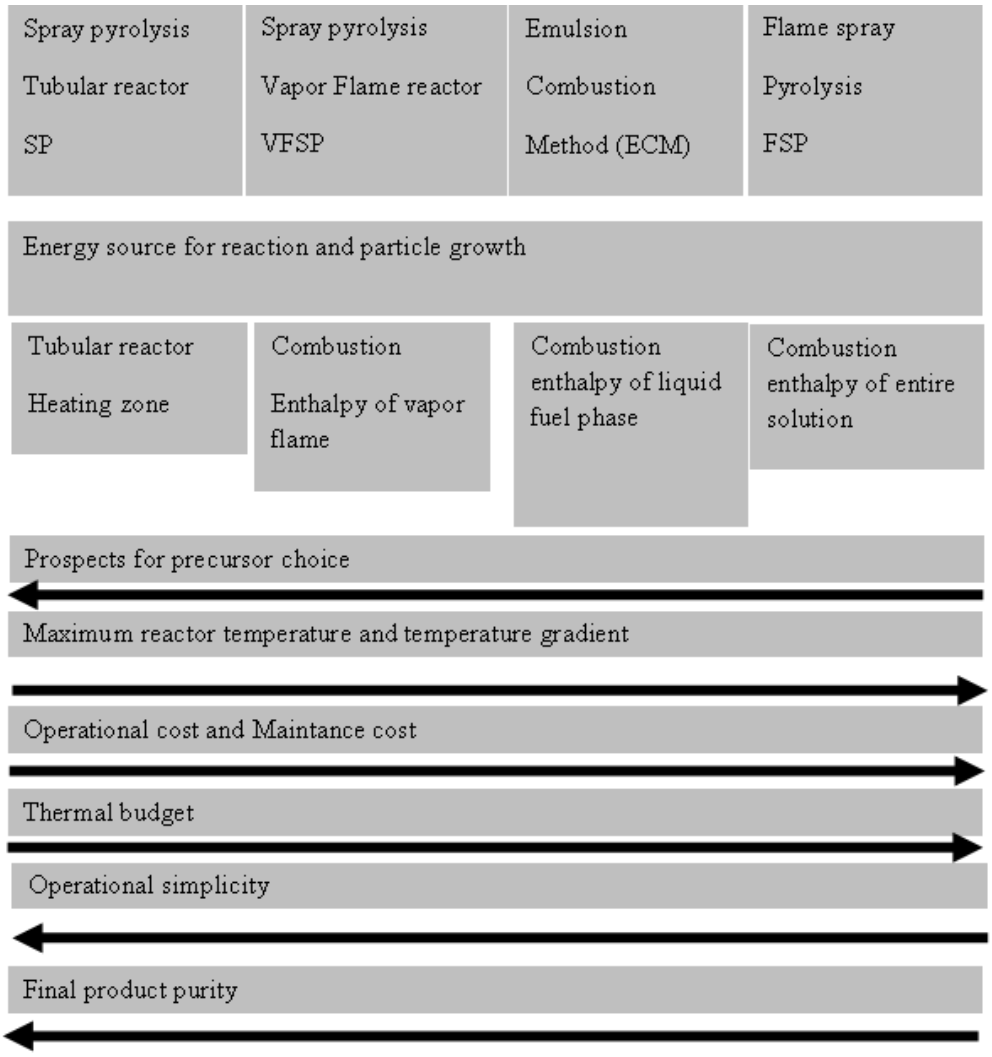


*Figure 4.8: Main spray methods operated at ambient pressure for gas phase nano-particle production from metal precursors. Precursor are delivered within a solvent into a reaction zone where reaction and the final product formation occurs*

Spray-supported methods for nano-particle production differ mainly by how thermal energy is provided to the precursor species, influencing main particle formation parameters such as temperature profile and residence time within the high-temperature environment. Figure 4.8 summarizes the four main spray methods discussed in this work, namely spray pyrolysis in a tubular reactor (SP) [44], spray pyrolysis using a vapor flame reactor (VFSP) [45], the emulsion combustion method (ECM) [16] and flame spray pyrolysis (FSP) [45]. In all four processes, the

precursor is delivered under ambient pressure to the reactive environment by dispersing it into fine droplets.

The main difference, however, is the energy source driving the solvent or fuel evaporation and precursor reaction (in some cases also liquid fuel reaction). Reactors with an external energy supply (energy which is not provided by the spray itself as in SP and VFSP) are less sensitive to the choice of precursors and solvents. Water is often chosen as the solvent in systems with an external energy supply (SP, VFSP, ECM) due to economic aspects, ease of handling and the excellent dissolution ability for many metal-containing precursors (e.g. nitrates, chlorides, acetates). In contrast, the combustion of the entire solution (as in FSP) results in higher maximum reactor temperatures and significantly larger temperature gradients compared with other methods; and more significantly, increase the thermal budget of the system and overall operation cost.

The success of producing functional metal oxides, mixed-metal oxides and metals on metal oxides from cheap precursors in an economical aerosol process has triggered the evolution of the reactor design. Tubular reactors used in SP provide a well-controlled temperature zone over long residence times for conversion of the precursor to the final product.

In addition spray pyrolysis methods that employ tubular reactor systems (furnace) offer several advantages such as (1) operational simplicity, (2) minimum through put (in terms of consumables) (3) lower thermal budget (4) lower operational cost. (5) There is no need for subsequent heat treatment after sample synthesis. Furthermore tubular reactor systems offer the opportunity of industrial scaling. These inherent advantages were some of the drivers of the choice of tubular reactor used at Fort Hare shown here in Figure 4.10.

Compared to liquid-phase precipitation methods, flame reactors and laser ablation systems powders produced by spray pyrolysis systems employing a furnace reactors are advantageous since they are more crystalline, less agglomerated (compared to annealed sol-gel-derived powders), of high purity and rarely require annealing [32]. In addition the spray method draws

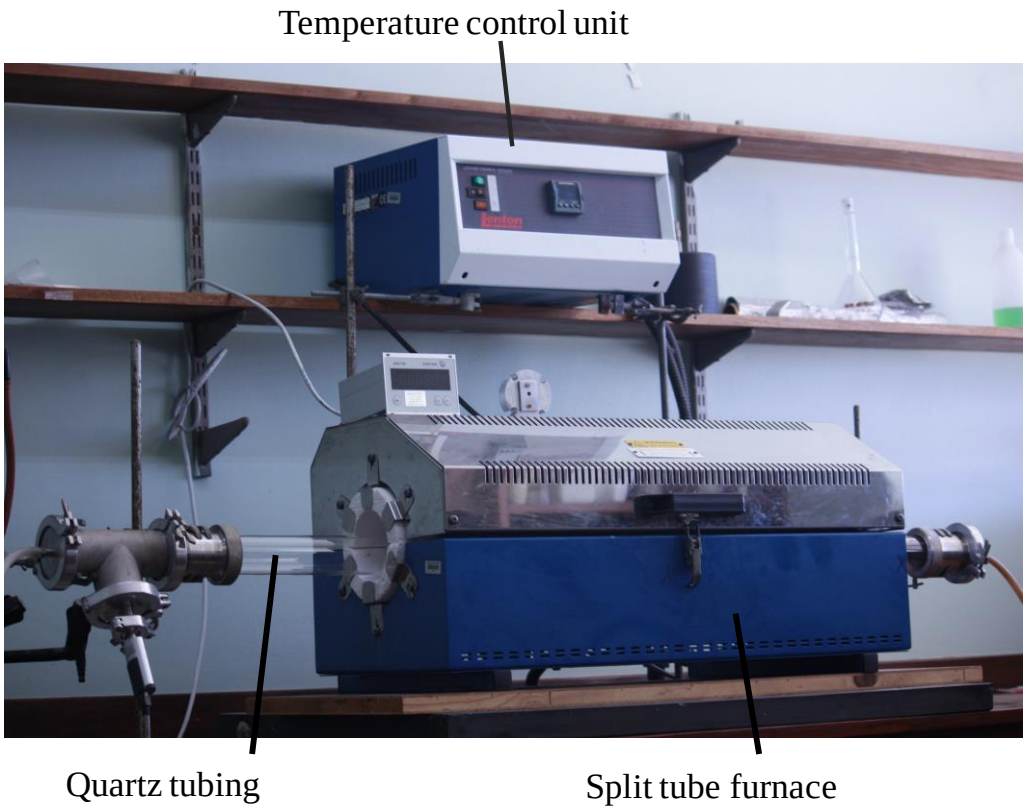


*Figure 4.9: Shows the actual photograph of the split tube furnace employed in the synthesis of $TiO_2$ nano structure in the study*

on the advantage of the excellent spatial mixing of the reactants; the spray pyrolysis process was also established for multi-component systems.


*Figure 4.10: Shows the aluminum reaction vessels employed in the study*

### 4.5.4 DESIGN OF SUBSTRATE HOLDER

The novelty of our USP system originates from the angle at which the substrate interacts with the incoming aerosol vapor. (shown here in Figure 4.12). Most systems that have been utilized a substrate holder with the substrate vertically parallel to the incoming aerosol beam. In the Fort Hare system, the substrate holder and hence the substrate is perpendicular to the aerosol stream as shown in the schematic representation of Figure 4.11.

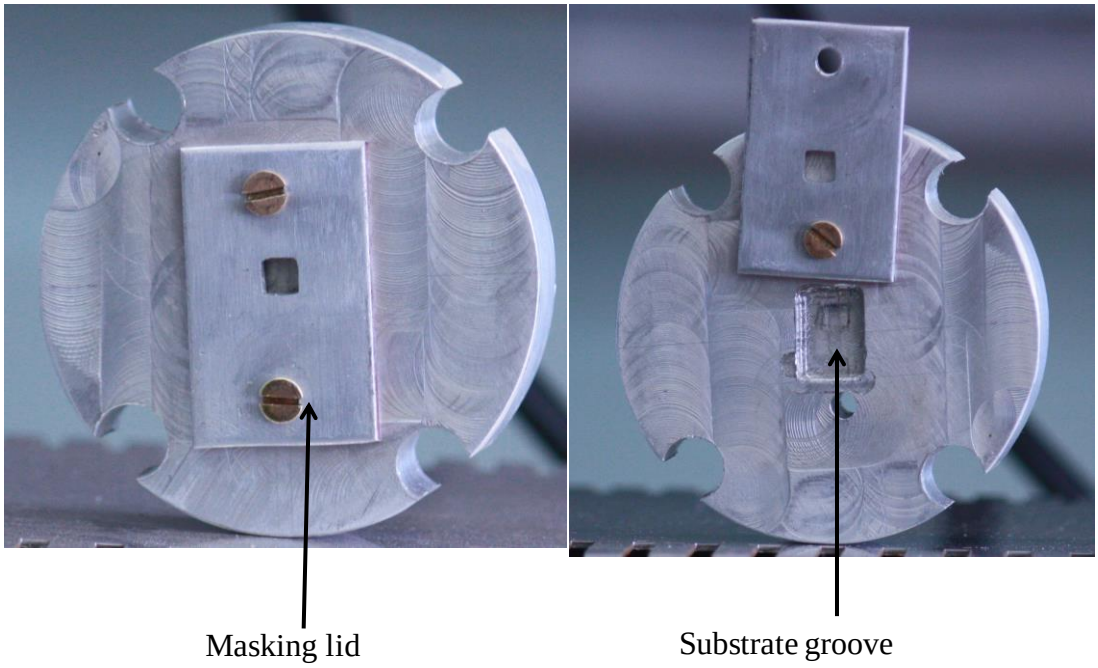


*Figure 4.11: shows the aluminum substrate holder employed in open and closed configuration*

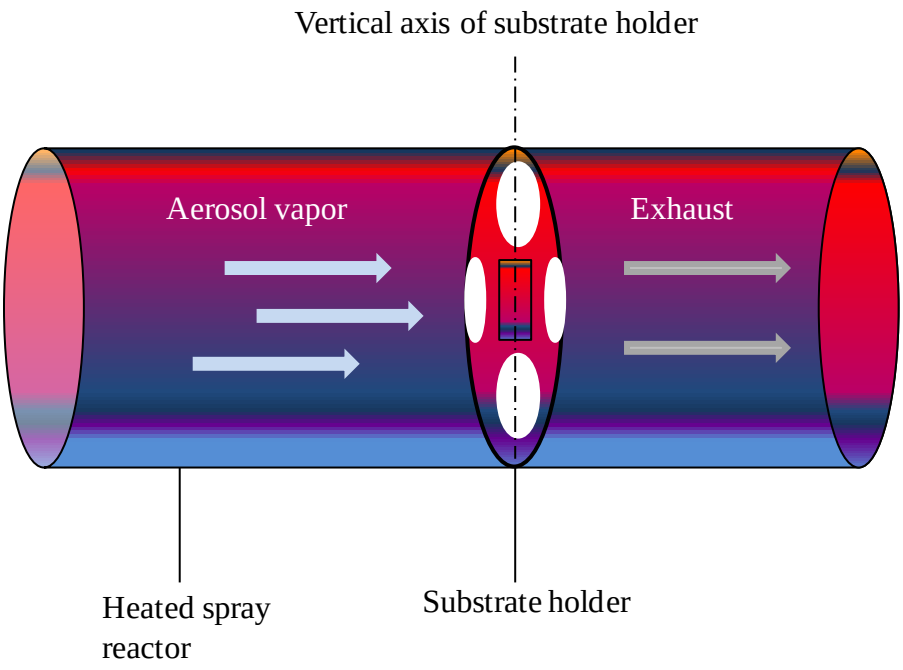


*Figure 4.12: Schematic presentation of substrate holder orientation in the spray reactor*

The choice of the deposition angle θ= 0º can be best explained by considering Figure 4.12 below. In this figure the aerosol vapor stream is incident at an angle θ with the normal to the substrate surface. Figure 4.13 (a) shows a schematic of the setup and Figure 4.13 (b) a corresponding vector diagram.

The glancing angle deposition (GLAD) technique is the extension of the commonly used oblique angle deposition (OAD) in thin film deposition industry. The experimental set up for the oblique angle deposition is shown here in Figure 4.12. In most ideal cases, the aerosol vapor stream has an incident angle, θ with the respect to the substrate surface normal.

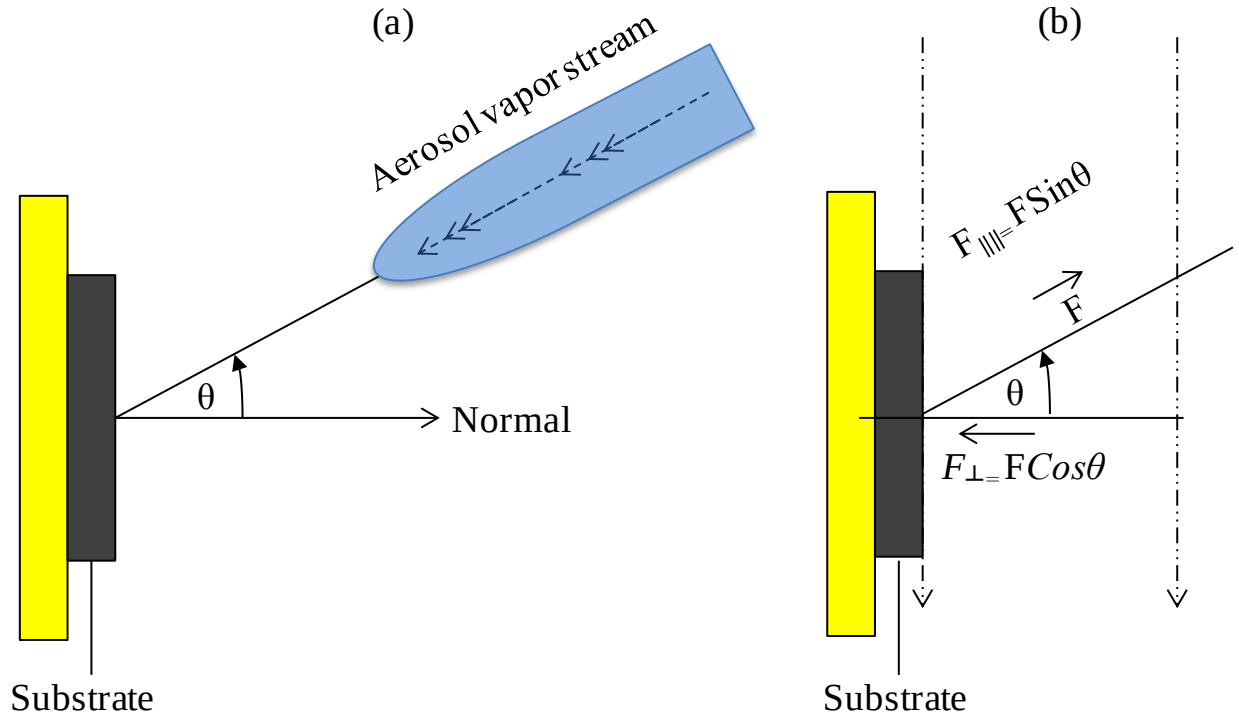


*Figure 4.13: (a) Schematic drawing for the experimental set up for oblique angle deposition (b) The incident aerosol vapor stream* $\boldsymbol{F}$ *can be decomposed into different components* $\boldsymbol{F}_{\perp}$ *is perpendicular to substrate, and* $\boldsymbol{F}_{///}$ *is parallel to the substrate*

At a glancing angle deposition θ, the substrate will receive the precursor aerosol vapor stream from both the vertical and lateral directions. During ultrasonic spray deposition of the thin film onto a flat substrate, initially the impinging nano particles will randomly form islands on the substrate. As the spray deposition proceeds, the preliminary nucleated islands will act as shadowing centers and all of the tallest nano-particle islands will expand into columns and nano columnar films will be formed. Cleary from the vector diagram in Figure 4.12 (b), it shows that the lateral component $\boldsymbol{F}_{///}$ is the source for the shadowing effect. For the oblique angle deposition, since $\boldsymbol{F}_{///}$ remains constant during spray deposition, a columnar film with tilt angle β will be formed.

Through scanning electron micrograph analysis Hawkeye *et al.*, [48] have shown that the shift of angle θ in deposition of silicon thin films had tremendous effects on the geometrical arrangement

of the deposited nano-particles. They found that at θ=30º small columns of silicon began to grow, at θ=60º the columnar structures of silicon became obvious and θ=80º the columnar structures of silicon become more pronounced. They also discovered that at θ=0º where the incoming aerosol vapor stream was not affected by lateral component of the vector **F** in figure 4.13 (hence the growth of nano structures was not affected by the shadowing effect) continuous and uniform nano thin films were developed as shown here in Figure 4.16. We therefore adopted this idea when designing the substrate holder for our horizontally orientated ultrasonic spray pyrolysis system as well as the aluminum reaction chamber that is capable of supporting the substrate in a vertical position shown in Figure 4.10. Thin film deposition were done at θ=0º, for the development of nano structures for photo voltaic application. Figure 4.13 shows the preliminary results that were obtained with the substrate holder in this configuration.

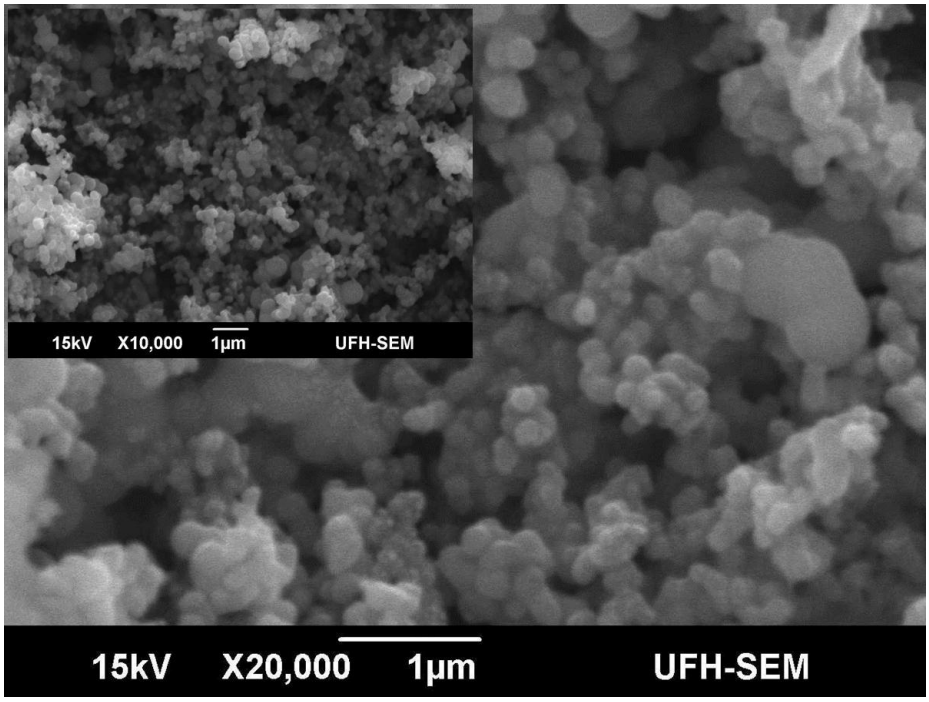


*Figure 4.13: Scanning electron microscopy images showing effects of the titanium dioxide thin film produced at θ=0° , with an insert showing the same sample on a different spot and on a lower magnification*

One can observe that the developed titanium dioxide thin films by this methodology were mesoporous and have spherical nano-structures which is a desirable property for dye solar cells.

## 4.6 OPERATION OF THE ULTRASONIC SPRAY SYSTEM

In its final form shown in Figure 4.13 the ultrasonic spray system incorporated all of the above component as well as those listed in section 4.5. Table 4.2 outlines the standard deposition parameters for the precursors chosen. Appendix A list the necessary steps to set-up and perform depositions with the $TiO_2$ ultrasonic spray pyrolysis system employing a horizontal reactor. The gas flow rates were optimized in order to extend thin film coverage in the forward direction. At lower flow rates of 1-2 ml/min. Ultrasonic spray depositions were performed at the lowest system operating temperature of 450°C, this is mainly because of high enough residence times spent by aerosol vapor droplets inside the heating zone. At higher flow rates of 5-6ml/min system operating temperature was increased to maximum value of 500°C to accommodate the short residence times spent by the aerosol vapor droplets. Throughout this whole project argon was used as the only carrier gas. Also the aluminum substrate holder was used in most cases for thin film synthesis.

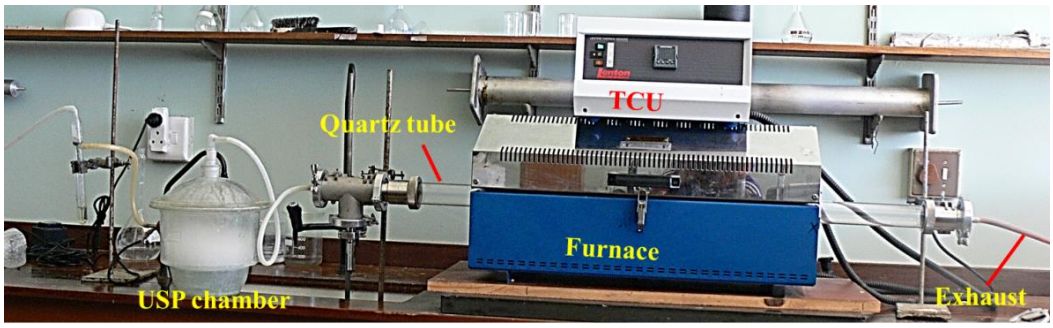


*Figure 4.14: Shows Actual photo graph of the horizontal ultrasonic spray pyrolysis system utilized in the study in its final form*

*Table 4.2: Showing operation conditions for USP system*

| | ULTRASONIC SPRAY PYROLYSIS | |
|---|---|---|
| **PROCESS PARAMETERS** | @ 450 °C | @500 °C |
| Argon flow rate | 1-2 ml/min | 5-6 ml/min |
| Ultrasonic vessel pressure (Atm) | 1 | 1 |
| Precursor temperature (°C) | 25 | 25 |
| Precursor pH | 1.95 | 1.95 |
| Substrate type & temperature (°C) | FTO Glass & 450 °C | FTO Glass & 550 (°C) |
| Deposition time (m) | 120 | 30 |
| Deposition Angle (°) | 0 | 0 |
| Annealing temperature (°C) | 450 | 450 |

## 4.7 CONCLUSION

A good understanding of basic $TiO_2$ material properties along with knowledge of a previous $TiO_2$ spray deposition system at ITHEMBA LABORATORIES in Gauteng formed the requirements for the $TiO_2$ thin films in this application. Films were required to be dense and defect-free, exhibit good thickness uniformity, possess a high refractive index and low optical absorption, and be semiconducting. Examination of deposition techniques described in the literature lead to the author designing and constructing an ultrasonic spray deposition (USP) system. USP system developed offered unique features in material in synthesis of pure un-doped $TiO_2$ and carbon doped $TiO_2$ thin films and nano structures. Firstly, we employed a horizontal furnace reactor as contrasted to most vertical systems in literature. *Secondly,* the horizontal system offered several many potential advantages for deposition of thin films without any shadowing effect observed in the glancing or oblique angle depositions employed in most CVD systems. We managed to deposit samples at 0° degree, which allows the aerosol beam containing precursor vapor to interact directly with the substrate uniformly. Furthermore this allowed the system to use, low deposition rates, and the ability to deposit for a wide range of thin films via this method using different liquid precursors. Many of the desired $TiO_2$ film properties were obtained from films deposited using the USP system.

## 4.8 REFERENCES


1 Funakoshi K.; Nonami T. *Ceramics International*. **2008**, 34, 1637-1642

2 Mohammad Reza Mohammadi, Farideh Ordikhani.; Fray D.J.; Farzard Khomamizadeh. *Particulogy*.**2011**, 9(2), 161-169

3 Kolen'ko, Y.V.; Korvnir, K.A.; Gavrillov, A.I.; Garshev, A.V.; Frantti, J.; Lebedev, O.I.; Churangulov, B.R.; Tendeloo, G.V.; Yoshimura, M.*J Phys. Chem*. B**2006**, 110, 4030-4038

4 Zukalova, M.; Kalbac, M.; Kavan, L.; Exanar, I.; Grätzel, M. *Chem. Mater*. **2005**,17, 1248-1255

5 Nizard H.; Kosinova M.L.; Fainer N.I.; Rumyanstev Yu.M.; Ayupov B.M.; Shubin Yu.V. *Surface and Coating Technology***. 2008**, 202(17), 4076-4085

6 Carette D.Li.M.; Granier A.; Landesman J.P.; Goullet A. *Thin Film Solids*.**2012**, 522, 366-371

7 Masahiko M.; Teruyoshi W.. *Thin Film Solids*. **2005**, 489, 320-324

8 Carette D.Li.M.; Granier A.; Landesman J.P.; Goullet A. *Applied Surface Science*.**2013**, 283, 234-239

9 Nolan M.G.; Pemble M.E.; Sheel. D.W.; Yates H.M. *Thin Solid Films.* **2006**, 515(4), 1956-1962

10 Zhang X.W.; Ha G.R. *Thin Solid Films. **2008**,* 516, 6140-6144

11 Evan P.E.; Pemble M.E.; Sheel D.W.; Yate H.M. *Journal of Photochemistry and Photobilogy A: Chemistry*. **2007**, 189, 387-397

12 Meakawa Takuji.; Kurosaki Ken.; Tanaka Takanori.; Yamanaka Shinsuke.*Surface and Coatings Technology*. **2008**, 202, 3067-3071

13 Yoon Y.S.; Kang W.N.; Yom S.S.; Kim T.W.; Jung M.; Park T.H.; Seo K.Y.; Jong Yong lee. *Thin Films Solids*. **1994**, 238, 12-14

14 Gao Y. *Thin Film Solids*. **1999**, 346, 73-71

15 Leeward Yi.; Zhang Wenjie.; Jin Wu. *Thin Film Solids. 2006*. 515, 2803-2806

16 Nolan M.G.; Pemble M.E. Sheel D.W. Yate H.M. *Thin Film Solids*. **2006**. 515, 1956-1962

17 Davinder Rathee.; Mukesh Kumar.; Sandeep K.A. *Solid State Electronics***. 2012**, 76, 71-76

18 Patil K.R.; Sathaye S.D.; Khollam Y.B.; Deshpande S.B.; Pawaskar N.R.; Mandale A.B. *Materials Letters*. **2003**, 17, 1775-1780

19 Lindgren T.; Mwabora J.M.; Avendano E.; Jonsson J.; Hoel A.; Granqvist Claes Goran.; Lindquist Sten-Eric. *J. Phys. Chem.B*. **2003**, 107(24), 5709-5716

20 Nakastu O.; Mastuo J.; Omoto K.; Seki T.; Takaoka G.; Yamada I. *Nuclear Instruments and Methods in Physics Research B*. **2003**, 206, 866-869

21 Barthwal Sumit.; Young Su Kim.; Si-Hyung Lim. *Journal of Colloid and Interface Science*.**2013**, 400, 123-129

22 Pierre M.; Sergrey G. *Renewable Hydrogen Technologies*. **2013**, 19-41

23 De Giacomo A.; Shakhatov V.A.; Senesi G.S. Orlando S. *Spectrochimica Acta Part B: Atomic spectroscopy*. **2001**, 56, 1459-1472

24 Bendavid A.; Martin P.J.; Preston E.W. *Thin Film Solids*. **2008**. 517, 494-499

25 Mc Daniel M.D.; Posadas A.; Wang T.; Demkov A.A.; Ekerdt J.G. *Thin Film Solids*. **2012**, 520(21), 6525-6530

26 Tsoukleris D.S.; Arabatzis I.M.; Chatzivasiogou E.; Kontos A.I.; Belessi V.; Bernard M.C.; Falaras P. *Solar Energy*.**2005**, 79, 422-430

27 Sanchez M.; Rincon M.E.*Sensors and Actautors B: Chemical*. **2009**, 140, 18, 17-23

28 Rincon M.E.; Gomez-Daza O.; Corripio C.; Orihuela A. *Thin Film Solids*. **2001**, 389, 1-2

29 Danjela Kuscer.; Marija Kosec.; janez Holc. *Ceramics International*. **2009**, 35, 1063-1069

30 Szlufcik J.; Majewski A.; Buczkowski J.; Radojewski.; L. Jedral.; E.Radojew-eska B. *Solar Energy Materials*. **1989.** 18, 241–252

31 Ji Sun Im.; Jumi Yun, Sung Kyu Lee.; Young-Seak Lee, *Journal of Alloys and Compounds*. **2012**, 513, 573-579

32 Quiping Liu.; Yang Zhou.; Yandong Duan.; Min Wang.; Yuan Lin. *Electrochemica Acta.* **2013**, 95, 45-53

33 Livraghi S.; Paginini C.M.; Giamello E.; Selloni A.; Di Valentin C.; Pacchioni G. *J. Am. Chem. Soc*. **2006**, 128(49), 15666-15671

34 Tang H.; Prasad.; Sanjines R.; Schmid P.E.; Levy F. *J. Appl. Phys*. **1994**, 75, 2042-2048

35 Ismagilov Z.R.; Tsykoza L.T.; Shikina N.V.; Zartyova V.F.; Zinoiviev V.V.; Zagrebelnyi. *Russian chemical Reviews*. **2009.** 78, 27-41

36 Wilska S. *Acta Chemica Scandnavica*. **1958**,8

37 Mac Kensize K.J.D The calcinations of Titania: Effect of Additives on Anatase-Rutile Transformation

38 Rao C.; Turner A.; Honig J. J. *Phys. Chem Solids*. **1959**, 11, 13-20

39 Navrotsky A.; Kleppa O.J. *Journal of American Cermic Society.* **1978**, 62, 15-22

40 Vigue J.C.; Splitz J. Electrochem. Soc: Solid State Science and Technology. **1975**, 122(4), 585-564

41 Mwakikunga B.W. *Masters thesis. University of Witwatersand* 2006

42 Priol L.; Baudel P.; Louste C.; Romat H. *J Electrostatics*. **2005**, 63, 899-904'

43 Taziwa R.; Meyer E.L.; Chinyama K.G. *Journal of Material Science*. **2012**, 47, 1531-1540

44 Taziwa R;. Meyer E.L.; Sideras-Haddad.; Erasmus R.M.; Manikandan E.; Mwakikunga B.W. *International Journal of Photoenergy*. **2012** , 2012, 323-332

45 Harra J.; Nikkanen J-P, Aromaa M.; Suhonen H.; Honkanen M.; Salminen T.; Levanen E.; Makela J.M. Powder Technology. **2013**, 243, 46-52

46 Sadeghian Z. New Carbon Materials. **2009**, 249(1), 33-38

47 Rudin T.; Wegner K.; Prastinis E.S. *Advanced Powder Technolgy*. **2013**, 24, 632-642

48 Hawkeye M.M.; Brett M.J. *Journal of Vaccum Science & Technology A. Vaccum, Surface and Films*. **2007**, 1317-1335

# CHAPTER 5

# MATERIALS AND EXPERIMENTAL METHODOLGIES

## 5.1 INTRODUCTION

This chapter outlines the experimental procedures used in the synthesis and characterization of nano carbon doped titanium dioxide. The synthesis of both pure and doped $TiO_2$, thin films, QDs and thin films, onto substrates requires careful optimization. In this chapter, the various processing steps as well the specific experimental details followed during the deposition of samples synthesized by USP and PSP techniques are given in detail. This chapter ends of by presenting the experimental details involved in the fabrication of a sandwich model photo chemical solar cell.

## 5.2 SYNTHESIS OF QUANTUM DOTS

### 5.2.1 SUBSTRATE CLEANING PROCEDURE

Only one type of substrate has been used in this project: sodalime glass coated with conductive material. The conductive oxide widely employed was FTO (Fluorine doped Tin Oxide, (F: $SnO_2$). The FTO coated glass substrates used in this study were purchased from Solaronix Switzerland. Table 5.1 outlines the material specifications of the substrates.

*Table 5.1: Outline materials specifications of the substrate employed in the study*

| | |
|---|---|
| **Glass type** | sodalime |
| **Glass thickness** | 2.2 mm |
| **Conductive layer** | FTO(Fluorine tin oxide, $SnO_2$:F) |
| **Surface resistivity** | ~ 7 ohm/sq |
| **Transmission** | >80% from 400 to 700 nm |
| **Size** | 10 x 10 cm (1 pc) |

FTO glass were carefully cut into pieces 5×10 mm for the development of C-$TiO_2$ photo electrodes for photochemical solar cells (PECs).The developed substrate could fit perfectly into the groove of the aluminum substrate holder depicted in Figure 4.13 of chapter 4. The substrates were then cleaned afterwards. Cleaning of the substrates is a critical factor for both correct homogeneity and adhesion of the future coatings deposited over them and it is absolutely essential to follow strict cleaning protocols in order to ensure there were no impurities on the surface of the substrates. FTO transparent glass substrates were first washed with detergent, to remove any paraffin, then thoroughly rinsed with hot tap water, distilled water, isopropanol, distilled water and finally ultrasonically washed in acetone. The glass substrates were then dried under hot air to evaporate the acetone and or organic material collected from the solvents.

### 5.2.2 REAGENTS AND RAW MATERIALS

Analytical grade liquid titanium tetrachloride ($TiCl_4$) was used. Other reagents and chemicals used were of analytical grade glucose (Merck), absolute ethanol (99.99%) purchased from Aldrich), Isopropanol (Aldrich), and acetone (Aldrich). C-$TiO_2$ QDs were deposited on F: $SnO_2$ transparent glass (purchased from Solaronix Switzerland). This type of glass is stable to temperatures less than 600 ºC, has a lower cut-off wavelength (≈ 280 nm), which is far away from that of bulk titanium dioxide (≈ 325 nm) and also not expensive which makes the produced QDs more attractive for solar applications. Prior to use the glass substrates were first washed as described in the previous section, and then dried. Nano-particle deposition was done on F: $SnO_2$ glass substrate at furnace temperatures of 450-455 ºC, at various substrate positions inside the furnace using argon as the carrier gas at a flow rate of 5-6 L/min. The USP and PSP experimental set up is illustrated in Figures 5.1 and Figure 5.2 respectively. The spray pyrolysis consisted of a furnace, (REX D100 supplied by RKC instruments, Inc., Tokyo, Japan) the carrier gas unit and exhaust. The ultrasonic nebulizers were composed of three piezoelectric transducers driven at a frequency of 1.67 MHz by a ultrasonic generator (supplied by TDC Power Products Co Ltd, Germany). The pneumatic pump was purchased from a local chemotherapy pharmacy.

### 5.2.3 SYNTHESIS OF C-$TiO_2$ QUANTUM DOTS USING USP

In a typical synthesis procedure an aliquot of 0.01 M precursor solution of titanium tetraethoxide was prepared by adding 1.18825 g of Titanium tetrachloride ($TiCl_4$). The glucose dopant solution was made by adding 0.2162 g of glucose into a 250 ml volumetric flask containing absolute ethanol (99.99%. Aldrich). The dopant solution was then mixed vigorously till all the glucose had dissolved in an ultrasonic bath. The precursor solution was then decanted into two chambers that were housing the ultrasonic nebulizers operating at a frequency of 1.67 MHz. The experimental set up is shown in Figure 5.1 C-$TiO_2$ deposition was done on F: $SnO_2$ glass substrate at furnace temperatures of 450-455 ºC.

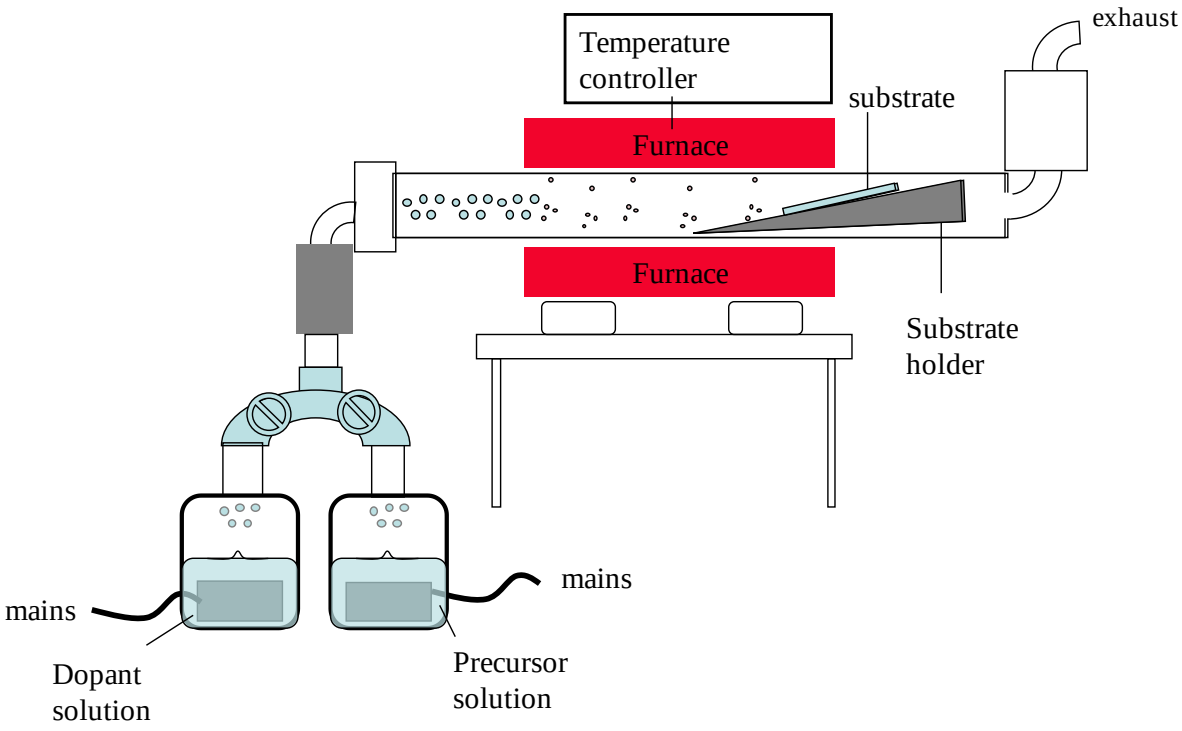


*Figure 5.1: Experimental set for USP that was employed for synthesis of C-$TiO_2$ QDs*

C-$TiO_2$ QDs were obtained at a flow rate of 6 L $min^{-1}$and the concentration of the precursor solution was 0.01M. The synthesized C-$TiO_2$ QDs formed where black spots on top of a F: $SnO_2$. The synthesized C-$TiO_2$ QDs had a glass substrate holder that was at an angle of 35º to the incoming aerosol vapor stream and volatile titanium tetra-chloride was utilized as the precursor.

### 5.2.4 SYNTHESIS OF C-$TiO_2$ QUANTUM DOTS USING PSP

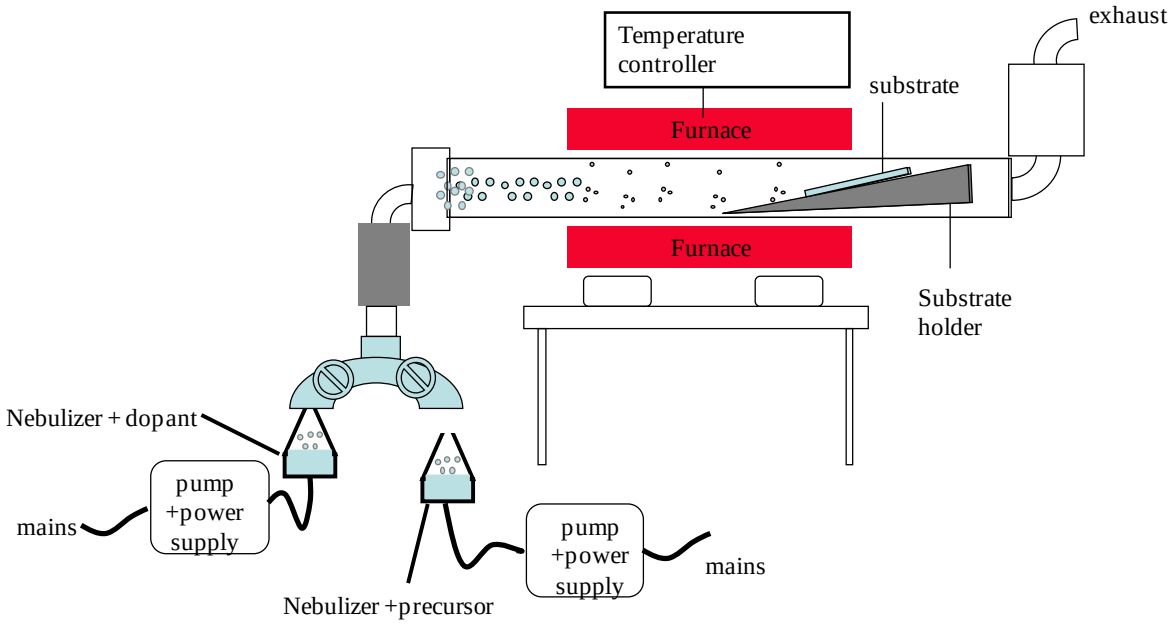


*Figure 5.2: Experimental set for PSP that was employed in study for synthesizes of C-$TiO_2$*

In a typical synthesis procedure an aliquot of 0.01 M precursor solution of titanium ethoxide was prepared by adding 1.18825g of Titanium tetrachloride ($TiCl_4$) to a 250 ml of absolute ethanol in a volumetric flask. The glucose dopant (source of carbon) was made weighing 0.2162g of glucose into a 250 ml volumetric flask containing absolute ethanol (99.99%. Aldrich). The dopant solution was then mixed vigorously till all the glucose particles had in an ultrasonic bath. 10.00 $cm^3$ of titanium tetraethoxide was added into tube connected to pneumatic pump and in a separate PSP container housing 10 .00 $cm^3$ of glucose dopant solution was added into a tube connected to a pneumatic pump. The experimental set for PSP is shown in Figure 5.2. C-$TiO_2$ QDs obtained formed black spots on top of a F: $SnO_2$ glass substrates.

### 5.2.5 REACTION MECHANISM FOR USP AND PSP

The reaction sequence for the production of C-$TiO_2$ QDs and C-$TiO_2$ QDS is as follows:

$$TiCl_{4(l)} + 4CH_3CH_2OH_{(aq)} \rightarrow Ti(OCH_2CH_3)_{4(aq)} + HCl_{(g)} \quad (5.1)$$

$$TiO(CH_3CH_2OH)_{4(aq)} \xrightarrow{HEAT+GLUCOSE} TiO_{2-x}C_{x(s)} + CO_{2(g)} + H_2O_{(l)} \quad (5.2)$$

*n*-C:$TiO_2$ QDs were synthesized by USP and PSP.

The USP technique involves focusing ultrasound waves of frequency *f* producing capillary waves of frequency $f_{USP}$ at the surface of the precursor liquid. This produces ultra-fine droplets of the precursor liquid. The ultrasonic nebulizer uses an ultrasound generator that is driven by a piezoelectric crystal at a fixed frequency, *f*. The surface of the liquid will break down when the longitudinal waves propagate from the crystal to the liquid-air interface.

The PSP involves blowing the precursor liquid through fine nozzles to produce a mist of the precursor liquid at audible sound frequencies, $f_{PSP}$. This produces ultrafine droplets of the precursor liquid.

The vapors generated are transported to a heated zone through a quartz tube onto the F: $SnO_2$ glass substrate inside a furnace with argon as the carrier gas. The spray deposition was carried out for an hour. The forcing sound causes the precursor to erupt into droplets of mean diameter. The wavelength of the capillary waves was governed by Kelvin [1]. In Chapter 3 Which is re written here as:

$$D_{USP} = (8\pi\sigma/\rho.f_{USP}^{\ 2})^{1/3} \quad (5.3)$$

and

$$D_{PSP} = (8\pi\sigma/\rho.f_{PSP}^{\ 2})^{1/3} \quad (5.4)$$

where $\sigma$ = Surface tension of precursor solutions

After decomposition and deposition in the pyrolysis process, the solid-state particles obtained have a mean diameter that can be estimated respectively as:

$$d_{USP} = \left( D_{USP} \frac{C_{pr} M_p}{\rho_p M_{pr}} \right)^{\frac{1}{3}} \tag{5.5}$$

and

$$d_{PSP} = \left( D_{PSP} \frac{C_{pr} M_p}{\rho_p M_{pr}} \right)^{\frac{1}{3}} \tag{5.6}$$

where $C_{\mathrm{pr}}$ is the concentration of the precursor. $M_{\mathrm{pr}}$ and $M_{\mathrm{p}}$ are the molar masses of the precursor and deposited particles respectively $\rho_{\mathrm{p}}$ and $\rho_{\mathrm{pr}}$ are the densities of the deposited particles and precursor liquid respectively [2].

## 5.3 SAMPLE CHARACTERIZATION

In this study, a variety of characterization techniques were used to evaluate the structural, electrical, optical and electronic properties of the C-$TiO_2$ QDs, thin films and nano structures. Of particular interest was phonon confinement by Raman Spectroscopy, the elemental analyses by EDS, optical absorption properties by UV-Vis spectroscopy, and the electrical measurements by current voltage measurements, and conductivity analyses, As important, were the investigation about of the morphological features and determination of grain size by HRTEM. The most relevant aspects of these analytical techniques are discussed here.

### 5.3.1 SCANNING ELECTRON MICROSCOPY

The properties of the C-$TiO_2$ photo anode, nano-powder, thin film, and PEC were scrutinized scanning electron microscopy morphology studies was done using a Jeol JSM–5600 scanning electron microscopy (SEM) microscope which was equipped with an EDX attachment for elemental analysis. Gold coating was used in order to avoid sample charging effects during SEM analysis. Preparing the sample required separating the $TiO_2$ particles from the bulk of the powder from a coated FTO glass substrate. 1 mg of the $TiO_2$ powder was dissolved in 5 ml portion of hexane (Adrich, chromasolvz 97%). The preparation solution was then subjection to the process of particle selection. Particles of size larger than nano-metrical were expected to be deposited at the bottom of the test tube as sediment and the smallest particles in nano-material range were expected to form a homogenous colloid solution. Our synthesized samples showed no signs of sediments at the bottom of the test tube. We observed a colloid solution after 24 hours. 20 µl of the colloid solution was collected and an additional 5 ml of hexane was added which resulted in formation of transparent homogenous solution. The resulting solution was deposited on the Au (111) surface. After solvent evaporation the samples were loaded onto the SEM for structural and elemental evaluation.

### 5.3.2 HRTEM

A JEOL 2100 Transmission Electron Microscopy (TEM) with 200kV acceleration voltage and LaB6 filament was used in the bright field mode, to determine the agglomeration, size, shape and crystallinity of the nanoparticles. It has a point resolution of 0.2 nm and is equipped with a Gatan US1000 camera with 2048x2048 pixel CCD. The HRTEM was also equipped with the energy dispersive X-ray spectroscopy (EDX) setup using a Thermo Fisher Scientific detector cooled at liquid nitrogen temperature small quantities of powder were added to methanol and dispersed for about 5 seconds with a 25 Watt tip sonicator. In a typical analyses procedure a glass pipette was used to collect the sample from the centre of the dispersant volume and release one drop of the liquid onto the centre of an Agar Scientific 300 µm holey carbon film, located on filter paper. The grids were allowed to dry in air.

For the high temperature measurements, the sample was loaded into a Linkam TS1500 microscope furnace stage and the x20 objective of the microscope was used to collect the backscattered light. Power at the sample was 1.2 mW in this case. Ultrahigh purity argon was flowed through the stage during heating at 10 °/min. The temperature was kept constant at the indicated value while the Raman spectrum was measured. Due to the low power at the sample and the triple subtractive configuration, it was necessary to count for 180 s to accumulate a satisfactory spectrum.

The photographic negative obtained from the HRTEM measurements were then digitized using a 2048×2048 pixel CCD to obtain HRTEM lattice images. Using a technique called *digital analyses of images* DALI; the digitized images are evaluated giving rise to 2-D colour coded maps defining the local lattice distance. DALI is a method which evaluates the positions of local brightness maxima in HRTEM images eventually leading to 2-D lattice of detected positions. By choosing the reference region inside the C-$TiO_2$ QDs the local distances and averaged displacements relative to that of $TiO_2$ reference are evaluated directly from the lattice images

### 5.3.3 X-RAY DIFFRACTION SPECTROSCOPY

X-ray diffraction patterns were gathered using a Philips Xpert powder diffractometer equipped with a CuKα wavelength of 0.154184 nm and graphite crystal monochromator. Survey scans from 2θ = 20° to 80° were performed with a step size of 0.05°. Regional high-resolution XRD scans were also conducted to investigate C-$TiO_2$ lattice parameters via the most prominent reflections, using a 0.002° step size. Region 1, from 2θ = 24°-30°, aimed to capture the anatase (101) and rutile (110) reflections. Region 2, from 2θ = 35°-43°, examined the A(004), A(112), R(101) and R(111) peaks

### 5.3.4 RAMAN SPECTROSCOPY

Raman spectroscopy was carried out using a Jobin-Yvon T6400 Raman spectrograph operated in triple subtractive mode using, 514.5 nm line from an argon ion laser and an Olympus BX40 microscope as micro-Raman attachment. The T64000 was operated in single spectrograph mode,

with 1800lines/mm grating and a 20 × objective for nano-powders analysis and a 100 ×objective were used for thin film analysis on the microscope. The laser power at the sample was 1.28mW for the temperature dependence analysis, except for the laser power dependence analysis, where the laser powers of 1.83mW, 2.47mW, 3.13mW, and 4.46mW were used. The light was collected in a backscattering configuration and dispersed using 1800 lines/mm gratings onto a liquid nitrogen cooled CCD detector for recording. The spectra were acquired and stored using LabSpec 4.18 software.

### 5.3.5 FTIR

In a typical analyses procedure 2 mg of dried sample was added to a pestle containing 40 mg of potassium bromide (FT-IR grade Aldrich), the mixture was then grounded with a motor to make a homogenous mixture of the sample and potassium bromide. Pellets of the mixture were generated by pressing the prepared mixture with a hydraulic pump into a circular hard disk. The pressed pellets (0.3 mm thickness) were then placed in a transmission sample holder and scanned 34 times using transmission mode with a resolution of 4 $cm^{-1}$. Background measurements were done by scanning KBr pellets alone and this spectra was subtracted from the spectra obtained for above. .Fourier transform infrared (FT-IR) spectra of both original and modified titanium dioxide samples were carried out in the 370-4000 $cm^{-1}$frequency range. The infrared absorption spectra were recorded on Nicolet Nexus 870 system FT-IR spectrometer at room temperature.

### 5.3.6 UV-Vis SPECTROSCOPY

The optical behavior of materials may be characterized using UV-visible absorption spectroscopy. In its simplest form, UV-Vis requires shooting a focused, monochromatic beam of light through a sample, and recording how much of the light is transmitted via a light-sensitive detector. The sample may be suspended in solution, pressed into a solid disc, or a thin film on a transparent substrate. In this study sample in powder form were pressed on a disk for analysis of nano-powders and for thin film measurements were done on thin films coated FTO glass substrate and the absorption from the bare FTO glass substrate was subtracted from the overall absorption spectra. In this study, general absorption spectra were obtained using a double beam

Lambda 35 Perkin-Elmer UV-Vis spectrometer with an integrating sphere. Incident wave was swept from 100 to 1500 nm

### 5.3.7 i-V MEASUREMENTS QDs

A co-linear four-point probe system from Cascade Microtech, Inc., Oregon, U.S.A. was used to perform conductance measurements on the C-$TiO_2$ quantum dots by following procedures from the University of Texas at Dallas. The equidistant tungsten carbide probes have a separation distance, *a*, of 0.127 cm and a probe radius of 0.005 cm. The Keithley 4200 Semiconductor Characterization System (SCS), equipped with four supply-and-measure units (SMUs) and a pre-amplifier, was used to perform high precision direct-current characterisation capable of probing sensitive voltages and injecting currents ranging from 1 *f*A – 1 *m*A with a resolution of 0.1 *f*A. In this work, a current was injected through two extreme probes through the sample. The potential difference was measured across the middle probes.

### 5.3.8 I-V CHARACTERIZATION SOLAR CELLS

I-V characteristics of the PECs were perfomed on a Keithely 2400 source meter under simulated sunlight. I-V and IPCE were made in a 2 electrode setup using a Keithley 2400 source meter and controlled by in house Labview applications. Lamp intestity data was collected using a Molectron EPM 200 power meter with PM3 thermopile head. Scans were perfomed under constant power conditions with a 150 W Xe lamp (Oriel). I-V characteristics were done at room temperature and were obtained under 1 Sun intensity (100 mW/$cm^2$). A glass filter cuvette filled with water was used as an IR Filter to minimize heating and a UV Filter was used to filter UV bandgap irradiation. The cell was placed in the path of the incident light and scanned from $I_{SC}$ (0 V) to $V_{OC\,(720}$ mV) at 68 mV/s with 16 mV increments and 10 point averaging at each increment.

## 5.4 FABRICATION OF PHOTOCHEMICAL SOLAR CELLS

This section describes in detail, the necessary steps and techniques required for fabrication of C-$TiO_2$/$TiO_2$ semiconductor solar cells and C-$TiO_2$ QDs sensitized solar cells, such as the photo electrode, the hole conducting electrolyte, and the counter electrode.

### 5.4.1 DEVELOPMENT OF PHOTOCATHODE

Counter electrodes with more catalytic activity are desired for fast reduction of redox species in photo chemical solar cells. Platinum activated FTO photo-cathodes has shown good catalytic activity toward $I^-/I_3$ redox couple in DSCs. However, transition metals such as Pt, Au have been reported to be less than ideal electro catalysts for the $S^{-2}/S^{-2}_x$ redox couple [3]. Numerous counter electrode materials have been extensively investigated, some of which have shown excellent electro catalytic property toward $S^{-2}/S^{-2}_x$, examples are CoS PbS, $Cu_2S$, and carbon [3]. However, some of these materials are not stable in the long run because of lower mechanical integrity and sometimes even contaminate the photo-anode. The counter electrode should have high conductivity and mechanical and electrochemical stability. In this study platinum coated FTO glass substrates were used as the photo-cathode.

*Figure 5.3: Experimental procedure for drilling holes in FTO glass substrate prior to platinum coating, for subsequent electrolyte injection.*

Platinum coated FTO counter electrodes were prepared with two (2) small holes drilled into one corner on FTO to facilitate injection of electrolyte into the cell. For example a single hole of 3 mm in diameter was drilled at the corner of the photo cathode using a carbide drill bit as shown here in figure 5.3. The substrates were then cleaned as describe before. Figure 5.4 shows the actual measurements of the drilled bare FTO glass substrates.

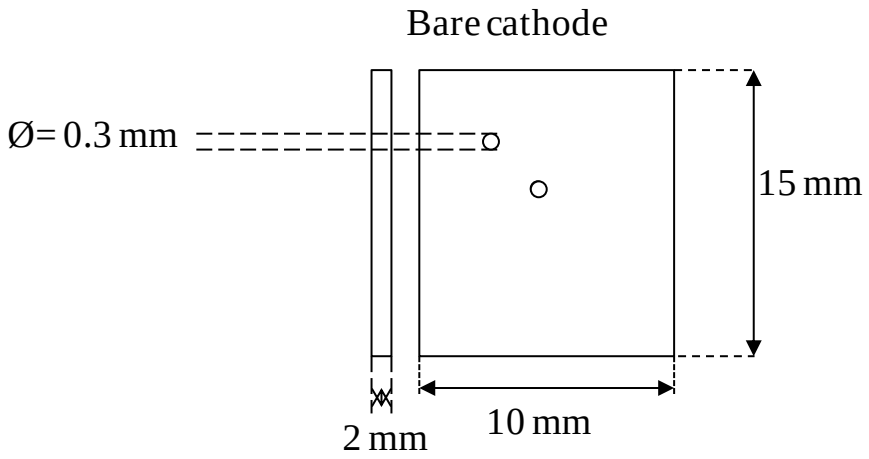


*Figure 5.4: Schematic presentation of drilled bare FTO glass substrate prior to platinum coating.*

With the holes drilled and cooled to room temperature the cleaned glass substrates were subjected to a platinum coating by a doctor blade technique. In a typical procedure an FTO glass substrate (10 × 15 mm) with the conductive side facing upwards two parallel strips of adhesive taps were applied to the edges of the glass of the FTO glass substrates on both ends excluding an area of 0.25 $cm^2$ for the platinum electrode. The adhesive tape was also used to fix the FTO glass substrates to the work bench as illustrated here in Figure 5.5.

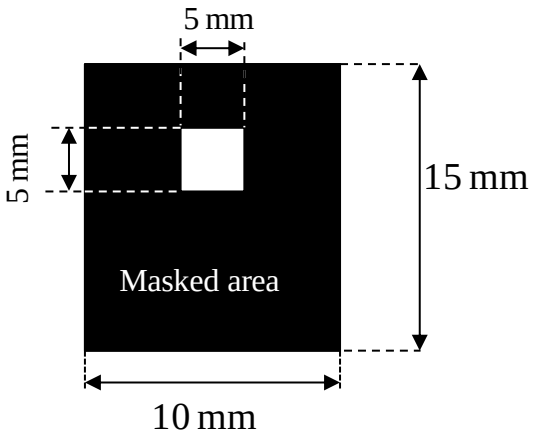


*Figure 5.5: Experimental procedures for masking of bare FTO glass substrate.*

A portion of Pt-catalysts T/SP (solaronix) was applied at the top right hand edge of the FTO glass substrates between the two pieces of tape. Using a glass rod the Pt. paste was carefully coated over the area between over the area between the two adhesive tapes. After 30 min when most dry visible film of platinum catalyst was observed the adhesive tapes on both edges were removed leaving behind a thin film layer of platinum coated. The resultant platinum coated glass was fired in an oven at 150 ºC for 30 min on a hot plate shown in Figure 5.6 insert (b). This resulted in formation of transparent activated platinum layer.


*Figure 5.6: Coating of the Pt-catalyst to the photo-cathode. Insert (a) shows the glass substrate fixed with adhesive tape before doctor blading of Pt catalyst onto FTO glass substrate (main picture). Insert (b) Firing of the Pt catalyst on a hot plate*

## 5.5 FABRICATION OF PHOTO ANODES USP SYSTEM

The synthesis of C-$TiO_2$ thin films for fabrication of photo-chemical solar cells (PEC) was done with two types of doping agents. Firstly, oxalic acid (OA) doped titanium dioxide thin films ($C_{OA}$-$TiO_2$) were developed. Secondly, tetra-butyl ammonium bromide (TBA) doped titanium dioxide thin films were also developed were developed with the ultrasonic spray pyrolysis system using titanium (IV) isopropoxide (TIP) as the precursor solution. The last invention of this work involved fabrication of self organized C-$TiO_2$ QDs sensitized $TiO_2$ photochemical solar cell. The synthesized quantum dots were used directly as sensitizers in PCSs. This ingenuity of this method allows a facile and rapid deposition QDs onto $TiO_2$ thin films without the need for post thermal treatments or the use of linker molecules to attaché QDs to thin Films.

### 5.5.1 SYNTHESIS OF OXALIC ACID DOPED PHOTO ANODES

In a synthesis procedure 781.24 μl of TIP were carefully added to a 100 ml beaker containing 60 mls of pH adjusted double distilled water in an ice bath maintained at 0ºC. The precursor solution was added drop wise whilst simultaneously stirring to avoid the formation of white precipitates of titanium hydroxides. The prepared solution was then carefully transferred into 250 ml volumetric flask containing 60 ml of pH adjusted double distilled water in an ice bath. 0.8103 g of oxalic acid dihydrate ($C_2H_2O.2H_2O$ Fluka) was then added to the volumetric flask and topped up to the mark whilst simultaneously stirring in an ice bath. The precursor solution was then sonicated for 360 min prior to ultrasonic spray. This resulted in preparation of a 9mM Oxalic acid doped titanium dioxide precursor solution which was coded 9mM $C_{OA}$-$TiO_2$. Several other precursor solutions of oxalic acid doped solutions were prepared in much the same way the only difference was the levels of dopant oxalic acid dehydrate as shown in Table 5.2.

*Table 5.2: Preparation of Oxalic acid doped titanium dioxide precursor solutions*

| **[TIP]** | Volume of TIP (µl) | $C_2H_2O.2H_2O$ (g) | Sample code |
|---|---|---|---|
| 1 ´ $10^{-2}$ M | 78.25 | 0.81027 | $9_{OA}$ C-$TiO_2$ |
| 1 ´ $10^{-2}$ M | 78.25 | 1.62054 | $18_{OA}$ C-$TiO_2$ |
| 1 ´ $10^{-2}$ M | 78.25 | 2.43081 | $27_{OA}$ C-$TiO_2$ |
| 1 ´ $10^{-2}$ M | 78.25 | 3.24108 | $36_{OA}$ C-$TiO_2$ |
| 1 ´ $10^{-2}$ M | 78.25 | 4.05135 | $45_{OA}$ C-$TiO_2$ |
| 1 ´ $10^{-2}$ M | 78.25 | 5.66771 | $54_{OA}$ C-$TiO_2$ |

The prepared solution was then precursor solution exposed to the previously discussed methodology in chapter 4 sections 4.6, but for the sake of clarity specific experimental details will be discussed.

The prepared precursor solution was then decanted into an ultrasonic shown in Figure 4.9 vessel housing an 1.7 MHz ultrasonic nebulizer shown in Figure 4.10 insert (b) for ultrasonic spray deposition. We also employed the aluminium reaction vessel shown in Figure 4.14 and the aluminium substrate holder depicted in Figure 4.1. The chosen substrate holder could accommodate (10 × 15 mm) FTO glass substrate. The selected substrate holder was specifically designed to allow an area of (5×5 mm) to be coated with carbon doped titanium dioxide nano particles during spray deposition which matches exactly the platinum coated photo cathode developed in section 6.4.1. Once the precursor solution was in the vessel and the substrate holder mounted in the uluminium reaction vessel the whole system was purged with argon carrier gas, while simultaneously allowing the furnace temperature to reach 450 ºC. Ultrasonic spray was then carried for 120 min using the spray deposition conditions outlined in Table 4.3 of chapter 4. This resulted in formation of white-grey transparent homogenous film which was employed as a photo anode in photo chemical solar cells (PECs). Various oxalic acid doped titanium dioxide photo electrodes were developed with different concentration as outlined in Table 5.6, at least six samples were fabricated for each dopant level.

### 5.5.2 SYNTHESIS OF TETRABUTYL AMOMINUM BROMIDE DOPED PHOTO ANODES

Another aspect of this work involved fabrication of tetra-butlyl ammonium doped titanium dioxide thin films also for photo chemical solar cell applications. In a typical procedure 781.25 µl of titanium (IV) isopropoxide (TIP) was carefully added to a 100 ml beaker containing 60 mls of pH adjusted double distilled water in an ice bath maintained at 0 ºC. The precursor solution was added drop wise whilst simultaneously stirring to avoid the formation of white precipitates of titanium hydroxides. The prepared solution was then carefully transferred into 250 ml volumetric flask containing 60 mls of pH adjusted double distilled water in an ice bath. 5.59 mls of tetra butyl ammonium bromide (Aldrich) was simultaneously added whilst stirring to the 250 ml volumetric flask in an ice bath and topped up to the mark with pH adjusted double distilled water. The precursor solution was then sonicated for 360 min prior to ultrasonic spray. This resulted in preparation of a 9mM tetrabutyl ammonium bromide doped titanium dioxide precursor solution which was coded 9mM $C_{TBA}$-$TiO_2$. Several other precursor solutions tetra butyl ammonium bromide doped solutions were prepared in much the same way the only difference was the level of dopant tetra butyl ammonium bromide as illustrated here in Table 6.4

*Table 5.4* *shows actual volume measurement employed in preparation of TBA doped titanium dioxide precursor solutions.*

| Volume of TIP (µl) | TBA (ml) | Sample code |
|---|---|---|
| 78.25 | 5.586 | $9_{TBA}$ C-$TiO_2$ |
| 78.25 | 11.17 | $18_{TBA}$ C-$TiO_2$ |
| 78.25 | 16. 759 | $27_{TBA}$ C-$TiO_2$ |
| 78.25 | 22.34 | $36_{TBA}$ C-$TiO_2$ |
| 78.25 | 27.93 | $45_{TBA}$ C-$TiO_2$ |
| 78.25 | 33.52 | $54_{TBA}$ C-$TiO_2$ |

The prepared precursor solution was then decanted into an ultrasonic shown in figure 4.9 vessel housing an 1.7 MHz ultrasonic nebulizer shown in Figure 4.10 insert (b) for ultrasonic spray deposition. We also employed the aluminium reaction vessel shown in Figure 4.14 and the aluminium substrate holder depicted in Figure 4.1. The chosen substrate holder could accommodate (10 × 15 mm) FTO glass substrate. The selected substrate holder was specifically designed to allow an area of (5×5 mm) to be coated with carbon doped titanium dioxide nano particles during spray deposition which matches exactly the platinum coated photo cathode

developed in section 4.4.1. Once the precursor solution was in the vessel and the substrate holder mounted in the aluminium reaction vessel the whole system was purged with argon carrier gas, while simultaneously allowing the furnace temperature to reach 450 ºC. Ultrasonic spray was then carried for 120 min using the spray deposition conditions outlined in Table 4.3 of chapter 4. This resulted in formation of white-grey transparent homogenous film which was employed as a photo anode in photo chemical solar cells (PECs). At least six sample were fabricated for each dopant level

## 5.6 SEALANT CUTTING

A rectangular sheet of meltonix 1170-100 gasket (10×15 mm) was cut out to cover the whole photo anode area and an inner rectangle of (7.5× 7.5 mm) was carefully cut around the double layer coated thin film of ***photo active carbon doped titanium dioxide layer.*** Figure 5.7 shows the experimental procedure for cutting out meltonix gasket (sealant) around a spray coated photo active area.

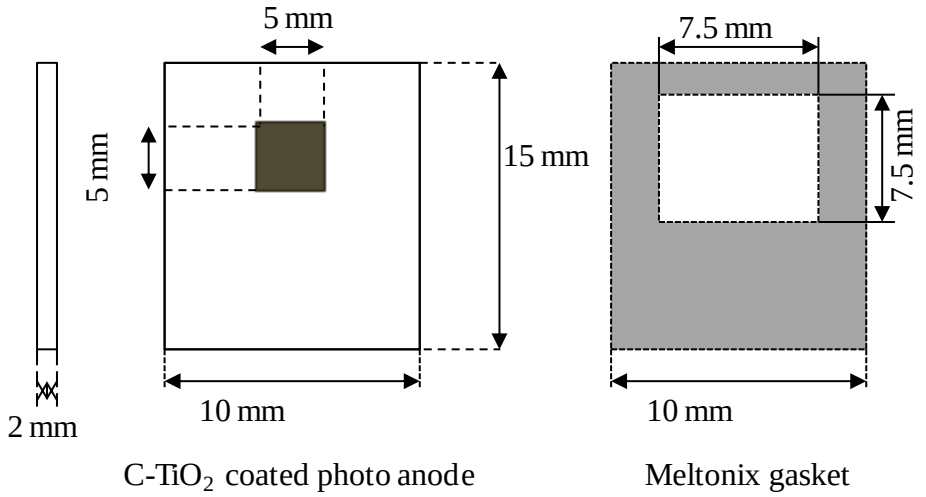


*Figure 5.7: Schematic showing the experimental procedure for cutting out meltonix gasket around a spray coated thin film area.*

## 5.7 ASSEMBLY OF PHOTOCHEMICAL SOLAR CELL

Using the spray pyrolysis developed photo anodes of (i) $C_{OA}$-$TiO_2$ (ii) $C_{TBA}$-$TiO_2$ (iii) QDs C-$TiO_2$/ $TiO_2$ sensitized photo anodes and the platinum coated photo-cathodes together in a sandwich configuration using meltonix in an oven at 120 ºC for 30 min. Figure 5.8 shows the experimental procedure involved in assembling the photochemical solar cell devices.

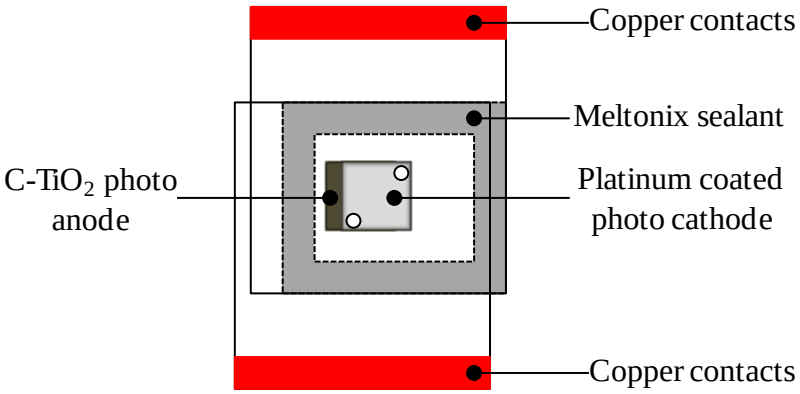


*Figure 5.8: Schematic presentation showing the arrangement of PEC solar device electrodes, with anode and cathode facing each other*

The Pt-coated photo cathode developed in section 5.4.1 was then placed onto the gasket on top of the photo anode with the conductive side facing down. This step keeps the sealant material in place between the two photo electrodes. The photo cathode was placed on top of the photo anode on top of the gasket in such a way that there was enough room on both electrodes for electrical contacts. The two electrodes were then glued together in an oven at 120ºC for 30 min.

## 5.8 REDOX ELECTROLYTE

Using a syringe liquid electrolyte was then flashed into the cavity left between the gasket and photo electrodes. This set up was maintained with the syringe filled with electrolyte firmly attached to the hole drilled on the photo cathode. The syringe was pumped until the electrolyte was observed to ooze out from the exit hole. This ensured that the whole PEC cell area was soaked with the electrolyte. After this the both holes were sealed using small piece of normal microscope glass side with the aid meltonix gasket. This was done using a soldering gun.

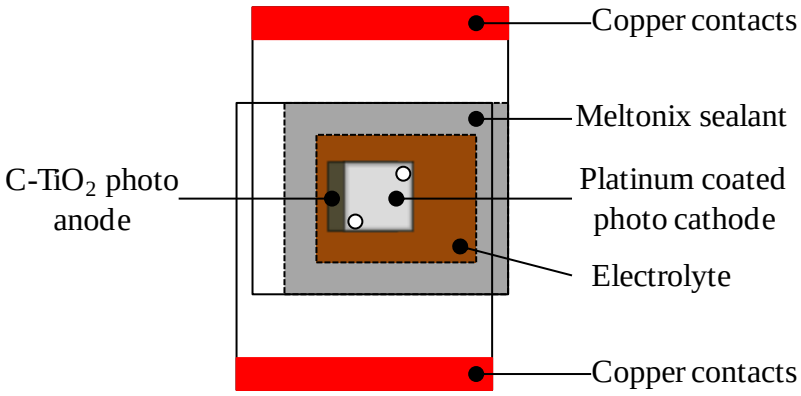


*Figure 5.9: Schematic presentation showing the arrangement of PEC solar device electrodes, with space left between the sealant and electrodes filled up with electrolyte.*

To enhance current collection at the electrodes as charge transport on the conductive FTO thin film is impaired by resistivity FTO coating. The space left for contacts on both electrodes was fully painted with silver paint. The increased conductivity of this silver paint allows better flow of electrons generated in the photo chemical solar cell (PEC). To further enhance current collection at the electrodes copper conductive tape was then coated over the silver paint to complete the solar cell contacts.

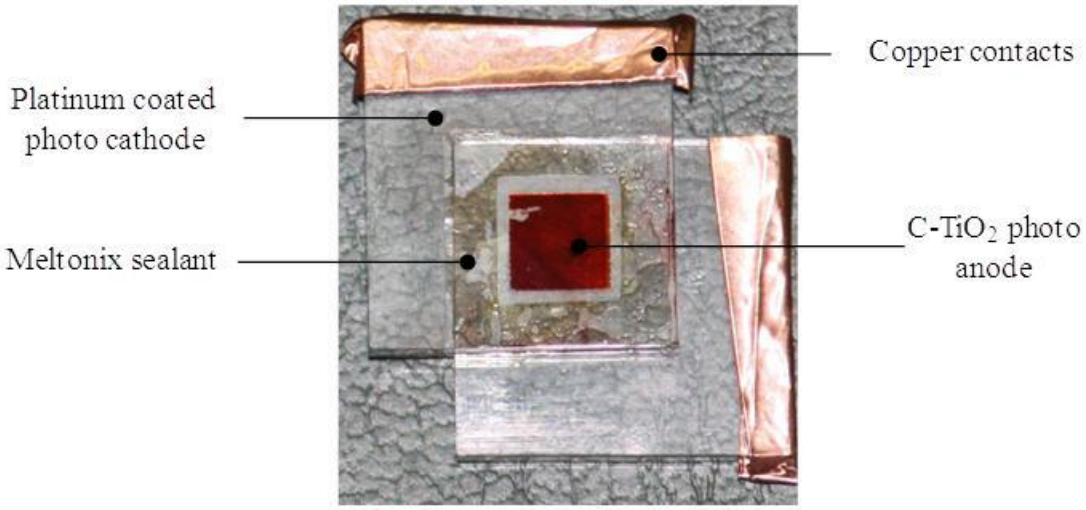


*Figure 5.10: A completed PEC solar cell device*

## 5.9 REFERENCES


1 Kelvin lord W.T.; *Phil Mag.* **1871**, 42 362-377

2 Taziwa R.; Meyer E.L.; Sideras-Haddad E.; Erasmus R.M.; Manikandan E.; Mwakikunga B.W. *International journal of photo energy*. **2012**, 2012, 904323-904337

3 Mikami, M.; Nakamura, S.; Kitao, O.; Arakawa, H.; Phys. Rev. B 66, **2002**, 155213

# CHAPTER 6

# SOLID STATE PHOTOCHEMICAL SOLAR CELLS INCORPORATING NANOCRYSTALLINE C-$TiO_2$ PHOTO-ANODES

## 6.1 INTRODUCTION

Titanium dioxide ($TiO_2$) is a typical n-type semiconductor that is extensively used for many applications, such as optical coating [1], gas sensing [2], photo catalysis [3] and more recently its playing a pivotal role in photo chemical solar cells [4-7] due to its favorable physical chemical non toxicity, optical electrical properties, good photo activity, as well as long term stability.

Photo electrochemical solar cells (PEC) are the most ambitious targets in the utilization of solar energy field [6-11]. Among the several contestants for photo-anode materials, $TiO_2$ has been usually adapted as adequate material since it has established best performance compared to other oxide materials [4]. However the wide spread utilization of $TiO_2$ is limited by its low absorption of the available suns radiation in the visible region of the solar spectrum (about 3-5%) because of the wide band gap 3.2 eV crystalline Anatase phase [11- 14]. Thus efforts have been made to enhance solar radiation absorption of un-doped $TiO_2$ in the visible region of the solar spectrum by doping with non-metal elements [13]. In dye sensitized solar cells (DSSC), this is being implemented successfully by anchoring low band gap ruthenium dye on to the surface of $TiO_2$ [8, 9]. But the ruthenium dyes are expensive and unstable in aqueous solutions. DSSCs have been recognized as the leading photovoltaic alternative to the currently dominant silicon-based solar cells [8]. DSSC has drawn considerable interest as an ideal photovoltaic concept for the production of renewable, clean, and affordable energy. High efficiency (up to 12%), low-cost and an eco-friendly fabrication process, transparency, and simplicity are some of the significant advantages offered by DSSCs [8-10]. In general, manipulation of semiconductor oxides with different morphologies, transition metal doped nano crystalline $TiO_2$ and the quest for new dyes are two major strategies explored for enhancing the absorption of incident light and the collection of photo-generated carriers to further improve the overall power conversion efficiency

of DSSCs [15-18]. To date, however, most efforts have not led to significantly improved photon conversion efficiency of DSSCs.

Alternatively visible light active nano crystalline $TiO_2$ has been successfully used in photo catalysis [3, 11, 12] more particularly the use of C-$TiO_2$ nano crystalline photo anodes has achieved great success with conversion efficiencies of 23%. C-$TiO_2$ nano electrodes have been used because of its capability to absorb visible light in the range 400- 650 nm. In addition C-$TiO_2$ has been proven to show improved electron gathering transporting behaviour and inhibiting charge recombination as compared to pure un doped $TiO_2$ nano electrodes [9-12].

Use of these type of hybrid nano-crystalline titanium systems in DSSC to supplement light absorption has been considered to be un necessary so far. Mainly because organic dyes has been are being used as solar sensitizers which are mainly Ru (II) complexes have been used to harvest solar radiation [1] Although this method increases the range of visible light response effectively. The incident photo current conversion efficiency (IPCE) for the dye absorbed semiconductor is relatively low below 500 nm and above 650 nm. In addition, the use of pure un-doped titanium dioxide nano crystalline particles which has oxygen deficiency in the crystalline does not help the situation, as it is known that oxygen deficiency can create electron-hole pairs. The oxidising holes are known to react with either the dye and destroy it and or are scavenged by the iodide ions. It is believed that the back reaction and corrosion of nanometals often take place at the nanometal/ dye and nanometal/electrolyte interfaces, decreasing the PCE and long-time stability of DSSCs [11, 15]. Therefore reduce the life span of the DSSC.

To minimize spectral losses and electron hole recombination we have fabricated a PEC consisting of a photo anode of carbon doped titanium dioxide (C-$TiO_2$) to replace the un-doped $TiO_2$ anode in the Grätzel type solar cell. A number of PECs have been fabricated which have different concentrations of carbon in the photo anodes. These types of photo anodes built with two or more nonmetals have attracted new attention with advantages ranging from improved spectral response, reduced electron hole recombination and amplified electron transport as compared to single type electrodes such pure Anatase $TiO_2$ [5,20]. The synthesized PEC solar cells were structurally, morphologically and optically characterized and its photovoltaic

properties were evaluated in this chapter. The results from this chapter have been accepted for an international conference on *2014 Energy, Environment and Materials Engineering in Shenzhen, China.*

## 6.2 STRUCTURAL CHARACTERIZATION

### 6.2.1 SEM ANALYSIS

Figure 6.1 shows the surface morphology of the $9_{TBA}$ C-$TiO_2$ photo electrode synthesized by USP technique.

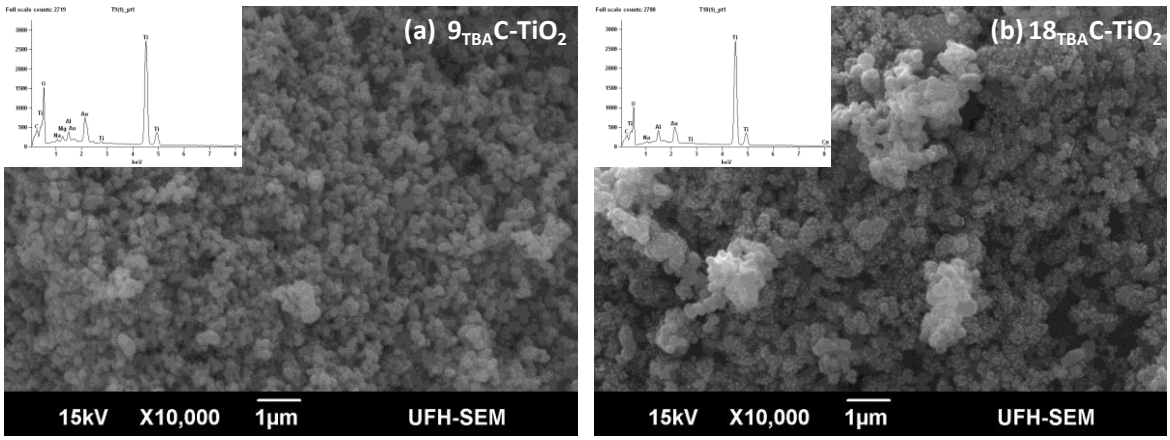


*Figure 6.1: SEM image of surface morphology of nano-crystalline and EDS spectra for (a) $9_{TBA}C$-$TiO_2$ thin film (b) $9_{TBA}C$-$TiO_2$ thin film*

The surface morphology of the as synthesized thin films has been analyzed by SEM. Clearly Figure 6.1 reveals that the deposited thin films for PEC application have multiple porous network structure. This is prerequisite for PEC solar cell application. This porous network structure of the thin films allows the redox electrolyte to percolate the entire nano-structure for efficient electron hole regeneration. Also a noteworthy feature in these thin Films is that as the carbon dopant level increases from 9 mM C-$TiO_2$ to 18 mM C-$TiO_2$ there shows a distinct change in arrangement of nano-structure. Cauliflower nano-structures develop as illustrated in Figure 6.1 (b). Inserts in Figure 6.1 (a) and Figure 6.1(b) also shows elemental analysis by EDS of the nano-crystalline $9_{TBA}$ C-$TiO_2$ thin film deposited on F: $SnO_2$ glass substrates using USP

technique has shown the presence titanium (Ti), oxygen (O) and carbon (C). The EDS spectra of the as synthesized thin films also indicate the presence of other elements (i.e.) gold (Au) from the gold coating in SEM sample preparation, aluminum (Al) from the aluminum reaction vessel or substrate holders used in the study. Sodium (Na) and magnesium (Mg) originate from the FTO glass substrate. The EDS spectrum also reveals that the titanium atom has different oxidation states. Titanium atom appears at 0.52 KeV, 2.75 KeV, 4.3 KeV and 4.9 KeV. This is due to different binging energies of the core electrons. The first peak of titanium at 0.52 KeV overlapping with oxygen might be due to the high oxidation state of Ti(IV) and other peaks at 4.2, 4.3 & 4.9 KeV are due to titanium in oxidation state of plus three Ti(III). The decline in titanium oxidation state has been ascribed due to carbon doping.

### 6.2.2 XRD ANALYSIS

XRD was used to investigate the crystalline structure of $TiO_2$ samples as well as the structural effects of carbon doping. Figure 6.2 shows that the XRD spectra of the as deposited nano-particles are very broad which indicates large crystallite sizes and/or strain. The synthesized samples showed Anatase $TiO_2$ as the main polymorph present in the samples. The Anatase peaks are indexed as (101), (004), (200), (105), (211), (116), (220) and (215) in order of increasing diffraction angles. These diffraction angles indicate a body centered tetragonal crystalline structure of $TiO_2$. The peaks of C-$TiO_2$ samples were shifted to higher diffraction angles as compared to that of un-doped $TiO_2$ samples by ~ 0.06. This shift implies that an oxygen atom in the $TiO_2$ was substituted by a small atom carbon. The recorded XRD patterns were further analyzed with JADE software to determine average particle sizes by use of the Scherer's formula .The analyses revealed that the particle size ranged from 18-19 nm which was decreasing with increase in carbon concentration.

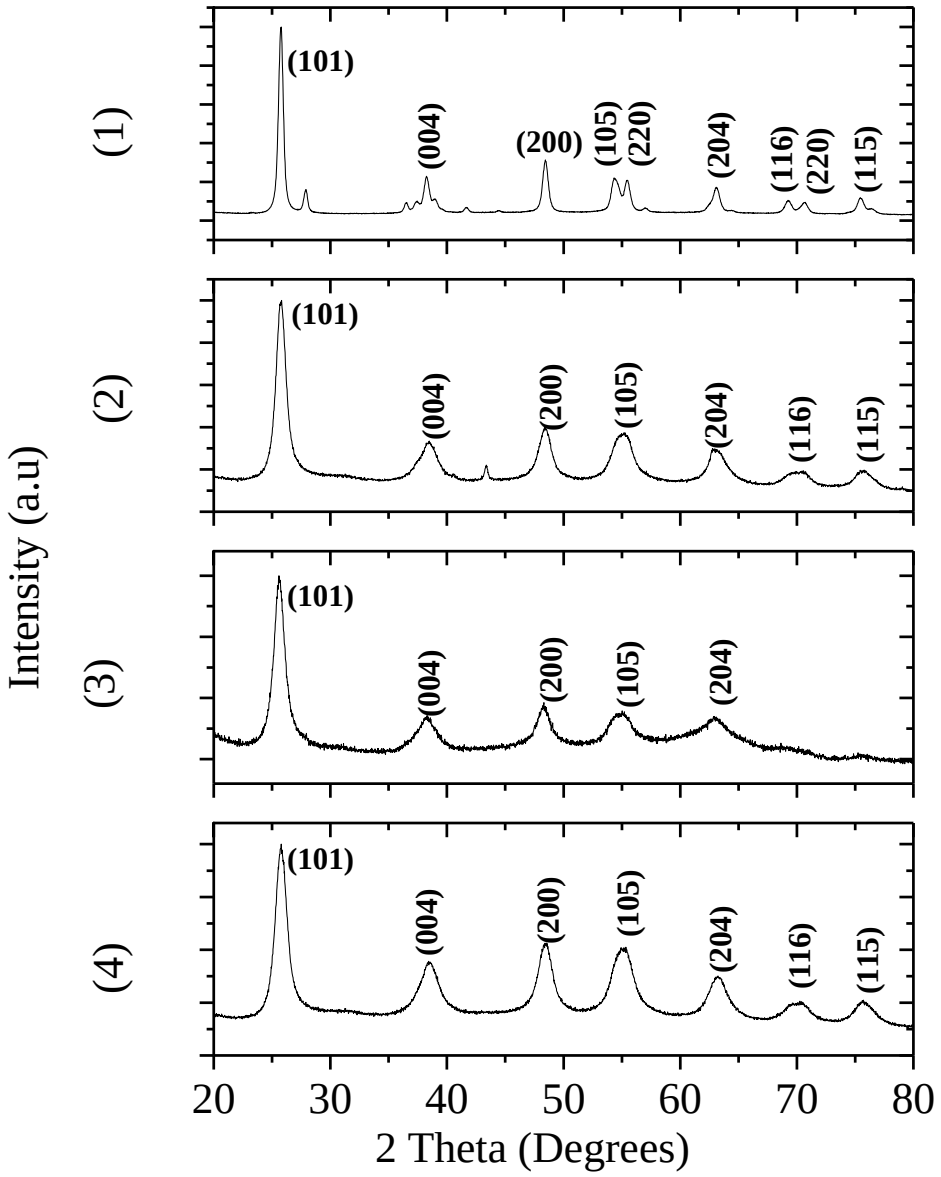


*Figure 6.2: XRD pattern for the as deposited thin films (1) un-doped $TiO_2$, (2)9 mM C-$TiO_2$, (3) 36 mM C-$TiO_2$, (4) 45 mM C-$TiO_2$*

### 6.2.3 RAMAN SPECTROSCOPY ANALYSIS

Raman spectroscopy was used to analyze the sample to complement XRD and HRTEM results for phase identification. The Rutile phase of $TiO_2$ is tetragonal and exhibits symmetry characters of the space group $D_{4h}^{14}$ with two $TiO_2$ formula per unit cell. Four active Raman modes with symmetry B1g (143 $cm^{-1}$), Eg (447 $cm^{-1}$), $A1_g$ (612 $cm^{-1}$) and $B_{2g}$ 826 $cm^{-1}$. While the Anatase phase has a tetragonal $D_{14h}^{19}$ containing two units per unit cell. According to group theory, there are 6 Raman Active modes with symmetry Eg (143 $cm^{-1}$), Eg (196 $cm^{-1}$), $B1_g$ (397 $cm^{-1}$), doublet (A1g+B1g) 516 $cm^{-1}$ and Eg (640 $cm^{-1}$). The measured Raman spectrum Figure 6.2 shows that the as deposited nano-particles both for un-doped $TiO_2$ and C-$TiO_2$ are well crystallized in the Anatase phase of $TiO_2$. Such a conclusion is in good agreement with the XRD analysis.

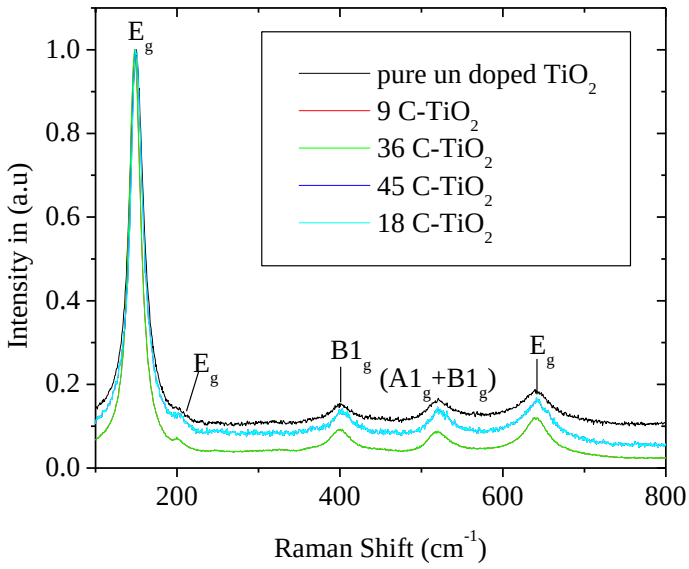


*Figure 6.3: Raman spectroscopy of the as deposited for the un-doped $TiO_2$ and C-$TiO_2$ samples*

## 6.3 DIFFUSE REFLECTANCE SPECTROSCOPY ANALYSIS

### 6.3.1 OXALIC ACID (OA) DOPEP $TiO_2$ THIN FILMS

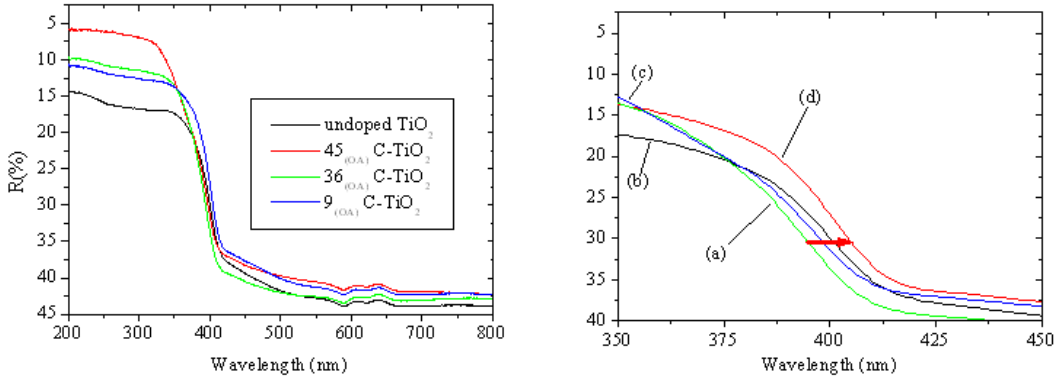


*Figure 6.4*: *Shows the DRS spectra of the as deposited thin films. Also shows the details of DRS spectra in the range 350 -500 nm (a) Un-doped $TiO_2$ (b) $9_{OA}$ C-$TiO_2$, (c) $36_{OA}$ C-$TiO_2$ (d) $45_{OA}$ C-$TiO_2$.*

It is well known that the photo sensitivity of semiconductors is related to its band gap [21-24]. The UV-Vis diffuse reflectance spectra of the as synthesized thin films are shown here in Figure 6.4, for comparison the spectrum for un-doped titanium dioxide is also shown. The 9 mM oxalic acid doped titanium dioxide ($9_{(OA)}$ C-$TiO_2$) showed a 6 nm shift absorption in visible spectrum with an absorption edge at 402 nm, whilst the $36_{(OA)}$ C-$TiO_2$, $45_{(OA)}$ C-$TiO_2$ showed absorption edges at 404 nm and 403 nm respectively. The USP synthesized samples for oxalic acid doped samples for $27_{(OA)}$ C-$TiO_2$ showed a band gap equal or lower than that of un-doped $TiO_2$ (spectra not shown). The blue shift of the absorption edge observed with $27_{(OA)}$ C-$TiO_2$ can be attributed to charge transfer transition between the metal ion d electrons and the conduction or valence band of $TiO_2$ [4].

The energy band gaps of the thin films were estimated by using equation (6.1) in this work. The calculated energy band gaps are presented in Tables 6.1 & 6.2.

$$Eg = \frac{1239}{\lambda_{edge}} eV \qquad (6.1)$$

Where $\lambda_{edge}$ is the wavelength of the absorption edge (where the absorption edge wavelength was found from the plot of the derivative (R%) versus wavelength)

*Table 6.1: Shows the $\lambda_{nm}$ and the determined energy band gap energies of the as synthesized sample at different dopant levels carbon in oxalic acid (source of carbon).*

| **Oxalic acid conc. [OA]** | **Absorption edge λ (nm)** | **Band Gap Energy (eV)** |
|---|---|---|
| (a) $TiO_2$ | 396 | 3.12 |
| (b) $9_{(OA)}$ C-$TiO_2$ | 404 | 3.06 |
| (c) $36_{(OA)}$ C-$TiO_2$ | 403 | 3.06 |
| (d) $45_{(OA)}$ C-$TiO_2$ | 405 | 3.05 |
| (e) $27_{(OA)}$ C-$TiO_2$ | 396 | 3.12 |

### 6.3.2 TETRABUTYL AMONIUM BROMIDE (TBA) DOPED $TiO_2$ THIN FILMS

The Uv-Vis diffuse reflectance spectra of the tetrabutyl ammonium (source of carbon) doped titanium dioxide thin films ($C_{TBA}$-$TiO_2$) deposited on FTO glass substrate by USP were obtained to determine the relationship between solar energy conversion efficiency and spectroscopic properties and the spectra is shown here in Figure 6.5. The absorption band for the tetrahedral symmetry of $Ti^{4+}$ normally appears approximately 350-380 nm. In the spectra of un-doped $TiO_2$ the absorption edge was observed at 346 nm. However the spectra for (b) $18_{(TBA)}$ C-$TiO_2$ showed an absorption edge that was red shifted to 495 nm, $36_{(TBA)}$ C-$TiO_2$ at 512 nm and 45 $_{(TBA)}$ C-$TiO_2$ had an absorption edge at 550 nm.

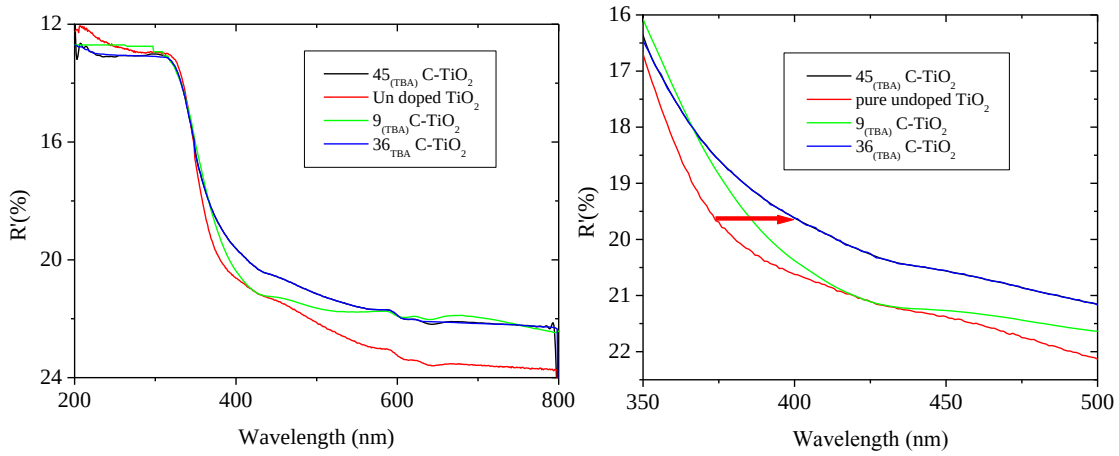


*Figure 6.5: The DRS spectra of the as deposited thin films un-doped $TiO_2$, $9_{(TBA)}$ C-$TiO_2$, $36_{(TBA)}$ C-$TiO_2$, $45_{(TBA)}$ C-$TiO_2$. Which also shows an expanded of DRS spectra in the range 350-500 nm*

The samples doped with TBA doped $TiO_2$ showed an enhanced shift than those of OA this mainly because TBA has a higher carbon composition than oxalic acid despite its lower diffusion mobilities into the $TiO_2$ and large molecular size as compared to OA [22]. The enhanced absorption might also be due to the presence of ammonium ion which contains the nitrogen atom in TBA. It is well known that nitrogen doping as compared to carbon doping shows enhanced doping hence a massive shift in the absorption edge. Nitrogen doping has proven more efficient at improving visible light activity. It has been theoretically proven that the carbon states are too

deep within the band gap to significantly increase visible light activity, unlike nitrogen doping 1s state, which successfully overlap with the band O2p states [15, 17, 22]. The estimated energy band gaps of the thin films are presented in Table 6.2.

*Table 6.2*: *The $\lambda_{nm}$ and the determined energy band gap energies of the as synthesized sample at different dopant levels of carbon in tetrabuyl ammonium (TBA)*

| **TBA conc. [TBA]** | **Absorption edge λ (nm)** | **Band Gap Energy (eV)** |
|---|---|---|
| (a) undoped$TiO_2$ | 346 | 3.60 |
| (b)9($_{TBA)}$ C-$TiO_2$ | 496 | 2.49 |
| (c)36($_{TBA)}$ C-$TiO_2$ | 512 | 2.41 |
| (d)45($_{TBA)}$C-$TiO_2$ | 550 | 2.25 |

## 6.4 *I-V* ANALYSIS PHOTOELECTROCHEMICAL SOLAR CELLS

During the J-V measurement four parameters such as short circuit current density ($J_{SC}$), open circuit voltage ($V_{OC}$), fill factor (FF) and overall solar cell efficiency (η) were obtained from the fabricated PEC solar cells Figure 6.6 shows the J-V curves for several PEC solar cells fabricated.

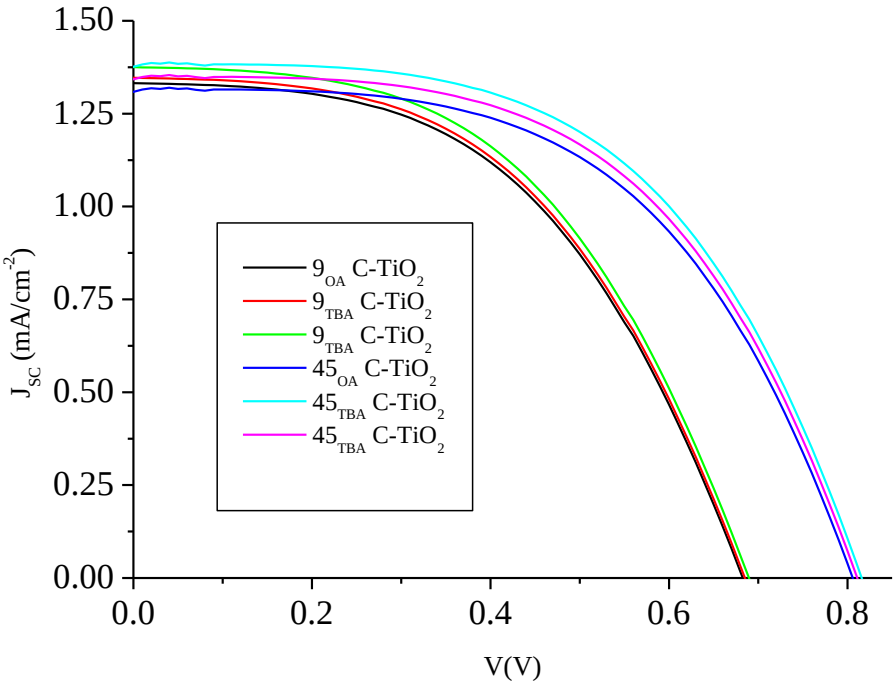


*Figure 6.6: J-V characteristics of photochemical solar cell with (C-$TiO_2$ photo anode with different dopants OA (source of carbon) and TBA (source of carbon) for selected solar cells) (b) Performance parameters of the PEC solar cells with change in constituent and dopant level*

An oxalic acid doped photo-electrode ($9_{OA}$ C-$TiO_2$) based in PEC showed an $V_{oc}$ of 0.682 V, $J_{sc}$ of 1.33201 mA.cm$^{-2}$, a fill factor of 50.2%, and an efficiency of 0.456%, $9_{TBA}$ C-TiO2 $V_{oc}$ of 0.683 V, $J_{sc}$ of 1.33465 mA.cm$^{-2}$, a fill factor of 50.3%, and an efficiency of 0.462%. $45_{TBA}$ C-$TiO_2$ 9 TBA doped photo-electrode showed photo electrode showed a maximum conversion with an open circuit voltage of ($V_{OC}$) of 0.817 V, photocurrent $J_{SC}$ of 1.37639 mA/cm$^2$ , a fill factor of 54.5% and an efficiency of 0.613%. The abrupt increase in $J_{SC}$ by 49% was particularly notable

from Figure 8.18. Light absorption as was noted from the DRS spectra of $9_{OA}$ C-$TiO_2$ showed an absorption edges around 404 as compared to the TBA doped photo-electrodes which showed an absorption edges at around 551 nm. This increase in photo current generation as the dopant type change might due to (1), The chemical structure of oxalic acid ($C_2O_4^{-2}$) has 27% by mass ratio of carbon as compared to 59% ration of carbon in tetra butyl ammonium ($C_{16}H_{36}BrN$) (2) it has been admitted that the incorporation of C in the nano structure $TiO_2$ can help fill some oxygen vacancies naturally present in pure un doped titanium leading to reduced trap state distributions and improved charge mobilities [25-27]. In addition pure un-doped titanium dioxide contains oxygen defects which cause carrier trapping at the surface of pure un-doped $TiO_2$ nano-particles leads to a low electron diffusion coefficient ($7 \times 10^{-6}$ $cm^{-2}V^{-1}s^{-1}$) [26].

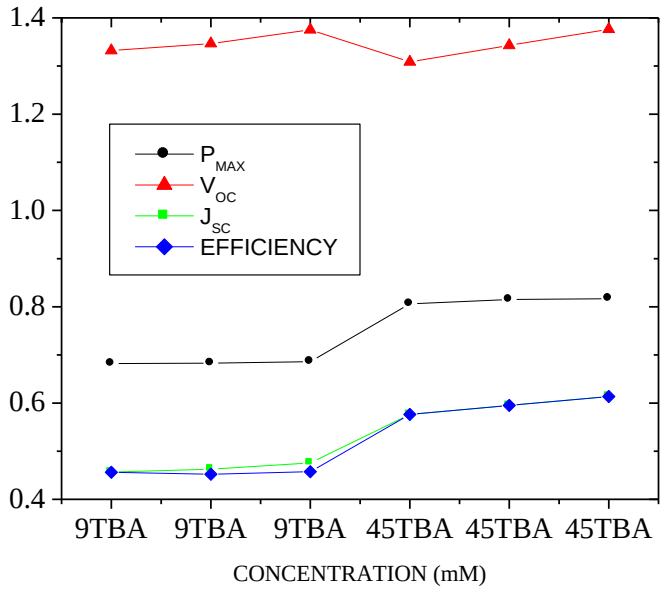


*Figure 6.7: performance parameters of the PEC solar cells with change constituent and dopant level*

A notable feature of the present results is that the open circuit voltage $V_{oc}$ of the carbon TBA doped electrode ($45_{TBA}$ C-$TiO_2$) shown here in Table 8.3 is relatively high (0.815V) about 4% than that of conventional DSSC typically~0.75V [8]. According to the kinetic model, the open circuit voltage is given by $E_F$-$E_{redox}$ where EF is the Fermi level of $TiO_2$ and $E_{redox}$ is the redox

potential of the electrolyte. The actual $V_{oc}$ obtained in experiments is lower than the theoretical upper limit due to the dark current in a solar cell. The dark current is mainly caused by carrier recombination between the photo injected electrons in the semiconductor and the positively charged electrolyte. Our current studies have shown a higher $V_{oc}$ which indicates that there is lower carrier recombination as compared to conventional DSSC and the mechanism for improved voltage has been fully discussed in 6.5.2.

The gap of Voc and V max (ΔV) for each sample illustrated a higher change ratio. The values of (ΔV/Voc) for each sample is shown in Table 6.3 each PEC device showed a higher change ratio. This trend is attributed to a decreased series resistance ($R_S$) and its beneficial for the higher FF and working electrode in PEC solar cell. The FF showed an increase with increase in solar cell efficiency with the TBA-doped electrode ($45_{TBA}$ C-$TiO_2$) having FF value of approximately 55%. However the overall solar cell efficiency of the PEC solar cell having combined TBA doped electrode $9_{TBA}$ C-$TiO_2$ is still very low this might be due to the poor fabrication technique and also that the coating of titanium dioxide to glass substrate did not provide a good adhesion of the nano particles to the FTO layer. This was observed when the deposited nano particles tend to easily get washed off with electrolyte upon electrolyte injection during the fabrication process.

*Table 6.3: The summary of J-V characteristics of PEC solar cells consisting of oxalic and tetra-butyl ammonium doped photo anodes (solar illumination intensity: 100mW.cm$^{-2}$)*

| **[Dopant] mM** | **Jsc** mA/cm$^2$ | **$V_{oc}$ (V)** | **P $_{Max}$** | **FF** | **Efficiency (%)** | **ΔV** | **Δ/$V_{OC}$** |
|---|---|---|---|---|---|---|---|
| **9OA** | 1.33201 | 0.682 | 0.45632 | 0.502466 | 0.456456 | 0.242 | 0.354839 |
| **9TBA** | 1.34651 | 0.683 | 0.45221 | 0.503141 | 0.462722 | 0.243 | 0.355783 |
| **9TBA** | 1.37522 | 0.686 | 0.45741 | 0.503929 | 0.475407 | 0.236 | 0.344023 |
| **45OA** | 1.30857 | 0.806 | 0.57634 | 0.546447 | 0.576342 | 0.266 | 0.330025 |
| **45TBA** | 1.3428 | 0.815 | 0.59508 | 0.543757 | 0.595078 | 0.265 | 0.325153 |
| **45TBA** | 1.37639 | 0.817 | 0.61347 | 0.545774 | 0.613729 | 0.267 | 0.326805 |

*$\Delta V = (V_{oc}-V_{Max})$

### 6.4.1 MECHANISM FOR IMPROVED $V_{OC}$

The suggested mechanism of PEC solar cells is not far off different from that of DSSC. The solar cell devices differ in the mechanism of light sensitization. In the Grätzel type of solar cell depicted in schematically in Figure 6.8, Ruthenium dyes (N3, N719 and Z907) act as solar sensitizers of an optically inactive $TiO_2$ nano particle structure. Whilst in the current PEC device depicted in Figure 6.9, C-$TiO_2$ nano-particles act as a solar sensitizer. In the current PEC solar cell device our nano C-$TiO_2$ nano structure serves two purposes (1) as a solar radiation absorber (2) as an efficient transport medium. Unlike in the Grätzel type of solar.

Considering a DSSC cell developed by Grätzel and co-workers [8, 9] in 1991 Figure 6.8.

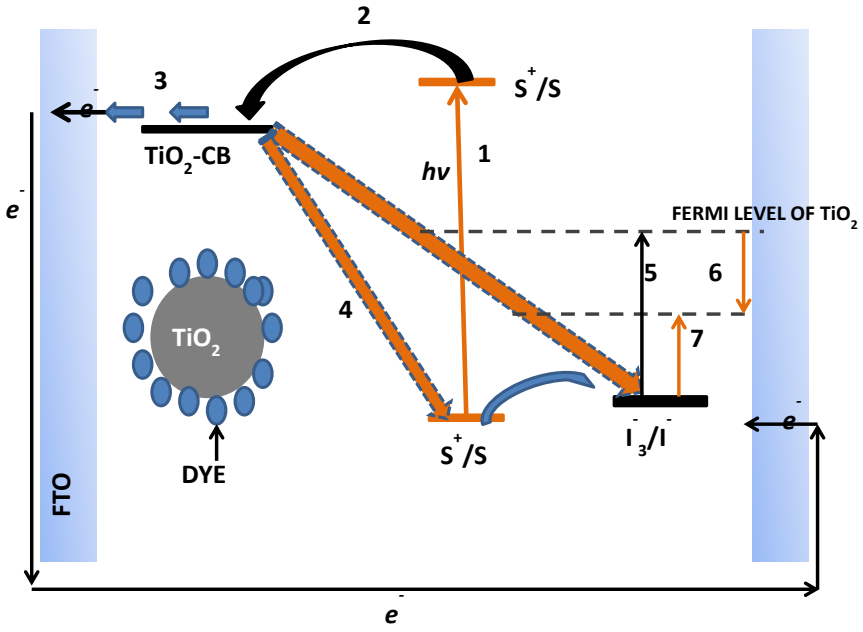


*Figure 6.8: Suggested mechanism for electron generation and electrical losses*

Electrons are excited by solar energy from the HOMO to the LUMO in the dye molecules as in indicated as (1). These excited electrons diffuse into the conduction band (CB) of $TiO_2$, indicated as (2). Then the electrons travel through the CB of the $TiO_2$ layered towards the FTO of the working electrode, indicated as (3). In this process a large volume of photo generated electrons move back to the LUMO of the dye or electrolyte via electron trapping effects. This process

results in electron recombination which is indicated by (4). In addition pure un-doped titanium dioxide contains oxygen defects which cause carrier trapping at the surface of pure un-doped $TiO_2$ nano-particles leads to a low electron diffusion coefficient ($7 \times 10\text{-}6\ cm^2V^{-1}s^{-1}$) [5, 26]. The reason is considered that the electron transfer time is a few nano seconds from the LUMO of the dye to the CB of $TiO_2$, whereas the electron transfer time in the CB of $TiO_2$ is a few milliseconds. Thus the original voltage intensity (indicated as (5)) drops significantly shown as (6). Eventually, the working voltage intensity is determined as (7). The mechanism of preventing voltage drop is shown here is shown in figure 6.9.

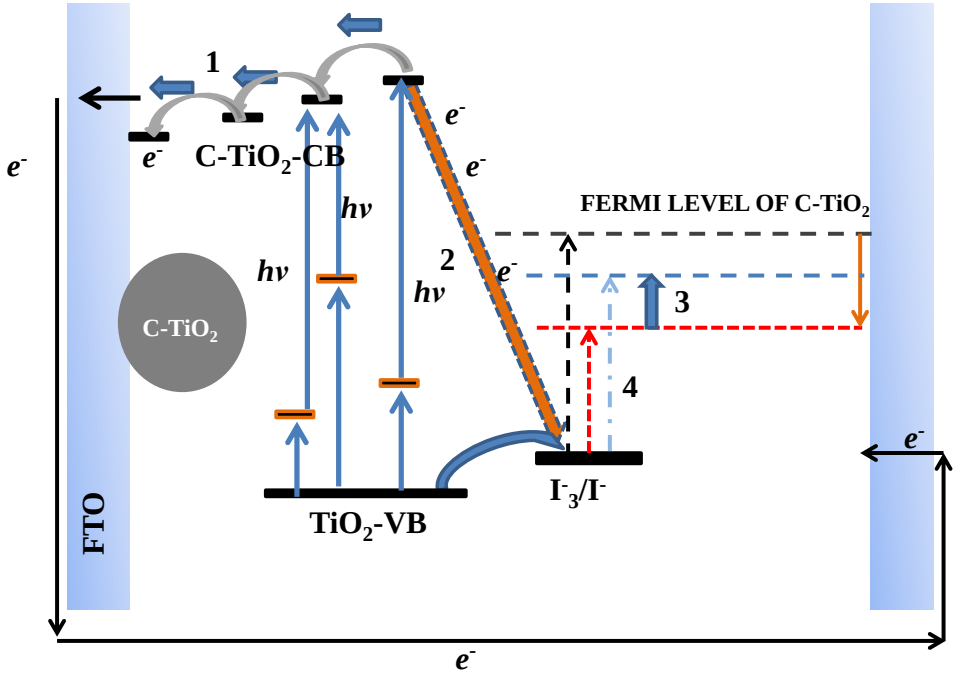


*Figure 6.9: Suggested mechanism for electron generation and minimized electron hole recombination.*

The photons generated electrons from the intermediate energy band gaps are transferred through the conduction band via lowered multiple energy band gap state of the conduction band (3) that have been formed due to doping with carbon. These multiple energy levels steps can accelerate the electron flow for lower energy resulting in an electron path valley. When comparing with the electron path in DSSC Figure 6.8. It can be noted that the route for electron transport is rather long and not efficient. Even though a little voltage drop can be estimated by the lowered CB band of $TiO_2$, it seems that the preventing effect of electron recombination is much more

powerful. Eventually, the enlarged electron path way constructed leading the efficient electron transfer pathway from the intermediate band gaps to the CB to the working electrode FTO is shown by (1). These electrons with reduced electron losses via (2) go to the working electrode as (1) resulting in an enhanced voltage intensity which is indicated by (3). Thus, improved voltage intensity can be obtain, which is indicated as (4). These results are correlated with increased $V_{Max}$ and decreased $\Delta V$ shown here in Table 6.3 and Figure 6.9. In conclusion, a drop in the voltage intensity is prevented by electron recombination and significantly improves the efficiency of the solar cell with increase in carbon dopant levels.

## 6.5 CONCLUSIONS

In summary, we demonstrated solid state photo- electrochemical solar cells (PECs) using C-$TiO_2$ photo electrodes, synthesized by ultrasonic spray pyrolysis. As reported carbon doping of nano crystalline titanium dioxide is found to be beneficial for PEC solar cell device performance, with significant improved photo voltage value of 0.817 V as compared to pure dye sensitized solar cells devices which employ pure un-doped $TiO_2$ with a max photo voltage of 0.75 V. This improvement in photo voltage output is found to be correlated with the electronic and optical properties of the nano-powders used in fabrication of PEC devices. In particular, there was a significant shift in the UV-Vis DRS spectrum of TBA doped C-$TiO_2$ photo electrodes which is responsible for conversion of photons in the blue region of the solar spectrum as compared to pure $TiO_2$ which has no photon activity in the visible section of the solar spectrum.

We have also demonstrated that C-$TiO_2$ nano-structured photo electrodes with optical band gaps in the visible section of the solar spectrum can be obtained with oxalic acid and tetrabutyl ammonium bromide as the carbon sources using spray pyrolysis technique. Our analysis has also shown that the TBA doped samples exhibit a greater shift in absorbance as compared to OA doped sample. The results are evidenced by extended absorption edges of $45_{TBA}$ C-$TiO_2$ photo electrode which were well above the 500 nm mark. Furthermore the respective solar cells have shown higher conversion efficiencies as compared to the OA doped photo electrodes. The PEC device with a $45_{TBA}$ C-$TiO_2$ photo electrode showed the highest solar conversion with an open circuit voltage of ($V_{OC}$) of 0.817 V, photocurrent $J_{SC}$ of 1.37639 mA/$cm^2$ , a fill factor of 54.5%

and an efficiency of 0.613%.Admittedly the overall solar cell efficiency for the PEC devices employing TBA doped titanium dioxide is still very low ~0.6% as compared to the dye sensitized counterpart fabricated by Grätzel in 1991 with an efficiency of ~11%. Therefore, C-doped $TiO_2$ nano-crystals prepared by our approach are ideal semiconductor materials for DSSC and PEC solar cell devices. This study has revealed that our method of fabricating PEC devices using ultrasonic spray pyrolysis has low cost, simple processing, excellent reproducibility, easy to extend on a large scale production and is applicable in the field of solar energy conversion.

## 6.6 REFERENCES


1 Markowska-Szczupak.; Ulfig K.; Morawski A.W. *Catalysis Today*. **2011**. 169, 249-257

2 Sanchez M.; Rincon M.E.; *Diamond & Related Materials***. 2012**, 21, 1-6

3 Yunxiao, B.;Wang Xiaochang a. Procedia Engineering. 2011, 24, 663-66

4 Daobao Chu.; Ximei Yuan.; Guoxu Qin.; Mai Xu.; Peng Zheng.; Jia Lu.; Longwu Zha. J Nanopart Res. 2008, 10, 357-363

5 Ji Sun Im.; Jumi Yun, Sung Kyu Lee.; Young-Seak Lee, *Journal of Alloys and Compounds*. **2012**, 513, 573-579

6 Yanan Xie, Niu Hung, Yumin Liu. Weiwei Sun, Hadja Fatima Mehanane, Sujian You, Linyuan Wang, Wei Liu, Shishang Guo, Xing Zhong Zhao. *Electrochimica Acta*. **2013**, 93, 202-206

7 Hussein Melhem, Pardis Simon, Jin Wang, Catherine Di Bin, Ratier B.; Leconte Y.; Herlin-Boime N.;Makowska-Janusik M.; Kassiba A.; Boucle J. *Solar Energy Materials & Solar Cells.* **2012**

8 Grätzel, M.; *Inorg Chem.* **2005,** 44, 20-25

9 Grätzel, M.; *J Photochem. Photobiol*. A**. 2004,** 164 , 3-7.

10 Murayama, M, Mori, T.T.; *Thin Solid Films*. **2008,** 516, 2716-2722

11 Nie, X.; Solberg, K., Matter. *Res. Soc. Symp. Proc.Matter.Technol. Hydrogen Econ*. **2004**

12 Nagaveni, K.; Hegde, M.S.; Ravishankar. N.; Subbana, G.N.; Madras, *G Langmuir*, **2004**, 20, 2900-2907

13 Ye Cong, Xuanke Li, Yun Qin, Zhijun Dong, Guanming Yuan, Zhengwei Cui, Xiaojun Lai. *Applied Catalysis B: Environmental*. **2011**, 107, 128-134

14 Hyun Uk Lee, Soon Chang Lee, Saehae Choi, Byoungchul Son, Sang Moon Lee, Hae Jin Kim Jouhahn Lee. *Chemical Engineering Journal*. 2013, 228, 756-764

15 Yella A.; Lee H.W.; Tsao H.N., Yi C.; Chandiran A.K.; Diau E.W.; Yeh C.Y.; Zakeerudin S.M., Gratzel M *Science*. **2011**, 85(6), 1172-1178

16 Monoishka R.N. *Renewable and Sustainable Energy Reviews*. **2012**,16, 208-215

17 Chuanjiang Qin.; Ashraful Islam.; Liyuan Han. *Dyes and Pigments*. **2012**, 94, 553-56

18 Bozic-Weber, B.; Edwin C.C.; Housecroft, C.E. *Coordination Chemistry Reviews*. **2013**

19 Hoffmann, M.R.;Martin, S.T.;Choi, W.;Bahnemann, D.W. *Chem.Rev*. **1995**, 95, 69-96

20 Quiping Liu.; Yang Zhou.; Yandong Duan.; Min Wang.; Yuan Lin. *Electrochemica Acta.* **2013**, 95, 45-53

21 Castro A.L.; Nune M.R.; Carvalho M.D.; Ferreira.; Jumas J.C. *Journal of Solid State Chemistry*. **2009**, 182, 1838-1845

22 Sasueng Lee.; Chang Yeon Yun.; Mi Sun Hahn.; Joengjin Lee.; Jonghoep Yi. *Korean J Chem, Eng*. **2008**, 25(4), 892-896

23 Djerdji I.; Acron D.; Jaglicic Z.; Niederberger M. *Journal of Solid State Chemistry*. **2008**, 181, 1571-1581

24 Chung Hung Huang.; Yu-Ming Lin.; I-Kai Wang.; Chun-Mei Lu. *International Journal of Photoenergy*. **2012**, 2012, 1-13

25 Soon Hyung Kang, Hyun Sik Kim, Jae Yup Kim, Yung-Eun Sung. *Materials Chemistry and Physics***. 2010**, 124, 422-426

26 Matos J.; Antienzar P.; Gracia H.; Hernandez-Garridio J.C. *Carbon*. **2013**, 53, 169-181

27 Wei Guo.; Liqiong Wu.; Gerrit Bochloo.; Anders Hagfeldt.; Tingli Ma. Journal of Photochemistry and Photobiology A: Chemistry. 2011, 219, 180-187

# CHAPTER 7
# PHONON CONFINEMENT ANALYSIS AND RAMAN SPECTROSCOPY IN C-$TiO_2$

## 7.1 INTRODUCTION

This chapter begins by addressing some theoretical aspects and the physics of the properties of the materials as their geometrical dimensions reduce down to nano scale. Phonon confinement has been studied widely. The phonon confinement by Ritchter *et al*., [1, 4] and the modifications for thin films, nanowires slabs and quantum dots have had their achievements. However, in some materials, when confining dimensions becomes lower than 5 nm, most of the phonon confinement theories fail. To fit the model to experimental data as surface phonons become predominant. In this chapter we attempt to resolve these conflicts by fitting a modified phonon confinement model to our 6nm C-$TiO_2$ QDs that addresses the limitations of Ritcher *et al*., [1, 4] models as particle reduce to nano-scale.

Raman spectroscopy is expected to produce interesting size dependent properties in nano-particles. This Chapter then ends by providing Raman temperature dependence analysis of C-$TiO_2$ nano-particles. This section tends to adds new knowledge in terms of material properties as temperatures changes. The following articles from this work have been published in peer reviewed journals

## 7.2 RAMAN SPECTROSCOPY

In the 1980's it became apparent that the Raman spectral line shapes for microcrystal could not follow the perfect Gaussian Profile. It was then realized that there was need for understanding of the origin of this asymmetry. Spatial correlation modeling, as it was called, then became one of the ways to extract information from Raman spectroscopy data. The justification is that for a perfect bulk crystal of diameter *d* having vibrational modes of momentum *q*, the Heisenberg's

uncertainty principles $(\delta d.\delta q \approx h)$ means that as $\delta d \to \infty$ (bulk) then $\delta q \to 0$ (the ‘‘$q = 0$” selection rule applies). As the diameter, $\delta d \to 0$ (nano –metric) then the vibrational momentum, $\delta q \to \infty$. In this case, the $q = 0$ selection rule breaks down; a contribution from $q \neq 0$ phonons determined by the dispersion relation $\omega(q)$ is allowed. This accounts for the asymmetric broadening of the peaks in a Raman spectrum. The Richter equation for confined phonons in spherical nano-particles was modified to include Gaussian distribution of the phonon momenta and particle size by Campbell & Faucet and given here as [1].

$$I(\omega) = A_0 \int_{-\infty}^{\infty} \left[ \frac{|C(0,q)|^2}{[\omega - \omega(q)]^2 + (\Gamma o/2)^2} \right] d^3q \qquad (7.1)$$

Where $\Gamma_0$= The full-width at half maximum (FWHM) , ω.is the vibrationa frequency. $|C(0, q)|^2$ is the Lorentz’s coefficient which may be Gaussian or any peak function and q is momentum

In the equation, $\Gamma_0$ is the full-width-at-half-maximum (FWHM) for bulk material Raman peak (for instance $\Gamma_0$ = 7.5 $cm^{-1}$ for Anatase $TiO_2$, $\omega(q)$ is the phonon dispersion curve relation (PDR) for the material (for instance $A$ = 713 $cm^{-1}$, $a$ = 0.76 nm for the 713 $cm^{-1}$ phonon branch whereas $A$ = 808 $cm^{-1}$ and $b$ = 0.38 nm [2, 3] for the 808 $cm^{-1}$ phonon branch in $WO_3$). The Richter *et al*. model is valid for spherical nano-crystals of mean diameter $d$ for which the Fourier coefficient C(0,q) was assumed to be Gaussian of the form exp ($-q^2d^2/14\pi^2$) with a phonon amplitude at the boundary of 1/e. When geometry deviates from a sphere then adjustment has to be carried out. For a nanowire shape for instance, confinement is in two dimensions of the diameter of the nanowire since the length of the rod can be as long as 1 μm. Campbell & Faucet [1, 4] extended the Richter *et al* model to (I) remove the non-phyical boundary condition of 1/e and tried other values (II) check the effect of other particle-size distribution functions such as (a) sin ($ar$)/($ar$) by analogy with the ground state of an electron in a hard sphere (b) exp($-\alpha r$) by analogy with a lossy medium and (c) exp($-\alpha\ r^2/d^2$).Another important step by Campbell & Faucet was their ability to extend the Richter model to other shapes of the micro-crystals such as what they called columnar (now we call it rod-like or nano-wires) and also thin films. They argued that for these

two additional shapes, the following Fourier co-efficients should be incorporated in the Richter *et al.,* [4] equation for a rod of diameter *d* and length *l*:

$$\left|C(0,q)\right|^2 \cong \exp\left(-\frac{{q_1}^2 d^2}{16\pi^2}\right).\exp\left(-\frac{{q_2}^2 l^2}{16\pi^2}\right)\left|1-erf\left(\frac{iq_2 l}{\sqrt{32\pi}}\right)\right|^2 \tag{7.2}$$

and For a thin film of thickness, $\tau$.

$$\left|C(0,q)\right|^2 \cong \exp\left(-\frac{{q_1}^2 \tau^2}{16\pi^2}\right).\exp\left|1-erf\left(\frac{iq_2 \tau}{\sqrt{32\pi}}\right)\right|^2 \tag{7.3}$$

Campbell & Faucet [1]admittedly saw very small significance in replacing the Gaussian with other size-distribution functions especially for spherical nano-crystals. Also the Fourier coefficients for thin films and columnar shapes make the Richter *et al.* [4] equation even more complicated in that one performs integration within another numerical integration. A simpler approach to modifying the Richter equation was to include other novel nano-crystal shapes has been considered.

Let us imagine a small slice of width *d*r and a distance r from the centre of the wire in real space as illustrated in Figure 7.1. In momentum space, this slice contains phonons of momentum d$q_\perp$ perpendicular to the length of the wire at a distance $q_\perp$. In this case, the cross-section surface area in the 2D confined phonons in phonon-momentum space of the wire is equal to $2\pi q \mathrm{d}q_\perp$.

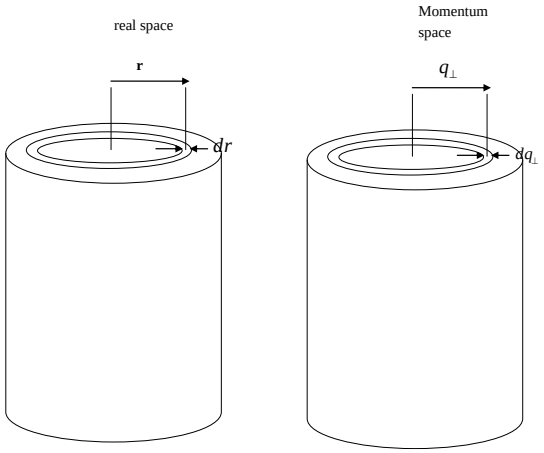


*Figure 7.1*: *Real space and q-space illustration of how the three-dimensional confinement, $d^3q$, is transformed to two-dimensional confinement $2\pi qdq$ in nanowires.*

Following this argument, the Richter equation has been modified to account for the geometry of nano-wires by Piscanec [5] and by Adu *et al.* [6, 7] by changing the $d^3q$ term for a sphere to $2\pi qdq$ for rods:

$$I(\omega) = A_0 \int_{-\infty}^{\infty} \left[ 2\pi q_\perp \frac{exp\left( \frac{q_\perp^2 d^2}{\alpha} \right)}{(\omega - \omega(q))^2 + (\Gamma_0 / 2)^2} \right] dq_\perp \qquad (7.4)$$

Note that the constant $16\pi^2$ has been replaced with a scaling parameter $\alpha$ that can be evaluated during the data fitting. An important result by Battacharyya *et al.*, [8] on the modification of the Richter equation to include size distribution of nano-structures is worth mentioning.

As for quantum dots, it is assumed that these structure are quasi-zero dimensional and hence all the atoms are surface atoms. Therefore, the $d^3q$ term in Richter *et al.*, [4] equation can be replaced by momentum volume of $4\pi q^2 dq$ [5].

$$I(\omega) = A_0 \int_{-\infty}^{\infty} \left[ 4\pi q^2 \frac{exp\left(\frac{q^2 d^2}{\alpha}\right)}{(\omega - \omega(q))^2 + (\Gamma_0 / 2)^2} \right] dq \qquad (7.5)$$

### 7.2.1 PHONON CONFIMENT ANALYSIS

During the choice of the proper model to fit our current Raman spectroscopy results, we reviewed similar work that has been done on Anatase $TiO_2$ previously. Many authors have used the Richter model in equation (7.1):

$$I(\omega) = A_0 \int_{-\infty}^{\infty} \left[ \frac{|C(0,q)|^2}{[\omega - \omega(q)]^2 + (\Gamma o/2)^2} \right] d^3 q \qquad (7.1)$$

For instance, Zhu *et.al,* [15] had crystallite sizes down to 3 nm but had in the Richter model the $d^3q$ term. Wang *et.al,* [16] like Battacharrya [17], they used the Richter model with a prefactor, $A_0$ replaced by an integral of the size-distribution equation. For Anatase quantum dots (particles with diameter less than about 10 nm) the above modification given by the modified Ritcher equation (7.1) is mandatory since for particles with diameter of 6 nm, almost all the atoms are surface atoms. Therefore apart from inclusion of the particle size distribution prefactor, the changing of the $d^3q$ term to $4\pi q^2 dq$ is also necessary. Another problem is that there is no consensus of the appropriate phonon dispersion relation (PDR) ω(q) for Anatase. This equation is not available in literature. Many authors on $TiO_2$ Raman spectroscopy have rather used phonon dispersion curves for Rutile. Some theoretical calculations of the phonon dispersion curve for Anatase were attempted by Mikami [18] but these have to be validated by experimental data. In this work we have used the simple phonon dispersion relation which works for most transitional metal oxides [19] given as:

$$\omega(q) = \omega_0 \pm Baq^2 \qquad (7.6)$$

where ω(q is the PDR, $\omega_0$ is the zone centre frequency in Raman spectroscopy or resonant frequency, and $a$ is a lattice constant for Anatase $TiO_2$

Where $a$ is the lattice constant 0.32 nm for the $TiO_2$ Anatase. The following equation was then fitted to the 6 nm mean diameter quantum dots.

$$I(\omega) = A_0 \int_{L_{min}}^{L_{max}} dL.\rho(L) \int_{-\infty}^{\infty} \left[ 4\pi q^2 \frac{exp\left(\frac{q^2 L^2}{\alpha}\right)}{\left(\omega - \omega_0 \pm Baq^2\right)^2 + \left(\Gamma_0 / 2\right)^2} \right] dq \qquad (7.7)$$

The fitting was performed by activating a "statistical Nonlinear Fit" routine in Mathematica 4.1 and by employing a short subroutine among other supporting commands. The model is presented graphically in Figure 7.2 for the 6 nm C-$TiO_2$ particles

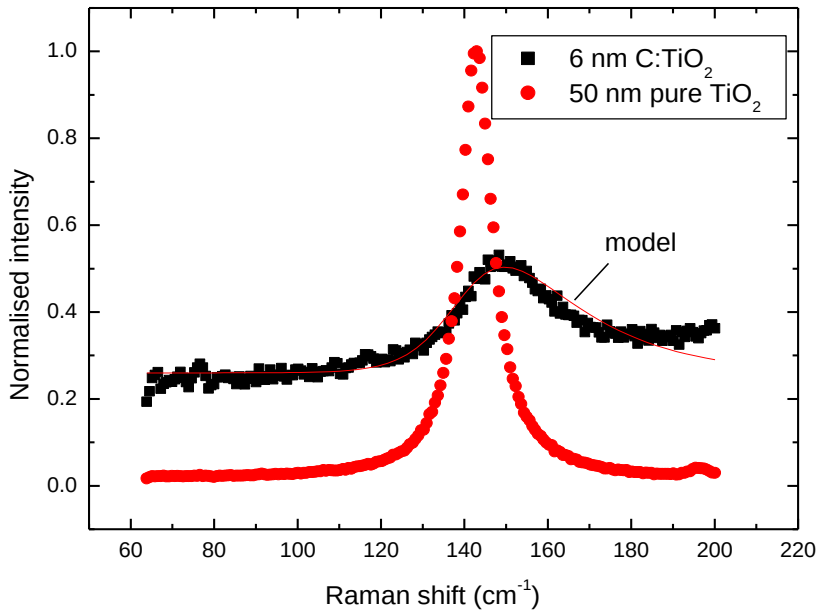


*Figure 7.2: Raman spectroscopy of the C-$TiO_2$ QDs synthesized by PSP technique showing the present confinement model fitted to the 6 nm particles data*

From this fit the following parameters are extracted $A_0$', $\alpha$, $\omega_0$, $B$ and $\Gamma_0$. Most authors have found that $\Gamma_0$ for bulk $TiO_2$ is equal to 7 $cm^{-1}$ and we tabulate our findings alongside the experimental findings from other authors table in Table 7.1.

*Table 7.1: Shows a comparison of the parameters extracted from the present model with those from other authors.*

| $A_0$ | $\alpha$, | $\omega_0$ | $B$ | $\Gamma_0$ | Ref. |
|---|---|---|---|---|---|
| | *25* | *144* | *20 (Rutile)* | *7 Rutile* | Zhu [15] |
| | | *143* | *28* | | |
| | | *142* | *102* | | |
| | | *142.5* | *164* | | *Wang [16]* |
| ***$10^{-17}$*** | ***28*** | ***150*** | ***70*** | ***20 (C-$TiO_2$)*** | ***Taziwa [19]*** |

From this fit the following parameters are extracted $A_0' = 10^{-17}$, $\alpha = 3\ \pi^2$ (~ 30), $\omega_0 = 150.4\ cm^{-1}$, $B = 0.005\ cm^{-2}$ and $\Gamma_0 = 20\ cm^{-1}$. Note that the value of 20 $cm^{-1}$ for $\Gamma_0$ is 13 $cm^{-1}$ above the value for bulk $TiO_2$. Also the size distribution integral in equation in 7.2 has been replaced by an expression $A_1 + m\ \omega = 0.25 + 0.008\ \omega$ to take into account the background noise inherent in the fluorescent nanostructures.

$$I(\omega) = A_1 + m\omega + A_0 \int_{L_{min}}^{L_{max}} dL.\rho(L) \int_{-\infty}^{\infty} \left[ 4\pi q^2 \frac{\exp\left(\frac{q^2 L^2}{\alpha}\right)}{\left(\omega - \omega_0 \pm Baq^2\right)^2 + \left(\Gamma_0 / 2\right)^2} \right] dq \qquad (7.8)$$

These results show that the shift of the central Brillouin zone phonon frequency from 143.4 $cm^{-1}$ for particles of mean diameter of 50 nm of un doped $TiO_2$ to 150.4 $cm^{-1}$ for particles of mean diameter of 6 nm is not only due to reduction of particle size but also could be due to the presence of carbon in the $TiO_2$ structure.

## 7.3 RAMAN SPECTROSCOPY TEMPERATURE ANALYSIS

Several authors have already proved both experimentally and theoretically that bulk, single- and nano-crystalline Anatase $TiO_2$ exhibits six Raman active bands characteristic at around 144, 197, 399, 515, 519, and 639 $cm^{-1}$ with symmetries of $E_{g(1)}$, $E_{g(2)}$, $B_{1g}$, $A_{1g}$, $B_{1g}$, and $E_{g(3)}$ respectively [15-23, 29,]. Figure 7.4 presents the Raman spectra for C-$TiO_2$ nano-particles for our USP synthesized samples.

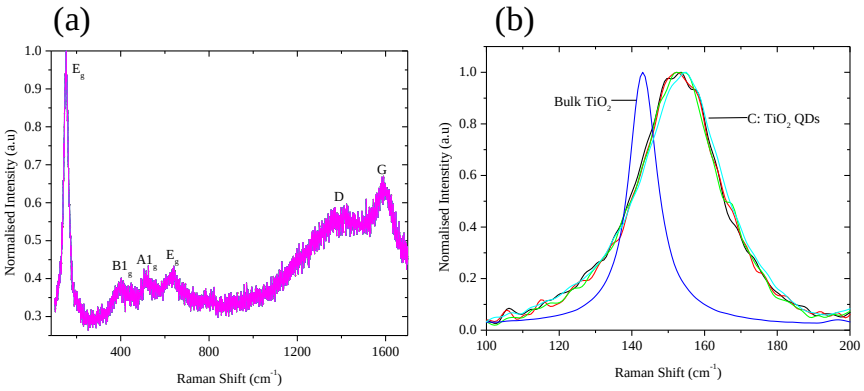


*Figure 7.4:* *(a) Raman spectrum for C-$TiO_2$ QDs synthesized by USP showing the presence of carbon D and G bands in the QD. (b) Illustrates peak shift of the main $E_{g1}$ mode caused by carbon doping and nano-sized effects*

Figure 7.4(a) confirms that the synthesized C-$TiO_2$ nano-particles are also Anatase, with the first $E_{g(1)}$ peak blue shifted to 152. 9 $cm^{-1}$ and broadened with a linewidth of ~20 $cm^{-1}$ as compared to that of bulk Anatase titanium dioxide sitting at 144 $cm^{-1}$ with a smaller FWHM value of ~7 $cm^{-1}$ illustrated here in figure 7.4(b) The broadening and blue shift of the Raman peaks observed in C-$TiO_2$ nano-particles are attributed to either phonon confinement as particle size decrease or non-stoichiometry effects caused by the incorporation of carbon dopants into the titanium dioxide tetragonal structure. It is also interesting to note that whereas the Raman peak for the bulk, single- and nano-crystalline $TiO_2$ show Lorentzian symmetry, the C-$TiO_2$ simulate a Gaussian distribution. The second mode $E_{g(2)}$ at ~204 $cm^{-1}$ is very weak hence it was difficult to be clearly detected. This can be attributed to three factors: a low precursor pH value, low measurement temperature and presence of carbon dopants [25, 15, 32]. Our solution pH was ~2.0 and this

Raman mode is more discernible when higher pH solutions are used (>5.0). At elevated temperatures above 300°C, this peak emerges stronger (for this particle size of 5.5 nm) but blue shifted. The Raman modes $B_{1g}$, the unresolved doublet [$A_{1g}$+$B_{1g(2)}$] and $E_{g(3)}$ are clearly observed in these samples and they are peaked at ~404, ~517, and 629 $cm^{-1}$, respectively.

The temperature dependence of the Raman peak frequencies of the three modes (two $E_g$ modes and one $B_{1g}$ mode) is shown in Figures 7.5, 7.6 and 7.7.

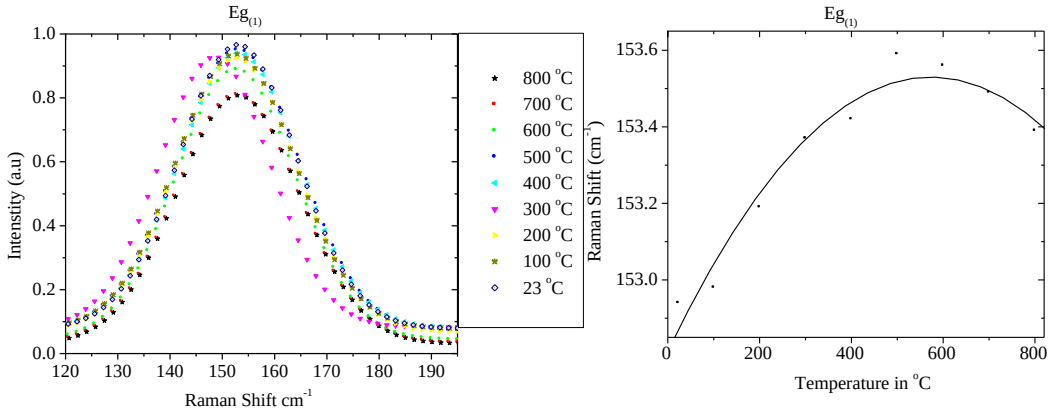


*Figure 7.5: Temperature dependence analysis of Raman peak frequency of the lowest order $E_{g(1)}$ mode in our Anatase C-$TiO_2$*

As displayed in Figure 7.5 the Raman peak of the lowest first order mode $E_{g(1)}$ exhibit a different temperature dependence to that of Anatase $TiO_2$ nano-crystals reported by Wang *et al.* [16] for the same particle size where it was shown that the Raman shift increases linearly in the low temperature regime (100-700 K), then levels off thereafter. Gao has also reported similar results to this for nano-crystals of Anatase $TiO_2$ where it levels off after 700 K [24]. In our case, it is not only linearly increasing from 152.9 $cm^{-1}$ at room temperature and reaches a maximum of 153.57 $cm^{-1}$ at 770 K. Rather than leveling off, it drops down with further increase in temperature. The linearity in the low temperature region has also been observed by Zhu *et al*., [15]. It is difficult to make accurate comparisons with this available data in literature because whereas our measurements covered from room temperature to 1073 K, published results for single- and nano-crystalline $TiO_2$ predominantly covers low temperatures to 800 K. Ohsaka [13] in a much earlier paper however scanned the 20-1100 K and he observed for this peak that the Raman frequency

increased with temperature in the entire range. We also observed a drop in the peak frequency after 770 K registered in these C-$TiO_2$ samples.

Figure 7.6 depicts the Raman temperature dependence analysis of the first order mode $E_{g(3)}$of the as synthesized nano-particle by USP technique.

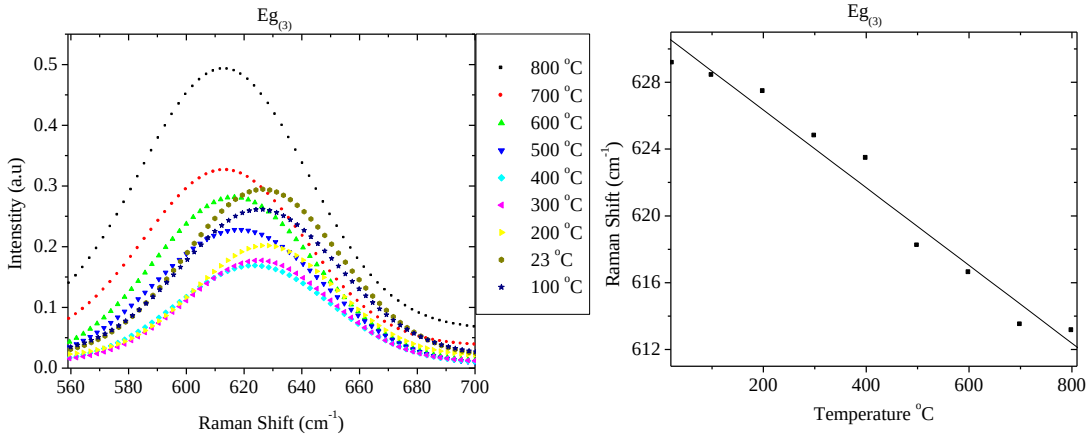


*Figure 7.6: Temperature dependence analysis of Raman shift of the first order mode $E_{g(3)}$ in Anatase C-$TiO_2$ quantum dots indicating a linear decrease with increase in temperature.*

The peak of the $E_{g(3)}$ mode at 629 $cm^{-1}$ at room temperature shifts linearly to lower frequencies with increasing temperature as shown in Figure 7.5. This shift to lower frequencies with temperature was also observed in nano-crystalline $TiO_2$ by Gao [25] and is typical of ionic crystals. On the other hand, the peak frequency temperature dependence of the $B_{1g}$ mode at 404 $cm^{-1}$ depicts rather subtle characteristics as shown in figure 7.6.

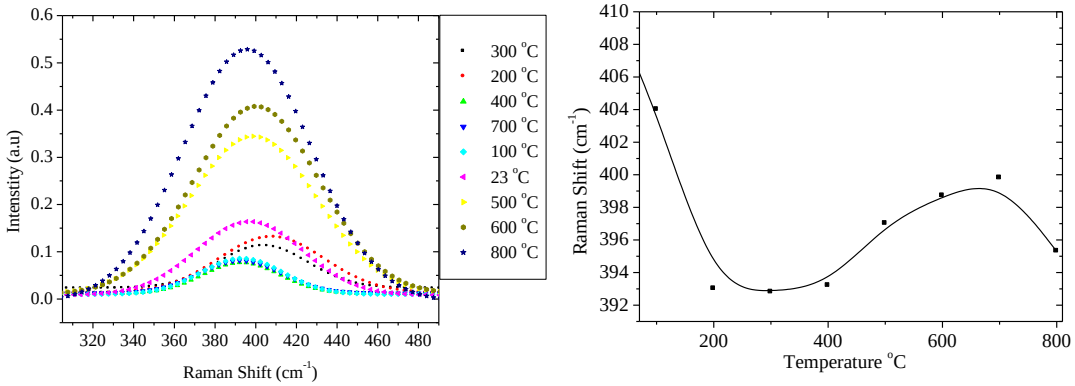


*Figure 7.7: Temperature dependence analysis of frequency shift of first order Raman mode* $B_{1g}$ *in Anatase C-TiO₂ quantum dots showing a somewhat sinusoidal behavior with increase in temperature*

Initially the peak red shifts to lower frequencies from room temperature to 300 $^{o}$C when it reaches the lowest point at 392.8 cm$^{-1}$, then blue shifts to 399.8 cm$^{-1}$ between 300 -700 $^{o}$C and thereafter falls down showing a somewhat sinusoidal variation with rising temperature. This effect can be attributed to the transition of the C-$TiO_2$ polymorph between the Anatase and Rutile phases. A similar analysis was done on nano-crystalline Anatase $TiO_2$ in reference [32]. He showed less complicated temperature dependence in that the peak frequency shifted to high values, reached a maximum, then gradually dropped with further increase in temperature

Most of the published results in literature on temperature dependence of both the Raman peak shifts and Raman line widths of Anatase $TiO_2$ are on single crystalline and nano-crystalline samples where these have been understood to behave differently. A large number of both experimental and theoretical work has gone into probing the temperature dynamics in these materials. In a bid to explain the Raman spectra evolution with temperature, several possible contributory factors and parameters have been considered like phonon confinement, an-harmonic phonon coupling, thermal expansion, surface stress, non-homogeneity of particle-size distribution, composition fluctuations, and defects. Which one of these plays the dominant role depends on the structural characteristics of the nano-particles and their vulnerability to local heating effects. In this work, we focus on the temperature-dependent experimental results

deduced from our C-$TiO_2$ nano-particles or NPs and the salient features they exhibit. Because of the carbon dopants inserted into the $TiO_2$ matrix, the theoretical formulations of, say, the phonon confinement and anharmonic effects take complicated forms, so for now we shall not go into the theoretical details of our results only.

Although the frequency variations with temperature of the Raman modes in Anatase C-$TiO_2$ nano-crystals may seem to illustrate a similar behavior to the corresponding $TiO_2$ single-crystals [20, 21] and nano-particles [15, 16, 25], there are still vivid differences between them. For example, the frequency variation of the lowest-frequency $E_{g(1)}$ mode at ~ 153 $cm^{-1}$ and the $E_{g(3)}$ mode at ~629 $cm^{-1}$ is more linear in single-crystalline $TiO_2$ than in C-TiO2 nano-crystals. Besides, the frequency variation with temperature of the $B_{1g}$ mode in single-crystals attains a maximum at 300 ºC lower than that of nano-crystals. Furthermore, the temperature dependence of the $B_{1g}$ mode in pure $TiO_2$ nano-crystals shows a completely opposite phenomenon to the one we have observed here in C-$TiO_2$ nano-crystals. In single crystals and pure $TiO_2$ nano-particles it shows an increase of frequency with increase in temperature until it reaches a maximum where the frequency tends to decrease with increase in temperature. In our material, we have observed a completely different phenomenon in that we observe a wave-like sinusoidal pattern. The exact root cause of this strange temperature dependence is yet to be understood properly. At this point, aside from the inherent phonon confinement, anharmonic coupling, and thermal effects, perhaps we need to focus on particle size distribution, doping levels, the deviation from stoichiometric and the type of non-stoichiometric effects which can have a critical influence on the Raman spectra.

A closer look at Figure 8.1 in chapter 8 reveals a dotty contrast pattern consisting of spherical islands of varying sizes, some bright and others faint, scattered around the image. The larger features that are ~15 nm in lateral extent may represent individual islands or regions consisting of several islands clustered together. These are similar in appearance to the growth features referred to as self-organised quantum dots. The degree of brightness of the C-$TiO_2$ pseudo-spherical nano-particle may signify the level of doping attached to the nano-particles. Clearly this is a signature of non-uniformity in the structure for carbon doping and stability. Generally, we have three possible ways we can dope the $TiO_2$ lattice with carbon [33]. The first one is to

replace the oxygen atom with the carbon, the second option is replacing the Ti atom with a C. In both these cases, there is breaking of the Ti-O bonds and replacing them with Ti-C or C-O bonds. Theoretical modeling shows that the former is more favorable for oxygen poor conditions. This substitution gives rise to longer and weaker Ti-C bonds in comparison to the original Ti-O bonds. In this configuration, the C atom is reduced. On the other hand, for the latter case where a C atom replaces one Ti atom, this does not change the valence electron configuration because these two atoms have the same number of valence electrons. Nonetheless even though the number of the valence electrons is the same, the hybridization of the 3d, 4s, and 4p orbitals will give rise to different coordination numbers since while the Ti is six-coordinated in Anatase, the substitutional C is four-coordinated. This will cause deformations in the Anatase structure because the carbon impurity assumes a tetrahedral geometry with the C-O being more shorter than the Ti-O bonds and also the remaining two O atoms' coordination is reduced to two from the three-fold before the substitution. In this case the oxidation state of C is positive having replaced the Ti atom, and gives away the four electrons to the lattice oxygens resulting in partly covalent bonds. The third one is when C atoms stabilizes in interstitial positions and because of the small size of the C atom, this occurs without inducing any strain in the structure. Here inclusion of, say, one C atom in an interstitial position of the anatase unit cell leads to the formation of three C-O bonds involving the C dopant and three lattice oxygens. In this case, carbon is oxidized and strongly forms covalent bonds with the O atoms. It's also possible that the C-substitutional configuration can transform into a C-interstitial one where we suppose that a C atom occupying a lattice oxygen position is displaced to an interstitial position with the simultaneous filling of the oxygen vacancy created by an O atom corresponding to an oxidation reaction. In fact theory [33] shows that in Anatase there is strong preference for the carbon to be oxidized and binds to the O lattice ions over being reduced by binding to Ti lattice ions because the C-O bonds are stronger than the Ti-C bonds and depending on whether there is an oxygen-rich or oxygen-poor environment. This complex structural dynamics in carbon doped $TiO_2$ means that the stoichiometry of the sample consists of both substitutional and interstitial carbon species in different amounts. In other words, a reduced $TiO_2$ sample rich in oxygen vacancies will favour inclusion of carbon in substitutional lattice positions initially occupied by O atoms and an oxized $TiO_2$ sample will favour C atoms in interstitial positions. These fluctuations in bond type and bond strengths will introduce several strange additional vibrational modes. The

room temperature shift in the Raman peak frequency of the Anatase C-$TiO_2$ nano-particles from the un-doped nanocrystalline Anatase $TiO_2$ value is ~ +8, +5 and -10 $cm^{-1}$ for the $E_{g(1),}$ $B_{1g}$ and $E_{g(3)}$ modes, respectively, where the positive is a blue-shift and negative a red-shift and the error margins for these measurements was ~ $\pm$0.5 $cm^{-1}$. Maximum peak shifts with temperature from their room temperature values is ~0.7, 11 and 7 $cm^{-1}$ for the Eg(1), B1g and Eg(3) modes, respectively. Despite the fact that these are small values, the pattern in Figures 7.4, 7.5 and 7.6 are very clear. Except for Eg(3) which red-shifts with increasing temperature as observed in undoped samples [3,25], the former two modes exhibit both red- and blue-shifts with increasing temperature. Alternatively from Figures 7.4, 7.5 and 7.6, one can observe that there is a sharp frequency shift in the second lowest Raman mode $B_1g$ upon increasing temperature as compared to the response of peak shift for the $E_{g1}$ mode at 152.9 $cm^{-1}$ and to that of the $E_{g(3)}$ mode at 627 $cm^{-1}$. This is a completely different behavior to what has been observed by Kun Gao, [24] where they observed for the bulk pure $TiO_2$ where they saw a sharp frequency shift for the highest Raman active mode at 628 $cm^{-1}$ as compared to the $B_{1g}$ mode and lowest $E_{g1}$ mode. This might be due to complete change of material property due to quantum confinement effects, size effects and non stoichiometry effects caused by the depletion of oxygen in the C-$TiO_2$ nanoparticles we synthesized.

Another interesting aspect revealed by Raman spectroscopy is it's sensitivity to the mechanical and electrical properties of the investigated materials [21] such that two kinds of situations influence the spectra: (i) parameters acting on the mechanics such as atomic mass, bond strength or the system geometry (like interatomic distances, atomic substitutions) do set the peak positions representing the eigen-frequencies of matter vibrations, and (ii) parameters acting on the charge transfer (iono-covalency, band structure, electronic insertion) set up intensity levels on the basis of the vibration-induced charge variations occurring at the bond scale. So the complex pattern of the Raman peak frequency variations with temperature makes its analysis very difficult. Moreover, because of the carbon dopants, the nano-particles do not possess compositional or structural homogeneity: diagonal and non-diagonal disordered nano-particles are distributed within the samples. The complexities inherent in these heterogeneous systems are associated with strain and chemical or diffusive effects due to the low binding carbon constituents. Problems related to inter-diffusion of $Ti^{2+}$ cation species and the tetragonal

attachment of carbon on $TiO_2$ result in changes to the composition of the nano-particles. In the low growth temperature regime (250-350 $^0$C) the lattice parameter effect is not supposed to predominate, in that contributions from the thermal expansion effects may be considered negligible. Thus a combination of particle-size, doping and non-stiochiometric changes may be the major contributing factors in that as the temperature goes up, these parameters are greatly affected due to increased thermal agitations. It is also known that the frequency shifts to Raman modes with temperature at constant pressure can be ascribed to a pure-volume contribution resulting from thermal expansion and a pure temperature contribution resulting from anharmonic effects [16]. Thus to theoretically model these results would require not only inclusion of phonon confinement and anharmonic effects but also the doping nature and the accompanying inherent non-stoichiometric effects that arises in these doped structures need to be taken into account.

Turning our attention to the peak widths, the temperature dependent results are shown in Figure 7.8. Figure 7.9 depicts the temperature dependence of peak width and peak height for the lowest Raman mode $E_{g1}$.

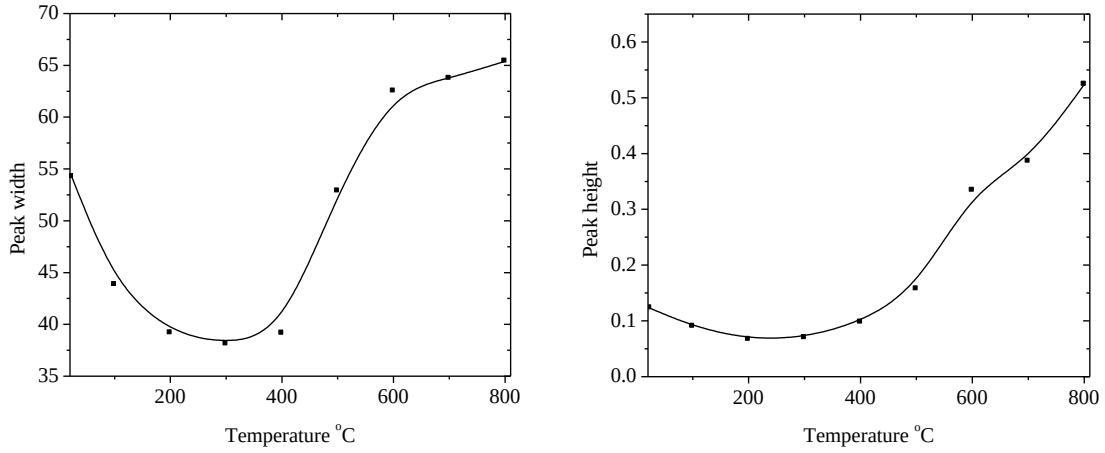


*Figure 7.8: Temperature dependence of peak width and peak height for the lowest $E_{g(1)}$ mode*

As can be seen in Figure 7.8 depicts, the line width of the lowest frequency $E_{g(1)}$ mode at room temperature of the as-prepared C:$TiO_2$ nano-particles was obtained to be 20 cm$^{-1}$ larger than the 7 cm$^{-1}$ reported for the Anatase single-crystals [25,30,31]. Its temperature-dependence reveals line narrowing from room temperature to300 $^o$C at which it reaches its lowest value, then the line

broadens as the temperature is further increased up to 600 $^{o}$C after which it appears to level off from 600 – 800$^{o}$C. Maximum change in linewidth with temperature is ~28 cm$^{-1}$ compared to about 5-9 cm$^{-1}$ reported in undoped nano-crystalline Anatase $TiO_2$ [29, 16, 33].

The broadening of this mode is usually ascribed to the phonon confinement effects, size effect, and non-stoichiometry effects. As the grain size decreases phonon momentum selection rule $\boldsymbol{q}$ = 0 breaks down as the phonons are confined in space and all the phonons over the Brillouin zone will contribute to the first order Raman spectra leading to the broadening of the lowest-frequency $E_{g(1)}$ mode of Anatase C-$TiO_2$ nano-crystals. However the magnitude of the change leads us to further conclude that phonon confinement effects may not be the major factor for this temperature behaviour. We suspect the interplay between the temperature-dependent anharmonic effects, doping, and resulting non-stoichiometry in the material play a critical role [29].

Figure 7.9 shows the Raman temperature dependence of the Eg(3) mode at 629 $cm^{-1}$.

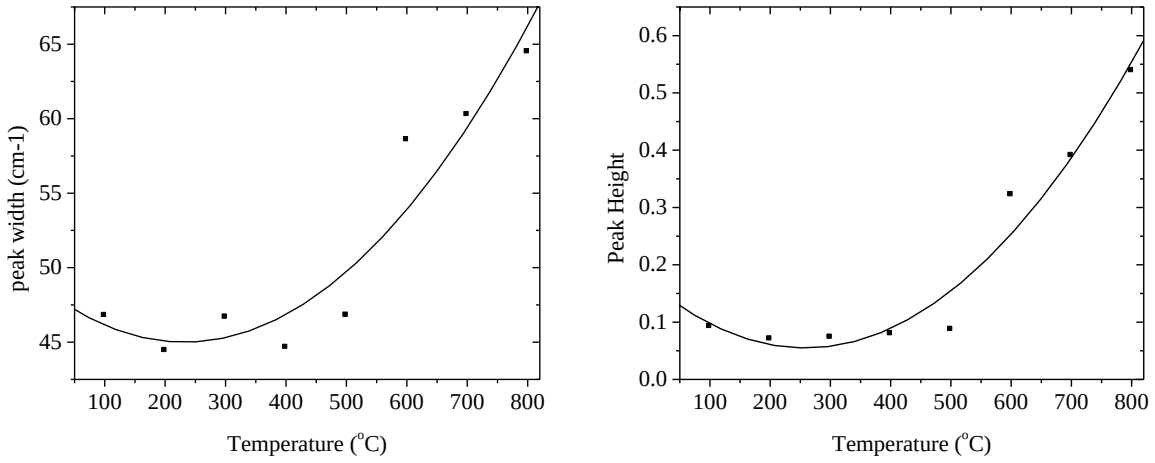


*Figure 7.9: Temperature dependence of peak width and peak height for the lowest $E_{g(3)}$ mode*

For the $E_{g(3)}$ mode at 629 $cm^{-1}$ shown above in Figure 7.9, its linewidth temperature dependence shows a general line broadening with increase in temperature just like reported by Gao [30] and Ohsaka [21] in pure Anatase single- and nano-crystals, respectively. Maximum deviation from room temperature value is of the order of 17 $cm^{-1}$ compared to about 27 $cm^{-1}$ and 53 $cm^{-1}$ for the quoted un-doped samples. This means that line broadening in the $E_{g(3)}$ peak with increased temperature is more pronounced in the pure samples than in the doped ones whereas for the $E_{g(1)}$ it is the exact opposite.

Figure 7.10 depicts the Raman temperature dependence analysis of B1g mode.

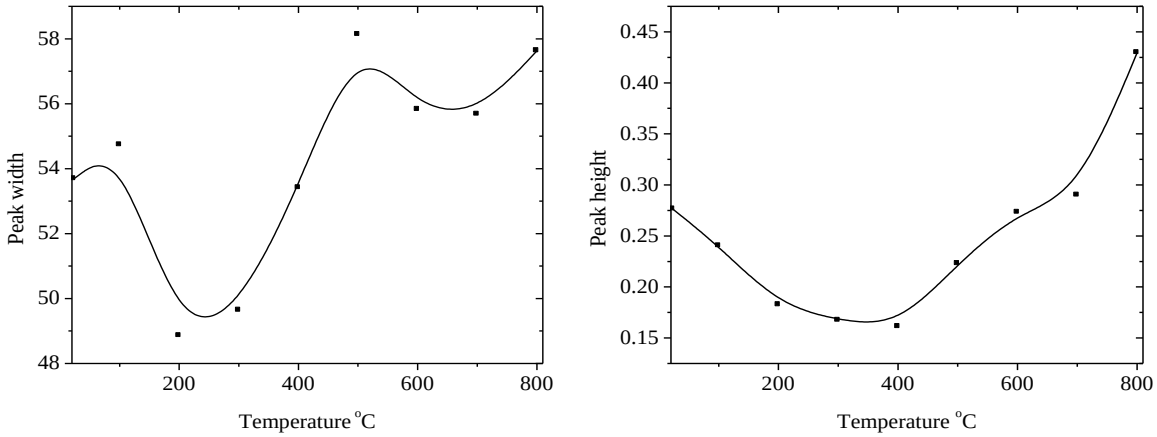


*Figure 7.10: Temperature dependence of peak width and peak height for the lowest $B_{1g}$ mode*

The temperature dependence of the peak width of $B_{1g}$ mode at 404 $cm^{-1}$ reveals strange characteristics like those seen in the temperature dependence of its peak frequency (Figure 7.6) displaying an oscillatory variation with linewidth variations with temperature of 5-10 $cm^{-1}$ compared to about 13 $cm^{-1}$ and 45 $cm^{-1}$ reported for un-doped single-crystals and nano-crystallite $TiO_2$. It is reported that the weakness of these two modes $B_{1g}$ and $E_{g(1)}$ indicate the lack of short-range order in Anatase $TiO_2$ nano-crystals [30, 31, 33]. Thus, the broadening of the two modes may mainly be ascribed to the non-stoichiometry in nano-crystals.

Table 7.2 clearly shows that carbon-doped nano-crystalline $TiO_2$ Raman peaks are very broad compared to their single- and nano-crystalline counterparts

*Table 7.2: Room temperature Raman linewidth values (in $cm^{-1}$) for the three lower energy modes for single crystalline (sc), nano-crystalline (nc) and C-$TiO_2$*

| | sc-$TiO_2$ | nc-$TiO_2$ | nc-C-$TiO_2$ |
|---|---|---|---|
| $E_{g(1)}$ | 0.4 | 13 | 54 |
| $B_{1g}$ | 5 | 17 | 53.7 |
| $E_{g2}$ | 6.5 | 22 | 47.5 |

The peak widths of all of the three Raman modes general increase approximately linearly with temperature. As we should expect, single crystals give sharp Raman peaks with Lorenztian lineshapes. Because of fluctuations in the particle size distribution, the nano-crystalline samples result in broadened spectral lines compared to their equivalent single crystalline samples. From the comparison, we can deduce that doping appears to play a significant role given the substantial increase to the spectral linewidth it has brought in. Aside from the contributory factors such as phonon confinement, thermal expansion, anharmonic phonon coupling, particle-size distributions and surface stress that are known to influence the temperature dependence of the Raman spectra, the nature and degree of doping, and the inherent non-stoichiometry that results must also be important parameters that need to be taken into account in explaining the temperature dynamics. Values for sc- and nc-$TiO_2$ were obtained from [15, 16, 32 and 25].

On the Raman peak intensity, the right hand sides of figures 7.8, 7.9 and 7.10 give the temperature dependence results of our samples. Here for the three modes, $E_{g(1)}$, $B_{1g}$ and $E_{g(3)}$, the peak height linearly or sub-linearly increases with temperature. This is as expected because the laser light interacts with molecular vibrations, rotational, and other low-frequency excitations in a system so that an increase in temperature results in more phonons being excited: i.e., the phonon number increases strengthening crystal-phonon coupling which tends to reinforce the Raman scattering processes hence the superior signals. Another factor that will set intensity are the parameters acting on the charge transfer (like iono-covalent, band structure, etc.) on the basis of the vibration-induced charge variations occurring at the very bond scale [30-32]. The presence of mobile charge carriers in ionic conductors can be revealed by temperature dependence of the intensity of the Raman bands because of strong crystal-phonon coupling. However, we must

concede that analysis of the temperature dependence of the peak intensities was a bit complicated because firstly, the $Ar^+$ ion laser source output was not stable hence there were fluctuations with time in the excitation beam power due to fluctuations in the electrical supply. Secondly, it was observed that the sample head shifts with increasing temperature due to expansion effects. This caused slight spatial shifts in the position of the beam spot on the sample surface resulting in the smearing of the excitation flux into neighboring areas instead of the fixed and preferentially selected measuring spot. Nonetheless, from the foregoing, we observe a general increase of the Raman intensity with increasing temperature in all the three modes.

## 7.4 CONCLUSION

### 7.4.1 PHONON CONFINEMENT ANALYSIS

It has been shown that phonon confinement by means of Raman spectroscopy was observed in C-$TiO_2$ quantum dots and the phonon confinement models available in literature have been used to obtain for the first time phonon dispersion relations of C-$TiO_2$ quantum dots. Also a new phonon confinement model was derived and fitted to C-$TiO_2$ data.

During the choice of the proper model to fit our current Raman spectroscopy results, we used the PDR that works for most transitional metal oxide and we also used a modified form of the Ritcher equation (eq.7.4) which incorporates a particle size distribution factor equation , The fitting was performed by activating a "Statistics Nonlinear Fit" routine in Mathematica 4.1 and by employing a short subroutine among other supporting commands: From this fit the following parameters are extracted $A_0' = 10^{-17}$, $\alpha = 3\,\pi^2$ (~ 30), $\omega_0 = 150.4$ $cm^{-1}$, $B = 0.005$ $cm^{-2}$ and $\Gamma_0 = 20$ $cm^{-1}$. Note that the value of 20 $cm^{-1}$ for $\Gamma_0$ is 13 $cm^{-1}$ above the value for bulk $TiO_2$. Also the size distribution integral in equation in 7.1 has been replaced by an expression $A_1 + m\,\omega = 0.25 + 0.008\,\omega$ in equation 7.2 to take into account the background noise inherent in the fluorescent nanostructures. Also the results have shown that the blue-shift of the central Brillouin zone phonon frequency from 143.4 $cm^{-1}$ for particles of mean diameter of 50 nm of pure $TiO_2$ to 150.4 $cm^{-1}$ for particles of mean diameter of 6 nm is not only due to reduction of particle size but also could be due to the presence of carbon in the $TiO_2$ structure.

### 7.4.2 RAMAN TEMPERATURE DEPENDENCE ANALYSIS

Room temperature Raman spectroscopy was done for the first time on C-$TiO_2$ and it revealed that the as-synthesized nano-particles are predominantly Anatase with the $E_{g(1)}$ at 152.9 $cm^{-1}$ blue shifted due to carbon doping and decrease in particle size. Raman temperature dependences analysis has been done for the modes $E_{g(1)}$, $B_{1g}$ and $E_{g(3)}$ from room temperature up to 800$^{\circ}$C and these three modes have shown rather different temperature dependence. The temperature dependence analysis of $E_{g(1)}$ has shown an initial increase in frequency with increase in temperature [100-450 ºC], until a critical temperature of 450 ºC, after which there was a decrease in Raman shift this has been attributed to change of phase of Anatase to Rutile. We have also shown that the peak width of the as synthesized nano-particles at room temperature is far much larger than that of bulk, single- and nano-crystalline Anatase un-doped $TiO_2$. We conclude that the type and nature of the doping, and the resulting stoichiometric disorder are key for a full description of the temperature dependence of the Raman spectra. This is the first time that temperature dependence of Anatase C-$TiO_2$ is being reported.

## 7.5 REFERENCES


1. Faucet H.; Campbell P. M. *Solid State Commun*. **1986**, 58, 739
2. Mwakikunga, B.W.; Forbes, A.; Sideras-Haddad, E.; Arendse, C.; 2008 *Phys. Stat. Solidi* (a), 205, 150
3. Bersani D.; Lottici, P.P.; Ding X.Z.; *Appl. Phys. Lett*.;**1998** 72, 73
4. Richter H.; Wang Z. P.; Ley L.; *Solid State Commun*. **1981**, 39, 625
5. Piscanec S.; Cantoro M.; Ferrari A.C.; Zapien J.A.; Lifshitz Y.; Lee, S.T.; Hoffmann S.; Robertson J. *Phys. Rev. B.* **2003**, 68, 241312
6. Adu K.W.; Gutierrez H.R.; Kim U.J.; Sumanasekera G.U.; Eklund P.C. *Nano Lett.* **2005**, 400
7. Adu K.W.; Gutierrez H.R.; Eklund P.C. *Vibrational Spectroscopy*. **2006**, 42 165-175
8. Bhattacharyya S.; Samui S. *Appl. Phys. Lett*. **2004**, 84, 1564

9. Arora, A. K.; Rajalakshmi, M.; Ravindran, T. R.; Sivasubramanian, V.; *J. Raman Spectrosc.* **2007**, 38, 604
10. Katumba, G.; Mwakikunga, B.W.; Mothibinyane, T.R.; *Nanoscale Res Lett.*, **2008** 3, 421
11. Sideras-Haddad, E.; Schenkel, T.; Shrivastava, S.; Makgato, T.; Batra, A.; Mwakikunga, B.W, Erasmus, R.; Persaud, A.; *Nucl. Instrum. & Methods in Phys Res* (submitted 2008
12. Mwakikunga, B. W.;. Sideras-Haddad, E.; Witcomb, M.; Arendse, C.; Forbes, A.; *Nanoscale Res. Lett*.; **2008**, 3, 372
13. Roca U.; Rentschler T.J. *J. Solid State Chem*. **1999,** 143, 210
14. Zhu, K. R.; Zhang, M. S.; Chen, Q.; Yin, Z..; *Phys. Lett. A.* **2005**, 340, 220
15. Wang, D.; Zhao, J.; Chen, B.; Zhu, C.; *J. Phys.: Condens. Matter*, **2008**, 20, 085212
16. Bhattacharyya, S.; Samui, S.; *Appl. Phys. Lett*. **2004**, 84, 1564
17. Mikami, M.; Nakamura, S.; Kitao, O.; Arakawa, H. *Phys. Rev. B*. **2002**, 66, 155213
18. Tuistra F.; Koenig J.L. *J. Chem. Phys*. **1970**, 53, 1126-1130
19. Taziwa R.; Meyer E.L.; Chinyama K.G. *Journal of Material Science*. **2012**, 47, 1531-1540
20. Tiong K.K.; Amirtharaj P.M.; Pollak F.H.; Aspnes D.E. *Appl. Phys. Lett*. **1984**, 44, 122-128
21. Xiong Qihua.; Wang Jinguo.; Reese O.; Lew Yan Voon L.C.; Eklund P.C. Nano Letters. **2004**, 4(10), 1991-1996
22. Tang H.Y.; Zhang Y.F.; Peng H.Y.; Wang N.; Lee C.S.; Lee S.T. *Chemical Physical Letters*. **1999**, 314, 16-20
23. Ohsaka, T.; Izumi, F.; Fujiki, Y.; *J Raman Spectrosc*. **1978**, 7, 321
24. Du, Y.L.; Deng, Y.; Zhang, M.S.; *Journal of Physics and Chemistry of Solids* **2006**, 67, 2405-2408
25. Balaji, S.; Djaoued, Y.; Robichaud, J.; *J. Raman Spectrosc* **2006**, 37, 1416-1422
26. Gao, K.; Physica B **2007**, 398, 33-37
27. Stefanocich, G.; Pergament, A.; Stefanovich, D.; *J. Phys. Condens. Matter* **2000**, 12, 8837
28. Gunn, J.B.; Solid State Commun. 1 **1963**, 88
29. Cope, R.G.; Penn, A.W.; Britt, J.; *Appl. Phys. (J. Phys.*D) **1968**, 1, 162
30. Fujimori N.; Imai T.; Doi A. *Vaccum*. **1986**, 36(1-3), 99-102

31. Valetin CD, Pacchioni G, Selloni A **2005** *Chem. Mater*. 17: 6656-6665.
32. Colomban PH, Lucazeau G **1980** *J. Chem. Phys*. 72: 1213
33. Colomban PH, Mercier R, Lucazeau G, *J. Chem. Phys*. **1981** 75, 1388

# CHAPTER 8

# STRUCTURAL, OPTICAL AND ELECTRICAL ANALYSIS OF C-$TiO_2$ QDs

## 8.1 INTRODUCTION

This chapter starts off by providing comparative analysis on structural, optical and elemental properties of the carbon doped titanium (C-$TiO_2$) quantum dots (QDs) synthesized by both ultrasonic spray pyrolysis (USP) and pneumatic spray pyrolysis techniques (PSP). The results and analysis of this chapter has been published in the peer reviewed journals in the appendix section of the thesis and more recently at the 2012 South African Institute of Physics (SAIP) conference where it received the award for the best PhD poster presentation.

## 8.2 STRUCTURAL CHARACTERIZATION

### 8.2.1 HRTEM RESULTS USP SAMPLES

Figure 8.1 shows the high resolution transmission electron microscopy (HRTEM) image of the C-$TiO_2$ quantum dots synthesized by ultrasonic spray pyrolysis technique (USP)

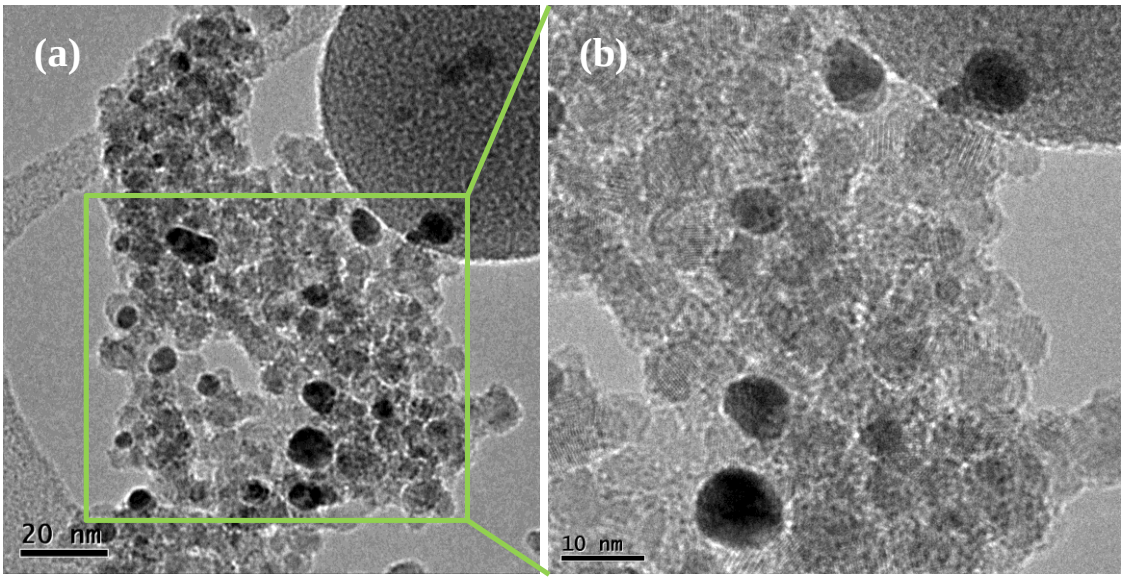


*Figure 8.1: (a) HRTEM image of C-$TiO_2$ QDS synthesized on F: $SnO_2$ glass substrates using USP technique, (b) also showing the same sample on a different spot.*

It is evident from the Figure 8.1 that the synthesized QDs comprise of mostly spherical nano-particles. Some QDs appear as dark spots of agglomerated and over layered nano-structures, as shown in Figure 8.1 (a). Figure 8.1 (b) shows a higher magnification of the green rectangle in Figure 1 (a). Figure 8.2 shows the associated size distribution of the particle size with the most probable particle size being 3.11±0.02 nm.

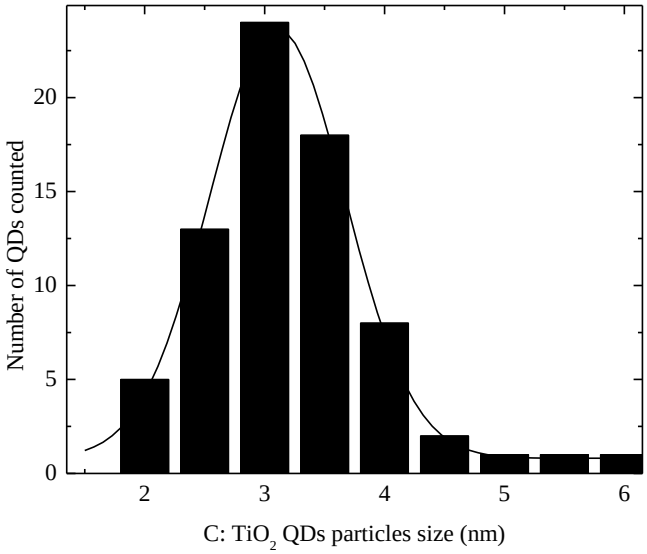


*Figure 8.2*: *A histograms showing particle size distribution with the most probable size being 3.11±0.02 nm for USP*

At even higher magnification, the HRTEM image in Figure 8.3 (a) clearly reveals that the USP synthesized C-$TiO_2$ QDs have a much smaller lattice spacing of 0.202 nm as compared to the bulk Anatase spacing of 0.352 nm. It has been reported that in synthesis of carbon doped Zinc oxide (C-ZnO) nano-particles where carbon (C) atoms from the dopant substitutes the oxygen atoms (O). It has observed that the ***d*** spacing of the C-ZnO decreased as compared to that of un doped ZnO [1]. Therefore we can conclude in our C-$TiO_2$ QDs the d spacing also decreased which confirms substitutional carbon doping in our C-$TiO_2$ QDs. Substitutional carbon doping is beneficial in increasing the UV-Visible absorption of C-$TiO_2$ QDs into the visible section of the solar spectrum. It is well known that subsititutional carbon doping introduces impurity energy level above the valence band (VB) of $TiO_2$ hence reduce the amount of energy required to excite an electron from the VB to the conduction band (CB) via the introduced intermediate state. Hence the synthesized C-$TiO_2$ QDs can be used as solar absorbers in photochemical solar cells or be used as effective photo catalyst for water and air purification and for self-cleaning surfaces.

The Fast Fourier Transform (FFT) of the image, Figure 8.3 (b) display a crosslike figures synonymous to the selected area electron diffraction, display the fact that only the main diffraction (reflection) plane of Miller indices (101) in $TiO_2$ [2] is responsible for diffraction pattern that gives rise to the HRTEM images.

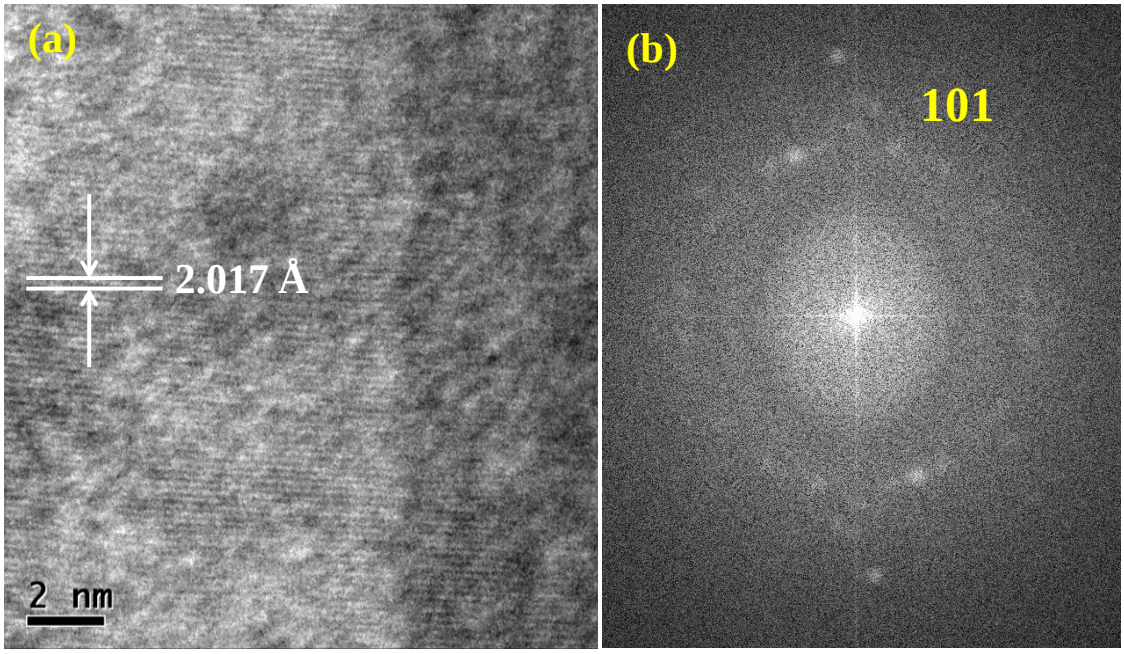


*Figure 8.3*: *(a) HRTEM of the USP C-$TiO_2$ QDs evident with a fringe separation of 2.017 Å (b) FFT of the high resolution image showing the reflection from the predominant (101) plane of the $TiO_2$ lattice.*

### 8.2.2 HRTEM RESULTS PSP SAMPLES

C-$TiO_2$ QDs were also synthesized by pneumatic spray pyrolysis technique (PSP) on F-SnO2 glass substrates. Figure 8.4 (a) shows the HRTEM of the C-$TiO_2$ QDs synthesized by PSP and Figure 8.4 (b) gives a histogram of particle size distribution. Soft image analysis has revealed that as synthesized C-$TiO_2$ QDs had a mean particles size of 5.5 nm as illustrated by the histogram of particle size distribution in Figure 8.4 (b). As compared to the USP synthesized C-$TiO_2$ QDs which had a modal particle size of 3.11 nm. The PSP synthesized C-$TiO_2$ QDs had a larger particle size and wider particle size distribution (1.5-9 nm). This can be attributed to mechanism of droplet generation. In USP Capillary wave mechanism of droplet generation dominates as the main mechanism of droplet generation. Whilst in PSP the Cavitation mechanism is the main mechanism of droplet generation. In PSP the generated droplets have high potential and kinetic energy resulting in high probability of two or more droplets conglomerating and consequently forming varying and large size particle sizes.

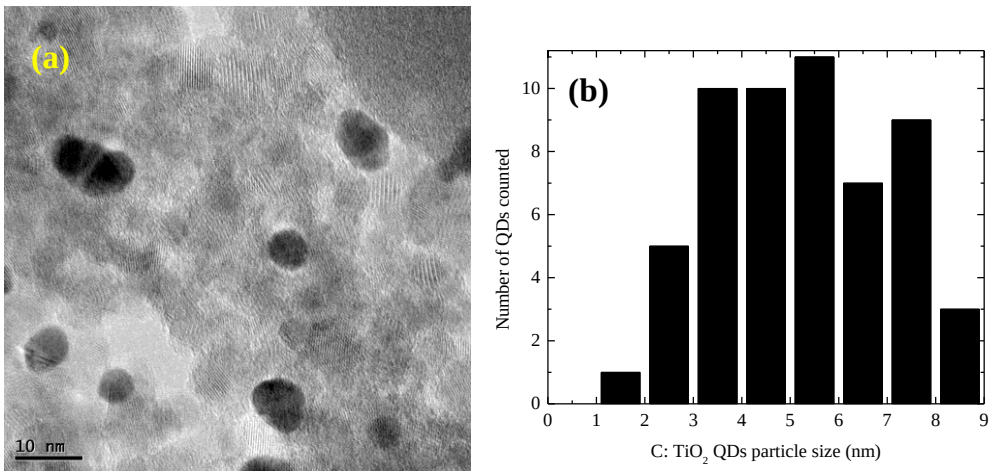


*Figure 8.4: (a) HRTEM image of C-$TiO_2$ QDs synthesized on F: $SnO_2$ glass substrates using PSP technique (b) A histograms showing particle size distribution with the most probable crystal size at 5.5 ± 0.02 nm for PSP.*

It is also notable that most nano-particles synthesized by PSP are not entirely spherical Figure 8.4. These oval ‘‘egg’’ like particles might be the new shape forming after coalescing. In PSP

there is no complete control of droplet shape and size unlike in USP, where the droplets generated has less momentum and less kinetic energy. One of the reason that also contributed to the variation of droplet size could be the fact that the air pumping rate of the pneumatic pump was not constant and this could not be controlled unlike in USP where the frequency *f* of the nebulizer is full controllable. This uncontrollable droplet formation could be one of the reasons why we found high number of clusters in the PSP as compared to the USP samples.

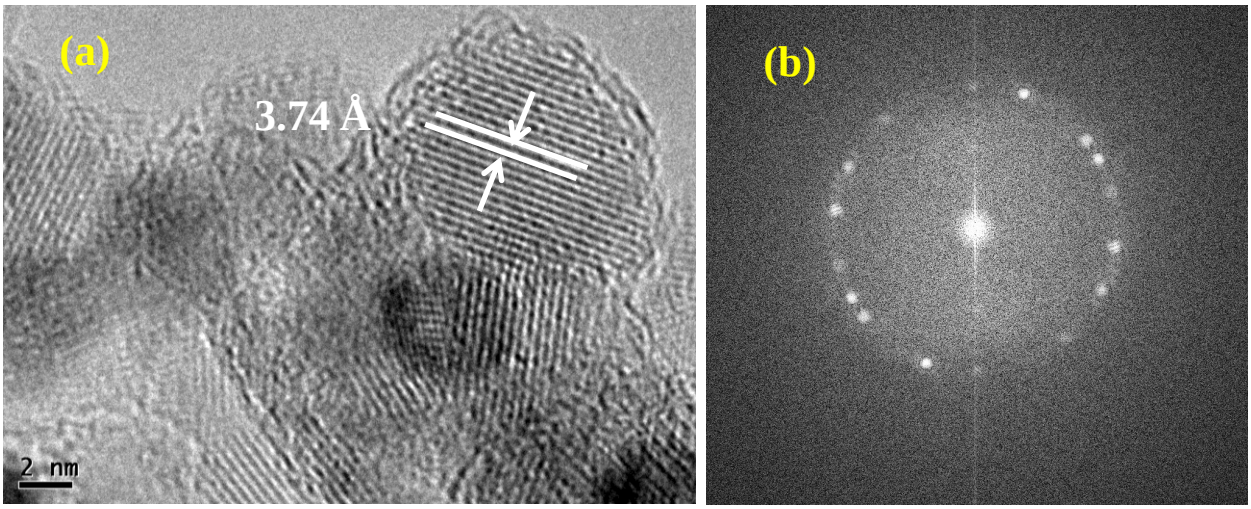


*Figure 8.5: (a) HRTEM of the PSP C-$TiO_2$ QDs. (b) is the FFT of the high resolution image showing the reflection from the predominant (101) plane of the $TiO_2$ lattice from a number of particles in the high resolution image.*

The Fast Fourier transform (FFT) of the images, synonymous to the selected area electron diffraction, display the fact that only the main diffraction (reflection) plane of Miller indices (101) in $TiO_2$ is responsible for diffraction pattern. In the PSP sample, the particles with the same Miller indices are oriented in different directions. This is why their spots on the FFT image Figure 8.5 (b) give a circle of uniform radius which is indexed to the (101) plane.

Figure 8.6 shows a histogram of interplanar *d* spacing of the as synthesized C-$TiO_2$ QDs synthesized QDs. HRTEM analyses also show the PSP synthesized C-$TiO_2$ QDs have a interplanar *d*-spacings whose distribution indicating that some particles have their *d*-spacings of 0.352 nm. In fact, most of the particles have most probably ***d-*** spacing of 0.374 nm in agreement with the Anatase $TiO_2$ as found by Howard *et al.*, [3]. It has been observed, especially in ZnO,

that carbon doping, where C substitutes O, tends to reduce the *d*-spacing of the C: ZnO [1]. It can therefore be concluded that those C-$TiO_2$ QDs that show large *d*-spacings that is less than that of pure Anatase observed in PSP samples have interstitial carbon doping as presented in Figure 8.6. The larger *d*-spacings suggest interstitial C doping as seen in some particles in the PSP sample. We can therefore speculate that USP is a more efficient technique for incorporating carbon uniformly in the $TiO_2$ matrix.

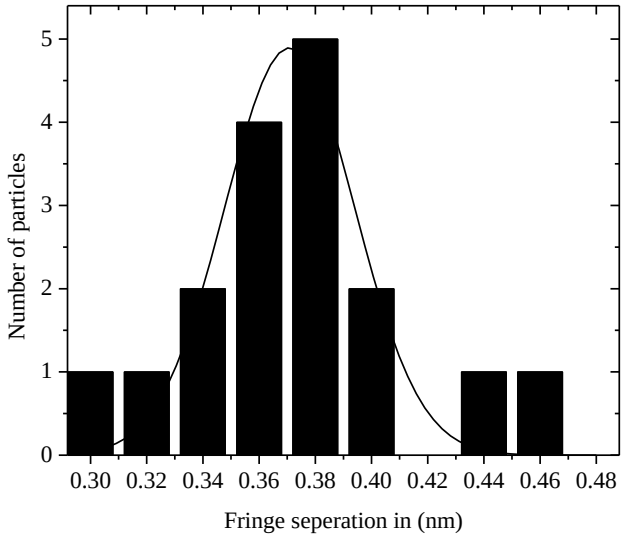


*Figure 8.6: Fringe separation distribution of the PSP C-$TiO_2$ QDs.*

## 8.3 ELEMENTAL ANALYSIS

### 8.3.1 EDS RESULTS USP

Figure 8.7 shows the energy dispersive spectrum (EDS) of C-$TiO_2$ QDs synthesized with USP technique. The presence of Ti, O, and C signifies the purity of the obtained samples. The doping effect of $TiO_2$ QDs is further observed by the elemental analysis from EDS which revealed the presence of carbon on the EDS spectrum. Cu peaks and *some* C intensity came from the carbon-holey copper grids used sample preparation. Interesting to note is that some Ti peaks are

overlapping with oxygen peaks. The presence of impurities such as Si and Ni might have originated from the quartz tube used as a heated reactor zone, since the same quartz tube was used previously used for nickel oxide thin film synthesis. Notable from the EDS is the absence of chloride peak (chloride originating from the precursor solution $TiCl_4$) on all EDS which confirms the complete conversion of titanium chloride into titanium dioxide.

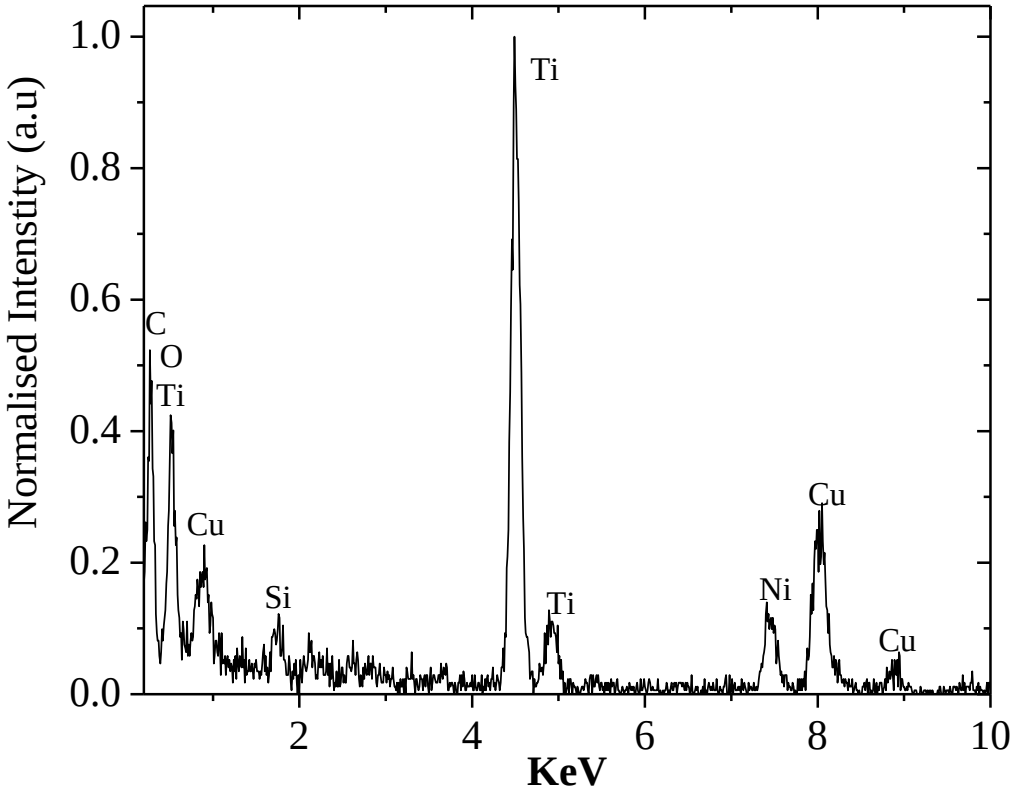


*Figure 8.7: The EDS analyses of the sample area in, Figure 8.1*

### 8.3.2 EDS RESULTS PSP

Figure 8.8 shows the EDS of the PSP synthesized C-$TiO_2$ QDs. The EDS shows the existence of Ti, C, O elements in addition to other elements such Cu (from the holey copper grids used in sample preparation in HRTEM analysis) and Ca, which could have originated from the F:SnO2

glass substrates. Interesting to note also like the USP synthesized samples the EDS clearly reveals that titanium atom has different oxidation states. This is due to different binding energies of the core electrons as shown by different positions on the spectra. The First peak of titanium at 0.52 KeV that is overlapping with oxygen might be due to high oxidation state Ti(IV) and the other peaks at 4.2 KeV that is due to titanium in oxidation state of plus three, Ti(III). The decline in oxidation state is due to doped carbon. the EDS analyses has also revealed the presence of carbon on the EDS spectrum Cu peaks and *some* C intensity came from the carbon-holey copper grids used in these experiments of EDS spectra.

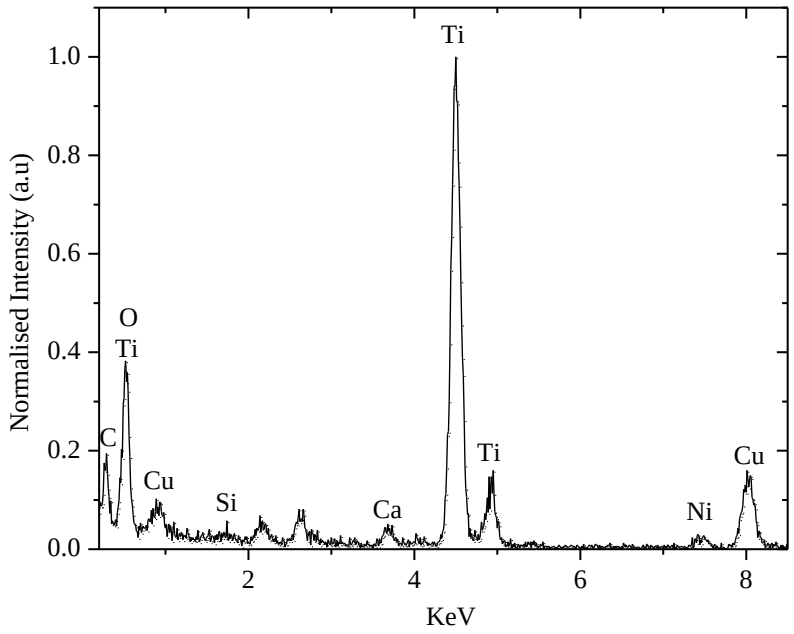


*Figure 8.8: EDS of C-$TiO_2$ QDs synthesized by PSP*

## 8.4 RAMAN RESULTS

Raman spectroscopy was used to analyze the samples and complement HRTEM results for phase identification. The Rutile phase of $TiO_2$ is tetragonal and exhibits symmetry characters of the space group $D_{4h}^{14}$ with two $TiO_2$ formulas per unit cell. Four active Raman modes, with symmetry $B_{1g}$ (143 $cm^{-1}$), $E_g$ (447 $cm^{-1}$), $A_{1g}$ (612 $cm^{-1}$) and $B_{2g}$ 826 $cm^{-1}$. Whilst the Anatase phase has a tetragonal $D_{14h}^{19}$ containing two units per unit cell. According to group theory, there are six Raman Active modes with symmetry $E_g$ (143 $cm^{-1}$), $E_g$ (196 $cm^{-1}$), $B_{1g}$ (397 $cm^{-1}$), doublet ($A_{1g}$+$B_{1g}$) 516 $cm^{-1}$ and $E_g$ (640 $cm^{-1}$).

### 8.4.1 USP SAMPLES

Figure 8.9 (a) shows the Raman spectra of C-$TiO_2$ QDs synthesized by USP technique. The measured Raman spectrum Figure 8.9 (a) shows that the as synthesized nano-particles for C-$TiO_2$ are well crystallized in the Anatase phase of $TiO_2$. Such a conclusion is in good agreement with the HRTEM analysis**.** Figure 8.9 (b) also further highlights the peak shift in the main Anatase $E_{g1}$ mode which is attributed to either non-stoichiometry effects, grain strain, decrease in particle and or quantum confinement effects.

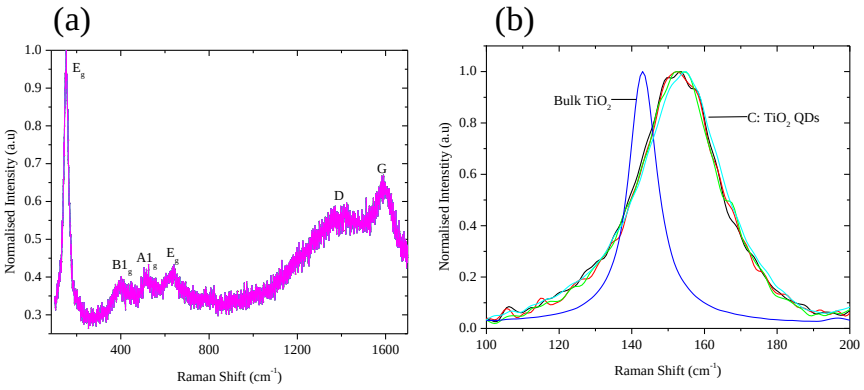


*Figure 8.9: (a) Raman spectrum for C-$TiO_2$ QDs synthesized by USP showing the presence of carbon D and G bands in the QD. (b) Illustrates peak shift of the main $E_{g1}$ mode caused by carbon doping and nano-sized effects*

It has been shown [9] that when $TiO_2$ are coated with carbon as core-shell particles, the main $E_{g1}$ mode of 144 $cm^{-1}$ shifts to ~150 $cm^{-1}$ as shown in Figure 8.9 (b). This is what we observed in our typical Raman spectrum for the USP sample where this phonon mode has shifted to 152 $cm^{-1}$. RS in this case suggests carbon doping in our samples which confirms the results from the EDS analysis where some carbon peaks originated from the doped samples and HRTEM results. We further extended our Raman spectrum to include the carbon bands as shown in Figure 8.9(a) We observed the D-band of the disordered carbon at 1354 $cm^{-1}$ and the perfect graphite peak at 1583 $cm^{-1}$ [1, 10]. This is a clear indication of the presence of carbon in these samples which supports the HRTEM results in this work. RS of the C-$TiO_2$ QDs also shows broadening and blue shift of the Anatase $E_{g1}$ phonon line shape Figure 8.9 (b) when compared to bulk $TiO_2$ of mean size of 50 nm. This is an indication that either there is optical phonon confinement [11] or the inhomogeous laser heating effects on the $TiO_2$ nanostructures [4, 12-14] or both. The measured Raman spectrum shows that the as-prepared $TiO_2$ nano-crystals are well-crystallized in the Anatase structure.

### 8.4.2 PSP SAMPLES

Figure 8.10 shows a Raman Spectra for C-$TiO_2$ QDs for three samples synthesized by PSP. $TiO_2$ is known to exhibit six Raman active bands characteristic of anatase phase at 144, 197, 399, 515, 519, and 639 $cm^{-1}$ with symmetries of $E_g$, $E_g$, $B_{1g}$, $A_{1g}$, $B_{1g}$, and $E_g$ respectively [4-8].

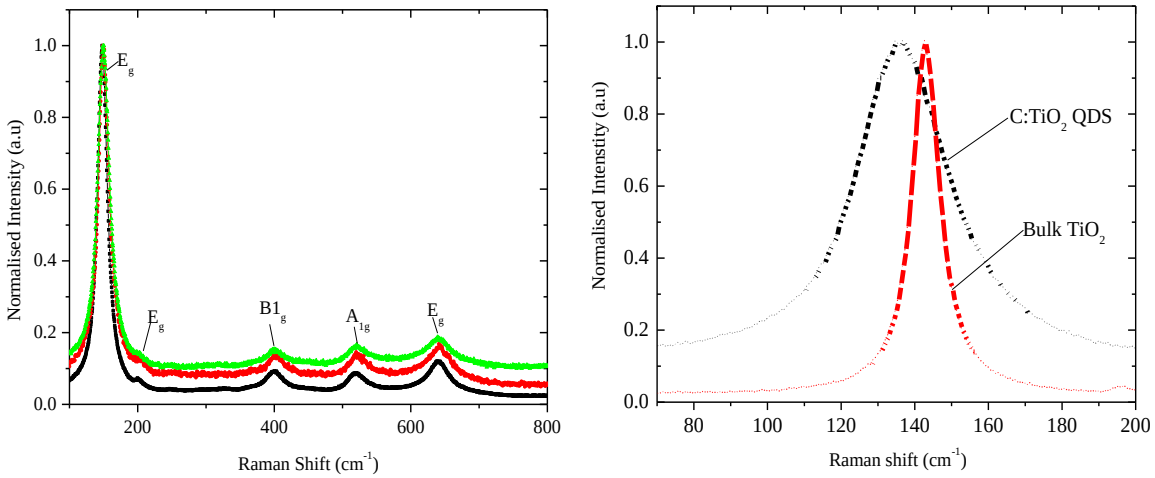


*Figure 8.10: Raman spectroscopy of the C-$TiO_2$ QDs synthesized by PSP technique showing characteristic Raman active modes. (b) Shows peak shift of the main $E_{g1}$ mode as compared to that of the bulk Anatase peak*

The Raman spectra in Figure 8.10 (a) confirms that the synthesized C-$TiO_2$ QDs have an Anatase crystalline state, with first $E_{g1}$ peak at 148 $cm^{-1}$ shifted and broadened as compared to that of bulk Anatase $TiO_2$. The broadening and shift of the Raman peaks observed in C-$TiO_2$ QDs are attributed to either phonon confinement as particle size decreases or non stoichiometry effects caused by the incorporation of carbon into the structure of $TiO_2$.

## 8.5 FT-IR ANALYSIS

### 8.5.1 USP SAMPLES

FT-IR spectroscopy in the transmission mode gives qualitative information about the way in which the adsorbed molecules are bonded to surfaces as well as the structural information of solids. Figure 8.11 reveals the FTIR spectra of the pure un-doped bulk Anatase $TiO_2$ compared with that of C-$TiO_2$ QDs synthesized by USP technique. The FTIR spectra of both bulk Anatase $TiO_2$ and C-$TiO_2$ QDs shows an absorption peak at 664 $cm^{-1}$ which is indicative of Ti-O bond in $TiO_2$.

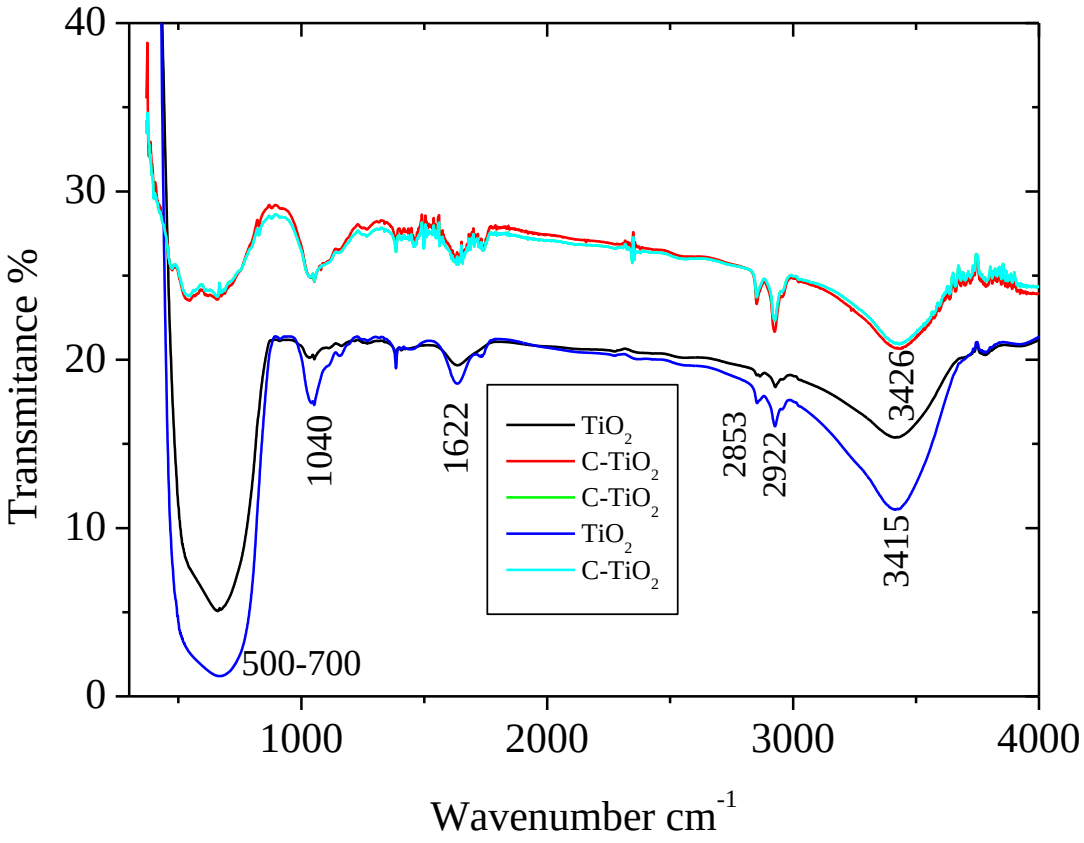


*Figure 8.11: FTIR presents spectrum of bulk Anatase $TiO_2$ compared with that of C-$TiO_2$ QDs synthesized by USP technique*

The measured FTIR shows that the as-prepared $TiO_2$ nano-crystals are well-crystallized in the Anatase structure. The analysis also show that the spectra for C-$TiO_2$ samples are very similar in general to that of the pure un-doped $TiO_2$ samples except for some of the differences in that the carbon modified sample visibly makes (1) the splitting of the main Ti-O phonon (at 664 $cm^{-1}$) into two – one at 659 $cm^{-1}$ and another at 536 $cm^{-1}$ (2) the emergence of new absorption peaks in the range from 1400 to 1600 $cm^{-1}$. The phonon splitting is due to small particle size whereas the new peaks in the range from 1400 to 1600 $cm^{-1}$ are due to the presence of carbon in the particle.. The spectra of C-$TiO_2$ QDs show peaks at 1635 and 3428 $cm^{-1}$ which can be attributed to the stretching and bending of the hydroxyl groups bonds on the $TiO_2$ surface respectively. The presence of the absorption peak at 1021 $cm^{-1}$ corresponds to (Ti-O-C-) carbonyl group this gives evidence of carbon doping which is good agreement with our HRTEM, RS and EDS measurements.

### 8.5.2 PSP SAMPLES

Figure 8.12 shows the FTIR spectra of C-$TiO_2$ QDs synthesized by PSP technique. We have to admit that both the FTIR spectra of USP synthesized samples (Figure 8.18) and that of PSP synthesized samples (Figure 8.19) showed similar spectra with no clear cut differences. But for the sake of completeness the FTIR spectra of C-$TiO_2$ QDs synthesized by PSP technique is shown in Figure 8.19.

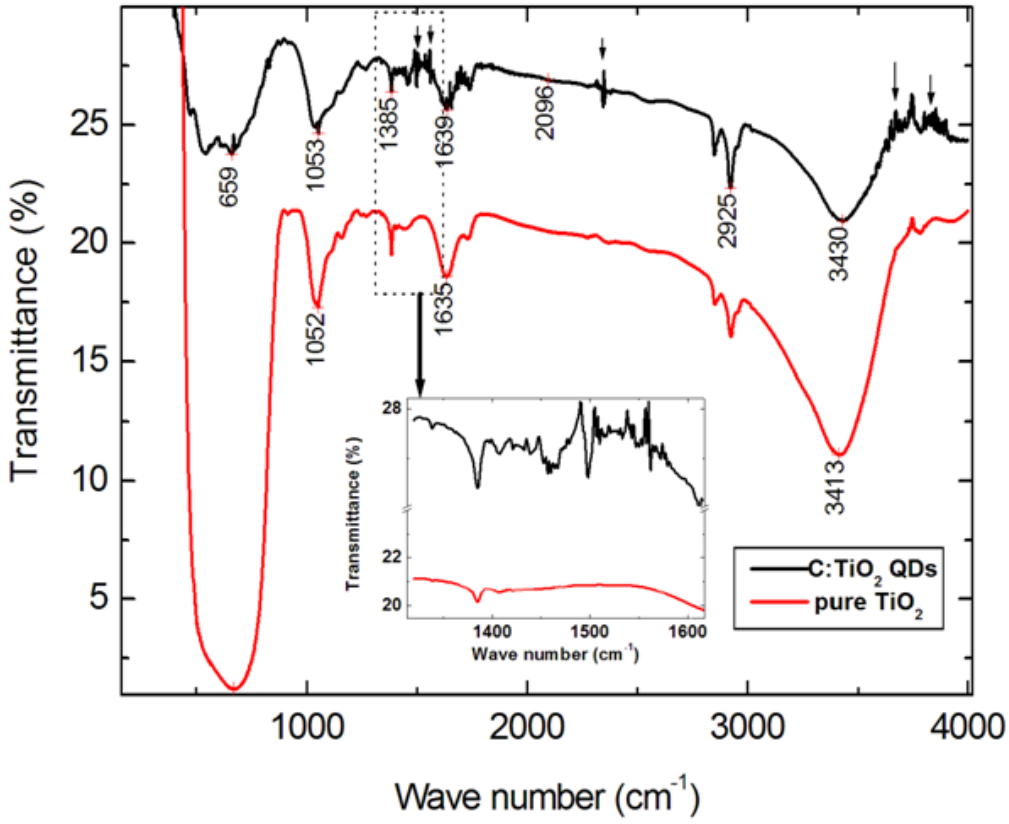


*Figure 8.12: Typical FT-IR spectrum of C-$TiO_2$ QDs synthesized by PSP*

The spectra also show that the QDs synthesized have Anatase crystalline structure. The analysis also show that the spectra for C-$TiO_2$ samples are very similar in general to that of the pure bulk Anatase $TiO_2$ samples except for some of the differences in that the carbon modified sample visibly makes (1) the splitting of the main Ti-O phonon (at 664 $cm^{-1}$) into two– one at 659 $cm^{-1}$

and another at 536 $cm^{-1}$ (2) the emergence of new absorption peaks in the range from 1400 to 1600 $cm^{-1}$. The phonon splitting is due to small particle size whereas the new peaks in the range from 1400 to 1600 $cm^{-1}$ are due to the presence of carbon in the particle. The analyses show that the spectra for both USP and PSP samples have similar spectra.

## 8.6 UV-VISIBLE SPECTRA FOR BOTH USP &PSP SAMPLES

As far as the absorption visible solar radiation is concerned, it is well known that pure $TiO_2$ can only absorb light below the wavelength of 387.5 nm because its band gap is $3.2\,eV$ . In order to extend the absorption region of $TiO_2$ to use the majority of the sunlight of the solar spectrum, doping of titanium dioxide with non metals, transition metals, and composite transition metal oxide has been employed [12-14,]. Doping of $TiO_2$ inhibits recombination of photo-generated electrons and holes by increasing the charge separation and therefore enhances the efficiency of photon generation [14]. Carbon has been found to be a suitable dopant for $TiO_2$, in applications that involve solar energy conversion. The presently carbon doped $TiO_2$ samples both by USP showed a strong and broad absorption band around 637 nm for PSP and 682 nm for USP in the UV-Vis-IR spectra (not shown). The solar emission spectrum ranges from 250 nm to 2500 nm. The shift in the absorption from below 387.5 nm (pure $TiO_2$) to 637 nm (C-$TiO_2$ QDs) is a positive indication that the C-$TiO_2$ samples will perform different in a solar cell. This shift in absorption spectra maybe due to incorporation of carbon into the titanium dioxide lattice structure, this might also be due to quantum confinement effects, and or non stoichiometry effects caused by the creation of oxygen vacancies. We also noted the USP sample had a much greater reder shift in the absorption spectrum of (682 nm) as compared to (637 nm) for PSP this might be due to the fact that USP techniques caused Substitutional carbon doping which led to high number of oxygen vacancies, where most of the oxygen atoms in the titanium dioxide lattice structure where replaced by carbon during doping. Whereas most carbon atoms are incorporated in between atoms in the titanium dioxide lattice structure which is called interstitial carbon doping, these analyses supports the HRTEM findings where we found out that *d* spacing in USP synthesized was smaller than that of pure Anatase $TiO_2$ hence in PSP interstitial carbon doping takes place and the same result has been observed by Howard ***et al.*** [3].

## 8.7 *I-V* ANALYSIS QDs

The four – point probe *i-V* curve characteristic of the glass substrate Figure 8.13(a) with a voltage sweep from -0.4 mV to 0.4 mV, the *i-V* curve shows that there is a linear relationship between current and voltage where I~σ. V (σ being the conductance) and it also shows that the F: $SnO_2$ on the glass substrate is indeed a transparent ohmic conductor.

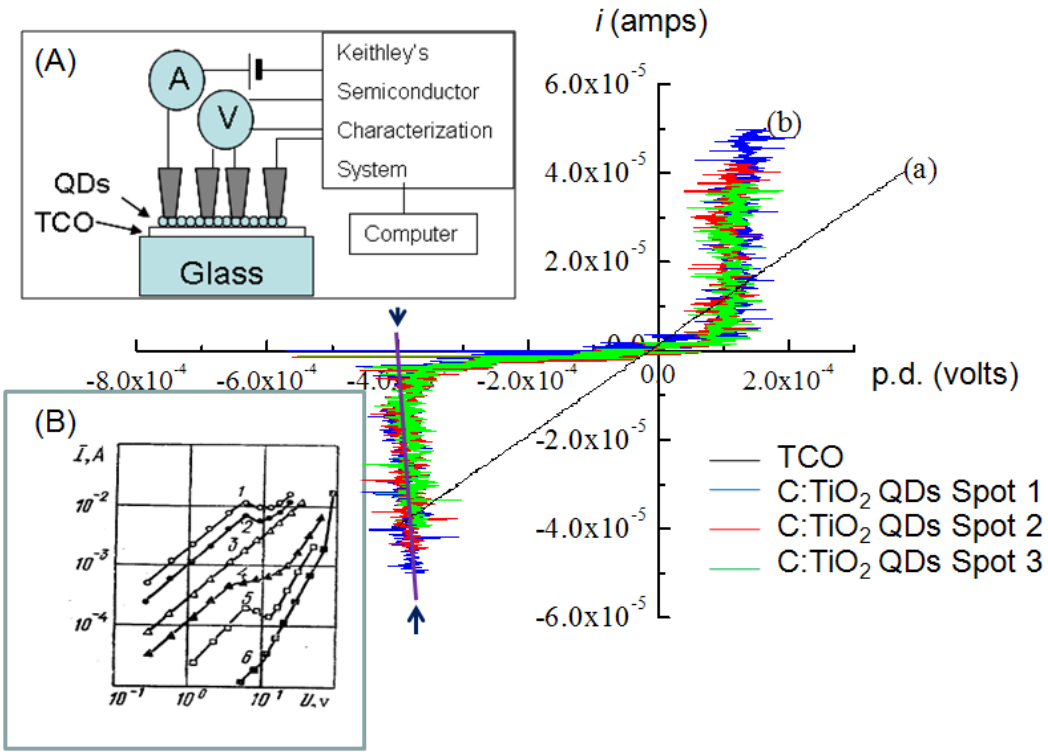


*Figure.8.13*: *Shows the i-V characteristics of the C-$TiO_2$ QDs synthesized by USP. Inset (a) of this Figure shows the schematic of the experimental set-up used in acquiring the current-voltage data on a Keithley 4200 semiconductor characterization system (SCS).*

Typical *i-V* characteristics of C-$TiO_2$ QDs deposited on FTO glass substrate are shown in figure 8.13 (b) with a voltage sweep in the range of -80 µV to +20 µV. The measurements from different spots gave slightly different values, which is caused by inhomogeneous deposition of the quantum dots onto the glass substrates during spray pyrolysis. However, there is a general similarity of the *i-V* curves for the different spots. On all spots of the C-$TiO_2$ QDS film, the *i-v*

curves clearly suggest that the QDs are semi-conducting with a band gap determined from the width of the *i-V* curve when current is nearly zero. The band gap here expressed in volts is found to be about $4 \times 10^{-4}$ V. Extra calibration is required to convert this reading into electron-volts (*eV*). This is beyond the scope of this work. However, this value could be comparable to the band gap of $TiO_2$ of 3.2 *eV* found by other methods [12-14, 24 ]. The deviation of the $E_g$ from 3.2 *eV* should be proportional to the amount of carbon doping and also particle size.

Also from the *i-V* curves one could speculate the type of conductivity one gets in the C-$TiO_2$ QDs. $TiO_2$ is naturally n-type semiconductor. Doping with carbon is expected to increase the electron density and make it more n-type. We have drawn a straight line on this portion of the curves and highlighted it with arrows to guide the reader's eye. This line [purple line with blue arrows] clearly indicates a negative slope which suggests "negative conductance". This apparent negative conductance could be due to the so-called Gunn effect which was discovered in III-V compounds such as GaAs and InP and reported by Gunn in 1963 [15-24]. Gunn saw that when an electric field reaches a threshold value in some materials the mobility of electrons decreases as the electric field is increased further, thereby producing negative resistance. Other authors such as Cope & Penn [26] and Stefanovich *et al.*, [15] have reported S-shaped *i-V* curves in $VO_2$ which show negative conductance.

At a critical current, a core of the low resistivity phase was seen to be formed and this was attributed to the falling of the voltage across the device while the current increased to a value dependent on a specific load line. With further increases in the circuit current, the voltage across the device was seen to decrease slightly. Also the role of doping on the negativity of the slope in the *i-v* curves has been reported in boron-doped diamond [16] pointing this phenomenon to the *n*-type conductivity of these type of diamonds. Furthermore, by inspection, the i-v curves are not symmetrical about the $V = 0$ point but rather shifted to negative voltages such that if one fits some analytical function $i(V)$ such as the Shockley's diode equation among others and calculates the area under the *i-V* curves in the negative voltage and positive voltage sections, one can state that

$$If \quad \int_{-V}^{0} i(V)dV > \int_{0}^{V} i(V)dV \quad \begin{matrix} then & n-type \\ else & p-type \end{matrix} \tag{8.3}$$

The integral of i(*V*)*dV* calculates the total electrical energy dissipated on charge carriers. The principle in Equation( 8.3) states that if more electrical energy is spent on driving the negative charge carriers in a semiconductor then such a material is intrinsically n-type and vice versa. From the curves in Figure 8.13, 20 nW are spent on electrons whereas only 5 nW are spent on the holes. We then sufficiently conclude that our carbon-doped $TiO_2$ QDs are indeed *n*-type which is a necessary precursor for our planned DSSC electrode and our photochemical solar cells (PECs). The as synthesized and characterized C-$TiO_2$ QDs where used as solar absorbers in photochemical solar cells (PECs) the results and findings will be discussed in the next section.

## 8.8 PHOTOCHEMICAL SOLAR CELLS DEVICES

With the carbon doped $TiO_2$ electrode results, we continued to build dye sensitized solar cells containing $TiO_2$ electrodes of varying carbon dopant concentrations. This concentration is calculated from the amount of dopant in *mg* for every litre of the total volume of the precursor material. The solar cell area was kept constant at 1.8 $cm^2$. The current-voltage characteristics of each individual cell are presented in Figure 8. 14 (a). Efficiency values were calculated from open-circuit voltage values and short-circuit current obtained from these current-voltage output characteristics.

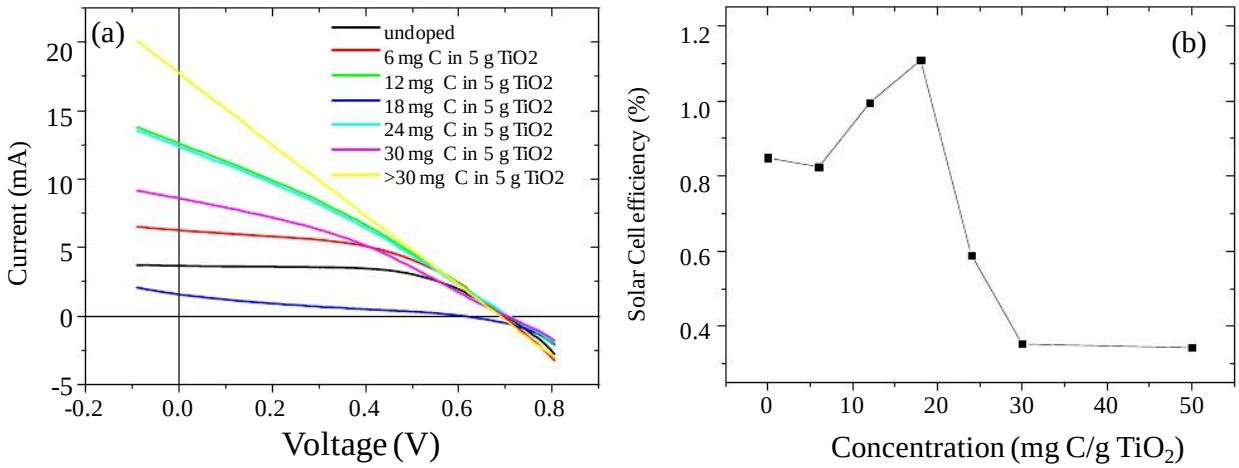


*Figure 8.14*: (*a) I-V characteristics of the typical PEC solar cell device containing varying mg of carbon in the $TiO_2$ as electrode (b) Efficiency of such solar cells as a function of carbon concentration*

The efficiency values at varying carbon concentration are given in Figure 8.14 (b). The current efficiency values (~0.08-0.5%) are admittedly much lower than those obtained for dye sensitized solar cells (~5-11%). This can be improved by employing more careful fabrication processes. However, the current results, at the laboratory scale, show that carbon concentration does increase the efficiency of the dye sensitized solar cell by about 5 times over the solar cell with prestine $TiO_2$ layer.

## 8.9 CONCLUSION

A spray pyrolysis (USP and PSP) route for production of C-$TiO_2$ nano powders was used and further developed. The decomposition of titanium tetraethoxide droplets produced gram quantities of nano-sized powder. The powder production at 450 °C in argon atmosphere formed nano-crystalline C-$TiO_2$ Anatase nano-powders. The samples synthesized further observed to be oxygen-deficient C-$TiO_2$, which is given as the reason for the presence of phase-stable Anatase. Nano-crystalline carbon doped titanium dioxide C-$TiO_2$ QDs were formed without annealing. Both micron-sized and ultrafine titanium dioxide particles were produced and characterized. The most important results from this study are briefly highlighted in the sections that follow.

### 8.9.1 HRTEM ANALYSES

C-$TiO_2$ QDs have been synthesized by a cost effective chemical spray pyrolysis route. HRTEM analysis has revealed that the synthesized QDs are mostly spherical for USP and are oval for PSP. The analyses has also revealed that the QDs synthesized by USP and PSP have nano particles in the range of 2.5-5.5 nm and 1.5-8.5 nm with modal QDs sizes of 3.5 nm and 5.5nm, respectively. The size measurements have revealed a wide particle size distribution for the QDs synthesized by PSP as compared to the narrow particle size distribution for USP. This might be due to the fact that Cavitation mechanism dominates as a mechanism for droplet generation in PSP, whilst in USP the capillary wave mechanism dominates. HRTEM analyses has also shown that lattice fringe separations for USP and PSP to be 2.017 Å and 3.74 Å, respectively, suggesting substitutional carbon doping for USP and a mixture of substitutional and interstitial carbon doping for PSP. This shows that USP is a better technique for incorporation of carbon into titanium dioxide matrixes. Elemental analysis by EDS has revealed the presence titanium, oxygen and carbon in both sample synthesized by USP and PSP, with the only exception that the samples synthesized by PSP had a higher purity as compared to those synthesized by USP. We also observed additional carbon from both USP and PSP synthesized samples which originated from the glucose dopant. These results also show us that titanium tetraethoxide was successfully converted to carbon doped titanium dioxide. Fast Fourier analyses also revealed that the as synthesized QDs have a display the fact that only the main diffraction (reflection) plane of Miller

indices (101) in $TiO_2$ is responsible for the diffraction pattern that gives rise to the HRTEM images. The higher magnification HRTEM clearly reveals that USP TiO2 QDs have a very small *d*-spacing compared to the normal anatase spacing of 0.352 nm. The *d*-spacing found in this sample is about 0.202 nm.

### 8.9.2 FT-IR ANALYSES

FT-IR analyses has revealed that the as synthesized C-$TIO_2$ QDs samples are well crystallized in anatase structure, the only difference with Ti-O bond at 664 $cm^{-1}$ and the spectra is similar to that of pure $TiO_2$ samples, with some exceptions. The FT-IR spectra of C-$TiO_2$ QDs samples also show (1) the splitting of the main Ti-O phonon (at 664 $cm^{-1}$) into two – one at 659 $cm^{-1}$ and another at 536 $cm^{-1}$ (2) the emergence of new absorption peaks in the range from 1400 to 1600 $cm^{-1}$. The phonon splitting is due to small particle size whereas the new peaks in the range from 1400 to 1600 $cm^{-1}$ are due to the presence of carbon in the particle. The spectra also showed peaks at 1635 and 3428 $cm^{-1}$ which can be attributed to the stretching and bending of the hydroxyl groups bonds on the $TiO_2$ surface respectively. The presence of the absorption peak at 1021 $cm^{-1}$ corresponds to (Ti-O-C-) carbonyl group this gives evidence of carbon doping which support the Raman, HRTEM and EDS analyses.

### 8.9.3 RAMAN SPECTROSCOPY

Raman spectroscopy analyses have revealed that the synthesized C-$TiO_2$ QDs have an Anatase crystalline structure, this has been evidence by the presence of main Anatase $E_g$ mode peak at 152 cm-$^{1}$, which has been blue shifted from 143 $cm^{-1}$. The RS has also revealed the presence of carbon in our samples, which agrees well with EDS analyses which also showed the presence of carbon peaks on our EDS spectra. The RS shows carbon peaks at 1354 $cm^{-1}$ for disordered carbon D band and a perfect graphite peak at 1583 $cm^{-1}$, this clear indication supports our HRTEM results.

### 8.9.4 I-V CHARACTERIZATION

*i-V* curves characterization for both PSP and USP samples have revealed the as synthesized C-$TiO_2$ QDs have a "negative conductance''. Furthermore we discovered that the *I-V* curves are not symmetrical about the $V = 0$ point but rather shifted to negative voltages. We then fitted an analytical function $i(V)$ such as the Shockley's diode Equation (8.3). Upon calculating the area under the *i*-V curves in the negative voltage and positive voltage sections we discovered that 20 nW are spent on electrons whereas only 5 nW are spent on the holes. We then sufficiently conclude that our C-$TiO_2$ QDs are indeed *n*-type which is a material property for our planned PECs electrodes. The C-$TiO_2$ QDs produced in this study show properties that would not only make the materials suitable for photo-catalytic activity, but also for electrodes in Grätzel-type of solar cells. Efficiency values for solar cells of varying carbon concentrations in their $TiO_2$ electrodes show up to 1.5 times improvement over the pure $TiO_2$ electrode based in photochemical solar cells.

### 8.9.5 UV-VIS SPECTROSCOPY

UV-Visible spectroscopy has shown that the synthesized QDs had absorption edges of 637 nm and 683 nm for a number of samples analysed for PSP and USP respectively. The red shift of the adsorption edge of C-$TiO_2$ QDs can be attributed the doping effect.

## 8.10 REFERENCES


1. Katumba, G.; Mwakikunga, B.W.; Mothibinyane, T.R.; *Nanoscale Res Lett.*, **2008** 3, 421
2. Xu, C.; Shaban, Y.A.; Ingler Jr W.B., Khan, U.M.; *Solar Energy Mater. & Solar Cells* **2007,** l91, 938
3. Howard, C.J.; Sabine, T.M.; Dickson, F.; *Acta Crystallogr*. *Section B: Structural Science* **1991**, 47, 462
4. Palaniappan PL.RM.; Pramod K.S. *Vibrational Spectroscopy*. **2011**, 56(2), 146-153
5. Balachandran U.; Eror N.G. *Journal of Solid State Chemistry*. **1982**, 42(3), 276-282
6. Bersani, D.; Lottici, P.P.; Ding, X.Z.; *Appl. Phys. Lett*.;**1998** 72, 73
7. Luca, D, Has, L.S.; J. *Optoelectronics & Advanced Mater*. **2003**' 5, 835
8. Suthyanoorthy, R.; Sudhagar, P.; Chadramohan, S.; Vijayakumar, K.P.; *Cryst. Res. & Technol*. **2007**, 42, 498
9. Hu, X.; Zhanga, T.; Jina; Z.; Zhanga, W.; Xua, J.; Yana, J.; Zhanga, L. Zhang, Y.; Wua, *Mater. Lett*. 2008 62, 4579
10. Blanpain B.; Franck M.; Mohrbancher H.; Vancoille E.; Celis J.P. Roos J.R. *Thin Films in Tribology*. **1993**, 25, 623-630
11. Mwakikunga, B.W.; Forbes, A.; Sideras-Haddad, E.; Arendse, C. *Phys. Stat. Solidi* (a). .**2008**, 205, 150
12. Lottici P.P.; Bersani D.; Braghini M.; Montenero A. *Journal of Material Science*. **1993**, 28, 177-183
13. Ibrahim A. Alhomoudi.; Newaz G. *Thin Film Solids*. **2009**, 517(15), 4372-4378
14. Karunangaran B. Kyunghae K.; Mangalaraj D.; Junsin Yi.; Velumani S. *Solar Energy Materials and Solar Cells*. **2005**, 88(2), 199-208
15. Zhu, K. R.; Zhang, M. S.; Chen, Q.; Yin, Z. *Phys. Lett. A*. **2005**, 340, 220
16. Wang, D.; Zhao, J.; Chen, B.; Zhu, C.; *J. Phys.: Condens. Matter*, **2008**, 20, 085212
17. Bhattacharyya, S.; Samui, S.; *Appl. Phys. Lett*. **2004**, 84, 1564
18. Mikami, M.; Nakamura, S.; Kitao, O.; Arakawa, H. *Phys. Rev. B 66*, **2002**, 155213
19. Arora, A. K.; Rajalakshmi, M.; Ravindran, T. R.; Sivasubramanian, V.; *J. Raman Spectrosc.* **2007**, 38, 604
20. Ohsaka, T.; *J. Phsc.Soc. Jpn* **1980**, 48, 1661

21. Gao, K.; Physica B **2007**, 398, 33-37
22. Stefanocich, G.; Pergament, A.; Stefanovich, D.; *J. Phys. Condens. Matter* **2000**, 12, 8837
23. Gunn, J.B.; Solid State Commun. 1 **1963**, 88
24. Cope, R.G.; Penn, A.W.; Britt, J.; *Appl. Phys. (J. Phys*.D) **1968**, 1, 162

# CHAPTER 9
# CONCLUDING REMARKS

## 9.1 ULTRASONIC SPRAY PROLYSIS

A detailed review was given on models for estimating droplet size generated by ultrasonic pyrolysis has been laid out from 1871 up to date. The shortfalls of these droplet relation models in estimating final droplet size have been given. We went further into deriving a new relation for estimation of the final nano-particle size given a set of initial reaction condition which has been done for the first time. Other droplet relations given in literature, when estimating final particle size, do not consider the physical conditions such as temperature of the precursor solution, viscosity of the precursor solution or the volume of the ultrasonic chamber. The derived nano-particle correlation model in this work considers all of these. We have to admit that the presently derived nano-particle correlation model is specifically for $TiO_2$ precursor solution and there is need to develop a model that is independent of the precursor solution type.

A simple and cost effective ultrasonic spray pyrolysis technique has been designed and constructed. The USP system has been used in fabricating from C-$TiO_2$ QDs to solar cells C-$TiO_2$ thin films with novel structural optical and electronic properties. The constructed USP system allows the operator to deposit samples at 0° degree, which allows the aerosol beam containing precursor vapor to interact directly with the substrate uniformly. Furthermore this allowed the system to use, low deposition rates, and the ability to deposit for a wide range of thin films via this method using different liquid precursors. Many of the desired $TiO_2$ film properties were obtained from films deposited using the USP system.

## 9.2 PHONON CONFINEMENT IN C-$TiO_2$ QDs

It has been shown that phonon confinement by means of Raman spectroscopy was observed in C-$TiO_2$ quantum dots and the phonon confinement models available in literature have been used to obtain for the first time phonon dispersion relations of C-$TiO_2$ quantum dots. Also a new phonon confinement model was derived and fitted to C-$TiO_2$ data. From this fit the following parameters were extracted $A_0' = 10^{-17}$, $\alpha = 3\ \pi^2$ (~ 30), $\omega_0 = 150.4$ cm$^{-1}$, $B = 0.005$ cm$^{-2}$ and $\Gamma_0 = 20$ cm$^{-1}$. Also the value of 20 cm$^{-1}$ for $\Gamma_0$ is 13 cm$^{-1}$ above the value for bulk $TiO_2$. Furthermore the size distribution integral in the phonon confinement model has been replaced by an expression $A_1 + m\ \omega = 0.25 + 0.008\ \omega$. The experimental findings have shown that the blue-shift of the central brillouin zone phonon frequency from 143.4 cm$^{-1}$ for particles of mean diameter of 50 nm of pure $TiO_2$ to 150.4 cm$^{-1}$ for particles of mean diameter of 6 nm is not only due to reduction of particle size and or phonon confinement but also could be due to the presence of carbon in the $TiO_2$ structure. Room temperature Raman spectroscopy was done for the first time on C-$TiO_2$ and it revealed that the as-synthesized nano-particles are predominantly Anatase with the $E_{g(1)}$ at 152.9 cm$^{-1}$ blue shifted due to carbon doping and decrease in particle size This is the first time that temperature dependence of Anatase C-$TiO_2$ is being reported.

## 9.3 STRUCTURAL OPTICAL AND ELECTRICAL PROPERTIES OF C-$TiO_2$

C-$TiO_2$ QDs have been synthesized by a cost effective chemical spray pyrolysis route. HRTEM analysis has revealed that the synthesized QDs are mostly spherical for USP and are oval for PSP. The analyses has also revealed that the QDs synthesized by USP and PSP have nano particles in the range of 2.5-5.5 nm and 1.5-8.5 nm with modal QDs sizes of 3.5 nm and 5.5nm, respectively. The synthesized C-$TiO_2$ QDs are *n*-type. The C-$TiO_2$ QDs produced in this study show properties that would not only make the materials suitable for photo-catalytic activity, but also for electrodes in Grätzel-type of solar cells. Efficiency values for solar cells of varying carbon concentrations in their $TiO_2$ electrodes show up to 1.5 times improvement over the pure $TiO_2$ electrode based in photochemical solar cells.

## 9.4 PEC SOLAR CELLS DEVICES

Solid state photo- electrochemical solar cells (PECs) were synthesized using C-$TiO_2$ photo electrodes. As reported carbon doping of nano crystalline titanium dioxide was found to be beneficial for PEC solar cell device performance, with significant improved photo voltage value of 0.817 V as compared to pure dye sensitized solar cells devices which employ pure un-doped $TiO_2$ with a max photo voltage of 0.75 V. This improvement in photo voltage output is found to be correlated with the electronic and optical properties of the nano-powders used in fabrication of PEC devices. PEC devices with a, $45_{TBA}$ C-$TiO_2$ photo electrode showed the highest solar conversion with an open circuit voltage of ($V_{OC}$) of 0.817 V, photocurrent $J_{SC}$ of 1.37639 $mA/cm^2$, a fill factor of 54.5% and an efficiency of 0.613%.Admittedly the overall solar cell efficiency for the PEC devices employing TBA doped titanium dioxide is still very low ~0.6% as compared to the dye sensitized counterpart fabricated by Grätzel in 1991 with an efficiency of ~11%. Therefore, C-doped $TiO_2$ nano-crystals prepared by our approach are ideal semiconductor materials for DSSC and PEC solar cell devices. This study has revealed that our method of fabricating PEC devices using ultrasonic spray pyrolysis has low cost, simple processing, excellent reproducibility, easy to extend on a large scale production and is applicable in the field of solar energy conversion.

## 9.5 POTENTIAL RESEARCH PROJECTS FROM THIS STUDY

To end this work one can propose by pointing out a few possible areas of this research that would need further pursuit as separate areas.

The first would be improvements of the ultrasonic spray pyrolysis technique. Whilst ultrasonic spray pyrolysis employing tube reactors allow the precise control process control and therefore allow for particle the production with desired structural, optical and electronic properties. There are high agglomeration rates in the produced nano-particles. There is need to prevent nano-particle agglomeration. They are various methods available for reduction of particle agglomeration. Furthermore ultrasonic spray pyrolysis systems employing tube reactors have high input volumes of reactants and low output volumes of nano-particles. They are

characterized by low production rates of nano-particles. Vast amounts of particles are lost within the tube reactor. During the production of C-$TiO_2$ we observed thick film layers of nano-particles on the walls of either the (1) aluminum tubing or the quartz tubing (2) substrate holder and (3) in the exhaust pipe. There is a need to reduce these loses. It would be ideal to replace the tube reactor with a wall less reactor such as laser beam.

There are numerous droplet correlation models that are available in literature that have been reviewed here in Chapter 3. However all these droplet relations focus on estimating the initial aerosol vapor droplet and up to date there are no relations that estimate the final particle size produced in ultrasonic spray pyrolysis systems. In Chapter 3 we have provided a correlation model that estimate final nano-particle size for pure titanium dioxide systems. However there is need to develop a universal final particle correlation model for estimating final nano-particle sizes produced by USP systems.

# APPENDIX A
# RESEARCH OUTPUTS

The research outputs associated with PhD thesis include papers presented at conferences both national and international, papers published in international journals and seminars presented at the University of Fort Hare.

## A.1 CONFERENCES

- 53rd SAIP Annual Conference – held in Polokwane at University of Limpopo in July 2008
- IBSA Conference held in Johannesburg 2008
- 54th SAIP Annual Conference – held in Durban at University of KZN in July 2009
- 55th SAIP Annual Conference – held in Pretoria, CSIR in September 2010
- 56th SAIP Annual Conference held in University of South Africa, Pretoria, 2011
- 57th SAIP Annual Conference held in Pretoria at the University of Pretoria 2012

## A.2 GENERAL PRESENTATIONS

- FHIT departmental seminar series proposal presentation: Fabrication of C-$TiO_2$ tandem solar cells 2011
- FHIT departmental seminar series: Modeling of final droplet diameter produced by ultrasonic spray pyrolysis technique
- FHIT departmental seminar series: Design of ultrasonic spray pyrolysis system
- FHIT departmental seminar series: Raman temperature dependency analysis of carbon doped titanium dioxide quantum dots synthesized by spray pyrolysis technique
- FHIT departmental seminar series progress report presentation: Structural optical and electrical properties of nano-sized titanium dioxide quantum dots synthesized by spray pyrolysis

## A.3 PUBLICATIONS

1. R Taziwa, E.L. Meyer, E. Sideras-Haddad, R.M. Erasmus, E Manikandan and B.W. Mwakikunga: Effect of Carbon Modification on the Electrical, Structural, and Optical Properties of $TiO_2$ Electrode and Their Performance in Labscale Dye Sensitized Solar cells: International journal of Photoenergy Volume 2012, Article ID 904323,9 doi10.1155/2012/904323

2 R Taziwa, E.L. Meyer, KG. Chinyama: Raman temperature dependence analysis of carbon doped titanium dioxide nano-particles synthesized by ultrasonic spray pyrolysis technique; Journal of Material Science Volume 47, Issue 3, pp1531-1540;DOI 10.1007/s10853011-5943-4

3 Carbon doped nano-crystalline $TiO_2$ photo- active thin film for solid state photochemical solar cells. ***Accepted for SASEC 2014 (ID54)/ Journal of Applied physics***

4 R Taziwa and E.L Meyer: Modeling droplet size and final nano-particle size in ultrasonic spray pyrolysis. ***Submitted to Journal of Aerosol Science (Chapter 2).***

5 R Taziwa and E.L Meyer: Design of ultrasonic spray pyrolysis system. ***Submitted Journal of Engineering Design and Technology (Chapter 4)***

## A.4 POSTER PRESENATION AND AWARDS

Achieved the best phD poster presentation at 52 th South African institute of physics (SAIP) held in Pretoria 2011.

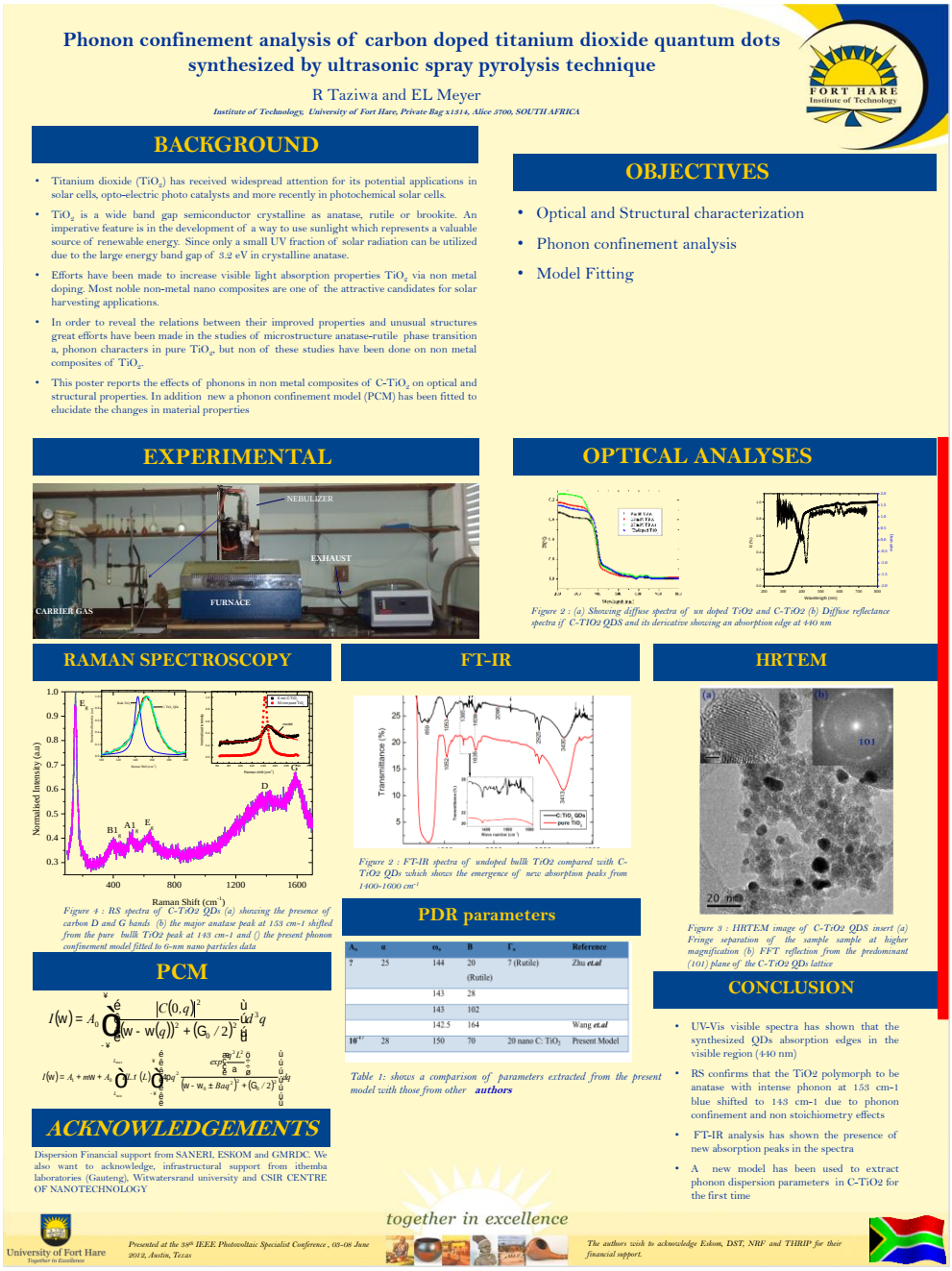


*Figure 4: Presents the award winning poster presented at the 57th South African institute of physics conference hosted by university of Pretoria 2012*

# Fort Hare Institute of Technology (FHIT) PhD student scoops award at SAIP conference

Recently, Raymond Taziwa, a PhD student with the University of Fort Hare's Institute of Technology, won the prize for the best poster presentation in the APPLIED PHYSICS category at the 57th South African Institute of Physics (SAIP) annual conference hosted by the University of Pretoria that run from 9 – 13 July 2012. This conference attracted around 300 delegates from all over South Africa and abroad.

Raymond is a second year PhD student under the supervision of Prof. Edson Meyer in the RENEWABLE ENERGY research group of FHIT where they are focusing on the development of a novel dye sensitized solar cell based on carbon-doped titanium dioxide nanoparticles. Commenting on the award, Prof Meyer said, "What is notable is that we managed to win an award which shows that the quality and standard of the work we do is cutting edge and is being recognized by other scientists."

Raymond, after receiving the best poster presentation prize for a PhD student, said, "I am extremely excited as I was not expecting to receive such an award given the stiff competition that comes with the many high quality presentations in SAIP conferences. I am really honored. This award was a culmination of a pioneering work we carried out where we were able to fit a phonon confinement model to the Raman spectra from carbon doped titanium dioxide quantum dots that we synthesized using ultrasonic and pneumatic spray pyrolysis techniques. These semiconductor nanostructures have light absorption properties in the visible region of the solar spectrum. These innovative materials are a key component in the development of low cost and efficient solar cells." He hopes that this prize will inspire many UFH students and boost their confidence that they can also conduct scientific research at a high level despite our classification as a rural and historically disadvantaged university.

***Raymond Taziwa pictured at the SAIP conference standing by his award-winning poster.***

***SAIP Prize presentation from Left- right R Taziwa, Dr. F Vorster (NMMU) and Prof. Simon Connell (U. Johannesburg)***

# Synthesis and characterization of Tandem dye-nanoparticle sensitized solar cells

*Novel Solar Cell Technology; efficient use of solar spectrum*

**Raymond Taziwa , Edson L. Meyer and Peter Ajibade**

**Institute of Technology, University of Fort Hare, Private Bag x1314, Alice 5700, SOUTH AFRICA**

## Objectives

- Broadening the Spectral Response of dye sensitized solar cells by fabricating a Tandem dye-nano particle sensitized solar cell with a carbon modified n-titanium dioxide photo anode and dye sensitized photo cathode.
- Synthesis and characterization of a stacked photo anode
- Fabrication and characterization of *p*-type photocathode
- Characterization of the tandem dye solar photovoltaic device.

## Introduction

- DSSC have achieved record efficiencies of 11% and have technical advantages or added value such as ease of fabrication, low cost and transparency.
- High spectral loses can be larger than 50 %. Large parts of the solar spectrum are not absorbed, this is because of the existence of a band gap $E_g$ of the dye.
- Photons with energy $E_{ph}$ larger than the band gap are not absorbed and the excess energy $E_{ph}$- $E_g$ is not used effectively due to thermalization of electrons . Photons with energy $E_{ph} < E_g$ are not absorbed.
- This inefficient exploitation of the solar spectrum is one the reasons why the PV-generated electricity is not cheap enough to compete with coal-based, hydroelectric and nuclear energies.

## Structure and Operation Principle

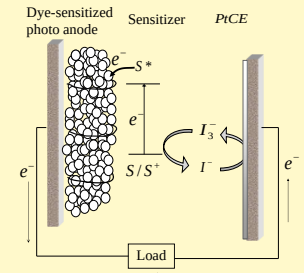


- $TiO_2/S + h\nu \longrightarrow TiO_2/S^*$
- $TiO_2/S^* \longrightarrow TiO_2/S^+ + e^-$
- $TiO_2/S^+ + {}^3/_2\, I^- \longrightarrow TiO_2/S + {}^1/_2 I_3^-$

## Background

- The Graztel photochemical solar cell has one photoactive dye sensitized anode and a passive photo cathode.
- To take the next big step next big step efficiencies of lets say 15% with nanocrystalline dye solar cells, there is a need to develop new concepts for DSSC.
- Replace the passive photocathode with a dye sensitized photoactive cathode as illustrated in the diagram on the left.
- And also develop a multijunction (stacked) photo anode as illustrated in the diagram on the left.

## Tandem Solar cell Structure

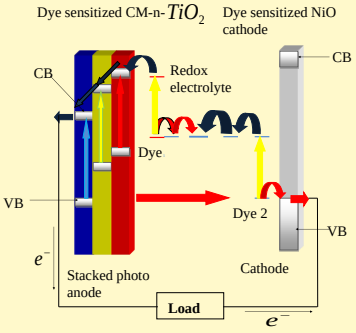


## Tandem solar cell Operation principle

1. **Dye sensitization**

$$CM-n-TiO_2/D_1 + h\nu_{D_1} \rightarrow CM-n-TiO_2/D_1^* + h_{D_1}^+$$

$$CM-n-TiO_2/D^*_1 \rightarrow CM-n-TiO_2/D^*_1 + \bar{e}_{CB}$$

2. **Nanoparticle Sensitization**

$$CM-n-TiO_2 + h\nu_n \rightarrow CM-n-TiO_2^{***}$$

$$CM-n-TiO_2^{***} \rightarrow CM-n-TiO_2/\bar{e}_{CB} + h^+$$

3. **Redox reactions**

$$CM-n-TiO_2/h^+ + \frac{3}{2}I^- \rightarrow CM-n-TiO_2 + \frac{1}{2}I^-_3$$

4. **Cathode reactions**

$$pNiO/h^+_{VB} \rightarrow h^+ + \bar{e}_{pt}$$

## Ultrasonic Spray pyrolysis

•Doping and deposition of stacked anode

•Development of a p-type nanoporous photocathode

Ultrasonic spray equipment at Wits University.

## Spectral response characterization

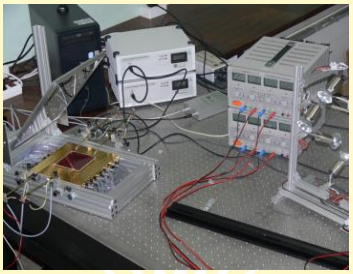

Spectral response setup at Fort Hare Institute of Technology.

## Expected Outcomes

- We expected to fabricate a tandem solar cell device with higher spectral response as compared to Graztel type solar cell.
- We expected to produce a solar cell with a higher photocurrent and photovoltage as compared to the Graztel solar cell.
- It is expected that the solar cell will have reduced electron-hole recombination.
- Its is expected that the solar cell will have a longer life span.

*together in excellence*

The authors wish to acknowledge Eskom, SANERI and GMRDC at the University of Fort Hare for financial support.

*Figure 5: A poster that was presented at 54th SAIP Annual conference Kwazulu Natal University 2009*